



**HAL**  
open science

## Development of rare-earth-free phosphors for LED-based lighting devices

Rachod Boonsin

► **To cite this version:**

Rachod Boonsin. Development of rare-earth-free phosphors for LED-based lighting devices. Other. Université Blaise Pascal - Clermont-Ferrand II, 2016. English. NNT : 2016CLF22704 . tel-01420122

**HAL Id: tel-01420122**

**<https://theses.hal.science/tel-01420122>**

Submitted on 20 Dec 2016

**HAL** is a multi-disciplinary open access archive for the deposit and dissemination of scientific research documents, whether they are published or not. The documents may come from teaching and research institutions in France or abroad, or from public or private research centers.

L'archive ouverte pluridisciplinaire **HAL**, est destinée au dépôt et à la diffusion de documents scientifiques de niveau recherche, publiés ou non, émanant des établissements d'enseignement et de recherche français ou étrangers, des laboratoires publics ou privés.

N° d'Ordre : D.U. 2704

**Université Blaise Pascal - Clermont-Ferrand**  
**U.F.R. Sciences et Technologies**

**ÉCOLE DOCTORALE DES SCIENCES FONDAMENTALES**  
**N° 867**

**THESE**

Présentée pour obtenir le grade de

**Docteur d'Université**

Spécialité : Chimie, Sciences des matériaux

Par

**Rachod BOONSIN**

Ingénieur Chimiste Diplôme de l'ENSCCF

Diplômé de Master II Sciences, Technologies, Santé : Chimie des Matériaux

**DEVELOPPEMENT DE LUMINOPHORES SANS TERRES RARES**  
**POUR L'ECLAIRAGE ECO-ENERGETIQUE A BASE DE DIODES**  
**ELECTROLUMINESCENTES**

Soutenue publiquement le 14 Juin 2016 devant la commission d'examen formée de :

- Président :** Raphaël SCHNEIDER, Professeur - Université de Lorraine
- Rapporteurs :** Alain IBANEZ, Directeur de recherche CNRS - Institut NEEL  
Stéphane DANIELE, Professeur - IRCELYON
- Examineurs :** Damien BOYER, Maître de conférences - Sigma Clermont - ICCF  
Jean-Philippe Roblin, Maître de conférences, Sigma Clermont - ICCF
- Invité :** Rachid MAHIOU, Directeur de recherche CNRS - ICCF
- Directeur de thèse :** Geneviève CHADEYRON, Professeur - Sigma Clermont - ICCF



Dedicated to My parents

My younger Brother

My cousins

Charassri



## Acknowledgements

It is an extreme pleasure to see my hard work and dedication that I authorized in my dissertation during all parts out of years of research since I came to the family of Chadeyron's group. During that time, I have worked with a great number of people who contributed to make this dissertation successfully with a special moment both intellectually and socially. Before starting the presentation of my Ph.D. thesis, I would like to express my heartfelt gratitude and sincere appreciation to all people who have helped and inspired me during my doctoral study.

First of all, I was ultimately lucky to have Pr. Geneviève Chadeyron, Dr. Damien Boyer and Dr. Jean-philippe Roblin as supervisors in my research work at Institute of Chemistry of Clermont-Ferrand (ICCF). Actually, I have worked with them since I was an international childlike student under the international program "N+I" at School of Chemistry of Clermont-Ferrand (ENSCCF). They are very nice and kindhearted person and I admire their abilities and friendly personality. They have taught me how to do the research, how to proceed the dissertation work. They have shared a huge amount of time on discussion and also on the revised procedures to complete the tasks in a limited time. I would like express my deep gratitude to all of you for their support, guidance, time, encouragement, motivation, inspiration, and immense knowledge from the beginning of study till the final revision of my dissertation.

I would like to give my sincerest appreciation to Dr. Rachid Mahiou, who is the research director of CNRS and the leader of Materials for Optics (MO) groups, for his support on my thesis and for his insightful advices in luminescent materials. Also, I offer my sincere thanks to Dr. Fabrice Leroux, who is the head of the Inorganic Materials (MI) team, for his help, discussions and invaluable expertise gifted to me throughout my field work.

I would like to express my gratefulness to members of jury that they accepted to judge this dissertation: xx, Alain Ibanez, Stéphane Daniele, Raphaël Schneider, Rachid Mahiou, Geneviève Chadeyron, Damien Boyer, and Jean-Philippe Roblin for their insightful comments and also for the hard question which incited me to widen my research from various perspective.

Throughout my Ph.D. life at the Institute of Chemistry of Clermont-Ferrand (ICCF) the continuous and generous support from the members of academic staff: Pr. Patrice Malfreyt, Pr. Sophie Commereuc, Pr. Sylvie Ducki, Pr. Philippe Boutinaud, Pr. Jean-Luc Gardette, Pr. Daniel Zambon, Dr. Khalil Bennis, Pr. Jean-Marie Nedelec, Pr. Agilio Padua, Pr. Claude Forano, Pr. Guillaume Renaudin, Pr. Yves Troin, Cr. Vincent Verney, Dr. Pierre-Olivier Bussière, Dr. Audrey Potdevin, Dr. Florence Delor-Jestin, Dr. Pascal Wong-Wah-Chung are greatly appreciated since I was a student under the international program "N+i". It was a great pleasure and honor to study and work with all of you.

The same gratitude is extended to Dr. Agnès Rivaton and Dr. Sandrine Therias for their expertise and advices of photo-degradation studies. Also I would like to thank Dr. Jérôme Deschamps and Dr. Rodolphe Deloncle, who were the former members of REVLUM, for their help and discussions in inorganic luminescent materials.

I owes special thanks to all the people who have dedicated part of their time to help me with the instrumentations needed to complete my dissertation: Anne-Sophie Besse and Règis Egrot (for their NMR experiments), Dr. Malika El-Ghozzi, Mr. Joël Cellier and Mr. Laurent Jouffret (for their XRD and single crystal measurements), Vincent Thery and Lionel Nauton (for their computational simulation), Rodolphe Thirouard, Elodie Petit, Martine Sancelme, Cecile Esparcieux, Yann Faschinetti, Gaelle Framery, Alexis Jean and Safia Laid (for all supports, experimental knowledge, and technical services)

I am also grateful to my family of Inorganic Materials (MI) team: Anthony Barros, Romain Jouve, Arthur Langry, Maimonatou Mar, Ayoub Nadi Yasser Ahmad, Elodie Sainton, Roger Borges, Diane Delbegue, Audrey Diouf-Lewis, Léa Doubtsof, Michaël Herraiz, Jeff Nyalosaso, Anthony Chapel, Anthony Perthue, Martial Pouzet, Sihem Sebai, Ahmedou Sidi, Qirong Wang, and all people of ICCF members for inspiring me in research and life through our interactions during the time in the laboratory.

Special thanks for my former colleagues at the office 5215: Jérémy Perroux, Nadège Francolon, Mohammed Amine Hassairi, Aicha Boukhriss, Zha Jinlong, Aristeo-Garrido Hernandez, and also the most sociable person in our office: Christophe Appoloni. Very special thanks also go to my new home at 3215: the super technician Nathalie Gaillard-Caperaa, Pierre Vialat and Anaïs Pons. They all had given me such a pleasure time and the feeling of being at home at work.

The last but not the least, a very, very special thanks goes to my beloved Parents Phadoong & Kunlayanee BOONSIN and also my younger brother Atiwat BOONSIN for all the support and time they have endured me during the ups and downs of my Ph.D. life. I can barely find words to express all of the wisdom, love and support given to me by my beloved Family. I owe my thanks to my beloved Charassri Chatrangsan for all the support, time, patience and also many special suggestions she has given me to accomplish my thesis

There may be so many others whom I may have inadvertently left out, I take this opportunity to thank all who, directly or indirectly, have lent their helping hand in this dissertation.

This thesis has been made possible in part to due to the financial support from the region Council of Auvergne, the industrial cluster called E2IA (green industries for Auvergne Innovation), and also the Institute of Chemistry of Clermont-Ferrand.





## Abbreviations

AIE	Aggregated-induced emission
ACQ	Aggregation-caused quenching
a.u.	Arbitrary units
Å	Angstrom
CCT	Correlated color temperature
CdSe	Cadmium selenide
CIE	Commission international de l'éclairage
CRI	Color rendering index
CuInS <sub>2</sub>	Copper indium sulfide
cm <sup>-1</sup>	Reciprocal centimeters
DCMSP	Dicyanomethylene-2,6-distyryl-4 <i>H</i> -pyran derivatives
DMPP	(2,6-dimethyl-1-methylpyridin-4(1 <i>H</i> )-ylidene)propanedinitrile derivatives
FC	Fluorescein
Fluo	Fluorescein ions
$f_w$	Water fraction
FWHM	Full width at half maximum
ICT	Intramolecular charge transfer
IR	Infrared
$\lambda$	lambda
LEDs	Light-emitting diodes
LDH	Layerd double hydroxides
MPBH	Methyl pyrazinylketone benzoyl hydrazone (ligand)
mL	Mililiters
nm	Nanometers

$\mu\text{m}$	Micrometers
OLEDs	Organic light-emitting diodes
QDs	Quantum dots
PL	Photoluminescence
PLQY	Photoluminescence quantum yield
PLQY <sub>abs</sub>	Absolute quantum yield
PDMS	Polydimethylsiloxanes
RTV	Room-temperature vulcanizing
SEM	Scanning electron microscope
SiO <sub>2</sub>	Silicon dioxide
TEOS	Tetraethoxysilane
TEM	Transmission electron microscope
TGA	Thermogravimetric analysis
THF	Tetrahydrofuran
TP	Terephthalate ions
UV	Ultraviolet
WLED	White Light-emitting diodes
wt. %	Weight percent
XRD	X-ray diffraction
XRPD	X-ray powder diffraction
ZnS	Zinc sulfide

# Table of contents

<b>Acknowledgements .....</b>	<b>5</b>
<b>Abbreviations .....</b>	<b>9</b>
<b>Table of contexts .....</b>	<b>11</b>
<b>List of figures.....</b>	<b>15</b>
<b>List of tables.....</b>	<b>21</b>
<b>General introduction .....</b>	<b>23</b>
<b>CHAPTER I Bibliographic research .....</b>	<b>29</b>
I. General information of lighting systems .....	31
II. The color quality parameters for white light sources .....	33
III. Lighting technologies.....	37
A. Introduction.....	37
B. Classical incandescent lamps .....	39
C. Halogen lamps.....	40
D. Compact fluorescent lamps (CFLs).....	40
E. Light emitting diode (LED) lamps .....	41
IV. Light-emitting diodes – Future lighting solution .....	44
A. Working principle of LED lamps .....	44
B. Designs of LED lamps .....	48
C. LED lighting in the market .....	51
V. Luminescent materials in LED lighting devices .....	53
A. Organic and organometallic compounds .....	54
i. Photoluminescence of organic molecules.....	54
ii. Organic photoluminescent compounds and LEDs for white light .....	56
B. Quantum dots .....	61
i. Introduction to quantum dots .....	61
ii. Core-shell quantum dots .....	64
iii. Quantum dots and LEDs for white light.....	65
<b>Summary.....</b>	<b>66</b>
<b>CHAPTER II Organic phosphors-based white light-emitting diodes .....</b>	<b>69</b>
I. Dicyanomethylene-4H-pyran derivatives for LEDs.....	71
A. Introduction.....	71
B. Results and discussion .....	73
a. Synthesis and characterizations of DMPP derivatives.....	73
C. Optical and photoluminescence studies of DMPP derivatives .....	77
a. Synthesis and characterizations of DCMSP derivatives .....	86

b.	Optical and photoluminescence studies of DCMSP derivatives .....	88
II.	Schiff base Al-complexes for LEDs .....	91
A.	Introduction .....	91
B.	Results and discussion .....	93
a.	Structural characterizations of compound 11 .....	93
b.	Structural characterization of compound 12 in dilute solution .....	94
c.	Structural characterization of compound 12 in solid state .....	96
d.	Synthesis and characterizations of similar complexes of 12 .....	99
III.	Characterizations of selected organic phosphors for LEDs .....	102
A.	Optical properties of organic phosphors composite films .....	107
a.	Polymer matrices: silicone resin film .....	107
i.	Physical properties of silicone resin .....	107
b.	Organic phosphors composite films .....	111
B.	Color simulation for mixture of selected organic compounds .....	114
C.	Optical properties of mixed phosphors composite films .....	115
D.	Study of photo-degradation of organic composite films .....	118
a.	Photo-degradation of silicone .....	120
b.	Photo-degradation of organic-silicone composite films .....	123
	<b>Summary.....</b>	<b>133</b>
	<b>CHAPTER III Encapsulation of organic phosphors for light-emitting applications....</b>	<b>135</b>
I.	General introduction.....	137
II.	Silica encapsulated organic phosphors .....	140
A.	Introduction .....	140
a.	Silica encapsulated fluorescein molecules.....	141
B.	Experimental .....	144
a.	Synthesis of fluorescein doped silica nanoparticles (FC@SiO <sub>2</sub> ) .....	144
b.	Preparation of composite films.....	144
C.	Results and discussion .....	145
a.	Fluorescein sodium salt doped silica nanoparticles (FC@SiO <sub>2</sub> ).....	145
b.	Silica encapsulated other organic phosphors .....	151
c.	FC@SiO <sub>2</sub> composite film.....	153
III.	Organic-inorganic hybrid-layered double hydroxides .....	159
A.	Introduction .....	159
B.	Experimental .....	162
a.	Synthesis of fluorescein intercalated Mg-Al-LDH .....	162
C.	Results and discussion .....	163
	<b>Summary.....</b>	<b>172</b>

<b>CHAPTER IV Quantum dots-based white light-emitting diodes .....</b>	<b>175</b>
I. Introduction .....	177
II. Experimental.....	178
A. Synthesis of the blue/green-emitting CdSe/ZnS QDs, and the red-emitting CuInS <sub>2</sub> QDs .....	178
B. Preparation of QDs – silicone films for white light-emitting diodes .....	178
III. Results and discussion .....	179
A. Blue-emitting CdSe/ZnS quantum dots .....	180
a. Morphological studies of blue-emitting CdSe/ZnS QDs .....	180
b. Optical studies of blue-emitting CdSe/ZnS QDs .....	181
B. Green-emitting CdSe/ZnS quantum dots.....	184
a. Morphological studies of green-emitting CdSe/ZnS QDs .....	184
b. Optical studies of green-emitting CdSe/ZnS QDs .....	185
C. Red-emitting CuInS <sub>2</sub> /ZnS quantum dots .....	186
a. Morphological studies of red-emitting CuInS <sub>2</sub> /ZnS QDs .....	187
b. Optical studies of red-emitting CuInS <sub>2</sub> /ZnS QDs .....	187
D. Photoluminescence properties of QDs composite films .....	189
a. Composite films: quantum dots/silicone film .....	189
b. Color simulation for mixture of different QDs at 365 nm. ....	194
c. Composite films: mixed quantum dots/silicone film .....	196
E. Study of photo-degradation of QDs composite films.....	200
a. Photo-degradation of QDs composite films.....	200
<b>Summary.....</b>	<b>208</b>
<b>General conclusion and Perspectives .....</b>	<b>211</b>
<b>Experimental section Organic phosphors.....</b>	<b>219</b>
A. (2,6-dimethyl-4H-pyran-4-ylidene)propanedinitrile .....	221
B. 2-(1,2,6-trimethylpyridin-4H-ylidene)malonitrile.....	222
C. 2-(1-butyl-2,6-dimethylpyridin-4H-ylidene)malonitrile .....	223
D. 2-(1-hexyl-2,6-dimethylpyridin-4(1H)-ylidene)malonitrile .....	224
E. 2-(1-octyl-2,6-dimethylpyridin-4H-ylidene)malonitrile.....	225
F. 2-(2,6-distyryl-4H-pyran-4'-ylidene)malonitrile .....	226
G. 2-(2,6-bis(2-naphthalen-2-yl)vinyl)-4H-pyran-4'-ylidene)malonitrile .....	227
H. 2-(2,6-bis(2-(anthracen-9-yl)vinyl)-4H-pyran-4'-ylidene)malonitrile .....	228
I. 2-(2,6-bis(2-(pyridin-3-yl)vinyl)-4H-pyran-4'-ylidene)malonitrile .....	229
J. 2-(2,6-bis(4-(methoxystyryl)-4H-pyran-4'-ylidene)malonitrile.....	230
K. Methyl pyrazinylketone benzoyl hydrazine (MPBH) ligand .....	231
L. Al-MPBH complex.....	232
M. N <sup>1</sup> ,N <sup>4</sup> -bis((E)-1-(pyrazin-2-yl)ethylidene)terephthalohydrazide (MPTH).....	233
N. Al-MPTH complex.....	234

O.	(E)-4-nitro-N'-(1-(pyrazin-2-yl)ethylidene)benzohydrazide (MPNBH)	235
P.	Al-MPNBH complex	236
Q.	(E)-4-(dimethylamino)-N'-(1-(pyrazin-2-yl)ethylidene)benzohydrazide (MPMABH)	237
R.	Al-MPMABH complex	238
<b>Annex</b>		<b>241</b>
I.	Annex A: Characterization techniques	243
A.	NMR spectroscopy	243
B.	UV-visible spectroscopy	244
C.	Fourier transform infrared (FTIR) spectroscopy	245
D.	Melting point	246
E.	Thin layer chromatography (TLC)	246
F.	Scanning electron microscopy (SEM)	247
G.	Transmission electron microscopy (TEM)	248
H.	Luminescence spectroscopy	248
I.	Photoluminescence quantum yield	249
J.	Photoluminescence decays	250
K.	Photoluminescence by integration sphere	250
L.	X-rays diffraction (XRD)	251
M.	UV irradiation	252
II.	Annex B: Glossary terms and definitions	253
<b>References</b>		<b>257</b>

## List of figures

Figure 1 Global lighting energy use <sup>10, 11</sup> .....	32
Figure 2 Global lighting electricity consumption by end-use sector in 1995-2030 <sup>11</sup> .....	32
Figure 3 CO <sub>2</sub> gas emissions from electricity and heat production in 2013 <sup>12</sup> .....	32
Figure 4 Color rendering index for high (CRI > 92) versus medium (CRI ≈ 80).....	35
Figure 5 Basic LED reference examples with their correlated color temperature.....	36
Figure 6 (left) Eye sensitivity function – luminous efficacy curve (right) CIE 1931 chromaticity coordinate diagram <sup>13</sup> .....	37
Figure 7 Evolution of luminous efficacy of commercial lighting products during 1940-2020.....	37
Figure 8 Life-cycle energy of incandescent lamps, CFLs, and LED lamps <sup>26</sup> .....	43
Figure 9 Historical evolution of commercial red, green, blue and phosphor-converted white LEDs <sup>30</sup> .....	45
Figure 10 Some approaches for generating white light with LEDs <sup>33</sup> .....	47
Figure 11 Examples of design configurations to making white light with LEDs and phosphors.....	48
Figure 12 Influence of junction temperature on luminaire output <sup>39</sup> .....	49
Figure 13 Depreciation of luminous flux over time for different junction temperatures <sup>40</sup> .....	49
Figure 14 a) reflection of light from Lambertian surface and b) schema of white light LED in cross-section under operation <sup>39, 40</sup> .....	50
Figure 15 Schematic fabrication of flexible white light LED device <sup>45</sup> .....	50
Figure 16 Evolution of LED market share by field of application <sup>46</sup> .....	51
Figure 17 LED lighting market share by region <sup>47</sup> .....	52
Figure 18 Enterprise LED lighting adoption timeline <sup>49</sup> .....	52
Figure 19 Jablonski energy diagram of typical photo-excited organic molecule.....	54
Figure 20 Optical excitation in a direct bandgap semiconductor <sup>120</sup> .....	61
Figure 21 the energy levels and bandgap with different sizes of semiconductors <sup>121</sup> .....	62
Figure 22 Summary of some quantum dots with different composition, size and emission ranges ; figure a) and b) are reproduced from [123, 124], respectively.....	63
Figure 23 (a) Type I and (b) Type II of core-shell semiconductors <sup>136</sup> .....	64
Figure 24 Schematic representation of common red-emitting organic dyes for OLEDs.....	72
Figure 25 Synthetic routes to blue-emitting DMPP derivatives.....	73
Figure 26 Schematic reaction mechanism for the reaction of DMPP derivatives.....	74
Figure 27 UV-visible absorption spectra of DMPP derivatives in acetonitrile (Concentration = 20 μM).....	75
Figure 28 (a) Photographs observed under (a) day light and (b) 365 nm UV lamp for compound 5 (15 x 10 <sup>-5</sup> M) in acetonitrile/water mixtures with f <sub>w</sub> range of 0-85%.....	75
Figure 29 (left) Absorption spectra (concentration = 15 μM) and (right) photoluminescence spectra (concentration = 15 x 10 <sup>-5</sup> M) of compound 4 in acetonitrile/water mixtures with f <sub>w</sub> range of 0-85%.....	76



<b>Figure 30 Absolute quantum yield of compound 4 as a function of water fraction in acetonitrile/water mixture (concentration = <math>15 \times 10^{-5}</math> M).</b>	77
<b>Figure 31 Excitation and emission spectra of DMPP derivatives under 365 nm UV-light illumination.</b>	77
<b>Figure 32 X-ray crystal structure of compound 2 with 50% probability thermal ellipsoids depicted.</b>	81
<b>Figure 33 X-ray crystal structure of compound 3 with 50% probability thermal ellipsoids depicted.</b>	82
<b>Figure 34 X-ray crystal structure of compound 4 with 50% probability thermal ellipsoids depicted.</b>	82
<b>Figure 35 X-ray crystal structure of compound 5 with 50% probability thermal ellipsoids depicted.</b>	82
<b>Figure 36 Part of the crystal structure of compound 2, showing the intermolecular distance between stacking molecules (right).</b>	83
<b>Figure 37 Part of the crystal structure of compound 3, showing the interaction between molecules. The red dashed lines represent hydrogen bonds and the intermolecular distance between molecules.</b>	83
<b>Figure 38 Part of the crystal structure of compound 4, showing the interaction between molecules along [100] (left) and [010] (right). The dashed lines represent hydrogen bonds between molecules.</b>	84
<b>Figure 39 Part of the crystal structure of compound 5, showing the interaction between molecules.</b>	84
<b>Figure 40 Synthetic routes to red-emitting DCMSP derivatives.</b>	86
<b>Figure 41 UV-visible absorption spectra of DCMSP derivatives in acetonitrile (Concentration=<math>12.5 \mu\text{M}</math>).</b>	87
<b>Figure 42 Excitation and emission spectra of DCMSP derivatives under 365 nm UV-light illumination.</b>	90
<b>Figure 43 Typical schematic route for the preparation of the Schiff base.</b>	91
<b>Figure 44 Synthesis of methyl pyrazinylketone benzoyl hydrazone (MPBH) Schiff base and their Al complex.</b>	92
<b>Figure 45 FTIR spectrum of compound 11 (MPBH ligand) in a KBr pellet.</b>	93
<b>Figure 46 UV-visible absorption (black line) and PL emission (blue line) spectra of MPBH (11) in ethanol. (Concentration = <math>50 \mu\text{M}</math>).</b>	94
<b>Figure 47 UV-visible absorption and emission spectra of Al-MPBH complex (compound 12) in ethanol. (Concentration = <math>50 \mu\text{M}</math>).</b>	95
<b>Figure 48 The SEM images of Al-MPBH complex (compound 12).</b>	96
<b>Figure 49 Powder XRD patterns of Al-MPBH complex (compound 12) and <math>\text{Al}(\text{NO}_3)_3 \cdot 9\text{H}_2\text{O}</math> as starting product.</b>	97
<b>Figure 50 FTIR spectra of Al-MPBH complex (compound 12) and MPBH ligand (compound 11).</b>	98
<b>Figure 51 Excitation and emission spectra of Al-MPBH complex (12) upon 365 nm UV-light illumination.</b>	99

<b>Figure 52 (left) Photographs of solid-state Al-complexes under normal light and under 365 nm UV lamp, (right) their emission spectra upon 365 nm UV-light illumination.</b>	101
<b>Figure 53 Absolute quantum yield of three selected organic phosphors recorded between 250-500 nm light illuminations.</b>	102
<b>Figure 54 Excitation and PL emission spectra of selected organic phosphors under 365 nm UV-light illumination.</b>	103
<b>Figure 55 Luminescence decay curves for the selected phosphors recorded upon 337.1 nm laser excitation at 300K.</b>	104
<b>Figure 56 Thermogravimetric analysis for selected organic phosphors.</b>	105
<b>Figure 57 (left) Temperature-dependent emission intensity and (right) Time-dependent relative emission intensity at temperature of 110°C of selected organic phosphors upon continuous 365 nm UV-light excitation.</b>	106
<b>Figure 58 Polyaddition reaction of two-component silicone resin<sup>206</sup>.</b>	107
<b>Figure 59 (a) TGA plots and (b) derivative curves of the silicone resin film.</b>	109
<b>Figure 60 (a) UV-visible and (b) infrared spectra of silicone resin film.</b>	109
<b>Figure 61 UV-visible absorption spectra of a silicone film before and after UV irradiation at 60°C. The red circle shows the absorption band of residual antioxidant.</b>	110
<b>Figure 62 Photographs of free-standing composite films of each selected organic phosphors embedded silicone resin: (left) under a day light and (right) under a 365 nm UV-LED excitation.</b>	111
<b>Figure 63 Absorption and PL emission spectra of selected organic phosphors (consisting of compound 4, 6 and 12) composite films.</b>	113
<b>Figure 64 Photographs of free-standing mixed organic phosphors-silicone composite film (Film B) (left) under normal light and (right) under a 365 nm UV-light illumination.</b>	115
<b>Figure 65 (a) CIE color coordinates of white LEDs based on the mixed phosphor composite films excited by a 365 nm UV-LED. (b) The emission spectra of films-based white LEDs.</b>	116
<b>Figure 66 Typical photo-oxidation of organic molecules: type I and type II<sup>9</sup>.</b>	119
<b>Figure 67 Photographs of free-standing mixed organic phosphors-silicone composite films (left) before and (right) after UV illumination for 2 hours by UV-LED based remote phosphor configuration system.</b>	120
<b>Figure 68 Mechanism of photo-oxidation of polydimethylsiloxanes under UV irradiation (<math>\lambda &gt; 300</math> nm).</b>	121
<b>Figure 69 Infrared spectrum of UV-unexposed silicone film. The inset graph presents the zoomed area from 2550-1350 <math>\text{cm}^{-1}</math>.</b>	122
<b>Figure 70 (a) IR spectra and (b) UV-visible spectra of UV-exposed silicone film during photo-oxidation.</b>	123
<b>Figure 71 Evolution of infrared spectra of compound 4-silicone composite film during photo-oxidation for 200 h in the absorption range: (a) zone 2250-2100 <math>\text{cm}^{-1}</math>, and (b) zone 1800-1450 <math>\text{cm}^{-1}</math>.</b>	124
<b>Figure 72 Evolution of infrared spectra of compound 6-silicone composite film during photo-oxidation for 200 h in the absorption range: (a) zone 2250-2100 <math>\text{cm}^{-1}</math> and (b) zone 1750-1450 <math>\text{cm}^{-1}</math>.</b>	124

<b>Figure 73 Evolution of infrared spectra of compound 12-silicone composite film during photo-oxidation for 200 h in the absorption range: (a) zone 2250-2050 <math>\text{cm}^{-1}</math>, and (b) zone 1775-1400 <math>\text{cm}^{-1}</math>.</b>	125
<b>Figure 74 Evolution of UV-visible absorption spectra of organic phosphors composite films during photo-oxidation for 200 h under accelerated artificial conditions.</b>	127
<b>Figure 75 Evolution of emission spectra of organic phosphors composite films before and after UV irradiation for 0 and 200 h under accelerated artificial conditions.</b>	128
<b>Figure 76 Photographs of organic composite films in vacuum-sealed glass tubes.</b>	129
<b>Figure 77 Evolution of infrared spectra of compound 4-silicone composite film before and after UV irradiation for 0 and 100 h under vacuum and accelerated artificial conditions. The absorption range: (a) zone 2250-2100 <math>\text{cm}^{-1}</math>, and (b) zone 1750-1450 <math>\text{cm}^{-1}</math>.</b>	130
<b>Figure 78 Evolution of infrared spectra of compound 6-silicone composite film before and after UV irradiation for 0 and 100 h under vacuum and accelerated artificial conditions. The absorption range: (a) zone 2250-2100 <math>\text{cm}^{-1}</math>, and (b) zone 1750-1450 <math>\text{cm}^{-1}</math>.</b>	130
<b>Figure 79 Evolution of infrared spectra of compound 12-silicone composite film before and after UV irradiation for 0 and 100 h under vacuum and accelerated artificial conditions. The absorption range: (a) zone 2250-2050 <math>\text{cm}^{-1}</math>, and (b) zone 1800-1400 <math>\text{cm}^{-1}</math>.</b>	130
<b>Figure 80 Evolution of UV-visible absorption spectra of organic phosphors composite films before and after UV irradiation for 0 and 100 h under vacuum and accelerated artificial conditions.</b>	131
<b>Figure 81 Evolution of emission spectra of organic phosphors composite films before and after UV irradiation for 0 and 100 h under vacuum and accelerated artificial conditions.</b>	132
<b>Figure 82 Chemical structure of fluorescein molecule at various pH.</b>	145
<b>Figure 83 Schematic diagram for the formation of FC@SiO<sub>2</sub> nanoparticles from a reverse microemulsion via hydrolysis and condensation.</b>	146
<b>Figure 84 FT-IR spectra of FC@SiO<sub>2</sub> nanoparticles and fluorescein sodium salt powder.</b>	147
<b>Figure 85 TEM images and the corresponding particle size distribution of the FC@SiO<sub>2</sub> nanoparticles with the different concentrations of fluorescein in W/O system: a) sample A, b) sample C, and c) sample F.</b>	148
<b>Figure 86 TGA plots of FC@SiO<sub>2</sub> nanoparticles, SiO<sub>2</sub> nanoparticles, and fluorescein sodium salt powder.</b>	149
<b>Figure 87 Concentration dependent of FC@SiO<sub>2</sub> nanoparticles of (a) absolute quantum yield and (b) PL emission spectra.</b>	149
<b>Figure 88 The absolute quantum yield efficiency of FC@SiO<sub>2</sub> nanoparticles (prepared from 10mM fluorescein solution) presented between 250-500 nm light illuminations.</b>	150
<b>Figure 89 a) Temperature-dependent measured in 1 cycle and b) time-dependent fluorescence intensity of FC@SiO<sub>2</sub> nanoparticles (sample C) and fluorescein sodium salt.</b>	151
<b>Figure 90 PL emission spectra of commercial organic phosphors encapsulated into silica nanoparticles upon 450 nm blue-light illumination.</b>	153
<b>Figure 91 a) UV-visible and b) FTIR spectra of both FC@SiO<sub>2</sub>-silicone composite film and pure silicone film.</b>	154
<b>Figure 92 SEM images of cross-section of a) 10 wt. % FC@SiO<sub>2</sub> and b) 15% FC@SiO<sub>2</sub>-silicone composite films.</b>	155

<b>Figure 93 a) Emission spectra and b) CIE chromaticity diagram measured for FC@SiO<sub>2</sub>-silicone/LED system, prepared using a blue LED (450nm) and 15 wt. % of FC@SiO<sub>2</sub> nanoparticles embedded in silicone. ....</b>	<b>156</b>
<b>Figure 94 Emission spectra of FC@SiO<sub>2</sub>-silicone hybrid LED (for 15 wt. %-V) at various forward currents from 100-500 mA. ....</b>	<b>157</b>
<b>Figure 95 Evolution of (a) CCT and CRI and (b) luminous efficacy of FC@SiO<sub>2</sub>-silicone composite film base (for 15 wt. %-V) at various forward currents from 100-600 mA. ....</b>	<b>158</b>
<b>Figure 96 Schematic of LDH structure<sup>288</sup>. ....</b>	<b>159</b>
<b>Figure 97 X-ray powder diffraction patterns of Mg-Al-Fluo (b) before and (a) after thermal treatment. (c) and (d) represent the originate forms of Mg-Al-LDH with intercalation of nitrate and carbonate ions. ....</b>	<b>164</b>
<b>Figure 98 FTIR spectra of Mg-Al-Fluo powders after thermal treatment and fluorescein disodium salt powders. ....</b>	<b>165</b>
<b>Figure 99 SEM micrographs of Mg-Al-Fluo powders: (a) and (b) represent the structures before thermal treatment, (c) and (d) after thermal treatment at 120°C. ....</b>	<b>166</b>
<b>Figure 100 PL emission spectra of Mg-Al-Fluo powders after thermal treatment upon light excitation at 365 nm and 450 nm. ....</b>	<b>167</b>
<b>Figure 101 X-ray powder diffraction patterns of Mg-Al-TP-Fluo with different compositions of fluorescein (Fluo) and terephthalate (TP): 1 = 100 wt. % Fluo, 2 = 20 wt. % Fluo + 80 wt. % TP, 3 = 5 wt. % Fluo + 95 wt. % TP and 4 = 1 wt. % Fluo + 99 wt. % TP. ....</b>	<b>168</b>
<b>Figure 102 FTIR spectra of of Mg-Al-TP-Fluo with different compositions of fluorescein (Fluo) and terephthalate (TP): 1 = 100 wt. % Fluo, 2 = 20 wt. % Fluo + 80 wt. % TP and 3 = 5 wt. % Fluo + 95 wt. % TP. ....</b>	<b>169</b>
<b>Figure 103 SEM micrographs of of Mg-Al-TP-Fluo with different compositions of fluorescein (Fluo) and terephthalate (TP): sample 2 = 20 wt. % Fluo + 80 wt.% TP, sample 3 = 5 wt. % Fluo + 95 wt. % TP. ....</b>	<b>170</b>
<b>Figure 104 PL emission spectra of of Mg-Al-TP-Fluo with different compositions of fluorescein (Fluo) and terephthalate (TP): 1 = 100 wt. % Fluo, 2 = 20 wt. % Fluo + 80 wt. % TP, 3 = 5 wt. % Fluo + 95 wt. % TP and 4 = 1 wt. % Fluo + 99 wt.% TP. ....</b>	<b>171</b>
<b>Figure 105 (left) UV-visible absorption and (right) PL emission spectra of a) blue-emitting CdSe/ZnS QDs (b) green-emitting CdSe/ZnS QDs and (c) red-emitting CuInS<sub>2</sub>/ZnS QDs. ....</b>	<b>179</b>
<b>Figure 106 TEM image of blue-emitting CdSe/ZnS core/shell QDs prepared by dispersing QDs in toluene. ....</b>	<b>181</b>
<b>Figure 107 (left) Excitation and (right) emission spectra of blue QDs of (a) solid form, (b) solution of 1.14 mg/mL in toluene, (c) solution of 0.114 mg/mL in toluene, and (d) solution of 1.16 mg/mL in chloroform. ....</b>	<b>182</b>
<b>Figure 108 TEM image of green-emitting CdSe/ZnS QDs prepared by dispersing QDs in toluene. ....</b>	<b>184</b>
<b>Figure 109 (left) Excitation and (right) emission spectra of green QDs of (a) solid form, (b) solution of 1.15 mg/mL in toluene, (c) solution of 1.15 mg/mL and (d) 0.115 mg/mL in chloroform. ....</b>	<b>185</b>
<b>Figure 110 TEM image of red-emitting CuInS<sub>2</sub>/ZnS QDs prepared by dispersing QDs in toluene. ....</b>	<b>187</b>

<b>Figure 111 (left) Excitation and (right) emission spectra of red QDs of (a) solid form, (b) solution of 1.16 mg/mL and (c) solution of 0.116 mg/mL in toluene.....</b>	<b>188</b>
<b>Figure 112 Absorption and emission spectra of three types of QDs dispersed in silicone resin: (a) blue-emitting CdSe/ZnS-silicone film, (b) green-emitting CdSe/ZnS-silicone film, and (c) red-emitting CuInS<sub>2</sub>/ZnS-silicone film. ....</b>	<b>190</b>
<b>Figure 113 Photographs of free-standing 1 wt. % QDs-silicone composite films (all above) under day light (all below) under a 365 nm UV illumination: (a) blue QDs, (b) green QDs, and (c) red QDs. ....</b>	<b>192</b>
<b>Figure 114 (a) PL spectra and (b) CIE coordinates of blue-emitting CdSe/ZnS QDs (QD-I), green-emitting CdSe/ZnS QDs (QD-II) and red-emitting CuInS<sub>2</sub>/ZnS QDs (QD-III) composite films under 365 nm UV irradiation. ....</b>	<b>193</b>
<b>Figure 115 Photographs of free-standing 1 wt. % mixed QDs-silicone composite film (left) under normal light and (right) under a 365 nm UV illumination. ....</b>	<b>196</b>
<b>Figure 116 PL spectra of multi-layered 1 wt. % mixed QDs-silicone composite films based white LED with increasing forward currents. ....</b>	<b>197</b>
<b>Figure 117 (a) Evolution of (a) CCT and CRI and (b) luminous efficacy of multi-layered mixed QDs-silicone composite films based white LED under different forward currents from 100 to 600 mA. ....</b>	<b>198</b>
<b>Figure 118 Photographs of free-standing 2 wt. % mixed QDs-silicone composite films (left) under normal light and (right) under a 365 nm UV illumination. ....</b>	<b>199</b>
<b>Figure 119 PL spectra of multi-layered 2 wt. % mixed QDs composite films based white LED with increasing forward currents. ....</b>	<b>200</b>
<b>Figure 120 (a) Evolution of infrared spectra of 1 wt. % blue-emitting CdSe/ZnS QDs-silicone composite film during photo-oxidation in the absorption range, (b) zone 4000-3200 cm<sup>-1</sup> and (c) zone 1800-1650 cm<sup>-1</sup>. ....</b>	<b>201</b>
<b>Figure 121 (a) Evolution of infrared spectra of 1 wt. % green-emitting CdSe/ZnS QDs-silicone composite film during photo-oxidation in the absorption range, (b) zone 4000-3200 cm<sup>-1</sup> and (c) zone 1800-1650 cm<sup>-1</sup>. ....</b>	<b>202</b>
<b>Figure 122 (a) Evolution of infrared spectra of 1 wt. % red-emitting CuInS<sub>2</sub>/ZnS QDs-silicone composite film during photo-oxidation in the absorption range, (b) zone 4000-3200 cm<sup>-1</sup> and (c) zone 1800-1650 cm<sup>-1</sup>. ....</b>	<b>202</b>
<b>Figure 123 a) Evolution of infrared spectra of 1 wt. % mixed QDs-silicone composite films during photo-oxidation in the absorption range, (b) zone 4000-3200 cm<sup>-1</sup> and (c) zone 1800-1650 cm<sup>-1</sup>. ....</b>	<b>203</b>
<b>Figure 124 Synthesis route of CuInS<sub>2</sub> QDs<sup>9</sup>. ....</b>	<b>204</b>
<b>Figure 125 Evolution of UV-visible absorption spectra of QDs composite films before and after UV irradiation for 0 and 200 h under accelerated artificial conditions. The inset in each graph illustrate the difference of absorbance at 237 nm as a function of irradiation time. ....</b>	<b>205</b>
<b>Figure 126 Evolution of emission spectra of QDs composite films before and after UV irradiation for 0 and 200 h under accelerated artificial conditions. ....</b>	<b>206</b>

## List of tables

Table 1 Summary of color quality parameters measured for LEDs. ....	33
Table 2 Luminous efficacy of common lighting devices <sup>14, 15</sup> .....	34
Table 3 Characteristics of lighting products <sup>14, 15</sup> .....	38
Table 4 Prices for LED lamps, Tested by PremiumLight, AEA and DTU Photonic <sup>25</sup> . ....	42
Table 5 Examples of white light based UV-LED with several phosphors (O=good, Δ=medium, ✕=bad) <sup>4</sup> .....	45
Table 6 Examples of white light based blue LED with several phosphors (O=good, Δ=medium, ✕=bad) <sup>4</sup> .....	46
Table 7 the highest luminous efficacies of WLEDs announced by leader manufacturers. ....	48
Table 8 Summary of organic / organometallic molecules based white-light LEDs.....	59
Table 9 Summary of quantum dots based white-light LEDs.....	60
Table 10 Comparison of properties of organic dyes, organometallic dyes and quantum dots....	67
Table 11 Optical characteristics of DMPP derivatives in solid state.....	78
Table 12 Crystal data of organic compounds 2-5. ....	79
Table 13 UV-visible data (in chloroform) and melting point of DCMSP derivatives. ....	87
Table 14 Optical characteristics of DCMSP derivatives in solid state. ....	88
Table 15 Characteristic IR bands of MPBH ligand and its Al complex. ....	98
Table 16 Optical characteristics of Al-complexes based on pyrazine Schiff base. ....	100
Table 17 Characteristics of luminescence decay curve by fitting two-exponential functions....	105
Table 18 Physical properties of two-component silicone resin. ....	108
Table 19 TGA and DTG results of silicone resin film. ....	108
Table 20 Typical infrared absorption frequencies of silicone resin film <sup>207</sup> .....	110
Table 21 Photoluminescence properties of organic phosphors-silicone composite films. The photoluminescence properties of their organic phosphors in solid state are also presented in comparison. ....	112
Table 22 Results from colorimetric simulation upon excitation at 365 nm. ....	114
Table 23 Compositions and their lighting performance parameters of two composite films based on organic phosphors under 365 nm UV-light illumination.....	116
Table 24 Absolute quantum yield of each organic phosphors composite films before and after UV irradiation for 0 and 100 h under accelerated artificial conditions. ....	127
Table 25 Absolute quantum yield of each organic phosphors composite films before and after UV irradiation for 0 and 100 h under vacuum and accelerated artificial conditions. ....	132
Table 26 Examples of commercial organic phosphors.....	139
Table 27 Optical characteristics of FC@SiO <sub>2</sub> nanoparticles. ....	146
Table 28 Optical characteristics of commercial organic phosphors in dilute solution. ....	152
Table 29 Optical characteristics of commercial organic phosphors encapsulated into silica nanoparticles. ....	152

<b>Table 30 The CIE color coordinates (x,y), color temperature (CCT), color rendering index (IRC), luminous flux (Y2), and luminous efficacy of an FC@SiO<sub>2</sub>-silicone hybrid LED under 450 nm blue light illumination. ....</b>	<b>156</b>
<b>Table 31 Solid composition of fluorescein intercalated Mg-Al-LDH with calculated parameters of intercalated layers. ....</b>	<b>169</b>
<b>Table 32 Photoluminescence properties of blue-emitting CdSe/ZnS QDs. ....</b>	<b>181</b>
<b>Table 33 Dipole, dielectric constant and polarity of chloroform and toluene<sup>337, 338</sup> .....</b>	<b>183</b>
<b>Table 34 Photoluminescence properties of green-emitting CdSe/ZnS QDs. ....</b>	<b>186</b>
<b>Table 35 Photoluminescence properties of red-emitting CuInS<sub>2</sub>/ZnS QDs. ....</b>	<b>188</b>
<b>Table 36 Photoluminescence properties of QDs-silicone composite films. The photoluminescence properties of their QDs in solution are also presented in comparison. ....</b>	<b>191</b>
<b>Table 37 Performance parameters of light obtained from remote-phosphor configurations consisting of 365 nm UV illumination and QDs-silicone composite films. ....</b>	<b>193</b>
<b>Table 38 Results obtained from colorimetric simulation with 365 nm LED chip for white light. ....</b>	<b>195</b>
<b>Table 39 Absolute quantum yields of QDs composite films before and after UV irradiation for 0 and 200 h under accelerated artificial conditions. ....</b>	<b>207</b>

---

# **General introduction**

---





### General introduction

Lighting is a remarkably important aspects for all living beings on the earth. With the developing technologies, the need of lighting is enlarged all the time in order to support all activities on the earth though some regions of the world have been waiting for lighting with modern productivity levels. During the human history, people have learnt how to establish the lighting by their experiences, from ancient campfires to electric lights. The understanding of light from the twenties centuries is the fundamental level for lighting development, starting with the great discovery of Thomas A. Edison for his invention of incandescent bulbs published in November 1879 <sup>1</sup>. Until now, thanks to the new knowledge based on quantum mechanics and optical physics, the improvement of lighting technologies have led us towards many advanced devices and techniques such as light-emitting diodes, lasers, optics and others. With progressively increasing of lighting demand, the planning for reduction of energy consumption and environmental concerns have been investigated for several years<sup>2,3</sup>. Obviously, over 90% of heat loss by thermal radiation in the incandescent bulbs and the mercury-containing devices should be replaced by other lighting technologies with more practical, low environmental impact and good energy efficiency.

Lighting technologies based on white light-emitting diodes (WLEDs) have become an alternative solution for replacing the obsolete technologies in recent years due to their high luminous efficacy, their low energy consumption compared to their size and energy input, their non-classified toxic materials, and their great promising long lifetime<sup>4-6</sup>. The white light emission with LEDs can be produced in various approaches and the common way is the combination of blue LEDs with rare earth-containing phosphors such as Ce-doped yttrium aluminum garnet (YAG: Ce<sup>3+</sup>). This combination between blue LEDs and luminescent materials is of interest regarding to their low thermal stress of inorganic phosphors, their high light extraction efficiency and their good light distribution over the lighted area. This kind of lighting technology has reached efficiencies which should promote itself to be a good candidate of alternative light sources for domestic luminaires.

However, according to the materials currently used, several problems of WLEDs have emerged such as the availability of rare earth materials affected by rising their prices followed by high quality control in manufacturing process and the exportation of products from rare earth-producing countries. Moreover, a comparison of average selling price of different lighting technologies also shows that the price of LED-based luminaires are ten times higher than the

incandescent lamps and two times higher than the fluorescent lamps. Solving these problems could take important steps for the developing technology and the expansion of white LEDs in the global market.

In order to limit the currently use of rare earth elements in lighting technologies, the development of alternative luminescent materials such as rare earth-free phosphors is of great interest. The general objective of this research is devoted to study and develop some rare earth-free phosphors which can be combined with UV or blue LEDs for producing white light emission. In this work, organic compounds and quantum dots as the phosphors were particularly investigated. The rare earth-free luminescent materials can be considered as great promising solutions for producing white LEDs lighting technologies as they can offer reduced costs in acquiring starting materials and practical ways to tune-up the color and light output by modifying their chemical structures. These solutions are likely not only to reduce the demand for the rare earth elements used in the production of LEDs, but also decrease the cost of LED lighting devices to compete with other products in the markets. Besides, the aspect of this project is devoted to the formulation of rare earth-free luminescent materials embedded in the silicone resin and combined with UV or blue LED chips. The composite films obtained provide a great promising lighting technology, which can be considered as large illuminating surfaces for LEDs.

As a part of regional environmental technology sector, this project has been developed for environmentally friendly materials and low-energy consuming technologies. Also, the aims of research are to propose new generation of LED lighting systems with rare earth-free luminescent materials. This project has then emerged from the industrial cluster called E2IA (green industries for Auvergne Innovation) by gathering three industrial actors in Auvergne (RevLum, Sibylux, and Fuji Electric France) and one regional academic institution (Institute of Chemistry of Clermont-Ferrand, ICCF). The main objective of E2IA cluster is to promote excellence and innovation for the eco-technologies sector in Auvergne by initiating research and development projects in collaboration with regional academic laboratories. Briefly, the commercial UV or blue LEDs were provided by Sibylux (DLS), which an expert in design, concept and manufacture of high performance LEDs based luminaires. Revlum Company takes part as a specialist in concept, research and development of industrial-scale production of luminescent materials to companies in lightings, visualizations, photovoltaics. The last partner Fuji Electric France is a specialist of power supply of the LED devices.

## General introduction

---

This research is categorized in different chapters corresponding with different types of rare earth-free luminescent materials. The various characterization methods such as the structural, morphological, chemical and optical analysis of different compounds were provided in each chapters.

The first chapter describes the state of art for lighting systems, the combination of LEDs with luminescent materials, the criteria and specifications for white light emission based LEDs and some information about rare earth-free luminescent materials: organic compounds, quantum dots and LEDs. Such information is provided as a general idea for the thesis results and discussion.

The second chapter is devoted to the synthesis and the characterizations of organic phosphors. The combination of a UV-LED with the selected phosphors are discussed in this chapter. The physical, chemical and optical stabilities of these compounds are also presented in detail.

The third chapter represents hybrid luminescent materials based commercial organic phosphors embedded into inorganic matrices such as layered double hydroxide (LDH) and amorphous silicon dioxide matrices (SiO<sub>2</sub>). The organic phosphors have been encapsulated inside inorganic matrices in order to enhance their thermal and optical properties<sup>7, 8</sup>. Some characterizations and the studies of stability under operating conditions were also considered

This last chapter reports the use of core/shell semiconductor nanocrystal quantum dots as luminescent thin films combined with blue LEDs. All quantum dots in this work are gratefully received under collaborative research group of Dr. Raphaël Scheider from University of Lorraine (Nancy, France). Their stability of quantum dots in the photo-aging conditions will be also addressed in the chapter.

Finally, the general conclusion and the perspectives are reported.

The synthesis methods and the characterization techniques used in this work are described in the annex section.



---

# **CHAPTER I**

## **Bibliographic research**

---



## I. General information of lighting systems

This chapter will be devoted to the general information of lighting systems. The timeline of technological evolution, several options of lighting sources, parameters used to lighting evaluation, and their envisaging problems will be briefly presented in this part. In the second part a short introduction of light-emitting diodes (LEDs) technology is reported. This chapter also shows the working principle and design in order to convert the monochromatic light from UV or blue LED chips to produce a broad spectrum white light. Finally, the use of the rare earth-free luminescent materials associated with LEDs and the principle of fluorescence spectroscopy for these rare earth-free luminescent materials are mentioned.

Lighting has become an essential commodity of our lives and the use of lighting has continuously increased in every part of the world. Considering the international energy statistics in 2013, the total electricity net consumption in France and in Thailand (author's country of origin) were estimated at around 486 and 167 terawatt-hours<sup>9</sup>. The lighting accounts for 19% of global electricity net consumption, as a major source of electricity consumption (Figure 1)<sup>10, 11</sup>. Obviously, the lighting has become the primary important service offered by electric utilities and has reached to be the largest part of electricity consumption<sup>11</sup>. Figure 2 shows the global lighting electricity consumption in 1995-2030 distributed by several service sectors: residential area, industrial area, outdoor stationary and commercial area<sup>11</sup>. The amount of consumption of lighting in the world has been raised in every countries and has been expected to increase even more in developing countries due to the increase in electrification rate in rural and remote areas, where people have no access to electricity and some essential commodities. Among the global lighting consumption, the less well appreciated is the formation of energy-related greenhouse gas emissions and the carbon dioxide (CO<sub>2</sub>) is considered as a major component of greenhouse gas emissions. As shown in Figure 3, the amount of CO<sub>2</sub> gas emissions for electricity generation in various countries was significantly at high level<sup>12</sup>. The environmental impacts of lighting have forced to find other energy efficient lightings in order to reduce the lighting energy consumption and, as a result, to decrease the emission of CO<sub>2</sub> gas.



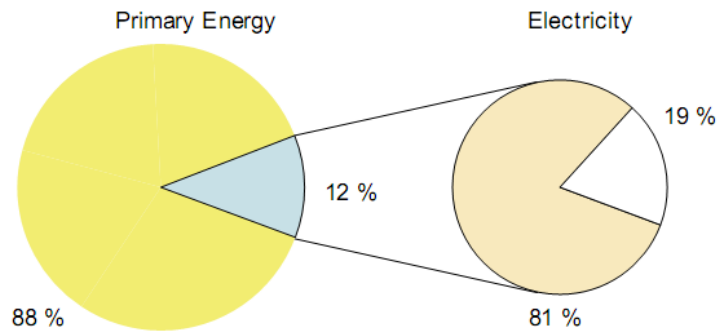


Figure 1 Global lighting energy use<sup>10,11</sup>.

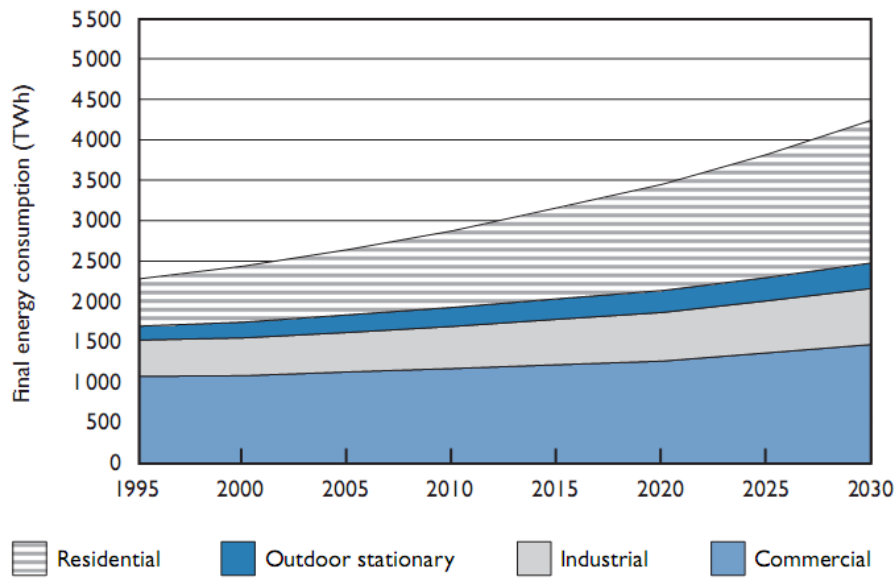


Figure 2 Global lighting electricity consumption by end-use sector in 1995-2030<sup>11</sup>.

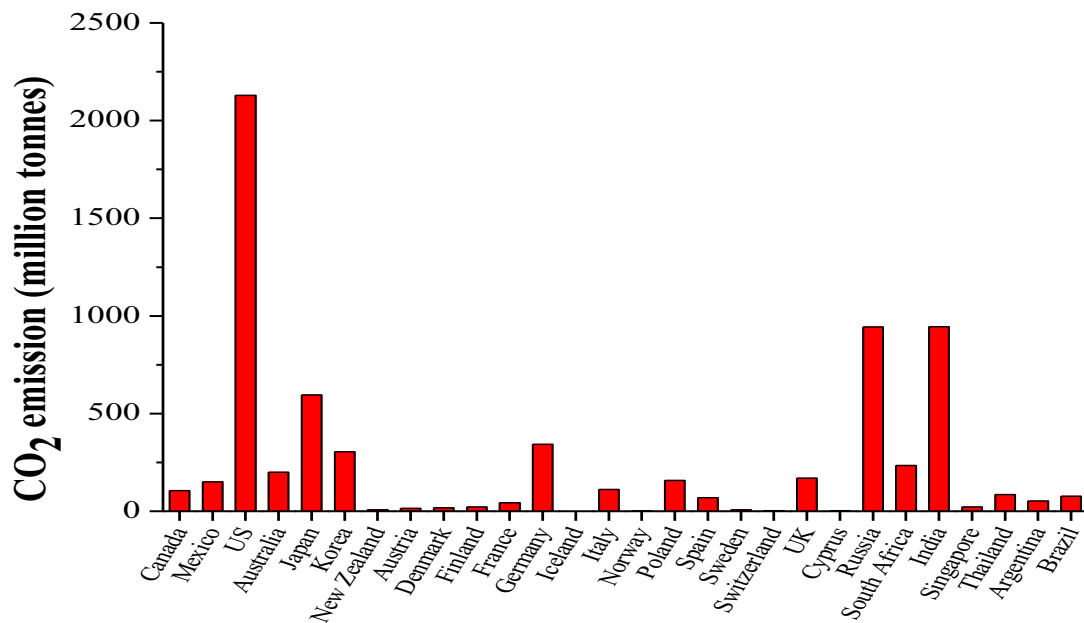


Figure 3 CO<sub>2</sub> gas emissions from electricity and heat production in 2013<sup>12</sup>.

The concern for decreasing the environmental impacts of lightings has become a topic of increasing importance in several countries. According to the European council, the European Union (EU) has decided some strategies to be achieved by the year 2020 including 20% reduction in energy consumption, 20% energy efficiency improvements, and 20% reduction of greenhouse gases<sup>2, 3</sup>. Since the year 2007, many countries have an intention of the regulations to phase-out of inefficient lightings (i.e. incandescent lamps) and to encourage the usage of high-efficient lightings such as compact fluorescent lamps (CFLs) and light-emitting diodes (LEDs). In order to emphasize the environmental impacts of lighting products, the briefly introduction of different lighting technologies will be mentioned as followed.

Before introducing the different lighting technologies available in the current market, I will present briefly the important parameters indicating the quality of lighting devices.

## II. The color quality parameters for white light sources

The performance and efficiency of lighting devices are the dominant aspects to take into consideration. Luminous flux, energy consumption used, color rendering index (CRI), correlated color temperature (CCT), and luminous efficacy are the important parameters to help the consumers taking decisions for choosing an appropriate luminaire for their behaviors and applications. The summary of some color quality parameters is presented in Table 1.

**Table 1 Summary of color quality parameters measured for LEDs.**

<b>Optical parameters</b>	<b>Description</b>	<b>Unit</b>
Luminous efficacy	Light output per power input	lm/W
Internal quantum efficiency	Photons emitted in active region per electron injected	%
Absolute quantum efficiency	Products of internal quantum yield and absorption coefficient	%
Color rendering index	Ability of light source to render the true colors of an object	-
Correlate color temperature	The dominant white color tone from warm to cool	K

**A luminous efficacy of a light source** is the total luminous flux emitted by the light source ( $\Phi_{lum}$ ) divided by the input electrical unit power of device. Its scale has units of lumens per watt (lm/W). In general, the luminous efficacy is referred to an efficiency of a light source that can produce visible light and can be defined as below<sup>13</sup> :

$$\text{Luminous efficacy} = \frac{\Phi_{lum}}{\text{voltage} \times \text{current}}$$

where the product of voltage and current is the electrical input power of the device. The luminous efficacy is an important parameter to indicate the energy efficient of luminaires. Table 2 represent the luminous efficacy of various lighting devices.

**Table 2 Luminous efficacy of common lighting devices<sup>14, 15</sup>.**

<b>Lighting devices</b>	<b>Typical luminous efficacy (lm/W)</b>
General lamp shape (GLS)	5 - 15
Tungsten halogen	12 – 25
Mercury vapour	40 – 60
Compact fluorescent lamp (CFL)	40 – 65
Fluorescent lamp	50 – 100
Metal halide	50 – 100
High pressure sodium (standard)	80 – 100
White LEDs	20 – 120

**Internal quantum efficiency (IQE)** is noted as the number of photons emitted in active region per electron injected to the system. In this report, the optical performance of luminescent components were reported in term of internal quantum efficiency, which can be defined as the ratio of the number of photons emitted by luminescent compounds to the number of photons absorbed:

$$\Phi_{Int} = \frac{\# \text{ photons emitted}}{\# \text{ photons absorbed}}$$

**Absolute quantum yield (PLQY<sub>abs</sub>)** is described for the total radiation-induced process as the number of times a specific event occurs per photon absorbed by the system. In this context, the absolute quantum efficiency were calculated by the product of internal quantum yield and absorption coefficient obtained from luminescent materials at the excitation wavelength:

$$PLQY_{abs} = \Phi_{int} \times \varepsilon$$

where  $\varepsilon$  is the absorption coefficient. It should be noted that the absorption coefficient takes into account of the proportion of incident photons absorbed by luminescent compounds.

**A color-rendering index (CRI)** represents the ability of light source to render the true colors of an object. The maximum value of CRI is 100 implying the great color quality identical to standardized daylight. For the domestic indoor lighting, the CRI goal should be equal or greater than 80 (CRI  $\geq$  80). The example of different CRI qualities is presented in Figure 4. The images on the left was shot with Lowel 27w day-flo lamps (CRI > 92) while the images on the right was taken with a household day-flo lamps (CRI  $\approx$  80). The image on the left obtained from the source with higher CRI enable a better distinction of each color.

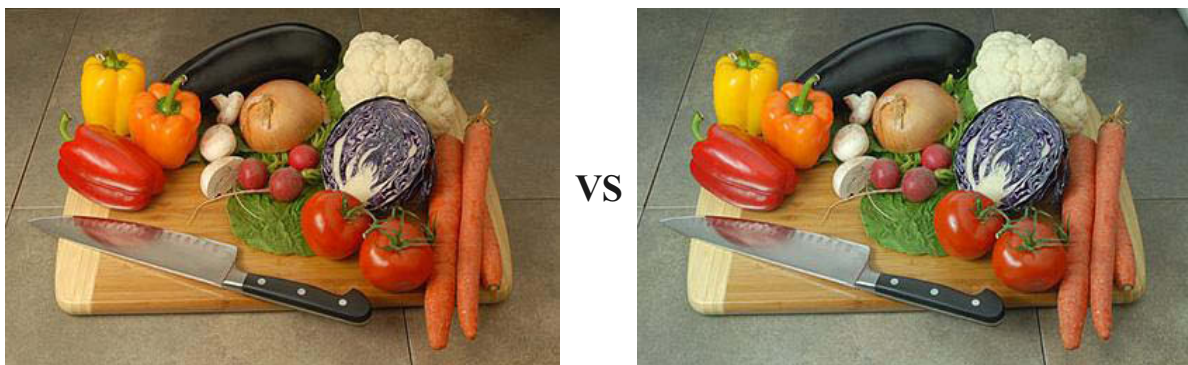


**Figure 4 Color rendering index for high (CRI > 92) versus medium (CRI  $\approx$  80).\***

**A correlated color temperature (CCT)** is defined as the temperature of a black body radiator whose chromaticity is close to that of the simultaneous light source on a CIE 1976 color space. The CCT can be measured on a temperature scale as Kelvin (K). The CCT indicates whether a white light emission is warm or cold (Figure 5). Many shades of color temperature of an LED allow the consumers to customize their activities. A warmer white lights (3500-4100 K) are mainly used for indoor applications while cooler white lights (> 4100 K) are more appropriate for outdoors and industrial applications.

---

\* Photo and some descriptions are available at [http://lowel.tiffen.com/edu/color\\_temperature\\_and\\_rendering\\_demystified.html](http://lowel.tiffen.com/edu/color_temperature_and_rendering_demystified.html)



**Figure 5 Basic LED reference examples with their correlated color temperature.**

In addition, some published studies have revealed that the color temperature can influence to human circadian regulation such as sleep quality, alertness and even health by regulating melatonin level<sup>16, 17</sup>. The short-wavelength light (i.e. blue light) was the potent wavelength for regulating melatonin secretion while the longer wavelength light did not take any effects under the same light intensity or required longer exposure times to stimulate the circadian system<sup>18, 19</sup>. Therefore, it is important to choose the best-fitted color temperature to meet human activities and also their circadian rhymes.

**The Commission Internationale de l'Éclairage (CIE)** is the international commission established in 1913 to provide a forum for the exchange of ideas and information relating to light, illumination, color and color space models. The CIE color space models were developed and standardized using a color-mapping function, which is based on the average human eye sensitivity (Figure 6-left). The original CIE chromaticity model was adopted in 1931 and called CIE 1931. This CIE uses a mathematical formula to convert the red, green and blue (RGB) tristimulus values obtained from color matching functions to create a standardized color model. The CIE 1931 chromaticity diagram is shown in Figure 6-right). The black body irradiation described by Planck's law is represented by black body curve as a function of wavelength and temperature. The middle of the plot situated at the coordinate system  $x = y = 0.333$  represents the white perceived from an equal-energy flat spectrum of radiation and is defined as a white reference. The white light temperature for general illumination is found in the range of 2,000-10,000 K.

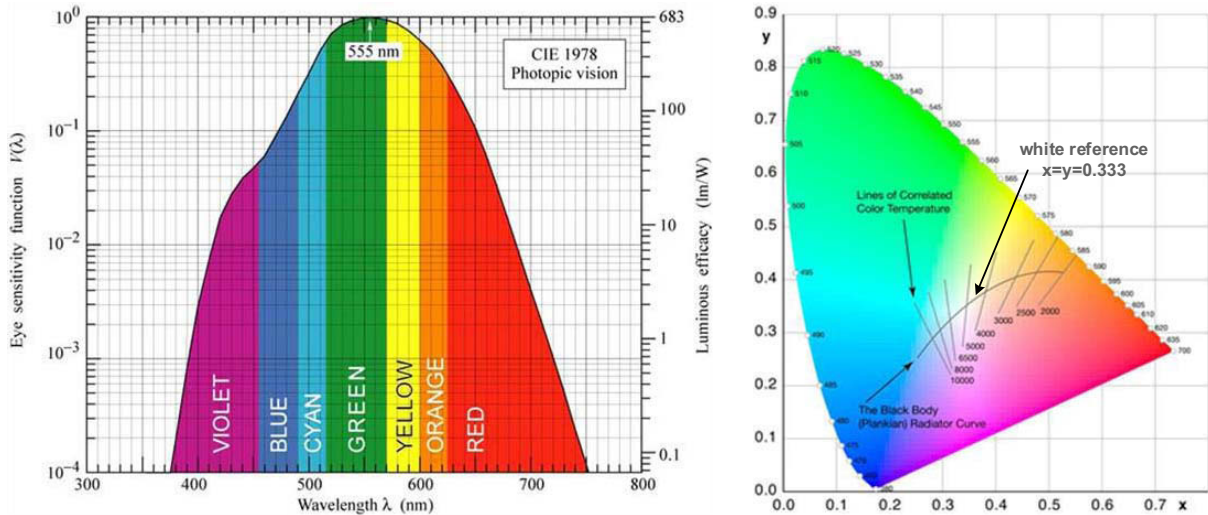


Figure 6 (left) Eye sensitivity function – luminous efficacy curve (right) CIE 1931 chromaticity coordinate diagram<sup>13</sup>.

### III. Lighting technologies

#### A. Introduction

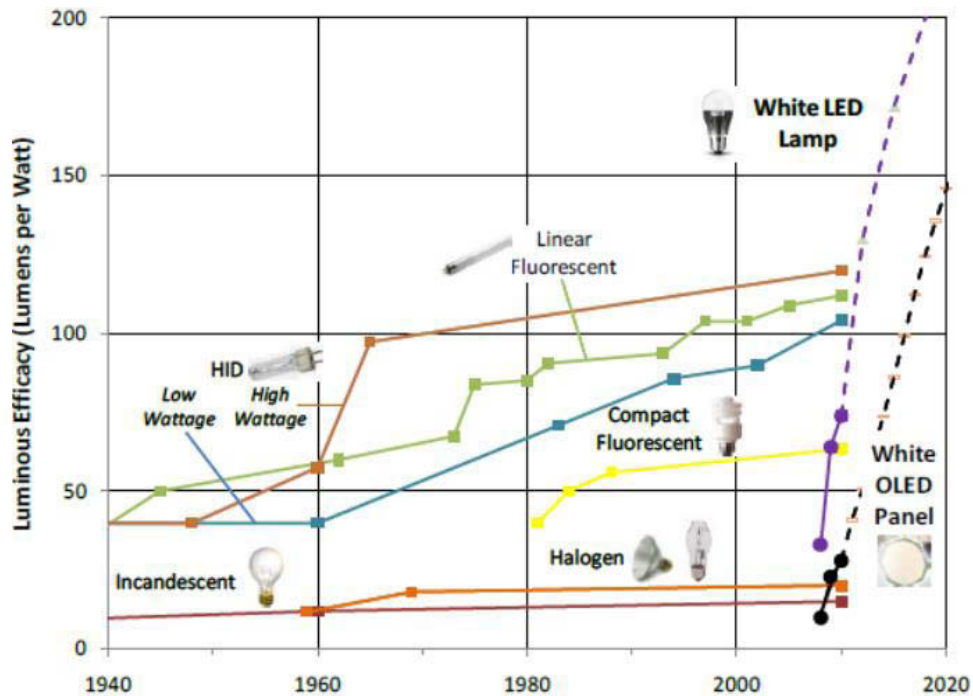


Figure 7 Evolution of luminous efficacy of commercial lighting products during 1940-2020.

Figure 7 presents the evolution of luminous efficacy of conventional lighting technologies over the 20<sup>th</sup> century<sup>20</sup>. More than 60 years that many researchers have been working on the lighting products in order to improve the previous technologies with the energy savings and the reduction of the greenhouse gas emissions. The characteristics of commercial lighting products are summarized in Table 3. Starting from the widespread use of incandescent lamps in the early 20<sup>th</sup> century, various types of artificial lightings have been made available on the market:

- ✓ Classical incandescent lamps
- ✓ Halogen lamps
- ✓ Compact fluorescent lamps (CFLs)
- ✓ White light-emitting diodes (WLEDs)

**Table 3 Characteristics of lighting products<sup>14, 15</sup>.**

Type	Characteristics					
	Luminous efficacy (lm/W)	Lifetime (h)	CRI	Cost of installation	Cost of operation	Applications
General lamp shape (GLS)	5 - 15	1000	100	Low	Very high	General lighting, decorative lighting
Tungsten halogen	12 - 25	2000 - 4000	100	Low	High	General lighting
Mercury vapour	40 - 60	12000	Poor to good	Medium	Medium	Outdoor lighting
Compact fluorescent lamp (CFL)	40 - 65	6000 - 12000	80 - 90	Low	Low	General lighting
Fluorescent lamp	50 - 100	10000 - 16000	70 - 90	High	Low	General lighting
Metal halide	50 - 100	6000 - 12000	Good	High	Low	Shopping malls, commercial building
High pressure sodium (standard)	80 - 100	6000 - 10000	Good	High	Low	Outdoor, commercial interior lighting
White LEDs	20 - 120	20000 - 100000	65 - 90	High	Low	All in near future

### B. Classical incandescent lamps

The incandescent lamps have been used since the first invention in 1906 by Carl Auer von Welsbach. For a typical incandescent lamp, the main component is tungsten filament which is sublimated at high temperature (around 2500°C) to produce the visible light. However, this operation causes the reduction of tungsten lifetime and the deposition of tungsten at the inner wall which results in the decrease of luminous efficiency. In addition, the incandescent lamps have both low manufacturing cost and low purchasing price but are extremely energy inefficient (only 5% of energy conversion to light emitted which means that 95% of energy transforms to heat rather than light). Since year 2009, the European union (EU) has started a huge decision to “phase out” all traditional incandescent lamps and some halogens of low energy efficiency effectively from the general lighting<sup>21</sup>. The objection for incandescent lamps and halogen lamps have been restricted in Europe by 2012 and 2016, respectively.



#### Advantages of incandescent lamps

- Cheap to manufacture and purchase
- No harmful to health
- Good color rendering index
- Available in very small scales (i.e. for decoration in the Christmas tree)

#### Drawbacks of incandescent lamps

- Short lifetime ( $\approx 1000$  h)
- Low luminous efficacy
- Unstable luminous efficiency under operation
- High energy dissipation (heat)



### C. Halogen lamps



The halogen lamps, quite similar to the incandescent lamps, are constituted of a main tungsten filament inside the light bulbs. But the halogen lamps contain halogen gas in order to prevent the sublimation of the tungsten filament and protect it from the rust. Halogen lamps are available in various designs and power ratings for some special applications (outdoor lightings and automotive headlamps). Soon, the halogen lamps will be obsoleted due to their highly energy consumption, short lifetime, and low luminous efficacy.

#### Advantages of halogen lamps

- Low price
- No harmful to health
- Brighter and whiter light output (compared to classical incandescent lamps)
- Good color rendering index

#### Drawbacks of halogen lamps

- Short lifetime ( $\approx 2000$  h)
- Low luminous efficacy
- High energy lost

### D. Compact fluorescent lamps (CFLs)

The compact fluorescent lamps have been fabricated in order to replace the household incandescent lamps. Comparing to classical lamps, the compact fluorescent lamps can produce the amount of light by consuming lower energy (up to 75% of energy savings). The CFLs exists in a large variety of shapes and types (tubular, circular or U-shaped) for supporting many usages at home, office, restaurant and other places. The major components inside the lamps are mercury gas and phosphor powder coated on the inside of the lamp in order to convert the 254 nm UV irradiation of mercury gas into visible light. However, the amount of mercury that ended up in the lamp (1-25 mg) and the leakage of UV irradiation have been the big questions that can be harmful to the environment and human.



### Advantages of compact fluorescent lamps

- Good lifetime (10,000-16,000h)
- High luminous efficiency (up to 5 times higher than incandescent lamps)
- Higher light output (compared to classical incandescent lamps)

### Drawbacks of compact fluorescent lamps

- Low color rendering index
- Mercury poisoning risks
- UV and electromagnetic irradiation from the lamps
- Special trash and recycle system required (due to toxic elements)

## **E. Light emitting diode (LED) lamps**



The purpose of LED projects have been expanded all over Europe as a fast developing and promising technology for the future. As a type of solid-state lighting, LED lamps can operate based on electroluminescence in semiconductors to convert electricity into visible light in a very narrow spectral band. The inventors and researchers have spent several years in academic and industrial sectors developing for commercial lightings. According to the European report in 2012, considering to 106 LED lamps test cases from 17 European countries, LEDs can replace an incumbent lighting technologies by demonstrating great energy savings and reduced operation and maintenance costs at the same time<sup>22</sup>. Apart from energy savings, the adoption of LEDs can also improve ambience and atmosphere for indoor and outdoor lighting qualities. Today, LED lamps are now available from a variety brand and model, with both price and quality improvement changing in favor of consumers (Table 4).

### Advantages of the LEDs

- High luminous efficacy and low energy consumption (power, operating voltage)
- Reduced maintenance costs
- Long lifetime expectancy (up to 10 years, which save 10-90% of the maintenance costs)
- Improved atmosphere and lighting characteristics
- Mercury-free components
- Flexibility in design

- Low operating temperature (i.e. room temperature) and higher efficacy at cold temperatures

### Drawbacks of the LEDs

- LED quality (delivering low luminance and lack of standardization)
- High acquisition costs than other lamps (expected to come down soon)
- Need for thermal management (to avoid degradation in lifetime)
- Health precautions concerning to the eyes for some kinds of LEDs<sup>23, 24</sup>

**Table 4 Prices for LED lamps, Tested by PremiumLight, AEA and DTU Photonic<sup>25†</sup>.**

<b>Brand</b>	<b>Model</b>	<b>Measured Lumens</b>	<b>Luminous Efficacy (lm/W)</b>	<b>Price per 500 lm</b>
Posco LED	9W	715	79.4	€ 3.51
OSRAM	LED Superstar Classic A 10W	880	88.0	€ 4.77
IKEA	Ledera 13W dimmable	1032	79.4	€ 4.80
Verbatim	LED Classic 9.5W	888	94.5	€ 5.39
IKEA	Ledare 10W	597	59.7	€ 5.51
IKEA	LED circular 16W dimmable	1026	64.1	€ 5.78
OSRAM	10W dimmable	874	87.4	€ 6.14
Philips	LED 13W	1076	82.8	€ 6.25
Soft LED	LED Gluhfaden Birne 6W	673	112.2	€ 7.39
Megaman	LED Classic 16.5W	1665	100.9	€ 8.33
GE LED	Energy Smart 10W	660	66,0	€ 8.98
Panasonic	LDAHV10L27CGEP 10W	895	89.5	€ 13.44
OSRAM	6W dimmable	493	82.2	€ 13.62
Verbatim	4W	260	65.0	€ 12.27
Luxinia LED	SunFlux 11W dimmable	828	75.3	€ 16.00
Megaman	10W	696	69.6	€ 16.31
OSRAM	LED star Classic B 4W	264	264.4	€ 21.63

---

† All LED price analysis are based on lamps that were tested as part of the Premium Light programme, the Austrian government and the Danish Technical University.

The incandescent lamps, compact fluorescent lamps, and LED lamps represent different lighting technologies under various operating performances and also different electricity consumption. Figure 8 reports the energy consumption of incandescent lamps, compact fluorescent lamps, and LED lamps. The energy consumption of incandescent lamps is four times higher than both CFLs and LED (product in 2011) lamps in order to provide the equivalent value of 20 million lumen-hours of lighting service<sup>25</sup>. In few years, the incandescent and other inefficient lighting sources will be out of the market in most countries. Then the consumption of fluorescent lamps will increase significantly competing with LED lamps for this market.

Considering the decision of reduction of energy consumption by 20% by 2020, it is therefore necessary to study and develop energy-efficient LED lighting sources to replace the incumbent technologies for producing white light emitting with high brightness and efficiency. The next section of this chapter will be focused on the working principle, designs and also trends of LED lightings for future.

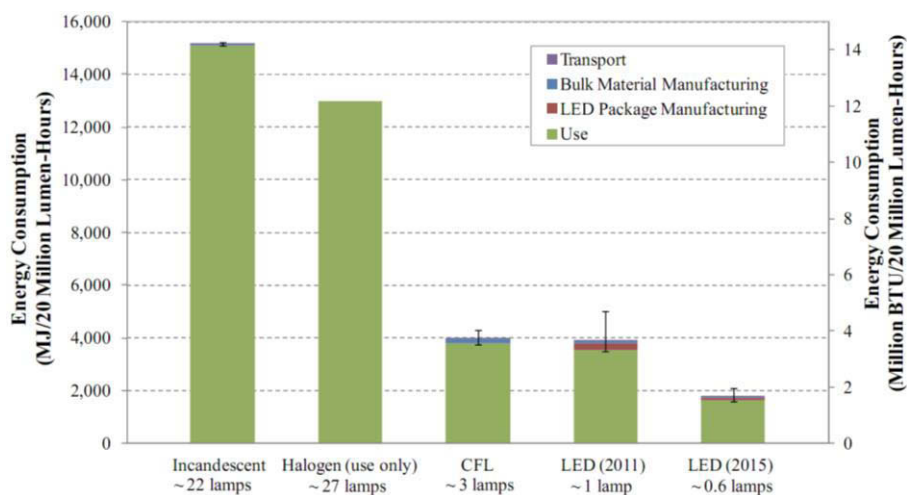


Figure 8 Life-cycle energy of incandescent lamps, CFLs, and LED lamps<sup>26‡</sup>.

‡ In order to compare the results for each lamp, it should be noted that the value of “20 million lumen-hours” was chosen as a reference. It represents the energy needed to supply 20 million lumen-hours of lighting service.

## IV. Light-emitting diodes – Future lighting solution

Let's back to the late October 2014, three scientists, Isamu Akasaki – Hiroshi Amano – Shuji Nakamura, were rewarded the Nobel Prize in physics for their extraordinary inventions on a new energy-efficient and eco-friendly blue light-emitting diode (LED). According to the Nobel Press Release, incandescent light bulbs lit the 20<sup>th</sup> century; the 21<sup>th</sup> century will be lit by LED lamps<sup>27</sup>. By using these blue LEDs, white light can be established in a different way and competed to replace the incumbent lamps. Obviously, unlike the incandescent light bulbs, the LED lamps are zero mercury technology. Moreover, the rapid growth and sustainable development of LED has opened up many fields of applications such as screens, computers and mobile phones, automotive vehicles, and decorations. In this section, we will introduce the working principle of LED, the evolution of white light based LEDs, the LED design and also the trends in future.

### A. Working principle of LED lamps

The LEDs are semiconductors that are composed of many layers of semiconductor materials. After switching on the LEDs by applied power, the monochromatic light is generated from P-N junction by the recombination of holes and electron within a semiconductor. Figure 9 shows the illustrated history of solid-state lighting and the color of semiconductor materials represent the light emitted from each material. Before the significant invention of blue LEDs from indium gallium nitride (InGaN), the red LEDs using gallium arsenide phosphide (GaAsP), the green LED using gallium phosphide (GaP) and the yellow-green LEDs using GaP: N have been discovered for almost 50 years. Therefore, the idea of white light from a combination of red, green and blue LEDs was introduced by mixing appropriate color ratios via electronic tuning (Figure 10-left)<sup>13</sup>. However, the color-mixing LEDs method still causes high production costs, unstable lighting output and color temperature, and needs different driving current for each LED<sup>28, 29</sup>.

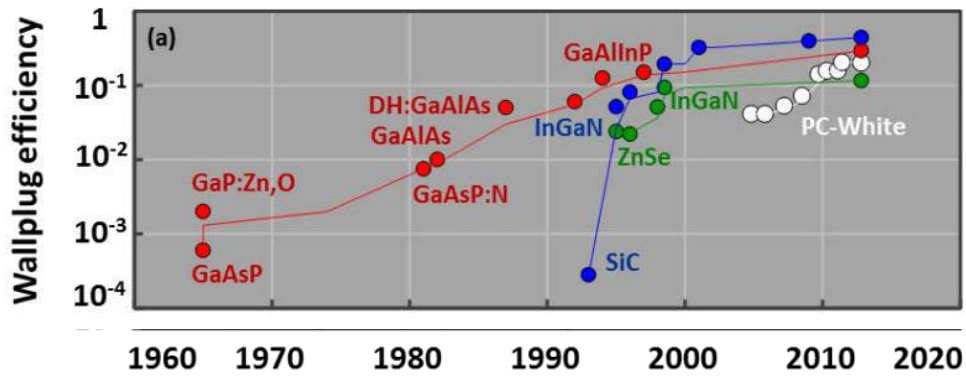


Figure 9 Historical evolution of commercial red, green, blue and phosphor-converted white LEDs<sup>30</sup>.

Table 5 Examples of white light based UV-LED with several phosphors (O=good, Δ=medium, ✖=bad)<sup>4</sup>.

LED	Phosphor	Chemical composition	Emission characteristics			
			Intensity	Width	Durability	Thermal quenching
UV	Blue phosphor	(Sr,Ca,Ba,Mg) <sub>10</sub> (PO <sub>4</sub> ) <sub>6</sub> Cl <sub>2</sub> /Eu	O	Narrow	O	Δ
		(Ba,Sr)MgAl <sub>10</sub> O <sub>17</sub> /Eu	O	Middle	O	O
		(Sr,Ba) <sub>3</sub> MgSi <sub>2</sub> O <sub>8</sub> /Eu	O	Narrow	Δ	Δ
	Green phosphor	SrGa <sub>2</sub> S <sub>4</sub> /Eu	O	Middle	✖	✖
		β-sialon/Eu	O	Middle	O	O
		SrSi <sub>2</sub> O <sub>2</sub> N <sub>2</sub> /Eu	O	Middle	O	O
		Ba <sub>3</sub> Si <sub>6</sub> O <sub>12</sub> N <sub>2</sub> /Eu	O	Middle	O	O
		BaMgAl <sub>10</sub> O <sub>17</sub> /Eu,Mn	O	Narrow	O	O
		SrAl <sub>2</sub> O <sub>4</sub> /Eu	Δ	Broad	Δ	Δ
	Red phosphor	(Sr,Ca)S/Eu	O	Broad	✖	✖
		(Ca,Sr) <sub>2</sub> Si <sub>5</sub> N <sub>8</sub> /Eu	Δ	Broad	Δ	Δ
		CaAlSiN <sub>3</sub> /Eu	O	Broad	O	O
		La <sub>2</sub> O <sub>2</sub> S/Eu	Δ	Narrow	Δ	Δ
		3.5MgO-0.5MgF <sub>2</sub> -GeO <sub>2</sub> /Mn	Δ	Narrow	O	O
		(Sr,Ca,Ba,Mg) <sub>10</sub> (PO <sub>4</sub> ) <sub>6</sub> Cl <sub>2</sub> /Eu,Mn	Δ	Broad	O	O
Ba <sub>3</sub> MgSi <sub>2</sub> O <sub>8</sub> /Eu,Mn		O	Broad	Δ	Δ	

Other approaches for generating white light are the combination of UV or blue LEDs and luminescent materials. It should be noted that the pseudo-white LEDs arises from the mixture of UV or blue LED and light emission from appropriate phosphors, thus the transmittance of light through the coated phosphors should be optimized to obtain a desired white emission. The first method is the combination of a UV-LED chip and phosphor mixtures involving red, green and blue emitting compounds (Table 5). Secondly, a combination of a blue LED and a mixing of red-green phosphors (Table 6) has been promoted. However, the low efficiency of red luminescent compound limits the performance of both systems. Furthermore, mixing several phosphors results in the reduction of emission due to the large overlapping spectra of phosphors and the re-absorption of emission by another phosphor.

**Table 6 Examples of white light based blue LED with several phosphors (O=good, Δ=medium, ✖=bad) <sup>4</sup>.**

LED	Phosphor	Chemical composition	Emission characteristics			
			Intensity	Width	Durability	Thermal quenching
Blue	Green phosphor	Y <sub>3</sub> (Al,Ga) <sub>5</sub> O <sub>12</sub> /Ce	Δ	Broad	O	Δ
		SiGa <sub>2</sub> S <sub>4</sub> /Eu	O	Middle	✖	✖
		(Ba,Sr)2SiO <sub>4</sub> /Eu	O	Middle	Δ	Δ
		Ca <sub>3</sub> Sc <sub>2</sub> Si <sub>3</sub> O <sub>12</sub> /Eu	O	Broad	O	O
		CaSc <sub>2</sub> O <sub>4</sub> /Eu	O	Broad	O	O
		β-sialon/Eu	O	Middle	O	O
	Yellow phosphor	(Y,Gd) <sub>3</sub> Al <sub>5</sub> O <sub>12</sub> /Ce	O	Broad	O	Δ
		Tb <sub>3</sub> Al <sub>5</sub> O <sub>12</sub> /Ce	Δ	Broad	O	Δ
		CaGa <sub>2</sub> S <sub>4</sub> /Eu	O	Middle	✖	✖
		(Sr,Ca,Ba) <sub>2</sub> SiO <sub>4</sub> /Eu	O	Broad	O	Δ
		Ca-α-sialon/Eu	O	Middle	O	O
	Red phosphor	(Sr,Ca)S/Eu	O	Broad	✖	✖
		(Ca,Sr) <sub>2</sub> Si <sub>5</sub> N <sub>8</sub> /Eu	O	Broad	Δ	Δ
		CaAlSiN <sub>3</sub> /Eu	O	Broad	O	O
		(Sr,Ba) <sub>3</sub> SiO <sub>5</sub> /Eu	O	Broad	✖	O
K <sub>2</sub> SiF <sub>6</sub> /Mn		O	Narrow	O	O	

The third one is a combination of a blue LED and a yellow phosphor (Figure 10-right). This combination shows high conversion efficiency and high manufacturability for mass-production. Notwithstanding the low CRI and cold color temperature, the InGaN-blue LED involving  $\text{Ce}^{3+}$  doped yttrium aluminum garnet (YAG: Ce) as a yellow phosphor is commercially available in the market today and is still the main choice for producing white light<sup>31, 32</sup>.

The performances of white LEDs has been enhanced rapidly every year. For example, an inorganic phosphor emitting a red light upon 450 nm excitation is generally added into white light systems in order to increase the color rendering index (CRI) and extend the correlated color temperature (CCT) to warmer (below 4000 K). Figure 7 presents the highest performance of white LEDs announced by industrial leaders.

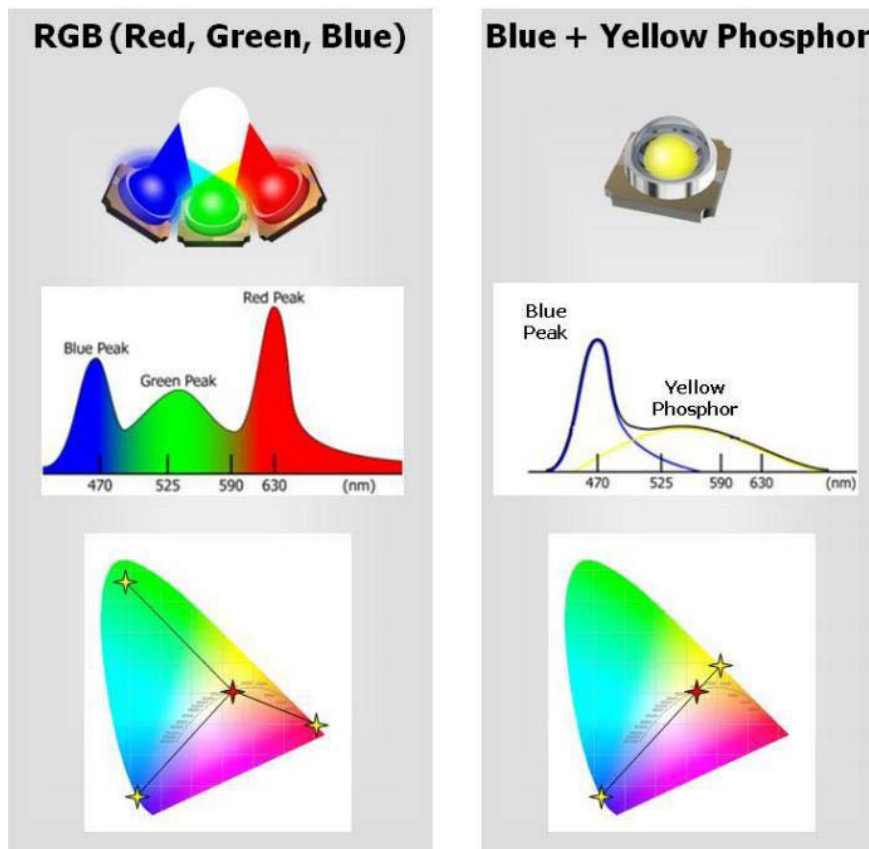


Figure 10 Some approaches for generating white light with LEDs<sup>33</sup>.



**Table 7 the highest luminous efficacies of WLEDs announced by leader manufacturers.**

Manufacturers	Models	Luminous efficacy	Ref.
Cree	Xlamp	303 lm/W (at 350mA, 5150K)	34
Nichia	757G series (3.0x3.0mm <sup>2</sup> )	200 lm/W	35
Osram Opto Semiconductors	Duris E5 (5.6x3.0mm <sup>2</sup> )	215 lm/W (at 19W, 3000K)	36
Philips	Prototype TLED	200 lm/W (4500-3000K)	37

## B. Designs of LED lamps

There are several designs of LED lamps for white light LEDs. Figure 11 presents possible design configurations for making white light with LEDs and phosphors. In general, the phosphor layer can be prepared by dispersing the solid-state phosphors into polymer matrix. The conventional design configurations apply the phosphors coated conformably in direct contact with the LED chips. However, the direct contact results in packaging-related photon loss owing to light scattering and reabsorption. In addition, the temperature control of LEDs becomes the point of interest for the development of LED quality. According to the performance of LEDs, 35% of input electricity is converted into visible light and 65% into dissipation energy (heat). In comparison to WLEDs, the fluorescent lamps convert 25% of electrical power into visible light and the dissipation energy is transformed into infrared or thermal radiation. When the LEDs chips operate, the junction temperature can reach the values in the range of 100- 120°C<sup>33,38</sup>. The generated heat arise from the LED chips and the phosphors during the operation causes the significantly decreases in lifetime, reliability and performance over the time. Figure 12 illustrates that the luminous output of LEDs decreases in increasing junction temperature<sup>39</sup>. Some research group reported that the temperature can also affect LED lifetimes (Figure 13)<sup>40</sup>.

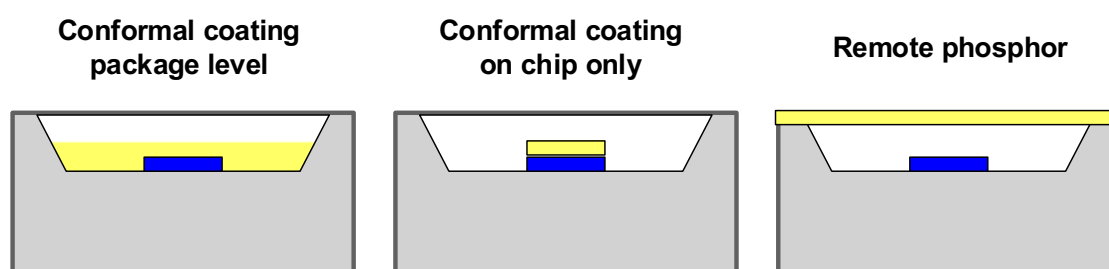


**Figure 11 Examples of design configurations to making white light with LEDs and phosphors.**

Consequently, the remote-phosphor configuration becomes a promising and remarkable alternative technology for white light LEDs because the phosphors are placed “remotely” away from the LED chip. So that their temperature in operating conditions can decrease to 60-80°C<sup>41</sup>. This configuration can limit the scattering and re-absorption of emission by LED chip, reduces the heat transfer between LED and phosphors, enhances the uniform illumination at the operating level, and ensure the excellent light stability over time than conventional dispersing method<sup>42</sup>. In a manufacturing process, a phosphor layer is prepared by dispersing the phosphor powder/solid particles in a polymer matrix. The thickness of the phosphor layer and the composition of the phosphor in the layer are considerably controlled to minimize the color quality variation during the manufacturing process. However, the amount of phosphors materials required for remote phosphors is the main barrier for adoption and applicability.

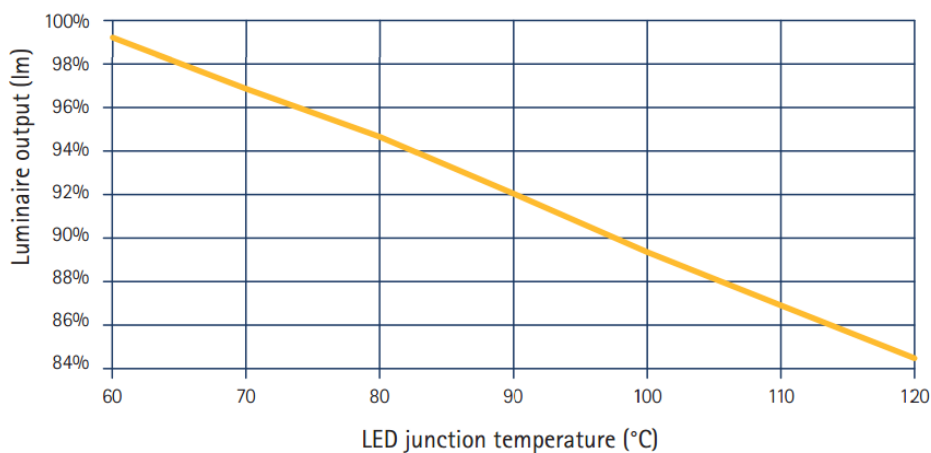


**Figure 12 Influence of junction temperature on luminaire output<sup>39</sup>.**

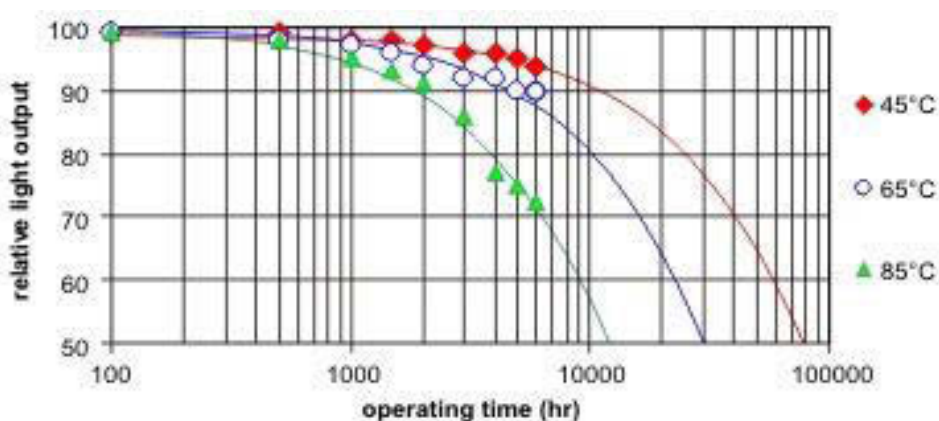


**Figure 13 Depreciation of luminous flux over time for different junction temperatures<sup>40</sup>.**

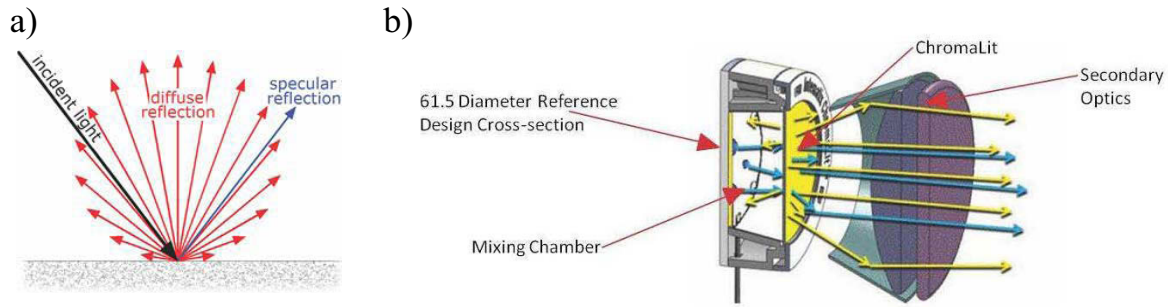


**Figure 14 a) reflection of light from Lambertian surface and b) schema of white light LED in cross-section under operation<sup>39, 40</sup>.**

The design of remote-phosphor system is a diffuse “Lambertian” source<sup>§</sup> which can enhance the system performance by recycling the blue photons inside the reflective chamber and then extracting through the remote-phosphor layer (Figure 14)<sup>43, 44</sup>. The diffuse properties take the advantages of decrease in number of blue LED chips per unit and also reduce the system cost by cutting down the materials costs for cooling unit.

Recently, the research team of Hao-Chung Kuo has successfully developed the first flexible white light LED devices using two different polymers (Figure 15)<sup>45</sup>. This device can generate warm white light emission with luminous efficiencies of 120 lm/W. The flexible LED approach offers many promising applications over conventional LED devices and seems to be an outstanding technology for many kinds of display like LEDs backlight screens.

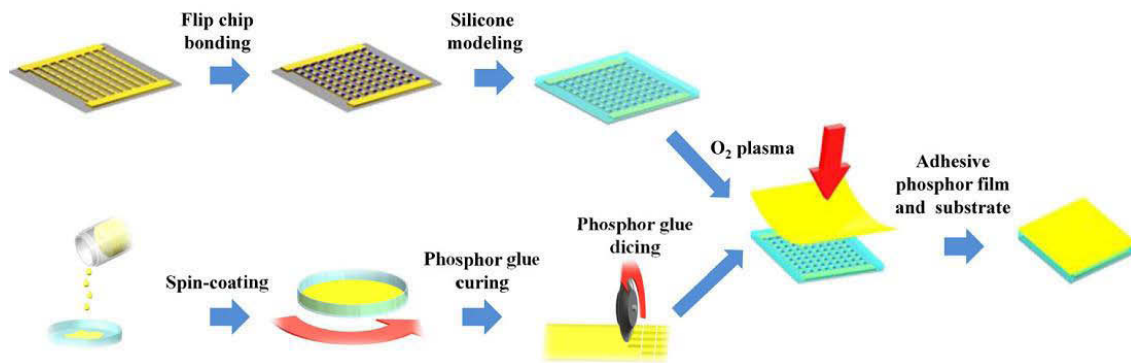


**Figure 15 Schematic fabrication of flexible white light LED device<sup>45</sup>.**

<sup>§</sup> Lambertian source = a specular material with very high reflection.

### C. LED lighting in the market

The perspective of LED technology in lighting market is very bright as the growth of demands has raised gradually in a wide array of applications. Figure 16 demonstrates the evolution of LED market share by different fields of application and the lightings are the sector of highest evolution for applications of LED technology<sup>46</sup>. The article “LEDinside” (Nov 2014), has reported that the LED market share will grow robustly at 31% in 2015, in which Europe is the largest LED lighting market by 23% of the global lighting market share (Figure 17)<sup>47</sup>. Moreover, the latest analysis (May 2015) predicted that the global market for LED lightings will reach \$26.65 billion by 2015<sup>48</sup>.

Concerning the CO<sub>2</sub> emission, not only the general consumers but also the industrial sectors are interested in the energy-efficient LED technologies in order to replace traditional lighting technology. Today, several industrial owners are very interested in applying cost-effective and energy-efficient lighting that can save their expenses. Figure 18 presents the adoption timeline of LED lighting in enterprise defined by installation locations and building area<sup>49</sup>. The outdoor area has been taking place and expanding into other sectors as the LED lighting conditions can be accepted in architectural lightings and designs over traditional lighting. In the next 10-20 years, LED-based luminaires will probably be the dominant sources of lighting at homes, offices, commercial area, and public sectors.

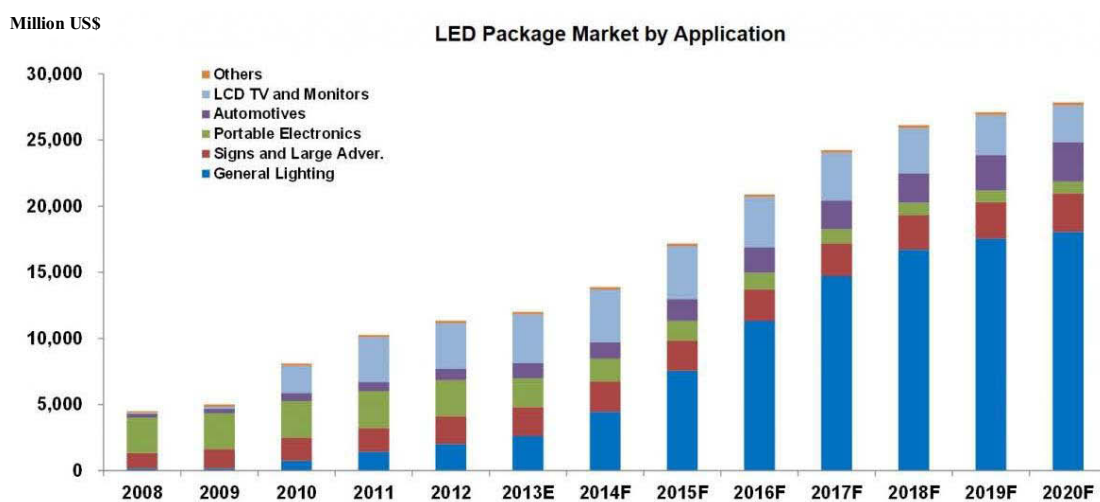


Figure 16 Evolution of LED market share by field of application<sup>46</sup>.

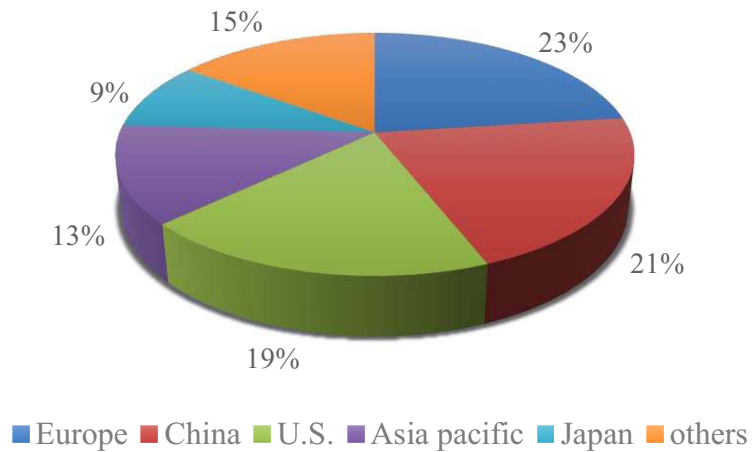


Figure 17 LED lighting market share by region<sup>47</sup>.

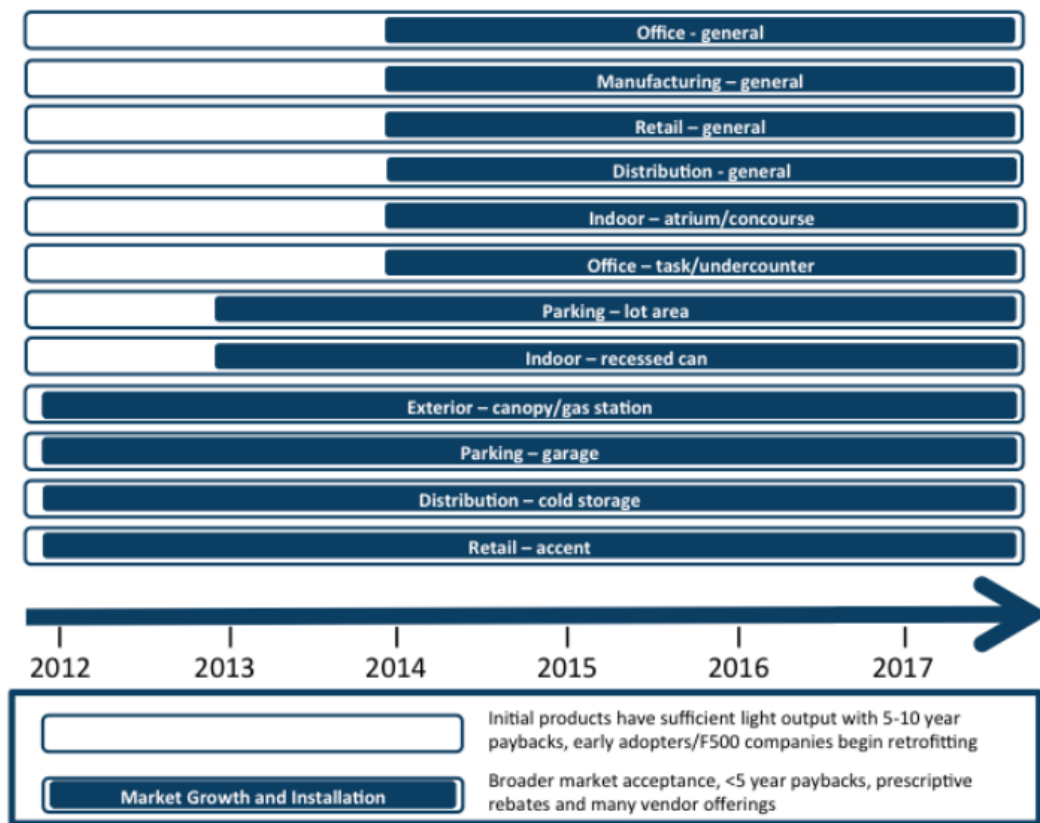


Figure 18 Enterprise LED lighting adoption timeline<sup>49</sup>.

## V. Luminescent materials in LED lighting devices

Considering the chemical composition of phosphors as mentioned previously, the rare-earth ions are a key component of luminescent materials in which they act as luminescent centers in inorganic matrices. Briefly, the rare-earth elements are the group of metals including scandium (Sc), yttrium (Y) and the 15 lanthanide elements (La, Ce, Pr, Nd, Pm, Sm, Eu, Gd, Tb, Dy, Ho, Er, Tm, Yb, and Lu)<sup>50</sup>. These rare-earth elements have become significantly important in many applications such as electronic devices, superconductors, optics, chemical catalysts, polishing and also lightings.

A free-market democracy has completely become a monopoly market when only one country has a potential power over the natural resources. On account to the rare-earth elements' market, China is presently the world's biggest producer and consumer of rare-earth elements. As a result the average price of rare-earth elements tends to be risen every year (800 % in 2011)<sup>51</sup> as China is controlling about 95% of rare-earth production (in 2009)<sup>52</sup> and about 50% of the world's rare-earth reserves.

Moreover, the large-scale production of rare-earth elements was operated under very extreme conditions (high temperature, high pressure, normal and/or reduce atmosphere). Thus the development of luminescent materials without rare-earth elements and the exploration of alternative materials to replace rare-earth elements can be considered as strategic achievements for future lighting applications.

In this work, we have used two classes of rare-earth-free luminescent materials: organic phosphors and quantum dots (QDs). Before going to the details, it is necessary to understand the luminescence mechanisms of these compounds.

## A. Organic and organometallic compounds

### i. Photoluminescence of organic molecules

Photoluminescence is the emission of light from the matter after excitation by photons. The photoluminescence can be categorized into two different phenomena relating to lifetime: fluorescence and phosphorescence (Figure 19)<sup>53</sup>. According to the IUPAC glossary of terms used in photochemistry, the fluorescence is a spontaneous radiative emission from the excited molecular levels with the retention of spin multiplicity, and the phosphorescence is the luminescence concerning the change in spin multiplicity typically from singlet to triplet state or vice versa<sup>54</sup>.

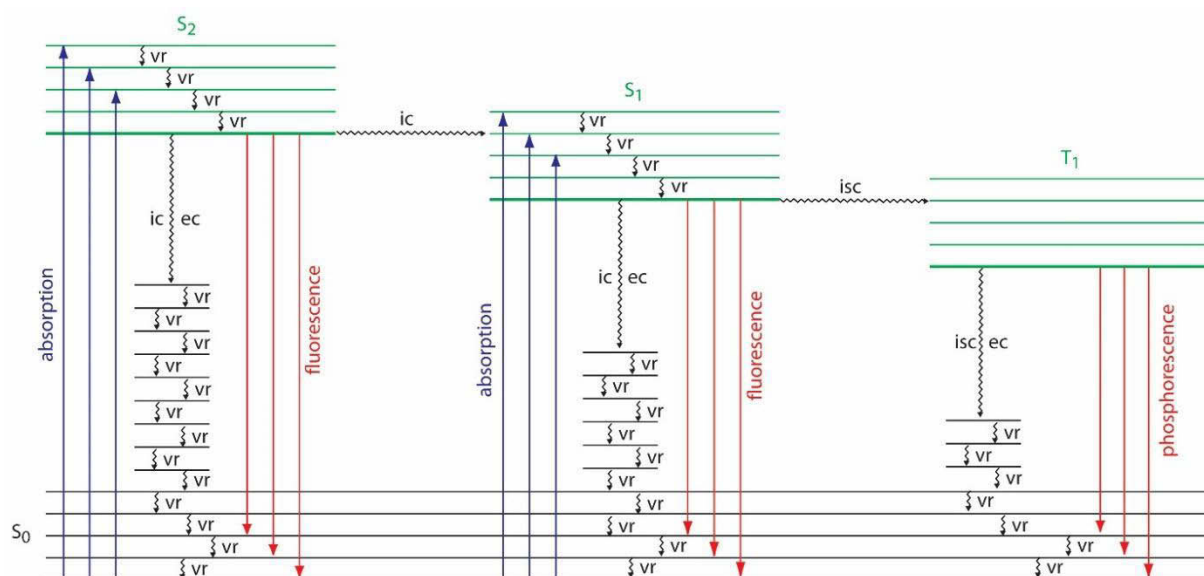


Figure 19 Jablonski energy diagram of typical photo-excited organic molecule\*\*

When the matter absorbs the energy of a photon, one of the valence electrons is promoted from the electronic ground state ( $S_0$ ) to the higher excited electronic state ( $S_1$  or  $S_2$  or higher) without change in the electron spin state (a singlet state). This transition occurs very fast on the order of  $10^{-15}$  seconds. After the electron is excited, the energy is lost as a kinetic energy due to the vibrational relaxation (vr) between vibrational energy levels at higher excited state. This vibrational relaxation is defined as a non-radiative process, that is, the electron returns to the

\*\* Jablonski energy diagram: available online at [http://chemwiki.ucdavis.edu/Analytical\\_Chemistry/Analytical\\_Chemistry\\_2.0/10\\_Spectroscopic\\_Methods/10F%3A\\_Photoluminescence\\_Spectroscopy](http://chemwiki.ucdavis.edu/Analytical_Chemistry/Analytical_Chemistry_2.0/10_Spectroscopic_Methods/10F%3A_Photoluminescence_Spectroscopy)

lowest energy of excited vibrational energy levels instantaneously without the emission of radiation.

At high excited electronic state, the matter can lose the energy in different relaxation processes. Firstly, it can possibly return to the electronic ground state by emitting a photon, called fluorescence. Secondly, the energy can be transferred to another lower electronic singlet state via the internal conversion (ic). The possibility of these phenomena depends on the lifetime of electrons at that energy level. It should be noted that fluorescence is a slow process, on the order of  $10^{-9}$  to  $10^{-7}$  seconds, occurred with a conservation of the electron spin state. The absorption and fluorescence processes are expressed as the vertical lines while the nuclear position is approximately unchanged during the processes, called Franck-Condon principle<sup>55</sup>. The energy of fluorescence is always lower than that of absorption energy due to the competitive dissipation of energy from internal conversion and vibrational relaxation. The difference energy between absorption and emission spectra is called the Stokes shift. Instead of the electronic transitions of inorganic materials, the absorption and the fluorescence spectra of organic compounds are usually broaden due to the combination of radiative transitions from the lowest electronic excited state to the different electronic ground states via non-radiative vibrational relaxation<sup>56</sup>.

Sometimes, another dissipation of energy can be occurred between the different multiplicities of electronic excited state, called intersystem crossing process (isc). In this case, the electron spin state changes from an excited singlet state to an excited triplet state ( $S_1$  to  $T_1$  in Figure 19). At the excited triplet states, the phosphorescent organic molecules have a long lifetime (on the order of  $10^{-6}$  to 10 seconds or more) before turning back to the electronic ground state<sup>57</sup>, resulting to the afterglow light emission at a low intensity up to several minutes (or more) after removing excitation source.

Generally, the transition from the singlet state is spin-allowed ( $\Delta S = 0$ ), resulting in fluorescence that can be measured even at room temperature. On the contrary, the phosphorescence is typically difficult to be observed at room temperature since this transition is considered as a spin-forbidden transition because of the electronic selection rules ( $\Delta S = 1$ )<sup>53</sup>. Although, the spin-forbidden transition may be allowed due to the spin-orbit coupling or vibrational coupling<sup>58</sup>. For the phosphorescence, the rate of intersystem crossing and the rate of phosphorescence radiative process should be favored over the non-radiative transitions<sup>59</sup>. In order to observe the phosphorescence effectively, the spectroscopy at very low temperature



(using 77 K liquid nitrogen) is required as a lab curiosity in order to reduce the collisions by molecules during the lifetime at excited states.

Fluorescent compounds are widely used in the field of science and technology for various purposes such as fluorescent probes, fluorescent indicators, fluorescent paint, and light-emitting devices<sup>60-63</sup>. For several years, many organic fluorescent compounds have been reported for the reasons that represent the good adjustability of optical properties, ease of synthesis and low production costs<sup>64-66</sup>. The number of fluorescence organic compounds are much greater than that of phosphorescence organic compounds. In addition to organometallic compounds, purely organic compounds presenting the phenomenon of phosphorescence is infrequent due to their weak and ineffective emission obtained<sup>64, 67</sup>. Some phosphorescence molecules have been reported such as aromatic carbonyl compounds<sup>68-71</sup>, quinone derivatives<sup>72, 73</sup> and halogenated aromatic compounds<sup>74-77</sup>. However, they were performed at the temperature of liquid nitrogen to the observation of phosphorescence. Recently, the phosphorescence of organic molecules can be observed at higher temperature such as at room temperature<sup>78-80</sup>. The polymer matrices and the silica cages can also enhance the phosphorescence from organic molecules at room temperature by increasing the degree of rigidity<sup>81-83</sup>. In addition to improvement of phosphorescence, the incorporation of organic molecules in these matrices can also influence on the absorption-emission spectra, photostability, and energy transfer between trapped organic molecules compared with organic dye in solution<sup>84-86</sup>. In this report, we will discuss to some organic/organometallic photoluminescent molecules which represent the interesting optical properties for light-emitting applications.

### **ii. Organic photoluminescent compounds and LEDs for white light**

According to the drawbacks of inorganic phosphor, the study of organic alternative photoluminescent materials for white light-emitting devices is greatly significant. The purpose of these photoluminescent compounds as the candidates for phosphor coating in the white light LED devices is very attractive due to their low-cost precursors, high absorption efficiencies, broad emission spectra, and several approaches to tune-up the colors by customizing their functional groups. The combinations of several high photoluminescence conjugated organic polymers with blue LEDs were studied<sup>87, 88</sup>. However, the intrinsic low electrical and chemical stability of organic compounds, which are indispensable to well-prepared expensive encapsulation method are important drawbacks confronting the organic materials used for light-emitting devices<sup>89</sup>.

In addition to photoluminescent conjugated organic polymers, there are some attempts to incorporate the organic dyes within LED modules (Table 8). The research group of Di Martino established the white light LED involving a blue light InGaN LED and the bulk polymerization of purely organic dyes doped PMMA. This combination proposed a white light with CIE coordinates of (0.32, 0.33), with a color rendering index of 80, but with a short-term stability of 72 hours<sup>90</sup>. The group of Seung-Yeon Kwak synthesized the several formulations of organic dye-siloxane hybrid structures for white light LED devices, offering the long-term thermal stability and the less temperature-dependent photoluminescent properties with acceptable color rendering index and warm white light emission<sup>91</sup>. The group of Schlotter reported the phosphor coating containing organic dye molecules embedded in an epoxy resin matrix<sup>92, 93</sup>. They showed that the white emitting organic-blue LED was obtained by adding the mixture of green and reddish emitting dyes to the epoxy resin<sup>93</sup>. However, this white emitting organic-blue LED reported still lacked of stability after testing under the real operating conditions. The research group of Ji-Young Jin has reported that white light emission can be obtained from an InGaN LED combined with bivalent fluorescein salt dispersed in an epoxy matrix. The CIE coordinates showed that this system could produce the near white light with the conversion efficiency of 84% and the fluorescence quantum yield of 94%<sup>94</sup>. However, the fluorescein based WLEDs was rapidly discolored within 1 hour after continuous irradiation. The group of Uthirakumar also studied the fluorescein derivative by attaching the copolymer chain to the fluorescein structure in order to avoid the formation of excimer and prevent the concentration quenching of fluorescein<sup>95</sup>.

Another choices of high photoluminescent organic molecules for light-emitting diodes are aggregation-induced emission (AIE) organic molecules<sup>96-100</sup>. Generally, many kinds of pure organic compounds including aromatic groups encounter the concentration-quenching effect that causes a reduction of fluorescence with an increase in their solution concentration<sup>101</sup>. The pure organic compounds such as pyrene, fluorescein and rhodamine are a good example of concentration-quenching compound in solution state<sup>102</sup>. The use of these compounds in very dilute solutions, however, diminishes the sensitivity and detectability of molecular target in biochemistry<sup>103, 104</sup>. For the lighting application, an amount of luminescent compounds have been embedded in the lighting device in order to reach the best lighting conditions. However, the aggregation-induce quenching becomes a barrier for pure organic compounds to be incorporated into the lighting devices. Thus, it will be great if an organic compound can be enlarged with an increase in fluorescence rather than quenching for light-emitting devices<sup>105</sup>.

<sup>106</sup>. The AIE organic molecules take the advantages of aggregation formation that induces the light emission rather than quenching (as observed for many organic fluorophores at high concentration). Moreover, the AIE organic molecules can be obtained as a solid form, which make them easily to use and incorporate into a formulation of phosphor coating with polymer matrices. An example of the AIE organic molecules is hexaphenylsilole (HPS) <sup>107</sup>. This molecule is soluble in organic solvent with non-emissive properties but becomes highly emissive when aggregated under UV lamp, which is an excellent candidate for further LED lighting applications.

According to the researches on the organic phosphors for light emitting applications, some kinds of organic molecules were studied. However, some organic molecules have to be modified because the molecules are limited by some functional groups in order to covalently bond with other supporting matrices such as silica or polymer resins. Also, the alteration of molecular structure can cause changes in electron density of organic molecules leading to shift in light emission. In this work, we will present some interesting organic luminescent molecules and also the hybrid luminescent materials based commercial organic phosphors in inorganic matrices such as layered double hydroxide (LDH) and amorphous silicon dioxide matrices (SiO<sub>2</sub>). The optical characterizations and some studies of chemical, physical and optical stabilities will be the criteria for choosing the molecules for being integrated with blue or UV-LEDs.

Table 8 Summary of organic / organometallic molecules based white-light LEDs

Sample configuration	Template	Photoluminescence Quantum Yield (PLQY)	Development conditions		Properties of White-light LED system						Year (Ref.)
			Thermal stability	Time-dependent stability	Type of LED	CIE x	CIE y	Ra	Luminous efficiency (lm/W)	CCT <sup>††,108</sup> (K)	
Coumarin 30 (green), diketopyrrolopyrrole (red)	PMMA	92% (coumarin 30 in PMMA) 100% (DPPth in PMMA)	-	✓	InGaN LED 450 nm	0.32	0.33	80	-	5980	2014 <sup>(90)</sup>
DBN-Red and DBN-green	Siloxane	85% (green) 41% (red)	✓	✓	InGaN LED 450 nm	0.348	0.334	85	23.7	4810	2011 <sup>(91)</sup>
Perylene-based dye	Epoxy resin	N/A	-	-	Cree LED chip 430 nm	0.33	0.33	-	-	5469	1998 <sup>(93)</sup>
Fluorescein (green), DCM2 (red)	Epoxy resin	94% (fluorescein in epoxy), 70% (DCM2 in epoxy)	-	-	InGaN LED 450 nm	0.31	0.34	-	-	6563	2007 <sup>(94)</sup>
Poly(fluoresceinyl terephthalate-co-bisphenol A terephthalate)	Epoxy resin	57% (in epoxy)	-	-	InGaN LED 450 nm	0.281	0.357	-	-	7854	2007 <sup>(95)</sup>
BTPETD	Epoxy resin	89% (in thin film epoxy)	-	✓	InGaN LED 450 nm	0.32	0.33	-	123.8 (30 mA)	6113	2013 <sup>(109)</sup>
PBITEG (orange-red), OPV (blue)	Polystyrene microbeads	20 – 30% (for mixture with PS)	-	-	Light source 350 nm	0.33	0.32	-	-	5618	2014 <sup>(110)</sup>

<sup>††</sup> To determine the correlated color temperature (CCT) of unreported cases, the modified McCamy's formula can be used from the chromaticity coordinates: LED colorcalculator, <http://www.sylvania.com/en-us/tools-and-resources/Pages/led-color-calculator.aspx>

Table 9 Summary of quantum dots based white-light LEDs

Sample configuration	Template	Photoluminescence Quantum Yield (PLQY)	Development conditions		Properties of White-light LED system						Year (Ref.)
			Thermal stability	Time-dependent stability	Type of LED	CIE x	CIE y	CRI	Luminous efficiency (lm/W)	CCT <sup>††,108</sup> (K)	
CdSe/ZnS/CdS/ZnS (green), CdSe/CdS/ZnS/CdS/ZnS (red) multishell QDs	Silicone resin	72% (green QD) 34% (red QD)	-	-	InGaN LED 450 nm	0.24	0.21	-	41	0	2010 (111)
Mn and Cu codoped Zn-In-S/ZnS QDs	Silicone resin	75% (mono QDs)	-	-	InGaN LED 450 nm	0.34	0.36	95	73.2	5216	2015 (112)
PiGs (YAG: Ce <sup>3+</sup> ) + CuInS <sub>2</sub> /ZnS red QDs embedded in silica	ETPTA	N/A	✓	✓	InGaN LED 450 nm	0.363	0.324	91	3.72	4121	2014 (113)
CdSe/ZnS green and CdSe/CdS/ZnS red QDs – silica monolith (SM)	Silica monolith	89% (green QD-SM) 63% (red QD-SM)	-	✓	InGaN LED 450 nm	0.23	0.21	-	47	0	2013 (114)
CdS (red), ZnS (green), ZnSeS (blue) QDs	Poly(St-MMA-AA) and PMMA	60% (matched PCs)	-	-	InGaN LED 365 nm	0.29	0.31	-	-	8263	2015 (115)
CdSexS1-x/ZnS QDs	Silicone epoxy	85% (green) 55% (yellow) 39% (red)	-	✓	InGaN LED 450 nm	0.4137	0.3955	81	-	3360	2013 (116)
CIS/ZnS/ZnS QDs	PMMA	92%	-	✓	InGaN LED 450 nm	0.322 – 0.325	0.294 – 0.298	70 – 72	24.6 – 68.6	5950 6150	2013 (117)

†† To determine the correlated color temperature (CCT) of unreported cases, the modified McCamy's formula can be used from the chromaticity coordinates: LED colorcalculator, <http://www.sylvania.com/en-us/tools-and-resources/Pages/led-color-calculator.aspx>

## B. Quantum dots

### i. Introduction to quantum dots

Quantum dots are size-dependent-fluorescent nanostructured semiconductors, typically with an average diameter of few nanometers, which were firstly discovered by Russian physicist Alexei Ekimov in the early 1980s<sup>118</sup>. The quantum dots have been intensively studied due to their fascinating properties such as size-tunable emission, their broad excitation and narrow emission spectra, high photo-stability and also high quantum efficiency<sup>119</sup>. According to general semiconductors at the ground state, the valence band is occupied by electrons and the conduction band is empty. When a photon with quanta of energy is absorbed, an electron from the valence band pumps to the conduction band and leaves a hole in the valence band (Figure 20)<sup>120</sup>. This energy should be higher than the interaction between the excited electron and the hole in order to separate each other. If the excitation energy occurs close to fundamental bandgap between the valence band and the conduction band, the electron-hole pair can be created with a weak attractive coulombic force, and resulted in the formation of a bound state called “exciton”. The exciton has several natural physical separation distances, and influence to the optical properties of direct bandgap semiconductors. This separation distance in an electron-hole pair is known as the “exciton Bohr radius”.

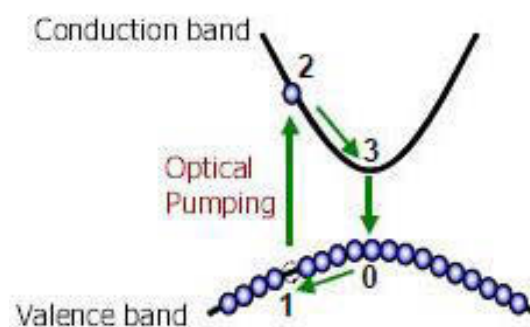


Figure 20 Optical excitation in a direct bandgap semiconductor<sup>120</sup>.

In the macroscopic semiconductors, the size of semiconductors are greatly larger than the exciton Bohr radius, the bandgap is small and the energy levels become continuous. When the size of semiconductors decreases toward the nanoscale (which is comparable to the exciton Bohr radius), the electronic and optical properties differ from the macroscopic scale. The size of quantum dots decrease to the same dimension as the Broglie wavelength, as a consequence,

the energy levels becomes discrete and the bandgap increases as size-dependent properties (Figure 21)<sup>121</sup>. Considering the bulk semiconductors, the recombination of electrons and holes results in the emission of a photon with the energy equal to the bandgap of the semiconductor. The larger bandgap between the conduction band and the valence band is, the shorter wavelength of emission energy can be emitted.

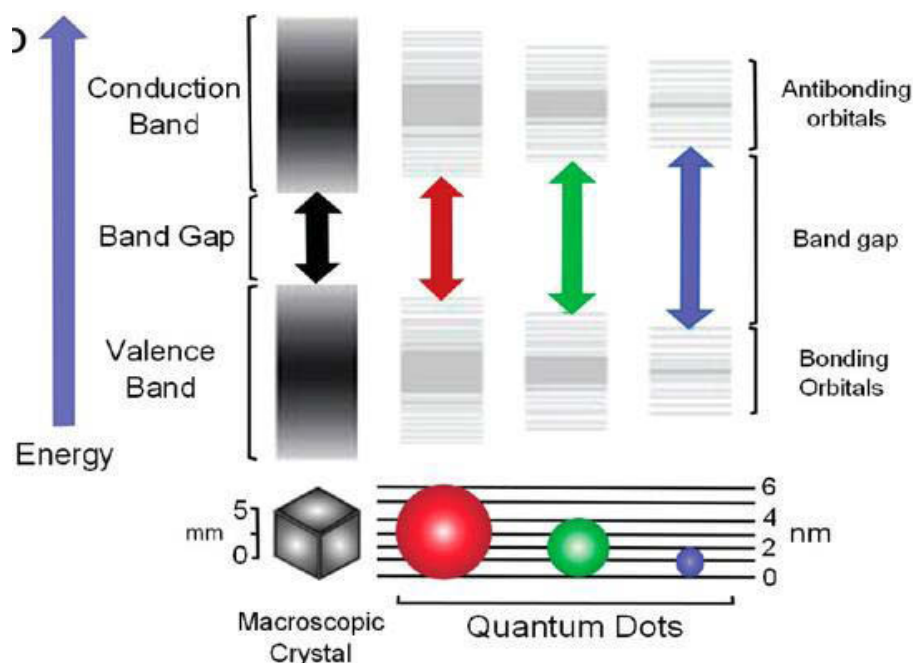


Figure 21 the energy levels and bandgap with different sizes of semiconductors<sup>121</sup>.

The synthesis of quantum dots are usually taken place in solution involving the coordinating solvent such as octadecene, hexadecylamine (HDA), trioctylphosphine (TOPO) or trioctylphosphine (TOP). The presence of these ligands on the surface of quantum dots can stabilize the nanoparticles, control the nucleation, and prevent the growth of quantum dots into the bulks. The quantum dots can be categorized into different types depending on the structure and composition such as CdSe, CdS, ZnSe, and so forth (Figure 22)<sup>122-124</sup>. However, it has been reported that the main degradation of CdSe quantum dots is the photo-oxidation at the surface of selenium atoms in the presence of oxygen and a hole<sup>125, 126</sup>. As a consequence, the quantum dot core showed a large blue shift of the absorption maximum and an decrease in optical density of absorption<sup>127</sup>. In addition, the toxic molecules are probably released from these quantum dots to environment, resulting to the decrease in nanocrystal size and the reduction of quantum yield efficiency. Kirchner et al. have been emphasized the cytotoxic effects of the leakage of Cd<sup>2+</sup> ions from quantum dots to cells<sup>126</sup>. In order to overcome and

protect the quantum dot core, the growth of inorganic material layers over the quantum dot core has been synthesized such as ZnS and silica coating.

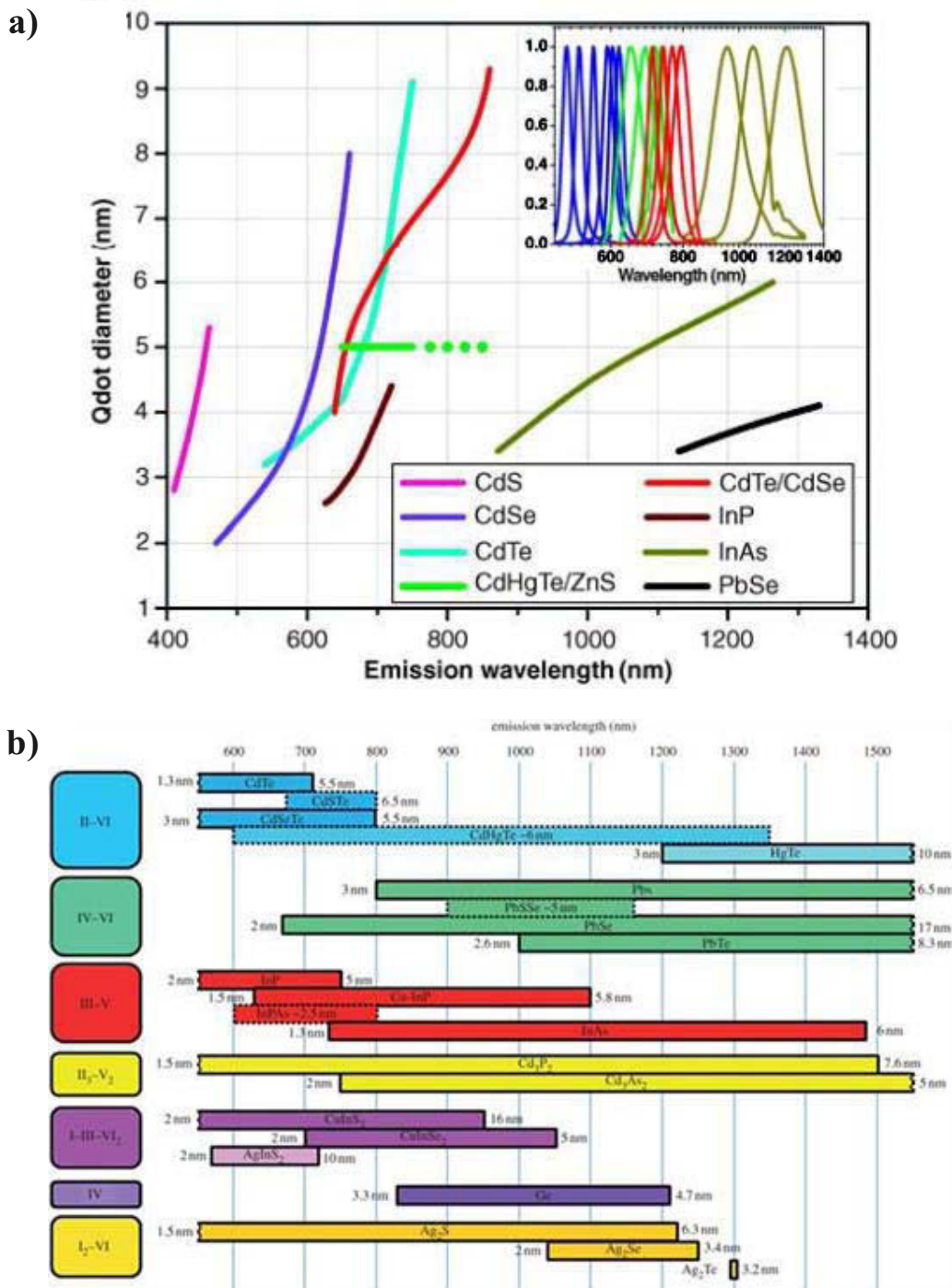


Figure 22 Summary of some quantum dots with different composition, size and emission ranges ; figure a) and b) are reproduced from [123, 124], respectively.



ii. Core-shell quantum dots

The core-shell quantum dots can be broadly categorized into four types corresponding to the position and the bandgap of the valence and conduction band (**Error! Reference source not found.**, the reverse types are not presented here)<sup>128</sup>. These core-shell quantum dots contain at least two different semiconductors in the structure. In the type I structure, the bandgap of shell structure is typically larger than core structure in order to protect from the surroundings and also to provide electronic insulation with the goal to enhance the quantum yield efficiency of core structure.<sup>124</sup> Therefore, the energy gap of core-shell structure is determined by bandgap of core structure ( $E_{g1}$  in Figure 23a). The examples of type I structure are CdSe/CdS<sup>129</sup>, CdSe/ZnS<sup>130</sup>, InAs/CdSe, and CuInS<sub>2</sub>/ZnS<sup>131</sup>. In the type II structure, the energy gap is dependent on both core and shell structure. The electron-hole pair is separated to different semiconductor. Therefore, the energy gap is determined by the energy difference between the valence band of semiconductor 2 and the conduction band of semiconductor 1, which is lower than the energy gap of either semiconductors ( $E_{g12}$  in Figure 23b). This type II structure is of interest for charge-transfer technologies (i.e. photovoltaic and electroluminescent applications) due to charge separation. The examples of type II structure are ZnTe/CdSe, CdTe/CdSe<sup>132</sup>, and CdTe/CdS<sup>133</sup>. It should be noted that in each of the examples discussed the core and the shell quantum dots have not been completely separated from each other. Instead, these semiconductors are partially miscible, allowing the formation of alloy materials of any arbitrary composition of either the core or the shell (or both) with a gradient composition from the center to the exterior surface<sup>134, 135</sup>.

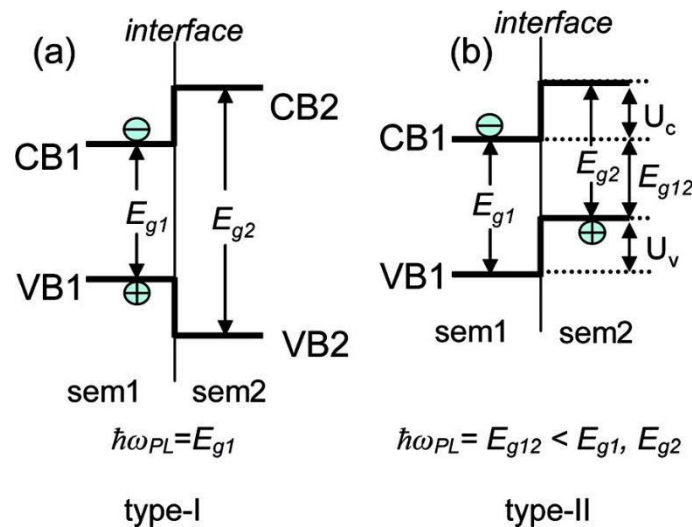


Figure 23 (a) Type I and (b) Type II of core-shell semiconductors<sup>136</sup>.

As mentioned previously, the stability of quantum dots increases when the surface is protected by shell layer in order to decrease the holes on surface and prevent contact with oxygen. The core of quantum dots can be modified after synthesis to improve the optical properties and stabilities<sup>137</sup> by shelling with large-bandgap semiconductors around them such as ZnS, ZnSe, and CdS. Several researches showed that ZnS shell provides a protecting layer of core part from oxidation reaction resulting to the formation of a selenium oxide<sup>125</sup>, avoids the release of toxic components such as Cd<sup>2+</sup> ion<sup>138, 139</sup>, and increases the quantum yield efficiency by adjusting the thickness of ZnS shell coated quantum dots<sup>140</sup>.

### iii. Quantum dots and LEDs for white light

The fascinating properties of quantum dots have attracted intense attention for lighting applications. Several approaches of quantum dots are used for electroluminescence devices (QLEDs) because they provide several advantages over conventional organic LEDs (OLEDs) such as wide absorption and narrow emission bands, low turn-on voltage, high thermal stability, good brightness and stable lifetime<sup>141-144</sup>. The remarkable mechanisms of quantum dots for QLEDs are the charge transfer into quantum dots after exciton formation and recombination processes. Therefore, the choice of quantum dots, charge transporting layers and also the specific requirement of electrodes should be appropriated.

Another approach is to generate white light by the combination of UV/blue LED together with quantum dots. The red-emitting phosphor-type quantum dots become one of the many red-emitting phosphors candidates which have been proposed to improve the weak red emission of Y<sub>3</sub>Al<sub>5</sub>O<sub>12</sub>: Ce<sup>3+</sup> (YAG: Ce<sup>3+</sup>) and raise the color rendering index of the white light. A few years ago, many groups have integrated the quantum dots with the UV/blue LEDs for white-emitting devices (see Table 9). There have been many efforts to develop the high-quality of quantum dots for LEDs.

The research group of Won Bin Im has developed the white light-emitting diodes involving PiGs materials based on YAG: Ce<sup>3+</sup> and core-shell CuInS<sub>2</sub>/ZnS quantum dots embedded silica<sup>113</sup>. This configuration presented a white light with CIE coordinates of (0.363, 0.324) and a color rendering index of 91 under an applied current of 20 mA. Moreover, the LED/PiGs/QD module exhibited an increase in luminescence stability during the operating time. However, the luminous efficiency was still low at 3.72 lm/W. The group of Eunjoo Jang has studied the high photostable quantum dots- silica monolith (QD-SM) covered onto the blue LEDs<sup>114</sup>. These

materials was prepared by preliminary surface exchange of the QDs and based-catalyzed sol-gel condensation of silica. The high quantum efficiency was obtained and the emission intensity was maintained at about 90% after 200 h of UV radiation. However, the CIE coordinates of prototype were still far from the ideal white light color (CIE  $x = 0.333$ ,  $y = 0.333$ ). The Song's team has improved the luminescence performance of quantum dots for white-light emission by combining red, green and blue QDs-photonic crystals with UV-LED chips<sup>115</sup>. This photonic crystals were introduced to the system in order to improve the dispersion of quantum dots and increase the luminous intensity of white light.

According to many groups of research above, many of them focused on white light emission with a blue LED. However, a few studies of white light-emitting diodes involving the quantum dots and an UV-LED were reported. According to Yole's report<sup>145</sup>, the UV-LED has become an interesting candidate for lighting technology by replacing the obsolete mercury lamps due to its compactness and its relative low cost of production. In addition, some quantum dots showed better quantum efficiency under UV irradiation rather than the quantum efficiency recorded under 450 nm irradiation. In this work, the studies of two types of core-shell quantum dots based on CdSe/ZnS and CuInS<sub>2</sub>/ZnS, and the quantum dots/polymer composite films with UV and/or blue LED will be presented.

## Summary

The phosphors based rare-earth elements have already become an important component in WLEDs and many lighting technologies. However, the upfront cost of rare earth element presented about 12% of the cost of WLED devices as well as their difficulty in rare-earth production could be the major problems for development of WLED technologies. The alternative luminescent materials without rare-earth elements such as organic molecules and/or quantum dots have become significant challenges for WLED markets. The properties of organic dyes and quantum dots for light-emitting applications can be summarized in Table 10. In our thesis work, we will report some interesting rare-earth-free phosphors based blue/UV-LEDs for producing white light emission. Firstly, we will present the study in organic luminescent molecules and also the hybrid luminescent materials based commercial organic phosphors embedded into inorganic matrices such as layered double hydroxide (LDH) and amorphous silicon dioxide matrices (SiO<sub>2</sub>). Then we will focus on the studies of core-shell

quantum dots based on CdSe/ZnS and CuInS<sub>2</sub>/ZnS. The combination of LED/rare-earth-free phosphors as well as their photoluminescence properties will be presented in details.

**Table 10 Comparison of properties of organic dyes, organometallic dyes and quantum dots.**

Properties	Organic / organometallic dyes	Quantum dots
Absorption spectrum	Discrete bands	High absorbance toward UVs and lower at higher wavelength
Molar absorption coefficient	Moderate, between 25,000-250,000 cm <sup>-1</sup> (146-150)	High, between 100,000-1,000,000 cm <sup>-1</sup> (151, 152)
Emission spectrum	Asymmetric and broad bands	Narrow and symmetric bands
Spectral position	Can be tuned by functional groups	Can be tuned by particle size
Quantum yield efficiency	0.05-1.0 (visible) <sup>149, 150, 153, 154</sup> 0.01-0.25 (NIR) <sup>144, 155</sup>	0.1-0.9 (visible) <sup>111, 112, 116</sup> 0.2-0.7 (NIR) <sup>156, 157</sup>
Solubility	Depend on functional groups	Depend on bonding ligands at the QD surface
Size	Molecular size (about 0.5 nm)	Colloidal size (1-100 nm)
Thermal stability	Depends on dye class and coating	High, also depends on encapsulating materials
Photostability	Moderate, typically sensible by photobleaching	Good to high
Toxicity	Vary from low to very high, depending on dye molecules	Very high (heavy metals leakage) but it can be prevented by encapsulation



---

# **CHAPTER II**

# **Organic phosphors-based white light-emitting diodes**

---



## I. Dicyanomethylene-4H-pyran derivatives for LEDs

This chapter represents the synthesis and the characterizations of organic phosphors which provide the interesting photoluminescence properties in solid state. The organic phosphors were categorized into 3 different groups due to their structure and their emission range upon 365 nm UV-light irradiation. The optical and photoluminescence properties of organic phosphors were investigated and the compounds in each group having the best value in absolute quantum yield were chosen to prepare the mixed phosphors composite films for building organic phosphors-based white light-emitting diodes using 365 nm UV-light excitation. Finally, the stability of selected organic phosphors under accelerated artificial conditions were mentioned.

### A. Introduction

The dicyanomethylene-4H-pyran compounds are the group of organic molecules that consist of a dicyanomethylene group and an aromatic group which are covalently linked to 4H-pyran core structure by  $\pi$ -conjugated system. The dicyanomethylene group which is a strong electron acceptor generates a donor-acceptor conjugated structure when combined with an aromatic donating group. This conjugated structure takes a responsibility for the action of significant red-shifted emissions to red spectral regions ( $\lambda_{\text{max}} > 610 \text{ nm}$ )<sup>158</sup>. The dicyanomethylene-4H-pyran derivatives are widely used in several optical applications such as organic light-emitting diodes<sup>159</sup>, organic solar cells<sup>160</sup>, fluorescent bio-imaging<sup>161</sup>, and also laser dyes<sup>162</sup> because of their highly sharp red emission with a small Stokes shift.

Some types of dicyanomethylene-4H-pyran derivatives have been used for fabrication of organic light-emitting diodes (OLEDs) as red emitter such as 4-(dicyanomethylene)-2-methyl-6-(*p*-(dimethylamino)styryl)-4H-pyran (DCM), 4-(dicyanomethylene)-2-methyl-6-[2-(2,3,6,7-tetrahydro-1*H*,5*H*-benzo[*ij*]quinolizin-8-yl)vinyl]-4H-pyran (DCM2) and 4-(Dicyanomethylene)-2-tert-butyl-6-(1,1,7,7-tetramethyljulolidin-4-yl-vinyl)-4H-pyran (DCJTB) as shown in Figure 24<sup>158, 163, 164</sup>. Chin-Ti Chen has also reviewed other pyran-containing red emitters for OLEDs<sup>158</sup>. DCM2 is an improved version of DCM in that DCM2 has a rigid ring of alkylamino group in order to improve the molecular rigidity and red emission compared of DCM. DCJTB molecule exhibits a strong red emission and excellent efficiency over DCM series for OLED devices by the presence of sterically hindered groups (tert-butyl and tetramethyl groups)<sup>165</sup>. However, these dicyanomethylene-4H-pyran derivatives are unsymmetrical products and their synthesis is not straight forward and purification may be complicated. Likewise many organic dyes, their



concentrated solution and solid-state aggregation cause the photoluminescence quenching due to dipole-dipole interaction or intermolecular  $\pi$ -stacking of planar molecules resulting from non-radiative deactivation of the excited states<sup>158, 166</sup>. These limitations could be a barrier to assign the molecules for solid-state light-emitting applications.

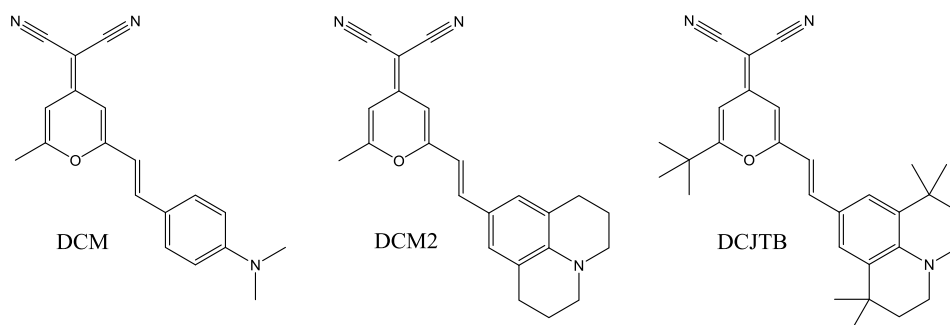


**Figure 24 Schematic representation of common red-emitting organic dyes for OLEDs.**

The synthesis of symmetrical dicyanomethylene-4H-pyran derivatives has provided a new strategy for fabrication of red-emitting organic compounds. The solid-state emission of these dicyanomethylene-4H-pyran compounds can be defined as aggregation-induced emission (AIE)<sup>158, 167, 168</sup>. These symmetrical dicyanomethylene-4H-pyran have been synthesized and showed a high red emission in solid state owing to the restriction of intramolecular rotation that promotes their photoluminescence properties<sup>168</sup>. On the other hand, these compounds emit weak photoluminescence in dilute solution by reason of free rotation of aromatic rings around the vinyl group<sup>168</sup>. To date, several examples of symmetrical dicyanomethylene-4H-pyran derivatives have been investigated for their aggregation-induced emission properties in THF-water mixture<sup>96, 167</sup>. As described in chapter 1, the photoluminescence properties of AIE organic molecules in solid form take the advantages over many concentration-quenching organic dyes, which represent as excellent alternative choices for solid-state lighting applications.

Additionally, we had discovered a series of highly blue-emitting organic molecules during the study of dicyanomethylene-4H-pyran derivatives by one-step reaction of 4H-pyran with primary aliphatic amines such as methylamine, butylamine, hexylamine and octylamine<sup>169</sup>. This similar study has been published by Man Sub Shin et al. by the reaction of 4H-pyran with 6-amino-hexyl-carbamic acid tert-butyl ester (HMDABOC) in acetonitrile but the obtained product showed weak emission bands near at 480 nm<sup>170</sup>. Moreover, there is no scientific research to study these blue-emitting dicyanomethylene-4H-pyran derivatives for optical and lighting applications. Hence, the development of this series of dicyanomethylene-4H-pyran

derivatives are expected to be useful as new candidates of solid-state luminescent organic dyes for further lighting applications.

In this chapter, we have synthesized and characterized two different series of dicyanomethylene-4H-pyran derivatives which lead to a blue emission (series I) and a red emission (series II). The series I represents the (2,6-DiMethyl-1-methylPyridin-4(1H)-ylidene)Propanedinitrile (DMPP) derivatives based on 4H-pyran with the changes in the alkyl chain length of n-alkylamine part. The series II involves symmetrical DiCyanoMethylene-2,6-diStyryl-4H-Pyran (DCMSP) derivatives. Their photoluminescence properties under UV excitation which are compatible with UV-LEDs will be discussed in details.

## B. Results and discussion

### a. Synthesis and characterizations of DMPP derivatives

Figure 25 illustrates the synthetic routes to blue-emitting DMPP derivatives. Firstly, (2,6-dimethyl-4H-pyran-4-ylidene)propanedinitrile (**1**) was prepared by the reaction of 2,6-dimethyl-4-pyrone and malononitrile in acetic acid anhydride as reported in the literature<sup>171</sup>. The DMPP derivatives were recrystallized in solvents. Then, all DMPP derivatives were synthesized by the reaction of compound **1** with primary aliphatic amines in acetonitrile under reflux temperature for 1-2 hours. The reaction mechanisms of DMPP derivatives was firstly proceeded by 1,6-addition of primary aliphatic amine to compound **1** following by the ring closure along intramolecular nucleophilic attack of secondary amine followed by dehydration (Figure 26). The melting point of all DMPP derivatives was obtained at temperature higher than 150°C, which can be the primary indication of thermal stability for all DMPP derivatives under operating condition of remote phosphor typed of LEDs.

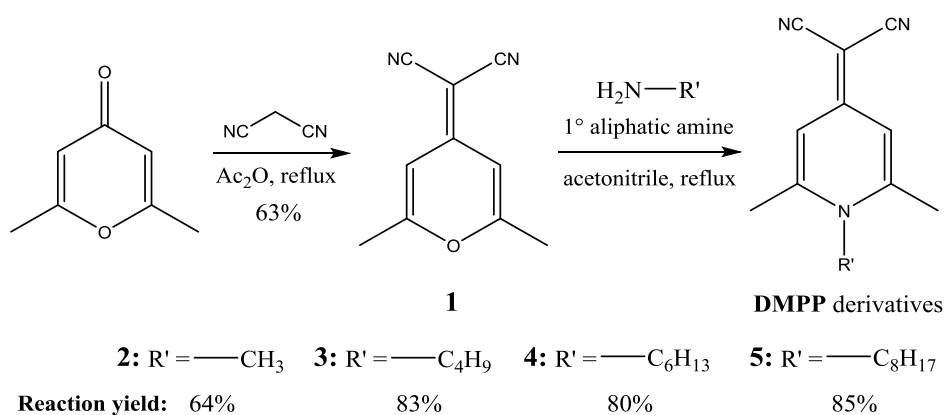
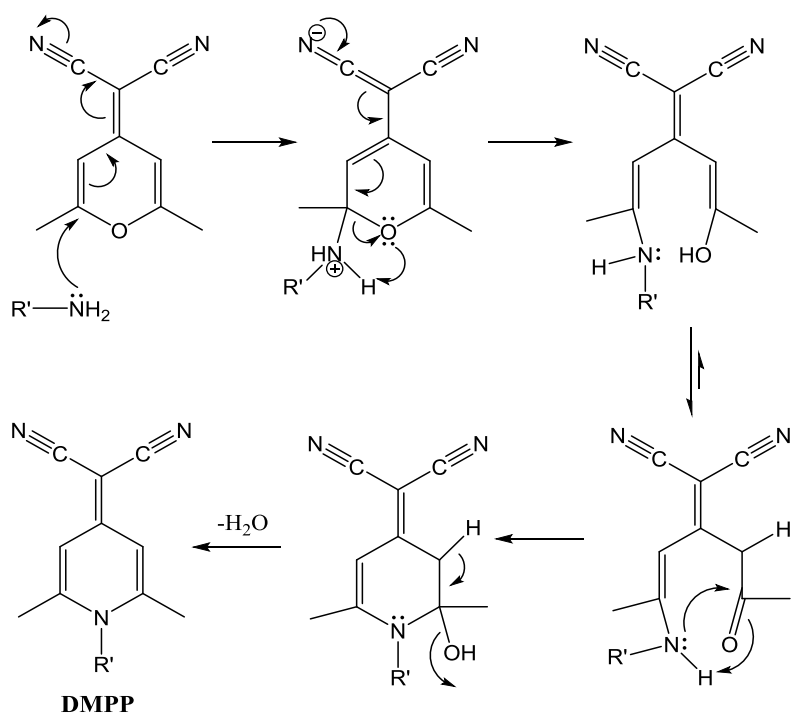
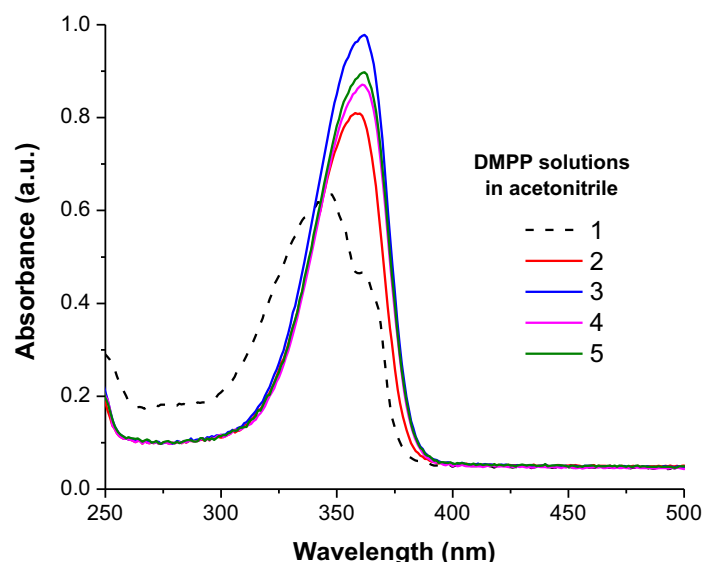


Figure 25 Synthetic routes to blue-emitting DMPP derivatives.



**Figure 26** Schematic reaction mechanism for the reaction of DMPP derivatives.

The UV-visible absorption spectra of DMPP derivatives were measured at room temperature in acetonitrile solution (Figure 27). The absorption spectra of compound **2-5** present single absorption peak situated between 358-361 nm. The absence of absorption peaks at higher wavelengths ( $> 400$  nm) of DMPP derivatives leads to the colorless solutions. The compound **3** exhibited the most intense absorption band at 361 nm. Moreover, these absorption spectra were shifted towards the higher wavelengths as well as the increase in absorbance compared with the absorption spectrum of compound **1**. The large absorption peaks of DMPP derivatives should be attributed to the  $\pi-\pi^*$  transition of conjugated system. This effect can be explained by the presence of nitrogen atom in DMPP derivatives that is less electronegative than oxygen atom in compound **1** (3.0 and 3.5, respectively). As shown in Figure 27, the absorption spectra of DMPP derivatives exhibited very small changes when the carbon chain length of aliphatic amine increased from 1C (methylamine) to 8C (octylamine).



**Figure 27 UV-visible absorption spectra of DMPP derivatives in acetonitrile (Concentration = 20  $\mu$ M).**

A point of interest in DMPP derivatives is the optical and photoluminescence properties in solution and the solid state. This phenomenon of DMPP derivatives should be also categorized into aggregation-induced emission (AIE) molecules. Figure 28 shows an example of aggregation-induced phenomenon of DMPP derivatives in acetonitrile/water mixture. The blue-emitting light of compound **4** in acetonitrile/water mixture ( $15 \times 10^{-5}$  M) were observed under 365 nm UV irradiation as water volume fraction ( $f_w$ ) increased to higher values ( $f_w \geq 70\%$ ). It should be noted that the acetonitrile solution of DMPP derivatives presented no emission under UV irradiation ( $f_w = 0\%$ ) but the blue emission in the mixture was affected by the formation of aggregates of compound **4** in acetonitrile/water mixture. They exhibited blue emission in their aggregated state. In order to ensure the aggregation-induced emission of compound **4**, we measured the absorption and emission spectra of compound **4** in acetonitrile/water mixtures with  $f_w$  ranging from 0% to 85%.

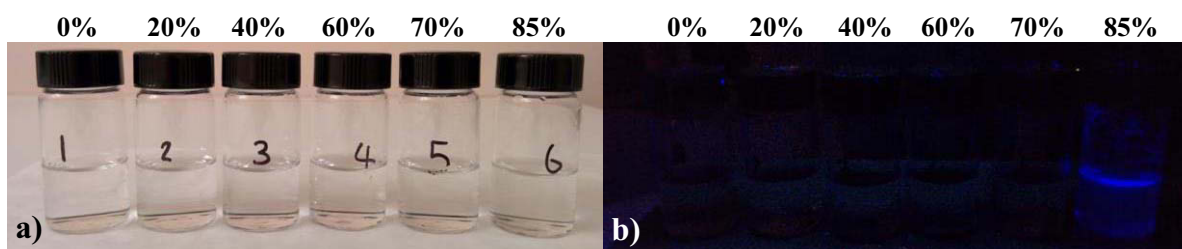


**Figure 28 (a) Photographs observed under (a) day light and (b) 365 nm UV lamp for compound 5 ( $15 \times 10^{-5}$  M) in acetonitrile/water mixtures with  $f_w$  range of 0-85%.**

Figure 29-left shows the absorption spectra of compound **4** in acetonitrile/water mixtures. When the water fraction increased from 0% to 85%, the absorption maximum peak presented a little blue-shifted by 2-4 nm. The change in position of absorption band toward the higher absorption energies might be due to the formation of H-aggregates in the solution mixture<sup>172§§</sup>. Figure 29-right shows the PL emission spectra of compound **4** in acetonitrile/water mixtures under excitation at 365 nm. It should be noted that the concentrations of mixtures was 10-times higher than those of mixtures in absorption spectra because the photoluminescence could not be recorded at the concentration of  $15 \times 10^{-6}$  M. The weakened emission was firstly observed at  $f_w = 0\%$  with an absolute quantum yield of 0.49% (Figure 30). The PL emission intensity was continuously unchanged as the water fraction increased from 0% to 70%. When the water fraction reaches to 85%, the PL emission intensity is amplified 3-times higher than the previous mixtures, with an absolute quantum yield of 1.60% (see Figure 30). The PL emission data is in agreement with the previous visual observation of blue-emitting aggregates in mixture ( $f_w = 85\%$ ) upon 365 nm UV-light irradiation (see Figure 28b).

As DMPP derivatives showed significant photoluminescence properties in aggregated state, it will be interesting to incorporate them onto LED chips to make solid-state lighting devices. In the next section, we reported on optical studies of solid-state DMPP derivatives.

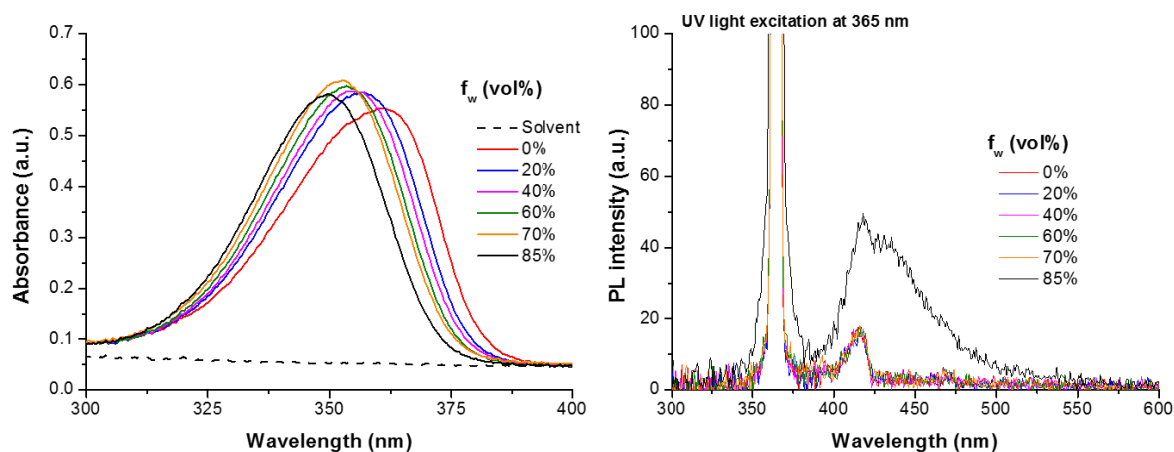


**Figure 29 (left) Absorption spectra (concentration =  $15 \mu\text{M}$ ) and (right) photoluminescence spectra (concentration =  $15 \times 10^{-5}$  M) of compound **4** in acetonitrile/water mixtures with  $f_w$  range of 0-85%.**

<sup>§§</sup> H-aggregates is defined by the molecules prefer to organize themselves as a side-by-side or a sandwiched-type arrangement ( $\theta = 90^\circ$ ).

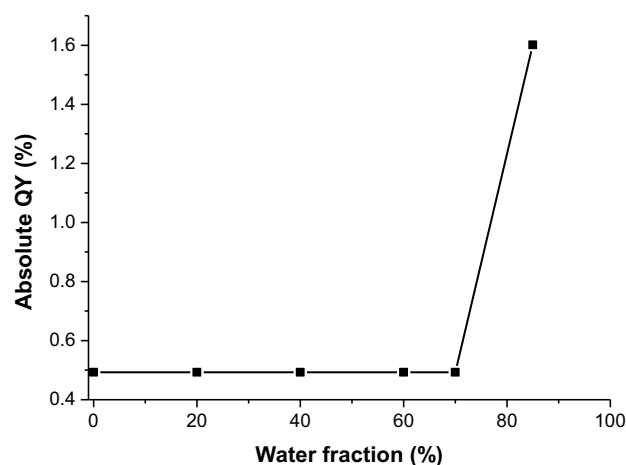


Figure 30 Absolute quantum yield of compound 4 as a function of water fraction in acetonitrile/water mixture (concentration =  $15 \times 10^{-5}$  M).

### C. Optical and photoluminescence studies of DMPP derivatives

Firstly, the photoluminescence properties of DMPP derivatives were studied and recorded at room temperature. Figure 31 presents the absorption and emission spectra of DMPP derivatives in solid state. The summary of their photoluminescence properties is also reported in Table 11.

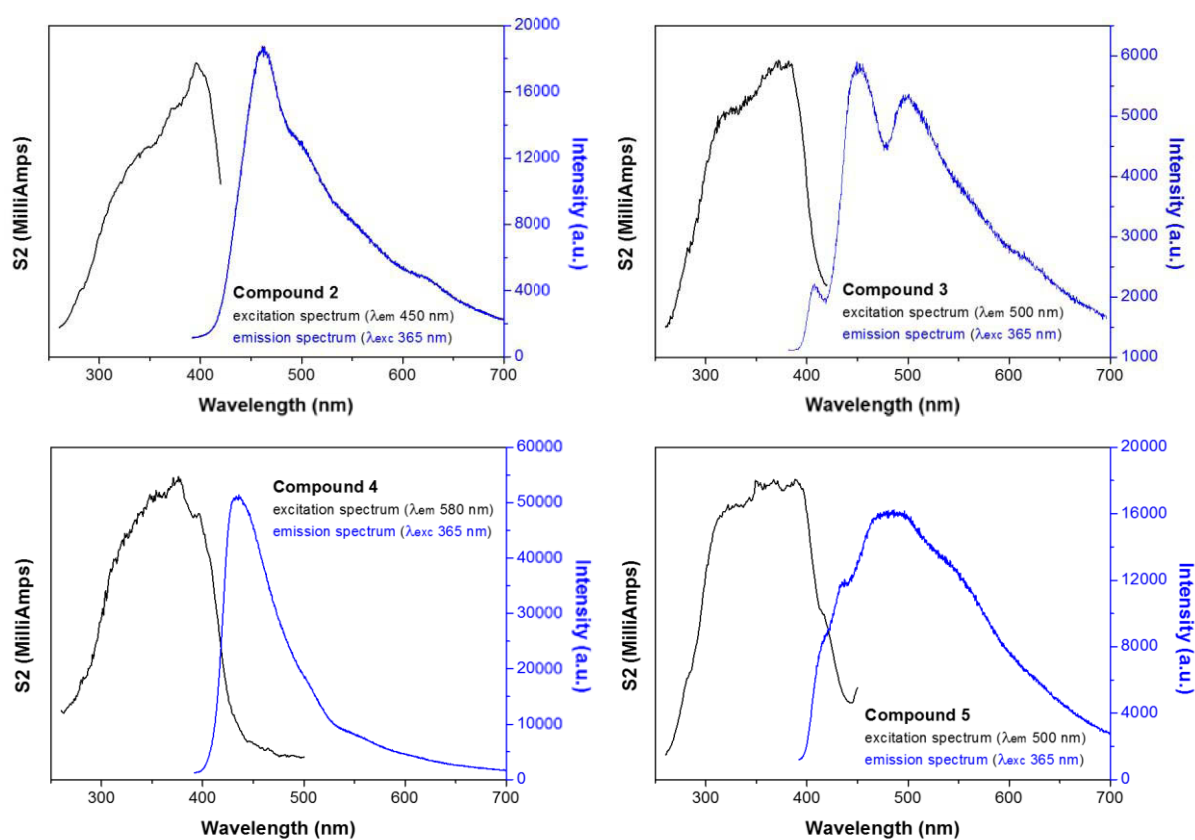


Figure 31 Excitation and emission spectra of DMPP derivatives under 365 nm UV-light illumination.

The excitation spectra show the large spectral range of 250-400 nm, which enable all compounds to be excited under UV-LEDs (365 or 385 nm for example). The PL emission spectra of all derivatives recorded after excitation at 365 nm UV-light irradiation show a wide photoluminescence from 400 to 700 nm with the maximum in blue-light emission region. The absolute quantum yield of all derivatives were also measured by using PLQY measurement system. The results pointed out that both emission intensity and absolute quantum yield did not develop as a function of alkyl chain length of primary aliphatic amine (see in Table 11). However, the most intense photoluminescence was observed for compound **4**, with the highest value in the absolute quantum yield (30%) under 365 nm UV excitation. As with the previous results, we suggested that the molecular structure of compound **4** might play an important role in the outstanding photoluminescence over other compounds in the series. In order to explain the photoluminescence properties of these organic compounds, the structural analysis by single crystal X-ray crystallography was performed. The details of the crystal data and a summary of the intensity data collection parameters for organic compounds **2-5** is given in Table 12.

**Table 11 Optical characteristics of DMPP derivatives in solid state.**

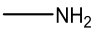
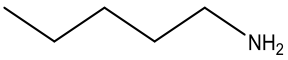
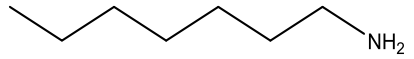
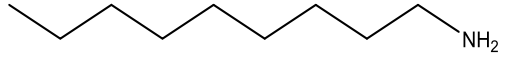
DMPP	Amine type (as a precursor)	Exc $\lambda_{\text{max}}$ (nm)	PL $\lambda_{\text{max}}$ (nm)	PLQY <sub>abs</sub> at 365 nm (%)
<b>2</b>		396	462	6
<b>3</b>		371	451	13
<b>4</b>		377	436	30
<b>5</b>		389	482	12

Table 12 Crystal data of organic compounds 2-5.

	2	3	4	5
<b>Crystal data</b>				
empirical formula	C <sub>22</sub> H <sub>22</sub> N <sub>6</sub>	C <sub>14</sub> H <sub>17</sub> N <sub>3</sub>	<u>C<sub>32</sub>H<sub>42</sub>N<sub>6</sub></u>	C <sub>74</sub> H <sub>100</sub> N <sub>10</sub>
molecular wt	370.45	227.30	<u>510.71</u>	1129.63
cryst syst	triclinic	triclinic	<u>triclinic</u>	triclinic
space group	P $\bar{1}$ (2)	P $\bar{1}$ (2)	<u>P <math>\bar{1}</math> (2)</u>	P 1 (1)
temperature (K)	100	100	<u>100</u>	100
a, Å	8.0692(7)	7.5813(6)	<u>7.0504(7)</u>	9.2959(7)
b, Å	10.7852(9)	8.9888(7)	<u>11.8724(11)</u>	12.7992(10)
c, Å	12.8057(11)	9.9103(8)	<u>17.0452(16)</u>	13.993(1)
$\alpha$ , deg	98.871(4)	79.116(3)	<u>89.957(4)</u>	89.728(4)
$\beta$ , deg	105.975(4)	84.038(3)	<u>88.210(4)</u>	89.939(4)
$\gamma$ , deg	108.649(4)	80.803(3)	<u>89.900(4)</u>	81.595(4)
V, Å <sup>3</sup>	978.61(15)	652.79(9)	<u>1426.07(20)</u>	1646.99(20)
Z	2	2	<u>2</u>	1
D <sub>calc</sub> , g cm <sup>-3</sup>	1.2571	1.15633	<u>1.18928</u>	1.13886
F(000)	392	244	<u>552</u>	614
abs coeff, mm <sup>-1</sup>	0.08	0.07	<u>0.07</u>	<u>0.07</u>
crystal size, mm	0.26 x 0.35 x 1.28	0.88 × 0.71 × 0.26	<u>0.39 × 0.24 × 0.21</u>	<u>0.30 × 0.30 × 0.27</u>
<b>Data collection</b>				
No. of measured, independent and observed [ $I > 2\sigma(I)$ ] reflections	<u>63802</u> , <u>7504</u> , <u>4001</u>	<u>43919</u> , <u>4893</u> , <u>4423</u>	<u>109444</u> , <u>10660</u> , <u>7985</u>	<u>149668</u> , <u>24681</u> , <u>18515</u>
$R_{int}$	0.032	<u>0.033</u>	<u>0.048</u>	<u>0.057</u>
( $\sin\theta/\lambda$ ) <sub>max</sub> (Å <sup>-1</sup> )	0.778	<u>0.790</u>	<u>0.795</u>	0.795
<b>Refinement</b>				
R[F <sup>2</sup> > 2σ(F <sup>2</sup> )], wR(F <sup>2</sup> ), S	0.058, 0.180, 1.08	<u>0.039, 0.121, 1.10</u>	<u>0.042, 0.132, 1.09</u>	<u>0.051, 0.159, 1.06</u>
No. of reflections	5907	4893	<u>10660</u>	<u>24681</u>
No. of parameters	259	157	<u>349</u>	<u>769</u>
$\Delta\rho_{max}$ , $\Delta\rho_{min}$ (e Å <sup>-3</sup> )	0.51, -0.43	0.51, -0.27	<u>0.46, -0.41</u>	<u>0.62, -0.41</u>



All crystal structure determinations were carried out at the temperature of 100 K on a Bruker APEXII CCD diffractometer with the use of the graphite-monochromatized MoK $\alpha$  radiation ( $\lambda=0.71073$  Å). A data collection strategy consisting of  $\varphi$  and  $\omega$  scans was devised using COSMO in APEXII<sup>173</sup>. The data frames were 0.5° in width and taken at a detector distance of 60 mm with exposure time of 10 s/frame. For compounds **3** to **5**, Initial cell refinements and data reduction were carried out with SAINT in APEX2<sup>173</sup>. A multi scan absorption correction was performed with SADABS. For compound **2**, cell\_now program was used to determine the twinning law in the compound. The twinning matrix was thus: (1 0 0 0 -1 0 0 0 -1). The multi scan absorption correction was performed with TWINABS. XPREP was then used for space group determination and to create file for SHELXTL. The structures were solved with SHELXS and refined by full matrix least-squares on F<sup>2</sup> with SHELXL of the HELX package<sup>174</sup>. All non-hydrogen atoms were refined anisotropically, whereas the hydrogen atoms constrained (HFIX options).

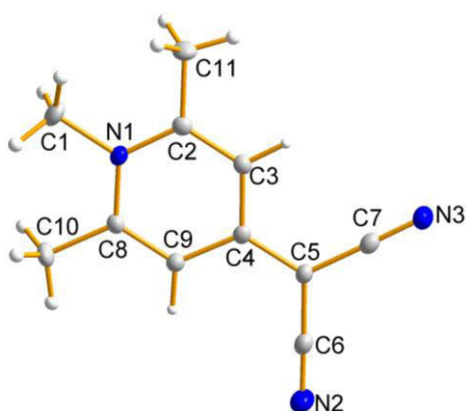
The organic compounds **2-4** crystallized in the space group P  $\bar{1}$  (2) with two molecules per unit cell, while the compound **5** was found to crystallize in a different crystal system from compound **2-4** in which its space group was P 1 (1) with only one molecule per unit cell. The compounds **2-4** exhibit molecular stacking between the planar molecular planes which tend to orient in favorable  $\pi$ - $\pi$  interactions between two molecules. The molecular structure of compound **2-5** with 50% probability thermal ellipsoids depicted are presented in Figure 32-Figure 35, respectively. As displayed in Figure 36-Figure 39, several molecular packing modes can be found in compound **2-5**: side-by-side or sandwiched-type arrangement (a distorted H-aggregation mode), head-to-head and/or head-to-tail arrangement (a distorted j-aggregation mode)<sup>175, 176</sup>. These ensemble molecular packing modes could explain the photoluminescence properties of DMPP derivatives in aggregated system as well as the feeble emission in solution state.

The crystal structure of compound **2** present molecular stacking layers in which molecules are  $\pi$ - $\pi$  stacked as a staircase arrangement with different orientation of each molecule in the layer (Figure 36). The intermolecular distance between stacking molecules in compound **2** was observed to be about 3.44 Å (N5-C13', N1''-C5'''). When the alkyl chain increased from CH<sub>3</sub> to C<sub>4</sub>H<sub>9</sub> (compound **3**), the alkyl chain was adjusted to align between two molecular stacking, resulting in the expansion of molecular stacking (Figure 37). The stacking molecular distance with alkyl chain alignment was measured to be around 6.36 Å. The  $\pi$ - $\pi$  stacking molecular distance, about 3.58 Å (C2-N2'), was slightly larger than that of compound **2**.

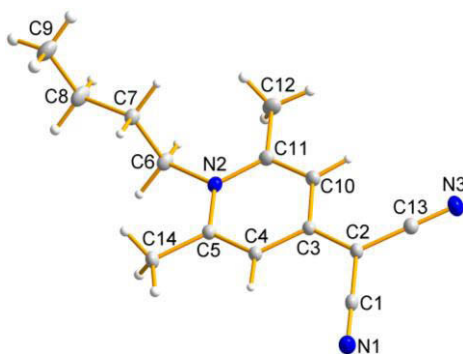
Interestingly, the alkyl chain can induce H-bonding (3.0 Å) between the molecules in the same layer. The presence of H-bonding, depicted as a red dashed line in Figure 37, were observed by the interaction of C8–H9 atom with H-bond acceptor (C≡N group) of another molecule (C2'–N3').

It was very interesting that the compound **4** showed the different molecular arrangement in crystal lattice with particular conformations from compound **2** and **3** (Figure 38, left). The crystal structure of compound **4** presented excellent  $\pi$ – $\pi$  stacked layers in [1 0 0] plane with stacking molecular distance of 3.49 Å (C25–C25'). Furthermore, the interaction of H atoms in alkyl chain with H-bond acceptor (C≡N group) of another molecule can promote H-bonding, resulting the special conformation of stacked molecules which becomes completely locked by themselves. Accordingly, the effects of  $\pi$ – $\pi$  interactions and H-bonding could be a good explanation of why the compound **4** showed the best performance in photoluminescence properties compared with other similar structures.

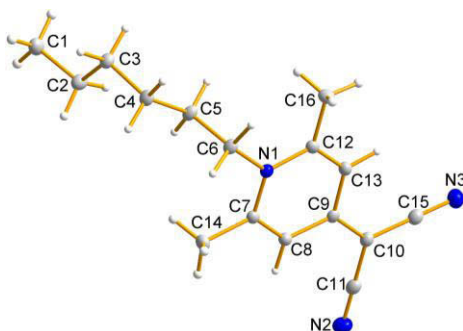
The compound **5** represent different conformation compared with other compounds in which it organizes without  $\pi$ – $\pi$  interactions (Figure 39). The alkyl chain was found in-plane molecular arrangement with its core structure. The possible intermolecular interactions of compound **5** were the Van der Waals between the alkyl chains of molecules in the same plane. The H-bonding could also occur as a long-distance interaction between alkyl chains of one molecule and C≡N group of molecule in another plane. As a consequence, the lack of  $\pi$ – $\pi$  interactions might be the main reason for the drop in photoluminescence properties of compound **5** after reaching the maximum values for compound **4**.



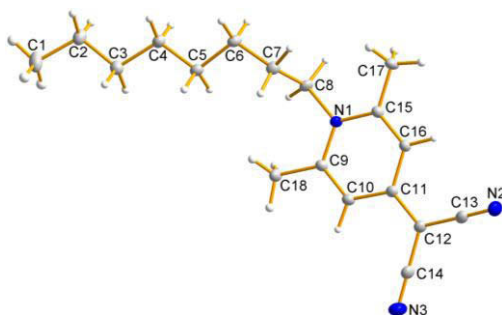
**Figure 32 X-ray crystal structure of compound 2 with 50% probability thermal ellipsoids depicted.**



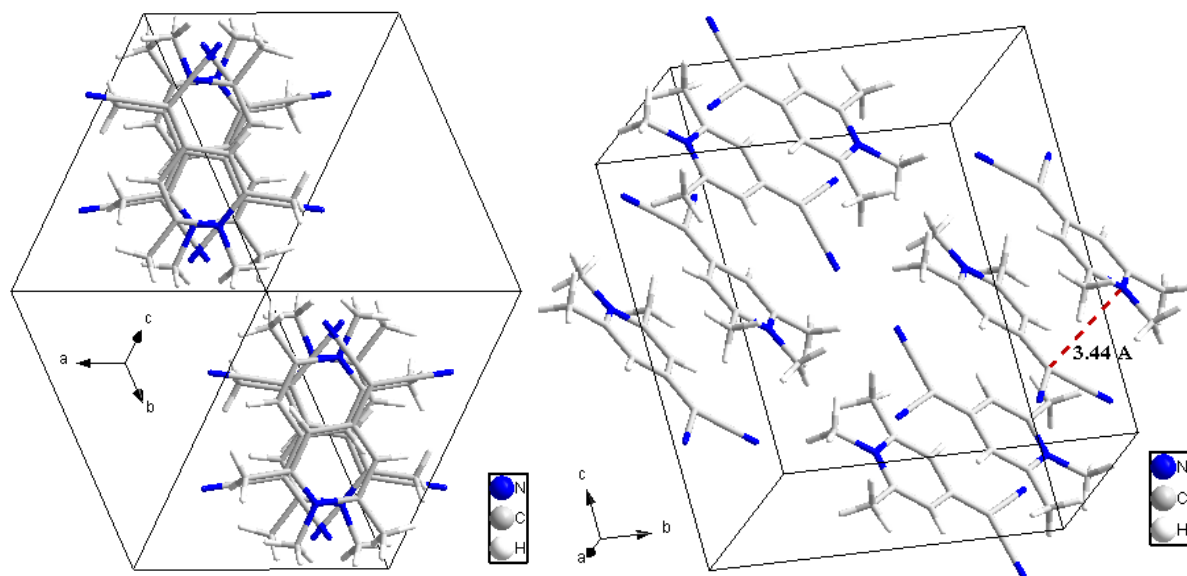
**Figure 33** X-ray crystal structure of compound 3 with 50% probability thermal ellipsoids depicted.



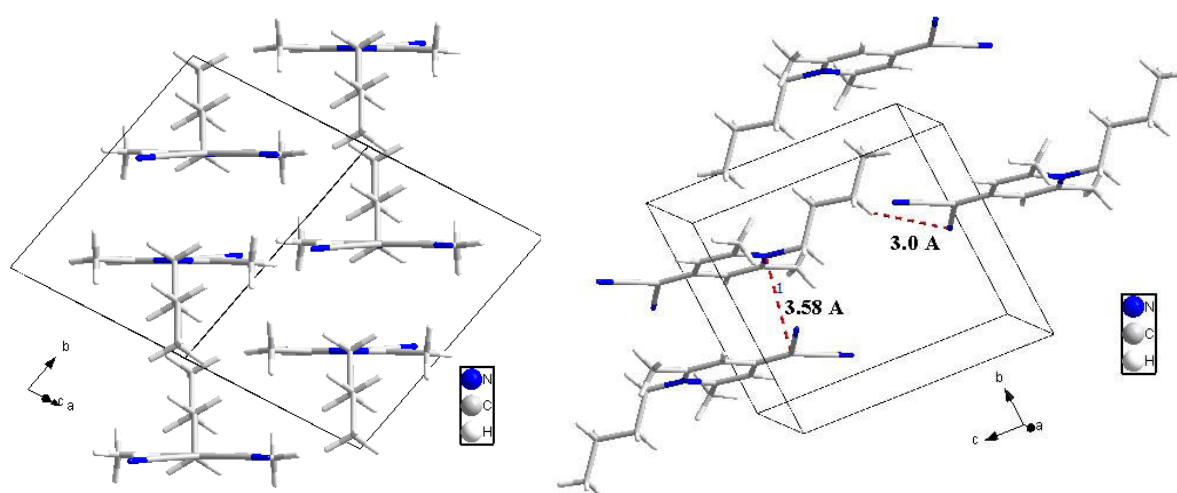
**Figure 34** X-ray crystal structure of compound 4 with 50% probability thermal ellipsoids depicted.



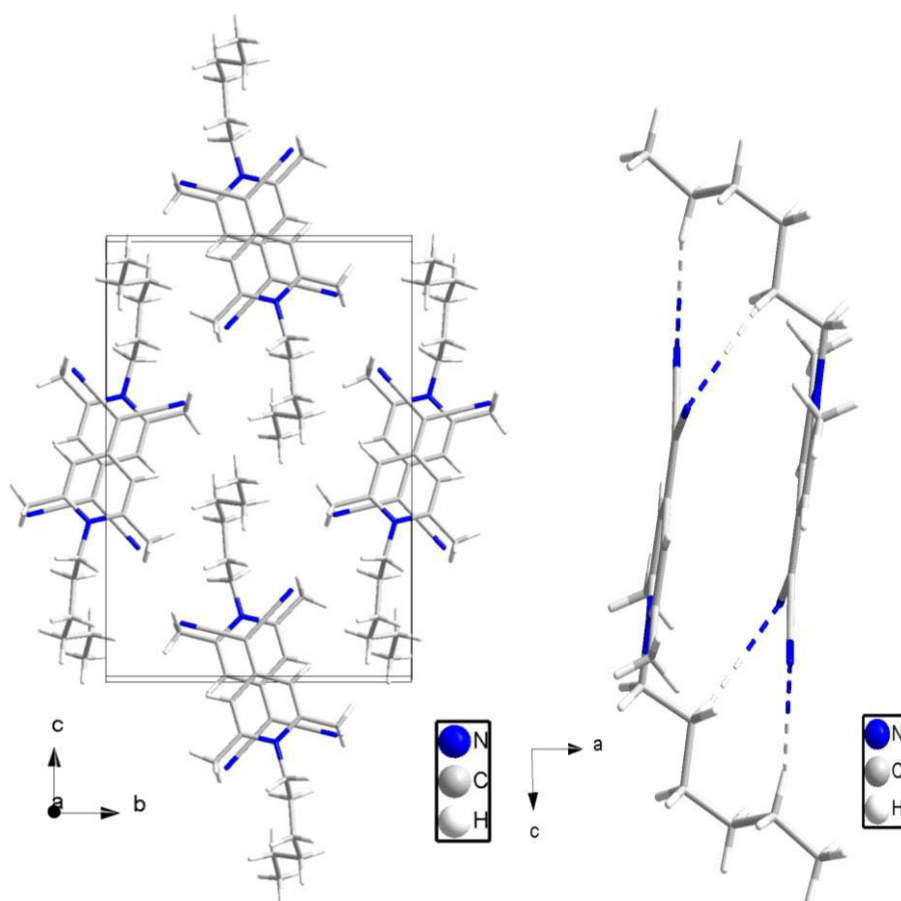
**Figure 35** X-ray crystal structure of compound 5 with 50% probability thermal ellipsoids depicted.



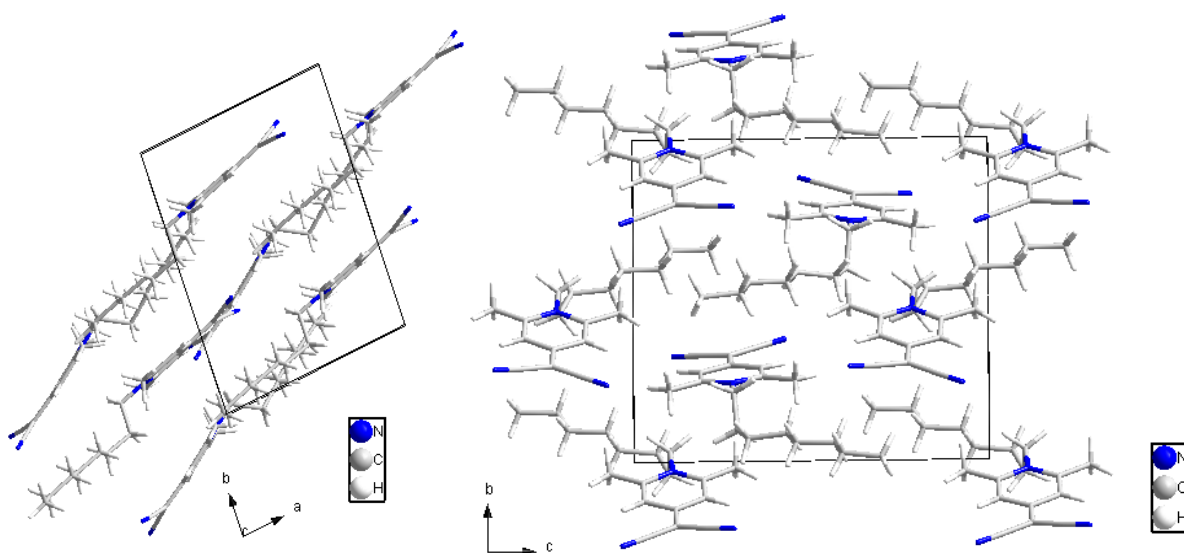
**Figure 36** Part of the crystal structure of compound 2, showing the intermolecular distance between stacking molecules (right).



**Figure 37** Part of the crystal structure of compound 3, showing the interaction between molecules. The red dashed lines represent hydrogen bonds and the intermolecular distance between molecules.

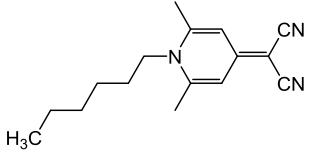


**Figure 38** Part of the crystal structure of compound 4, showing the interaction between molecules along [100] (left) and [010] (right). The dashed lines represent hydrogen bonds between molecules.



**Figure 39** Part of the crystal structure of compound 5, showing the interaction between molecules.

As expressed, the DMPP derivatives are aggregation-induced emission (AIE) active in term of UV-absorption shifts and PL emission which could be explained by their own molecular packing structures. The analysis of single crystal X-ray diffraction exposed the important information about molecular packing modes in solid state. Computational modeling of their electronic properties as well as PL emission are becoming ongoing projects in order to collect more insights about the connectivity between PL emission and their molecular structure of DMPP derivatives. The solid-state DMPP derivatives exhibited high photoluminescence in blue-light emission region, which lead to new AIE-active candidates for further lighting applications. Compound 4, which was prepared by reaction of (2,6-dimethyl-4H-pyran-4'-ylidene)malononitrile with 1-hexylamine, presented the best photoluminescence properties of the solid-state blue-emitting organic phosphors typed DMPP under 365 nm LED excitation. The summary of compound 4 is described in table below.

COMPOUND 4	Chemical structure	Exc $\lambda_{\max}$ (nm)	PL $\lambda_{\max}$ (nm)	PLQY <sub>abs</sub> at 365 nm (%)
Blue-emitting organic phosphor		377	436	30

## a. Synthesis and characterizations of DCMSP derivatives

Figure 40 represents the synthetic routes to red-emitting DCMSP derivatives. As mentioned previously, (2,6-dimethyl-4H-pyran-4'-ylidene)malononitrile (**1**) was prepared by the Knoevenagel reaction of 2,6-dimethyl-4-pyrone and malononitrile in acetic acid anhydride as recorded in the literature<sup>171</sup>. All compounds of DCMSP derivatives were recrystallized in solvents before further characterization. The DCMSP derivatives were prepared by nucleophilic addition of the methyl group of compound **1** to an aromatic aldehyde in the presence of piperidine followed by dehydration. The melting point of all DCMSP derivatives was recorded at temperature higher than 200°C (see Table 13), indicating that all DMPP derivatives could be thermally stable under operating condition of LED devices.

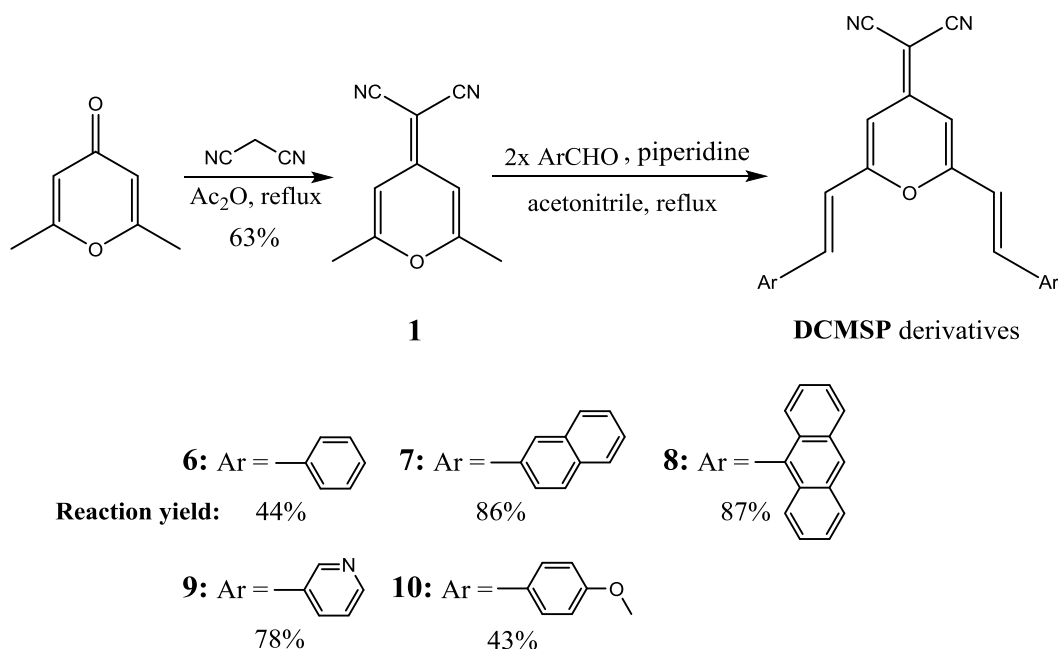


**Figure 40** Synthetic routes to red-emitting DCMSP derivatives.

According to the theoretical study of Sung Soo Park et al, the possible geometry of dicyanomethylene-4H-pyran derivatives could be calculated by optimizing intermolecular rotations to obtain the lowest hydrogen repulsion<sup>177</sup>. The hydrogen repulsions resulted from hydrogen atoms at vinyl group that bound to both 4H-pyran core structure and aromatic rings. The optimized geometry of dicyanomethylene-4H-pyran derivatives was proposed with minimum energy and less intramolecular hydrogen repulsion<sup>177</sup>. Therefore, all structures of DCMSP derivatives in this report will be illustrated with the suggested conformation.

Table 13 UV-visible data (in chloroform) and melting point of DCMSP derivatives.

DCMSP derivatives	Melting point (°C)	$\lambda_{\text{max}}$ (abs) nm	$\epsilon$ (at $\lambda_{\text{max}}$ , abs) $\text{M}^{-1} \text{cm}^{-1}$
6	252.9 - 253.4	387	48,704
7	267.8 - 268.6	416	66,071
8	>300	252	190,269
9	>300	378	40,071
10	236.0 - 238.2	418	68,544

Figure 41 shows the UV-visible absorption spectra of DCMSP derivatives in chloroform solution. The compounds **6-10** have 2 distinct groups of absorption bands with high molar absorption coefficients ( $\epsilon$ ) in the range of 250-350 nm and 322-570 nm, respectively. The strong and broad absorption peaks in the range of 400-570 nm lead to the visible color of orange-red of DCMSP derivatives in chloroform solutions. The bands observed at the shorter wavelengths (250-350 nm) can be attributed to the  $\pi-\pi^*$  electronic transitions and the longer wavelengths (322-570 nm) are ascribed to the absorption of  $\pi$ -conjugated system due to intramolecular charge transfer band of conjugated structure<sup>178, 179</sup>. Moreover, the absorption spectra of DCMSP derivatives are shifted towards the longer wavelengths as well as the increase in absorbance compared with the absorption spectrum of compound **1**. These red-shift of DCMSP derivatives in comparison to compound **1** can be arisen from the expansion of delocalized  $\pi$ -conjugated system over the entire molecule.

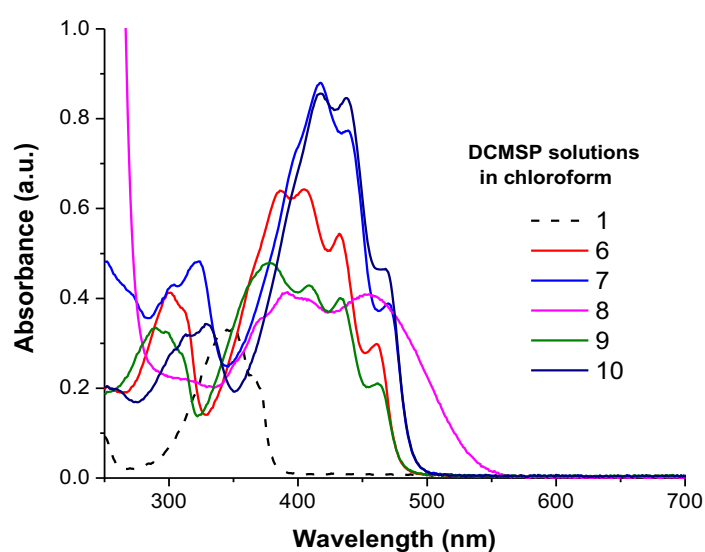


Figure 41 UV-visible absorption spectra of DCMSP derivatives in acetonitrile (Concentration=12.5  $\mu\text{M}$ ).



As with the previous mention of aggregation-induced emission (AIE) for some symmetrical dicyanomethylene-4H-pyran derivatives, the DCMSP derivatives emit their light emission due to their aggregate formation. Except for compound **7** and **8**, DCMSP derivatives have been studied for aggregation-induced emission in THF/water mixture<sup>180, 181</sup>. According to the published works, the aromatic groups as well as the 4-methoxyphenyl group of DCMSP derivatives were not strong enough to have the donor-acceptor interactions with dicyanomethylene group ( $=C-C(C\equiv N)_2$ ) as an acceptor unit. Therefore, the aromatic rings could have free rotations around the vinyl group making the DCMSP derivatives non-emissive in solution state. However, the restriction of intramolecular conformation convinces the DCMSP derivatives to have an aggregation-induced photoluminescence properties. According to the AIE phenomenon of DCMSP derivatives, it is very interesting to investigate these compounds in solid state in order to combine with UV and/or blue LED chips for LED lighting applications. In the next section, we will present the optical and photoluminescence properties of DCMSP derivatives in solid form.

### b. Optical and photoluminescence studies of DCMSP derivatives

The photoluminescence properties and the fluorescence quantum yield of DCMSP derivatives in solid form were investigated at room temperature and summarized in Table 14.

**Table 14 Optical characteristics of DCMSP derivatives in solid state.**

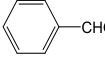
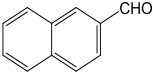
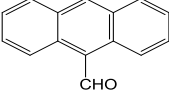
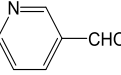
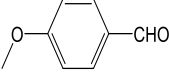
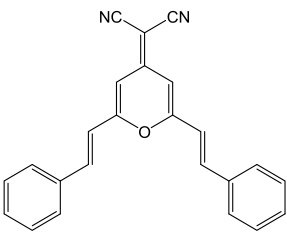
DCMSP	aryl aldehyde type (as a precursor)	Exc $\lambda_{max}$ (nm)	PL $\lambda_{max}$ (nm)	PLQY <sub>abs</sub> at 365 nm (%)	PLQY <sub>abs</sub> at 450 nm (%)
<b>6</b>		379	611	10	9
<b>7</b>		382	624	3	2
<b>8</b>		377	681	2	1
<b>9</b>		375	585	2	1
<b>10</b>		351	618	4	3

Figure 42 presents the excitation and PL emission spectra of solid-state DCMSP derivatives under 365 nm UV-light excitation. The excitation spectra show the large spectral region between 250-650 nm with the fluorescence excitation maximum located around 350-380 nm, which allowed the compounds to be excited by commercial UV-LEDs (365 or 385 nm). The fluorescence excitation shoulders are also observed around 400-650 nm indicating that the compounds can be excited by using a blue-light LED as excitation source for several application. Additionally, the extent of excitation spectra from the maximum wavelength as an indication of the contribution of intramolecular charge transfer (ICT) through the  $\pi-\pi^*$  excited states. The PL emission spectra of compound **6-10** recorded after excitation at 365 nm UV-light irradiation have a wide photoluminescence from 500-900 nm with the maximum in red-light emission region. The absolute quantum yield of these compounds recorded at room temperature was found between 2-10% under 365 nm UV excitation, depending on the aromatic group which are covalently linked to 4*H*-pyran core structure. However, it is possible that the conjugated structure of solid-state DCMSP derivatives which induced the bathochromic shift in PL emission<sup>56, 182</sup> was not effectively enough and led to a drop in both emission intensity and absolute quantum yield. Accordingly, the compound **6**, which obtained by reaction of (2,6-dimethyl-4*H*-pyran-4'-ylidene)malononitrile with benzaldehyde, displays the best photoluminescence properties with highest values in the absolute quantum yield of 10% upon 365 nm excitation. The summary of compound **6** is described in table below.

<b>COMPOUND 6</b>	<b>Chemical structure</b>	<b>Exc <math>\lambda_{max}</math> (nm)</b>	<b>PL <math>\lambda_{max}</math> (nm)</b>	<b>PLQY<sub>abs</sub> at 365 nm (%)</b>
Red-emitting organic phosphor		379	611	10

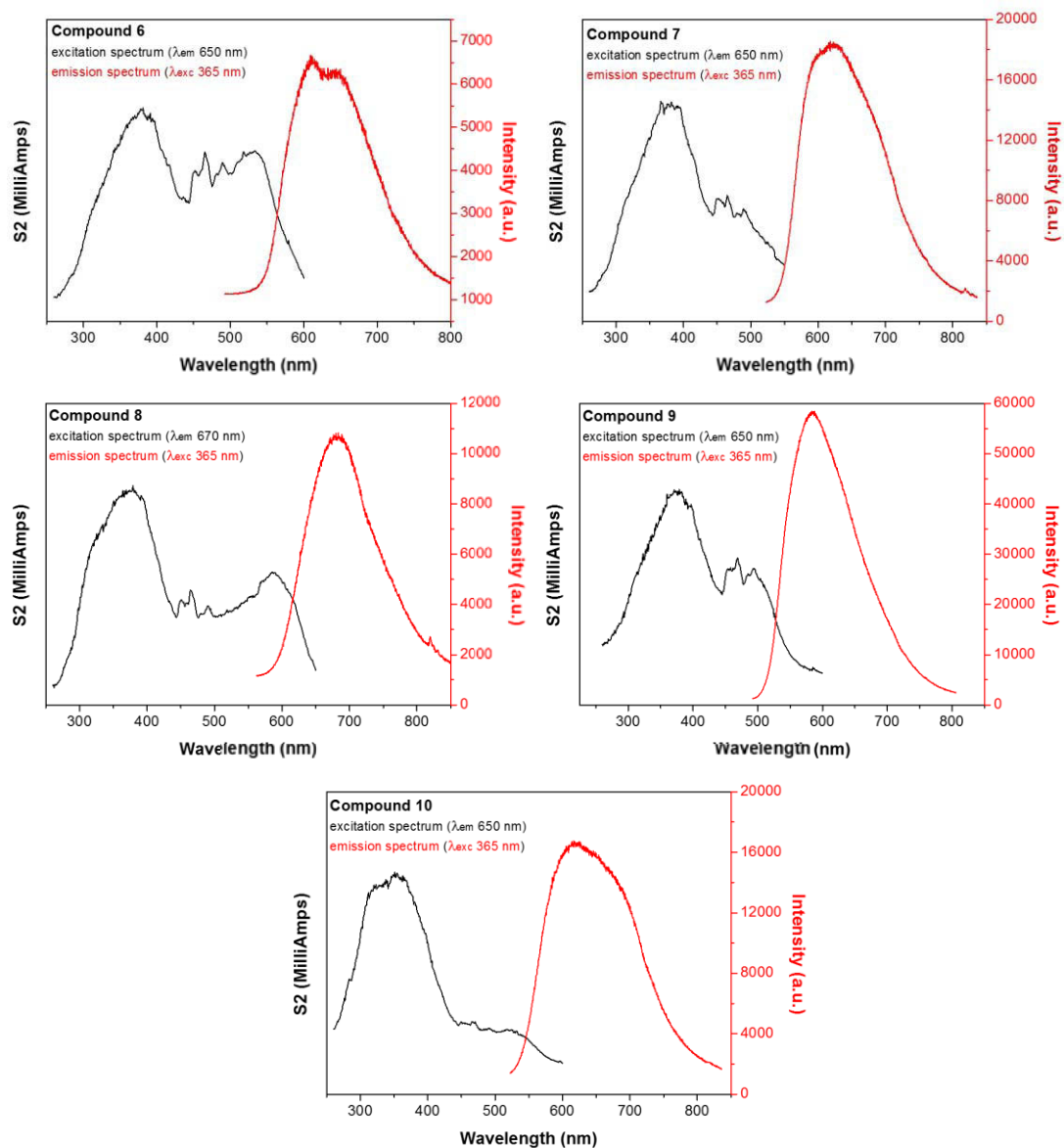
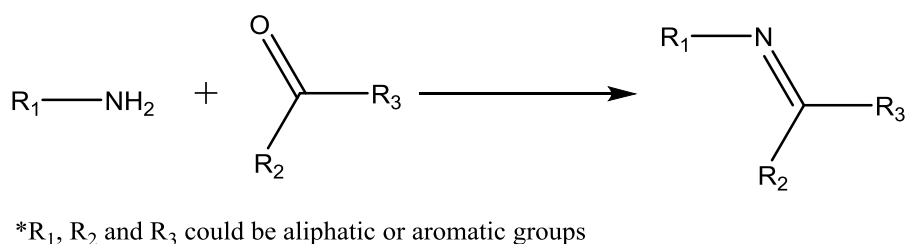


Figure 42 Excitation and emission spectra of DCMSP derivatives under 365 nm UV-light illumination.

## II. Schiff base Al-complexes for LEDs

### A. Introduction

Schiff bases are N-containing organic compound that consists of an imine group ( $-\text{CH}=\text{N}-$ )<sup>183</sup>. The chemistry behind the formation of many Schiff bases is a simple condensation reaction of an aliphatic or aromatic amine and an aromatic aldehyde or ketone forming an imine or an iminium salt. The typical reaction of Schiff base is depicted in Figure 43.



**Figure 43 Typical schematic route for the preparation of the Schiff base.**

Schiff bases are able to form a stable complex with several metal ions such as zinc ( $\text{Zn}^{2+}$ )<sup>183, 184</sup>, copper ( $\text{Cu}^{2+}$ )<sup>185, 186</sup>, aluminum ( $\text{Al}^{3+}$ )<sup>186</sup>, cobalt ( $\text{Co}^{2+}$ )<sup>185</sup>, and manganese ( $\text{Mn}^{2+}$ )<sup>187</sup> by the coordinate interaction between N- and O- donor atoms of Schiff base and metal ions<sup>185</sup>. It is known that Schiff bases can present photoluminescence properties when their coordination complexes formed with metal ions of appropriate size afford a rigid planar structure. The rigidity of the planar structure of Schiff base complex facilitates conjugated electron systems to absorb visible light and enhances fluorescence emission spectra of these compounds by increasing internal conversion rate and minimizing the probability of radiationless deactivation process<sup>56, 188</sup>. The great photoluminescence ability of Schiff base complexes are relative to the metal ions that can be used to fit in several applications such as chemical probes and chemosensors<sup>186, 189</sup>.

Among the Schiff base metal-complexes, the aluminum complex based on Schiff base ligands are a point of interest for lighting applications due to their high emission and stability at high temperature as well as high photoluminescence quantum yield. Furthermore, aluminum is the most abundant metal and the third most abundant element behind oxygen and silicon found in the Earth's solid surface (at about 8 wt.%)<sup>190, 191</sup>. Therefore, it could be a great challenge for researchers and scientists to use these Earth's abundant supply of aluminum to develop photoluminescence materials for lighting applications instead of rare-earth elements. Since an

early work published in 1987, the great examples of aluminum complexes exhibiting high photoluminescence are tris-(8-hydroxy-quinolate) ( $\text{Alq}_3$ ), which has important applications in organic light-emitting diodes (OLEDs) as a green emitter and an electron-transporting layer<sup>192, 193</sup>.

In 2013, Zhen-Chuan Liao and collaborators reported a highly selective and sensitive fluorescent chemosensor based on methyl pyrazinylketone benzoyl hydrazine (MPBH, compound **11**)<sup>60</sup>. According to their published work, the MBPH ligand and its Al complex were studied in dilute solution. Regardless the high sensitivity and selectivity to  $\text{Al}^{3+}$ , compound **11** proposes a simple one-step Schiff base reaction derived from the condensation of benzoic acid hydrazide and acetyl pyrazine with 1:1 in molar stoichiometric ratio as published (Figure 44).

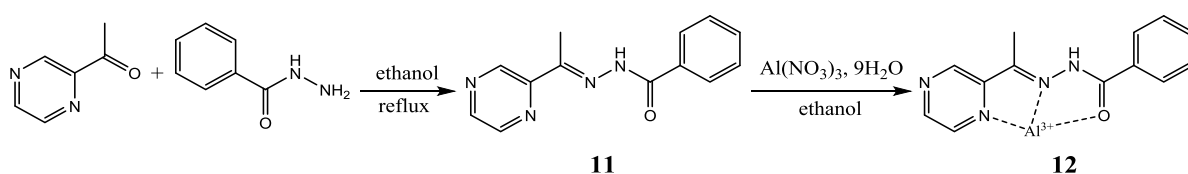


**Figure 44** Synthesis of methyl pyrazinylketone benzoyl hydrazine (MPBH) Schiff base and their Al complex.

The compound **11** was quite highly selective to  $\text{Al}^{3+}$  ions over other metals ions and presented a high and broad emission spectrum with maximum emission wavelength situated at 506 nm upon excitation at 390 nm<sup>60</sup>. The single crystal X-ray crystallography of compound **11** showed that the E-conformation of Schiff base C=N bond was preferable for metal chelation<sup>194</sup>. Considering the photoluminescence properties mentioned previously, we decided to develop the Schiff based fluorescent complex derived from compound **11** as a coordinate ligand to aluminum ions in solid states for LED lighting applications.

## B. Results and discussion

### a. Structural characterizations of compound **11**

The synthesis of compound **11** were firstly prepared by condensation reaction of benzoic acid hydrazide and acetyl pyrazine in 1:1 stoichiometric ratio as published<sup>169</sup>. The crude product was recrystallized in ethanol to give a pure compound **11** as white crystals with a 45% reaction yield. The compound **11** presented a good solubility (at room temperature) in several organic solvents such as ethanol, acetonitrile, toluene and dimethylsulfoxide. FT-IR spectrum of compound **11** in a KBr pellet was investigated to confirm the formation of C=N bond of Schiff base and shows a characteristic vibration band at about 1640 cm<sup>-1</sup> as reference (Figure 45)<sup>60</sup>.

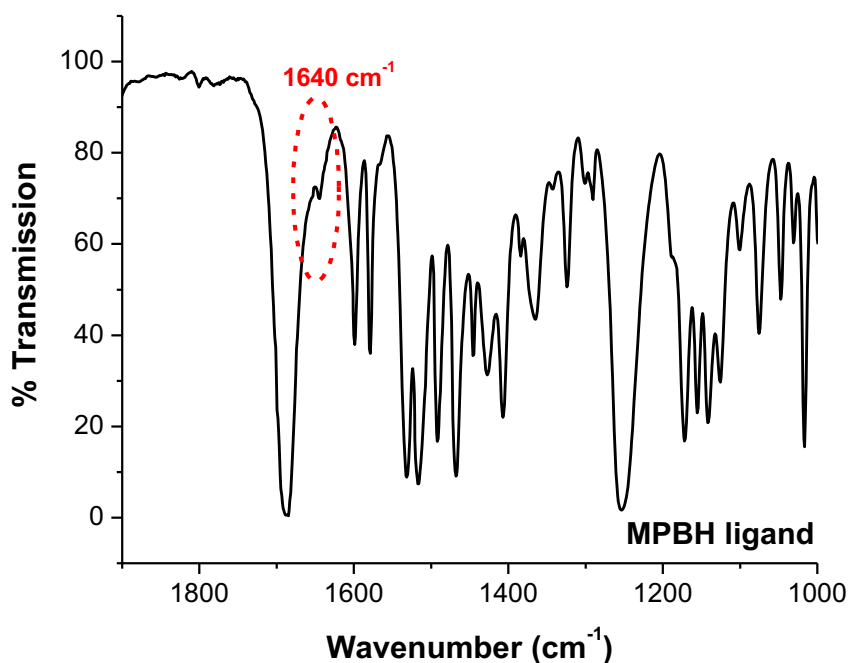
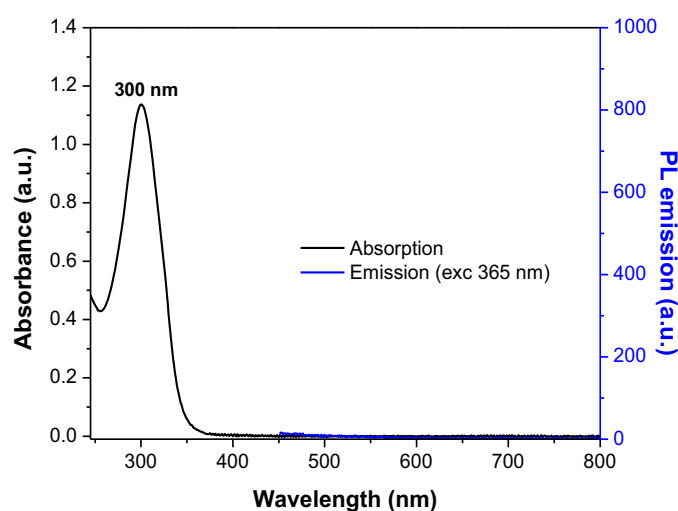


Figure 45 FTIR spectrum of compound **11** (MPBH ligand) in a KBr pellet.

Figure 46 presents the UV-visible absorption and emission spectra of compound **11** (with the concentration of 50  $\mu\text{M}$  in ethanol). The absorption spectrum of compound **11** recorded in ethanol presents a single absorption peak located at 300 nm. The molar absorption coefficient ( $\epsilon = 2.48 \times 10^4 \text{ M}^{-1} \text{ cm}^{-1}$ ) of compound **11** at 300 nm signified that the absorption should be attributed to  $\pi-\pi^*$  transition because the nitrogen lone pair in MPBH was in a *p* orbital and was part of the conjugated system. The fluorescence emission spectrum of compound **11** in solid state was not observed upon excitation at 365 nm, corresponding to a wavelength of commercial UV-LEDs. The absolute quantum yield of compound **11** in solid state was recorded about 0.3% under 365 nm excitation. Furthermore, it is interesting to note that the compound

**11** in solid state does not exhibit light emission under UV lamp and under 365 nm LED, corresponding to very low value of absolute quantum yield ( $PLQY_{abs} \approx 0\%$ ). The absence of emission spectrum for compound **11** in solid state was explained by photo-induced electron transfer from the aliphatic or aromatic amines to the aromatic system<sup>195</sup>. Similar case was observed by the group of Wang<sup>196</sup>. They suggested that the absence of emission for Schiff base ligand was possibly due to quenching by the carbonyl group influenced by a lone pairs of nitrogen atoms through the photo-induced electron transfer<sup>196</sup>. However, the electron transfer could be quenched by cation binding corresponding to the evidences of very high fluorescence intensity that were observed for many N-containing organic chelating ligands<sup>195</sup>.



**Figure 46** UV-visible absorption (black line) and PL emission (blue line) spectra of MPBH (**11**) in ethanol. (Concentration = 50  $\mu$ M).

### b. Structural characterization of compound **12** in dilute solution

Al-MPBH complex (compound **12**) was prepared by mixing the solution of **11** in ethanol and the solution of aluminum nitrate nonahydrate in absolute ethanol according to the literature<sup>60</sup>. The concentration of each component was controlled at 50  $\mu$ M with 1 equivalent of  $Al^{3+}$  in the presence of 1 equivalent of compound **11**. The optical properties of compound **12** was investigated in absolute ethanol at room temperature.

Figure 47 presents the UV-visible absorption and PL emission spectra of compound **12** in ethanol at the concentration of 50  $\mu$ M. The absorption spectrum of compound **12** exhibited an additional absorption peak observed at 380 nm compared with the absorption spectrum of compound **11**. This absorption band should be attributed to the formation of Al-MPBH complex via charge transfer from ligand to  $Al^{3+}$ . According to hybrid orbitals on the aluminum

ion ( $\text{Al}^{3+}$ ), all the 3d orbitals become empty. In this case,  $\text{Al}^{3+}$  can use six of these empty hybrid orbitals to receive the lone pairs from ligands (and/or their counter ions i.e.  $\text{NO}_3^-$  and  $\text{H}_2\text{O}$ ) to stabilize the positive charges. Moreover,  $\text{Al}^{3+}$  can favorably organize its multidentate structure consisting of three metal binding atoms (N, N, O donor atoms) to form Al-MPBH complex. As a result, the formation of Al-MPBH complex can occur even very dilute solution ( $50\ \mu\text{M}$ ) because of favorable coordinating structure, corresponding to similar published study<sup>194</sup>.

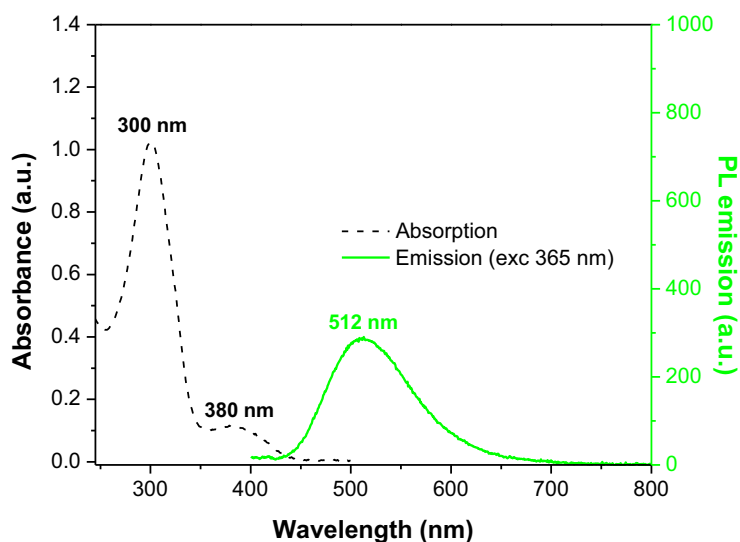


**Figure 47** UV-visible absorption and emission spectra of Al-MPBH complex (compound **12**) in ethanol. (Concentration =  $50\ \mu\text{M}$ ).

The fluorescence spectra of compound **12** was also performed in ethanol (see in Figure 47). As previously stated in Figure 46, MPBH represented very low fluorescence values with 365 nm excitation. Upon the presence of  $\text{Al}^{3+}$  ion in solution of MPBH, the very large enhancement of emission intensity can be observed. The PL emission spectrum of compound **12** in the dilute solution (with the concentration of  $50\ \mu\text{M}$  in ethanol) shows a broad band in the green range with a maximum emission at 512 nm. The absolute quantum yield of compound **12** was recorded at about 24% upon 365 nm excitation. According to the studies above, this kind of compound is becoming of interest due to its exceptional photoluminescence properties in dilute solution. Therefore, the attempt to synthesize the compound **12** in solid-state was investigated for LED applications, which will be described in the next section.



**c. Structural characterization of compound 12 in solid state**

The synthesis of compound **12** in solid state were prepared by addition of aluminum nitrate nonahydrate (  $\text{Al}(\text{NO}_3)_3 \cdot 9\text{H}_2\text{O}$  ) solution in ethanol to the solution containing the compound **11** in ethanol according to our recent published work<sup>169</sup>. After the reflux period, compound **12** was obtained as a green powder with moderate chemical yield (55%). Compound **12** had been characterized by  $^1\text{H}$  NMR spectroscopy, FTIR spectroscopy and some physical analysis. The typical morphology of compound **12** was carried out by using SEM measurement (Figure 48). The images shows the rectangular-shaped structure and loosely agglomeration, with wide variation in particle sizes between 1-10  $\mu\text{m}$ .

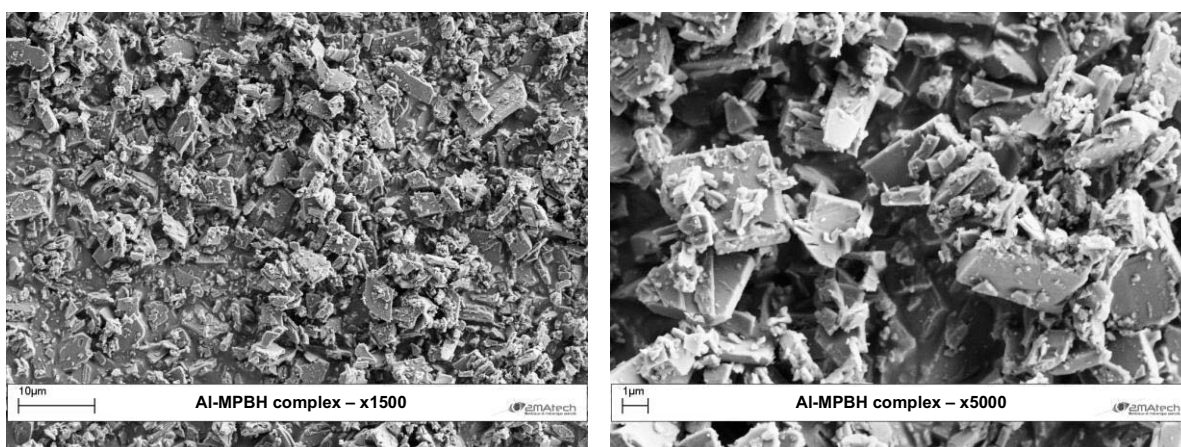


**Figure 48** The SEM images of Al-MPBH complex (compound **12**).

Powder XRD data indicated that the X-ray diffraction pattern of compound **12** was a different from a starting material (  $\text{Al}(\text{NO}_3)_3 \cdot 9\text{H}_2\text{O}$  ) as depicted in Figure 49. As the compound **12** was obtained as a microcrystalline powder with a poor solubility in many organic solvents, it was not suitable to give crystals for structure determination using single-crystal XRD.

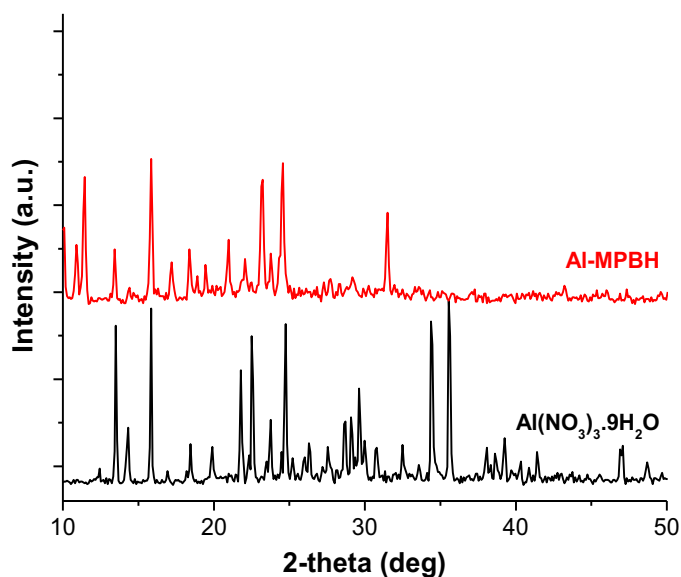


**Figure 49 Powder XRD patterns of Al-MPBH complex (compound 12) and  $\text{Al}(\text{NO}_3)_3 \cdot 9\text{H}_2\text{O}$  as starting product.**

Figure 50 depicts the FTIR spectra of compound **12** and its free ligand (compound **11**). The FTIR spectra were recorded particularly in the range of  $2000\text{--}500\text{ cm}^{-1}$  in order to investigate the vibration frequencies of the coordination bonds of the ligand in the complex. The disappearance of the large  $\nu(\text{C}=\text{O})$  band, present in the compound **11** at  $1688\text{ cm}^{-1}$ , and the presence of the intense  $\nu(\text{C}-\text{O})$  band at  $1388\text{ cm}^{-1}$  showed that the double bond of this functional group was broken to form a new bond to the  $\text{Al}^{3+}$  center. This result was a good evidence that the metallation induces the delocalization of the nitrogen lone pair to the carbonyl group. The slightly IR shifts of the  $\nu(\text{C}=\text{N})$  weak bands at  $1639$ ,  $1599$  and  $1588\text{ cm}^{-1}$  (compound **12**) from the free ligand (at  $1640$ ,  $1599$  and  $1579\text{ cm}^{-1}$ ) were not used as a clear evidence of coordination of azomethine group ( $-\text{C}=\text{N}-$ ) to the  $\text{Al}^{3+}$  center as mentioned in some published studies<sup>197, 198</sup>. In addition to these bands, some new bands observed at the low frequency region in IR spectra of compound **12** ( $725\text{--}660\text{ cm}^{-1}$  and  $574\text{ cm}^{-1}$ ) might be attributed to the  $\nu(\text{Al}-\text{O})$  and  $\nu(\text{Al}-\text{N})$  vibrations of Al-MPBH complex. The summary of characteristic IR bands of the ligand (compound **11**) and its complex (compound **12**) is presented in Table 15.

Table 15 Characteristic IR bands of MPBH ligand and its Al complex.

Compound	IR frequency (cm <sup>-1</sup> )			
	C=O	C=N	C-O	Al-O / Al-N
MPBH (11)	1688	1640, 1599, 1579	-	-
Al-MPBH (12)	-	1639, 1599, 1588	1388	725-660, 574

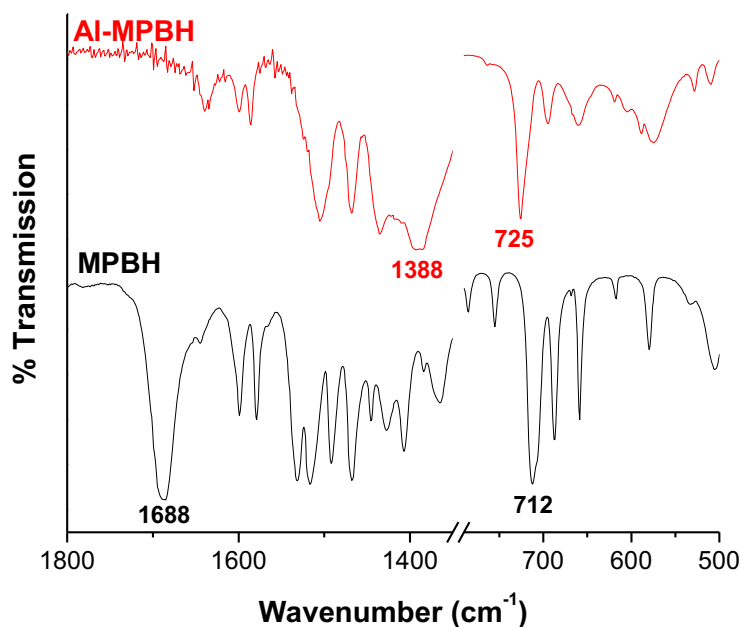
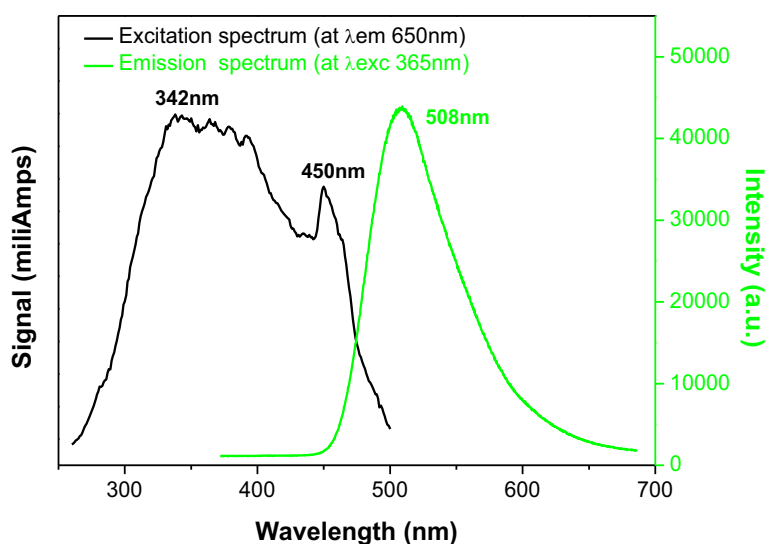


Figure 50 FTIR spectra of Al-MPBH complex (compound 12) and MPBH ligand (compound 11).

The photoluminescence properties of compound **12** in solid state were also investigated. Figure 51 shows the excitation and emission spectra of Al-MPBH complex (compound **12**) at room temperature upon 365 nm UV-light excitation. The excitation spectrum of compound **12** was characterized a large spectral range from 250 to 500 nm with a maximum wavelength at 342 nm, which allows the use of 365 nm UV-LED for further study. The PL emission spectrum showed the broad band in green range with a maximum emission at 508 nm upon 365 nm UV-light excitation. The absolute quantum yield of compound **12** in solid state was recorded at about 28% after excitation at the wavelength of the maximum of the excitation (at 342 nm).



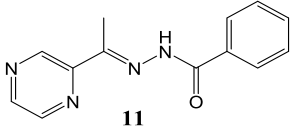
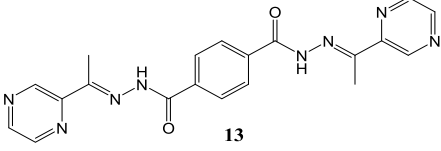
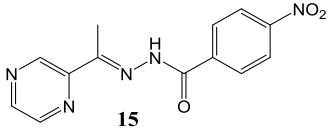
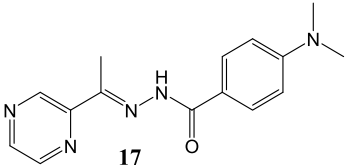
**Figure 51** Excitation and emission spectra of Al-MPBH complex (**12**) upon 365 nm UV-light illumination.

Comparing with the emission spectrum of compound **12** in dilute solution, the PL emission spectrum in solid state presented a blue-shifted of 4 nm. Among the results of photoluminescence, the solid-state Al-MPBH complex (**12**) displays high fluorescence at room temperature, thus providing a new promising green-emitting compound for LED applications.

#### **d. Synthesis and characterizations of similar complexes of 12**

Accordingly, the MBPH Schiff base (**11**) exhibited an attractive optical properties when it bound to  $Al^{3+}$  ions to form Al-MBPH complex. Therefore, similar compounds in solid state based on pyrazine structure were also synthesized and compared with Al-MPBH complex. The ligands and Al-complexes were synthesized following a procedure described in the experimental section. The preliminary investigation of emission spectrum of Al-complexes had been carried out by using PLQY measurement system (Table 16).

Table 16 Optical characteristics of Al-complexes based on pyrazine Schiff base.

Al-Complex	Ligand type	Exc $\lambda_{\text{max}}$ (nm)	PL $\lambda_{\text{max}}$ (nm)	PLQY <sub>abs</sub> at 365 nm (%)
Al-MPBH (12)	 11	342	508	24
Al-MPTH (14)	 13	365	523	≈ 1
Al-MPNBH (16)	 15	445	522	4.6
Al-MPMABH (18)	 17	305	680	2.3

All complexes exhibit similar structures. The compound **14** presents two metal-binding sites in the structure to coordinate two  $\text{Al}^{3+}$  ions. The compound **16** has a similar structure to MPBH (**11**) involving an additional strong electron-withdrawing substituent ( $\text{NO}_2$ ). Such group could make benzene less reactive by withdrawing electrons from the benzene ring. The compound **18** presents an aryl group having a strong electron-donor substituent ( $\text{N}(\text{CH}_3)_2$ ) on the aromatic ring. Such electron donating group could activate the benzene ring towards electrophilic substitution.

Figure 52 shows the visual observation of Al-complexes under normal light and under 365 nm UV illumination. This observation can give a first indicating comparison of emission intensity of solid-state samples. Compound **12** exhibits a very high photoluminescence under a 365 nm UV irradiation compared with other Al-complexes. The emission spectra of Al-complexes presents low emission intensity for compound **14**, **16** and **18** and a shift of the maximum emission at 523, 522 and 680 nm under excitation at 365 nm, respectively. The absolute quantum yield was recorded for compound **14** and presented a very weak quantum yield close to zero, corresponding to its weak emission spectra recorded previously. The red-shifted

emission of Al complexes was significantly observed at about 170 nm with the significant decrease in both emission intensities and photoluminescence quantum yields when the strong electron-withdrawing substituent ( $\text{NO}_2$ ) was presented as a substituent group on the aryl group of MBPH ligand.

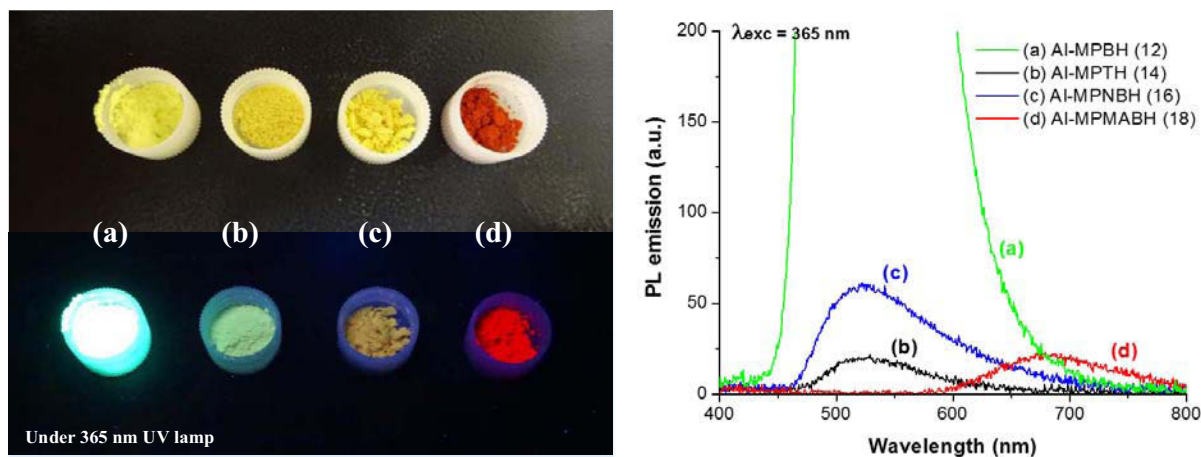


**Figure 52 (left) Photographs of solid-state Al-complexes under normal light and under 365 nm UV lamp, (right) their emission spectra upon 365 nm UV-light illumination.**

Accordingly, the aluminum complex based on MPBH Schiff base ligands were proposed as new organic light-emitting compounds for lighting applications. The chemical modification of MPBH ligand which were conducted allows to modify the photoluminescence properties of Al complex. However, among the Al complexes based on pyrazine Schiff base, the compound **12** exhibits the best photoluminescence properties with the highest value in absolute quantum yield of 24% under 365 nm UV excitation and can be chosen as green-emitting phosphor for LED applications. The summary of compound **12** is described in table below.

COMPOUND 12	Chemical structure	Exc $\lambda_{max}$ (nm)	PL $\lambda_{max}$ (nm)	PLQY <sub>abs</sub> at 365 nm (%)
Green-emitting organic phosphor		342	508	24

### III. Characterizations of selected organic phosphors for LEDs

As with the previous studies, the organic phosphors have been classified into three different groups due to their structure and their emission range upon 365 nm LED excitation. These organic phosphors were selected since they can emit the three primary colors under a commercial UV-LEDs at 365 nm<sup>60, 170, 171</sup>. According to previous studies of organic phosphors, the compounds in each group having the best value in the absolute quantum yield were chosen for further studies. The compound **4** (with hexylamino part) from the DMPP derivatives, the compound **6** (with phenyl part) from the DCMSP derivatives, and the compound **12** (Al-MPBH complex) present the greatest value of absolute quantum yield at 30%, 8% and 24%, respectively under excitation at 365 nm (Figure 53). These organic phosphors with the three primary colors could be associated with commercial UV-LEDs at 365 nm after mixing them in the proper proportion to achieve the white emission over a wide range of excitation wavelength.

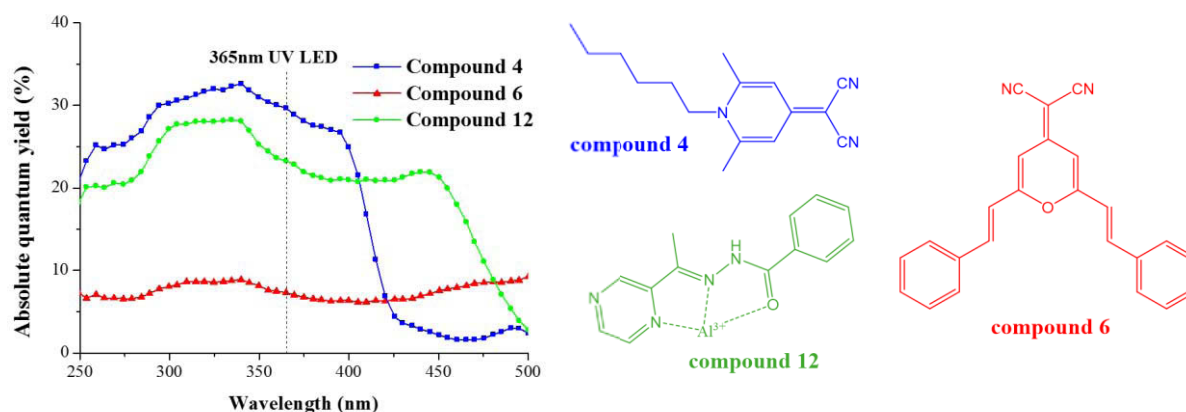


**Figure 53 Absolute quantum yield of three selected organic phosphors recorded between 250-500 nm light illuminations.**

Figure 54 gathered the PL emission spectra of the selected organic phosphors. Referring to our previous results, the emission spectra of compound **4**, **6** and **12** exhibited a broad emission in visible range with the maximum wavelength at 436, 611 and 508 nm, respectively. The excitation spectra are broad notably for compound **6** and **12**. The extent of the excitation spectra can be an indication of the contribution of intramolecular charge transfer (ICT) through the  $\pi-\pi^*$  excited states. The  $\pi-\pi^*$  are characterized by small shift since the peak positions of the related excitation bands lie at around 377, 379 and 342 nm for compound **4**, **6** and **12** respectively. The band peaking at 533 and 450 nm for compound **6** and **12** can be attributed to the ICT. In order to produce a white light emission, the concentration of each organic phosphor in the mixed component should be considered. Since the emission spectra of these phosphors

show a very broad band in the visible region, the combination of the phosphors might exhibit a high color rendering index (CRI)<sup>199</sup>.

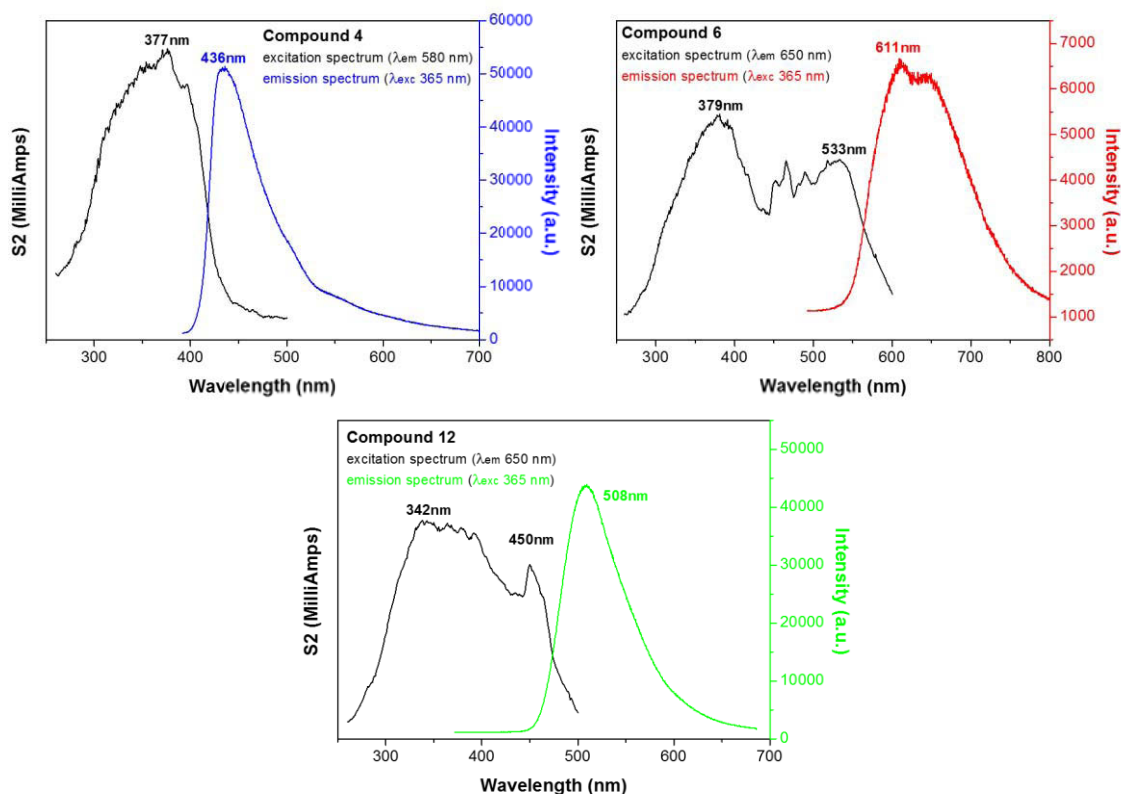


**Figure 54** Excitation and PL emission spectra of selected organic phosphors under 365 nm UV-light illumination.

To study the nature of emitting excited states of the selected organic phosphors, the luminescence lifetime at room temperature using a pulsed laser excitation at 337.1 nm were measured as shown in Figure 55. In first approach, the luminescence decay time were calculated using the effective emission decay's equation according to R. Pazik<sup>200</sup> (Equation 1) where  $I(t)$  was the luminescence intensity at time  $t$  corrected for the background and the integrals are evaluated on a range  $0 < t < t_{max}$  and  $t_{max} \gg \tau_m$ ,  $t_{max} \gg \tau_m$ . Using the fitted curves, the effective emission decay times were calculated to be approximately 9.68, 2.58 and 2.54  $\mu$ s for compound 4, 6 and 12, respectively. The selected organic phosphors which reported the long luminescence lifetime (in microseconds) can confirm that they can be classified as organic phosphorescent compounds<sup>201</sup>.

$$\tau_m = \frac{\int_0^{\infty} tI(t)dt}{\int_0^{\infty} I(t)dt} \cong \frac{\int_0^{t_{max}} tI(t)dt}{\int_0^{t_{max}} I(t)dt} \quad \text{(Equation 1)}$$



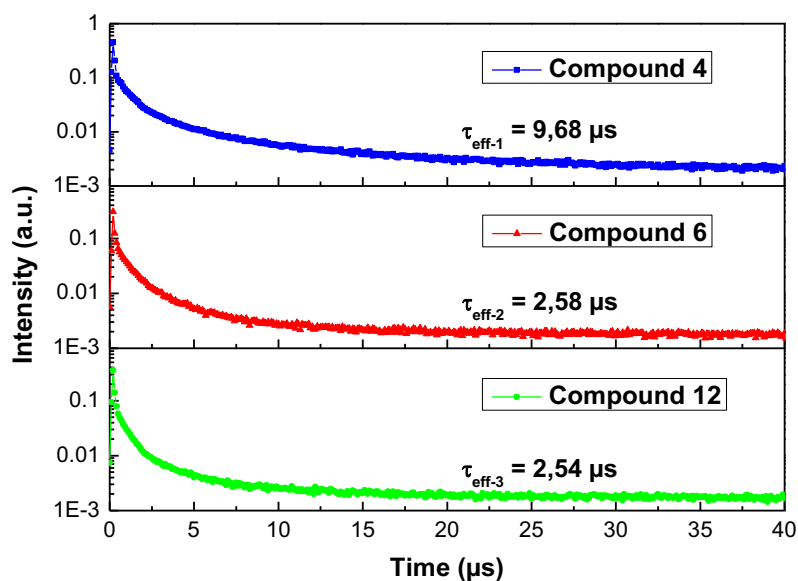


**Figure 55 Luminescence decay curves for the selected phosphors recorded upon 337.1 nm laser excitation at 300K.**

In the case of heterogeneous structures of organic compounds, the luminescence decay can also be described by applying a multi-exponential model<sup>56</sup>. As classically used for organic compounds<sup>202,203</sup> the decays are fitted by two-exponential functions. The characteristics of the luminescence decay curve of selected organic compounds by fitting two-exponential functions are shown in Table 17. The derived time constants from the fits are 0.74 and 5.1  $\mu\text{s}$  for compound **4**, 0.71 and 3.2  $\mu\text{s}$  for compound **6**, and 0.43 and 2.33  $\mu\text{s}$  for compound **12**. Despite a possible emission arising from the ICT, these values are very high and can indicate that the major part of emitting light arises from the forbidden radiative (phosphorescence, triplet to singlet state)<sup>201</sup>. The contribution of the long-life components ( $A_2$ ) of the decay times to the global emission are weak since they reach 15%, 15.5% and 13 % for compound **4**, **6** and **12** respectively. This contribution is assumed to be due to the single molecules not aggregated while the short contribution from short-life component ( $A_1$ ) may come from aggregates into which the distances between the emitting species are short enough to increase energy transfer efficiency leading to the decrease of radiative emission. The important contribution of the short component (more than 80 %) can be explained by the synthesis process which can be not enough efficient to prevent agglomeration.

Table 17 Characteristics of luminescence decay curve by fitting two-exponential functions.

	Decay components of two-exponential model			
	A <sub>1</sub>	τ <sub>1</sub> (μs)	A <sub>2</sub>	τ <sub>2</sub> (μs)
Compound 4	0.136	0.746	0.025	5.064
Compound 6	0.095	0.708	0.017	3.165
Compound 12	0.138	0.428	0.021	2.328

As we have mentioned in the first chapter of this manuscript, the LEDs are electronic components which can also produce heat. The optical properties of organic phosphors can be then modified by reason of built-up temperature from LEDs. Therefore, we have studied the thermal stability behavior of selected organic phosphors as a function of temperature. The thermal properties of selected phosphors were investigated by thermogravimetric analysis (TGA), which was carried out under normal atmosphere at the fixed heating rate of 10°C/min. As shown in Figure 56, the first weight loss of compound 12 was recorded at 100°C and at 250°C for compound 4 and 6. The results provide the desirable thermal properties of these phosphors for the normal operating conditions of remote-type phosphor reported to be lower than 120°C<sup>41, 204, 205</sup>.

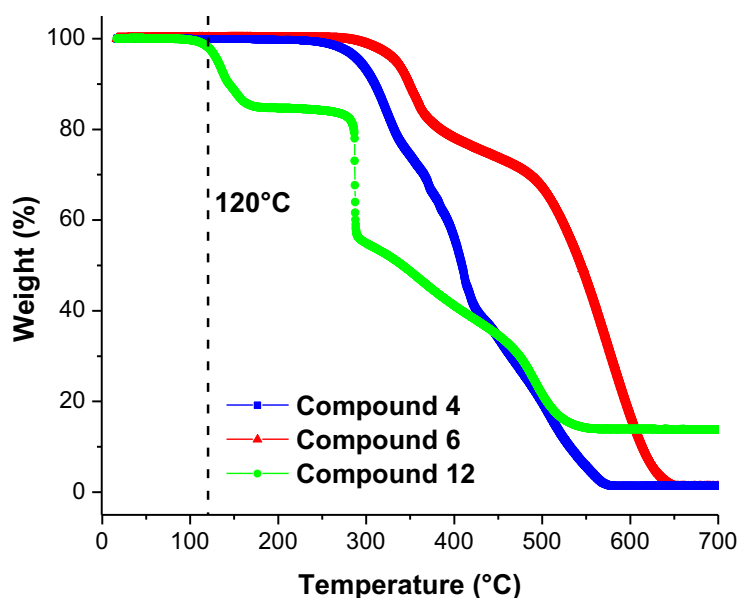


Figure 56 Thermogravimetric analysis for selected organic phosphors.

Figure 57-left presents the temperature-dependent emission intensity of selected organic phosphors. However, the emission intensity of phosphors drops significantly with increasing

temperature from room temperature to 150°C. Figure 57-right shows the time-dependent relative emission intensity of selected organic phosphors upon continuous excitation at temperature of 110°C. With increasing time, the intensity decrease importantly from 0 to 4 hours. As shown in Figure 57-right, the relative emission intensity of selected organic phosphors becomes less stable at higher temperature in spite of the fact that they present the good thermal properties at that temperature as reported previously. Our results confirm that our luminescent materials have low thermal stability, especially at the operating temperature of LEDs.

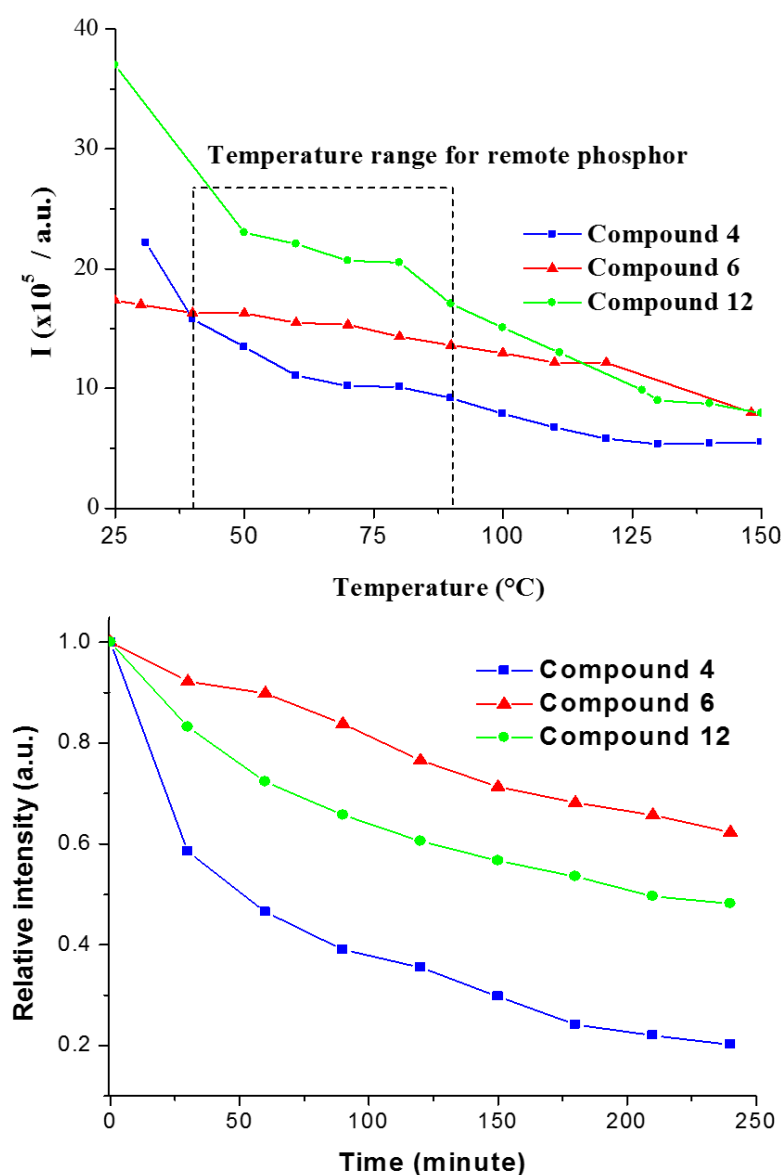


Figure 57 (left) Temperature-dependent emission intensity and (right) Time-dependent relative emission intensity at temperature of 110°C of selected organic phosphors upon continuous 365 nm UV-light excitation.

## A. Optical properties of organic phosphors composite films

One of the most attractive matrix materials for embedding phosphors is silicone resin because it provides a high optical transmittance in the applicable wavelength (from UV to infrared), low curable temperature and high thermal stability. Moreover, the organic compounds can be easily dispersed into the silicone resin.

### a. Polymer matrices: silicone resin film

The two-component silicone resin was used as polymer matrices for composite films due to their flexibility, free-standing matrices, high transparency, and high thermal stability. Furthermore, the silicone resin presents a good solubility in organic solvents which facilitates the dispersion and homogeneity of quantum dots in the composite films. Some published studies have reported the combination of quantum dots embedded in the silicone resin for white-light LED system<sup>111, 112, 116</sup>.

#### i. Physical properties of silicone resin

The type of silicone resin used in this work was the BLUESIL Room Temperature Vulcanizing (RTV) 141 A&B that is an elastomeric two-component polymer cured at room temperature via the addition reaction catalyzed by platinum (Figure 58).

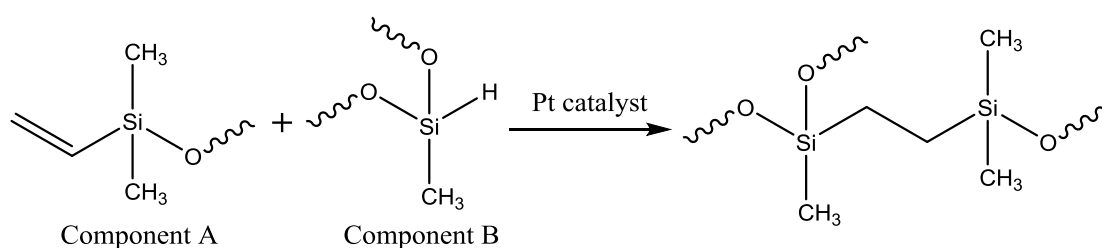


Figure 58 Polyaddition reaction of two-component silicone resin<sup>206</sup>.

The two-component silicones were used as a matrix for the preparation of composite film, where a component A consisted of silicone polymers and a component B contained the cross-linking agent and a platinum catalyst (10-500 ppm) that induces the silicone hydrosilylation reaction. The polydimethylsiloxanes (PDMS) polymer was formed by mixing these components A and B in proportion by 9 wt.% of component A and 91 wt.% of component B and then the crosslinking was carried out at a temperature in the range from 50°C to 150°C. Some physical properties of the two-component silicone resin are presented in Table 18.

**Table 18 Physical properties of two-component silicone resin.\*\*\***

Viscosity before curing (mPa.s) at 25°C	4000
Curing time (hour)	4h (at 60°C) / 2h (at 100°C) / 1h (at 150°C)
Refractive index n <sup>25</sup>	1.406
Thermal conductivity (m.K)	0.16
Brittle point (°C)	- 70
Peak thermal withstand (°C)	+ 200

The thermogravimetric analysis (TGA) and the differential thermogravimetric (DTG) curves of silicone resin film are shown in Figure 59. The silicone films were also characterized by the temperature of 5 wt. % and 50 wt. % weight loss (T<sub>-5wt.%</sub> and T<sub>-50wt.%</sub>, respectively) and the char residue left at 800°C obtained from the TGA curve (Figure 59a). The temperature at the maximum weight loss rate of silicone resin film was gathered from the DTG curve (Figure 59b). These results are presented in Table 19.

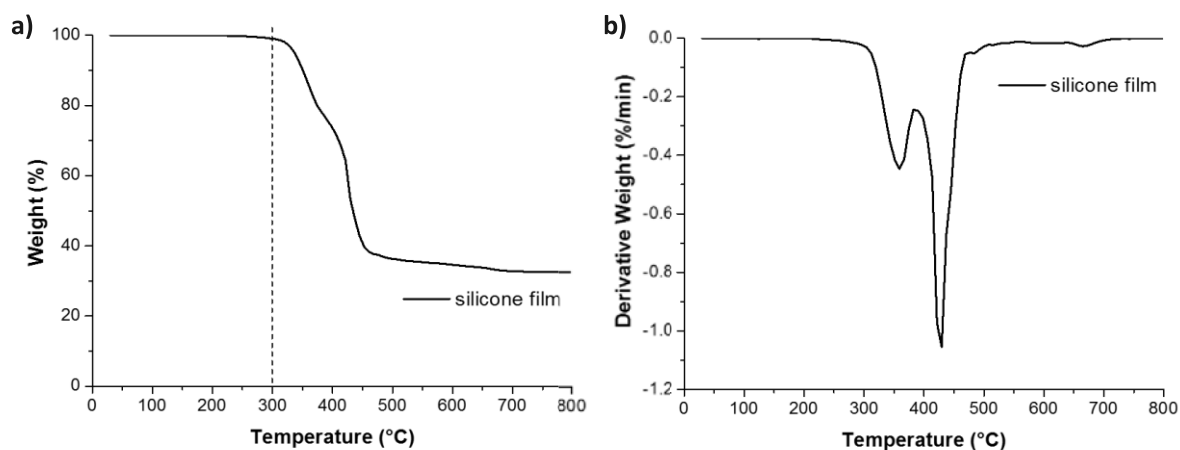
**Table 19 TGA and DTG results of silicone resin film.**

Film	T <sub>-5wt.%</sub> (°C)	T <sub>-50wt.%</sub> (°C)	T <sub>max</sub> (°C)		Char residue (%) at 800°C
			Step I	Step II	
Silicone resin	336	430	358	428	32.6

The rapid weight loss was observed in two stages: at around 300-386°C and 390-480°C. These weight losses were attributed to the segmental decomposition of silicone network and organic-silicon parts, respectively. The char residue at 800°C of silicone resin film were 32.6 wt. %. Consequently, it can be concluded that the silicone resin film typed PDMS presents a good thermal stability up to 300°C which can be further handled as a polymer matrix for white LEDs.

---

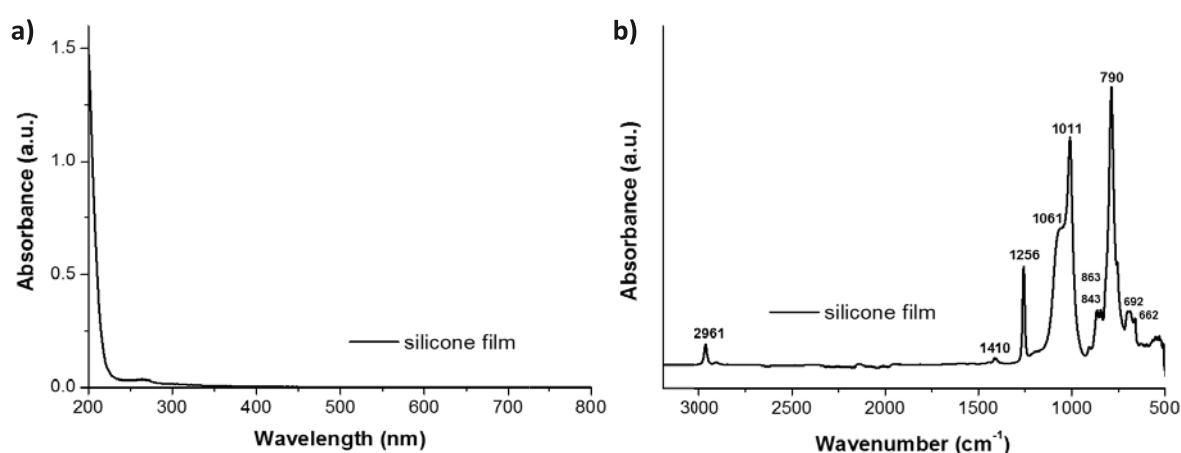
\*\*\* BLUESIL RTV 141A&B: available online at <http://www.benam.co.uk/uploads/tds/RTV141-TDS.pdf>



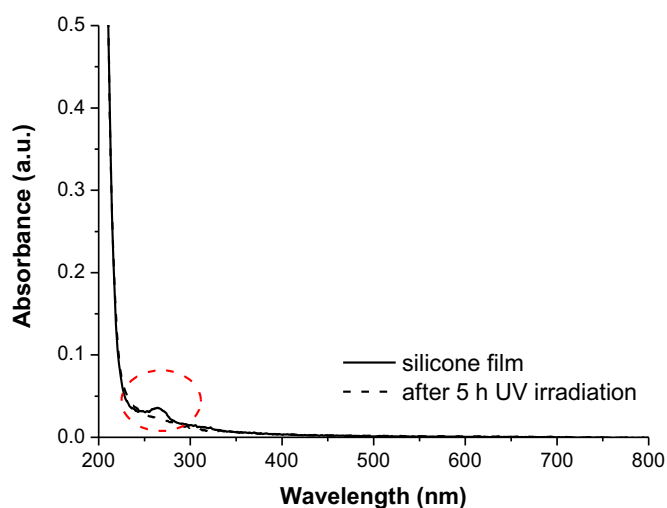
**Figure 59 (a) TGA plots and (b) derivative curves of the silicone resin film.**

Figure 60 presents the UV-visible absorption and infrared spectra of silicone resin film after reticulation. The UV-visible spectrum shows that the silicone resin does not absorb significantly the photons above 300 nm, covering a range from near UV to visible light (Figure 60a). Therefore, the silicone resin film will not hamper the optical signals of phosphors.

It should be indicated that the small absorption peak observed at about 263 nm was probably the absorption of residual stabilizer (i.e. antioxidant or UV absorber) in silicone resin film. In order to confirm the presence of residual antioxidant, the silicone film was treated under UV irradiation at 60°C for 5 hours. The absorption peak at 265 nm disappeared when the silicone resin film was continuously irradiated under UV-light illumination at 60°C (Figure 61).



**Figure 60 (a) UV-visible and (b) infrared spectra of silicone resin film.**



**Figure 61 UV-visible absorption spectra of a silicone film before and after UV irradiation at 60°C. The red circle shows the absorption band of residual antioxidant.**

Figure 60b shows the infrared spectrum of silicone resin film with characteristic absorption bands as presented in Table 20<sup>207</sup>. This infrared spectrum was very useful in analytical techniques for identifying the functional groups and monitoring the photo-degradation of composite films consisting of silicone resin and phosphors.

**Table 20 Typical infrared absorption frequencies of silicone resin film<sup>207</sup>.**

IR absorption frequency (cm <sup>-1</sup> )	IR assignments
2961	CH <sub>3</sub> asymmetric stretching
2907	CH <sub>3</sub> symmetric stretching
1410	CH <sub>3</sub> asymmetric bending
1256	CH <sub>3</sub> symmetric bending
1061	Si-O-Si asymmetric stretching
1011	Si-O-Si symmetric stretching
863-843	CH <sub>3</sub> symmetric rocking
790	CH <sub>3</sub> asymmetric rocking, Si-C asymmetric stretching
692-662	Si-C symmetric stretching, Si-CH <sub>3</sub> symmetric rocking

### b. Organic phosphors composite films

In this work, the three selected organic phosphors were prepared by dispersing solid-state organic phosphors in silicone resin. The mechanic mixing was applied in order to obtain a well-dispersed mixture composed of the phosphors and the silicone resin. The mixture was deposited on the Teflon sheets and the film was set at 50°C for 24 hours. The composite films obtained were opaque, free-standing and flexible but slightly translucent due to the thickness and the variation of composition of solid powders in the composite films. The concentration of solid powders in the composite films was adjusted to reach at 15 wt. % with 85 wt. % of silicone resin. In some characterizations, the concentration of solid powders in the composite films have to be diluted to 2 wt. % in order to investigate the evolution of optical and photoluminescence properties under light irradiations. Figure 62 presents the examples of composite films indicating that they are homogeneously dispersed in the silicone resin. The photoluminescence data of these composite films as well as their solid powders are summarized in Table 21.

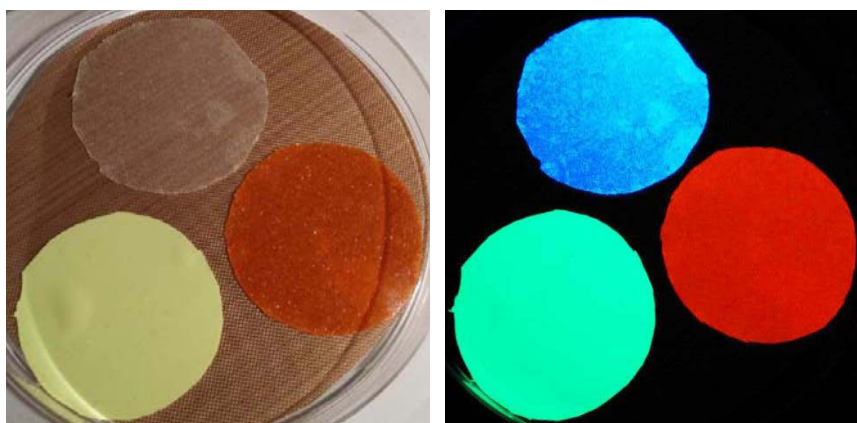


**Figure 62** Photographs of free-standing composite films of each selected organic phosphors embedded silicone resin: (left) under a day light and (right) under a 365 nm UV-LED excitation.



**Table 21 Photoluminescence properties of organic phosphors-silicone composite films. The photoluminescence properties of their organic phosphors in solid state are also presented in comparison.**

	Film thickness ( $\mu\text{m}$ )	PL $\lambda_{\text{max}}$ (nm)	PLQY <sub>abs</sub> at 365 nm (%)	PLQY <sub>abs</sub> at 450 nm (%)
15 wt.% compound 4-silicone film	80.9 $\pm$ 10.7	433	21	-
2 wt.% compound 4-silicone film	76.3 $\pm$ 8.0	430	18	-
Compound 4 solid powder	-	436	30	-
15 wt.% compound 6-silicone film	64.9 $\pm$ 6.0	603	8	7
2 wt.% compound 6-silicone film	76.5 $\pm$ 9.5	600	8	8
Compound 6 solid powder	-	611	8	8
15 wt.% compound 12-silicone film	126.7 $\pm$ 16.7	502	11	7
1 wt.% compound 12-silicone film	69.6 $\pm$ 11.6	487	9	6
Compound 12 solid powder	-	508	24	21

Figure 63 shows the absorption and PL emission spectra of each organic phosphors-silicone composite films. The emission spectra of composite films were slightly shifted towards the blue end compared to their organic compounds in solid state. The absolute quantum yield (PLQY<sub>abs</sub>) of composite films were lower than solid-state organic compounds due to their low concentration embedded in silicone resin (1-2 wt. %). For composite films of compound **4** and **12**, the absolute quantum yields were lower than the same compound in solid-state powder due to decreasing the concentration of solid powders in composite films. On the other hand, the difference in concentration of compound **6** between solid-state powder and composite films have shown small effects on the absolute quantum yields. In this case, we have not any explanations about these behaviors. The spectral overlap between absorption and emission spectra of each composite film was observed at the upper end of the absorption spectrum and the lower wavelength of the emission spectrum. Furthermore, a large overlap between the absorption spectra of composite films confirmed that they could be excited at the same wavelength that is compatible with commercial UV-LEDs. However, the possibility of emission reabsorption by mixed organic phosphors could occur in the mixed phosphors-silicone composite film. In order to avoid these problems, the color simulation should be taken care to determine the appropriate quantities of each organic compounds blended with silicone, which will be discussed in the next section.

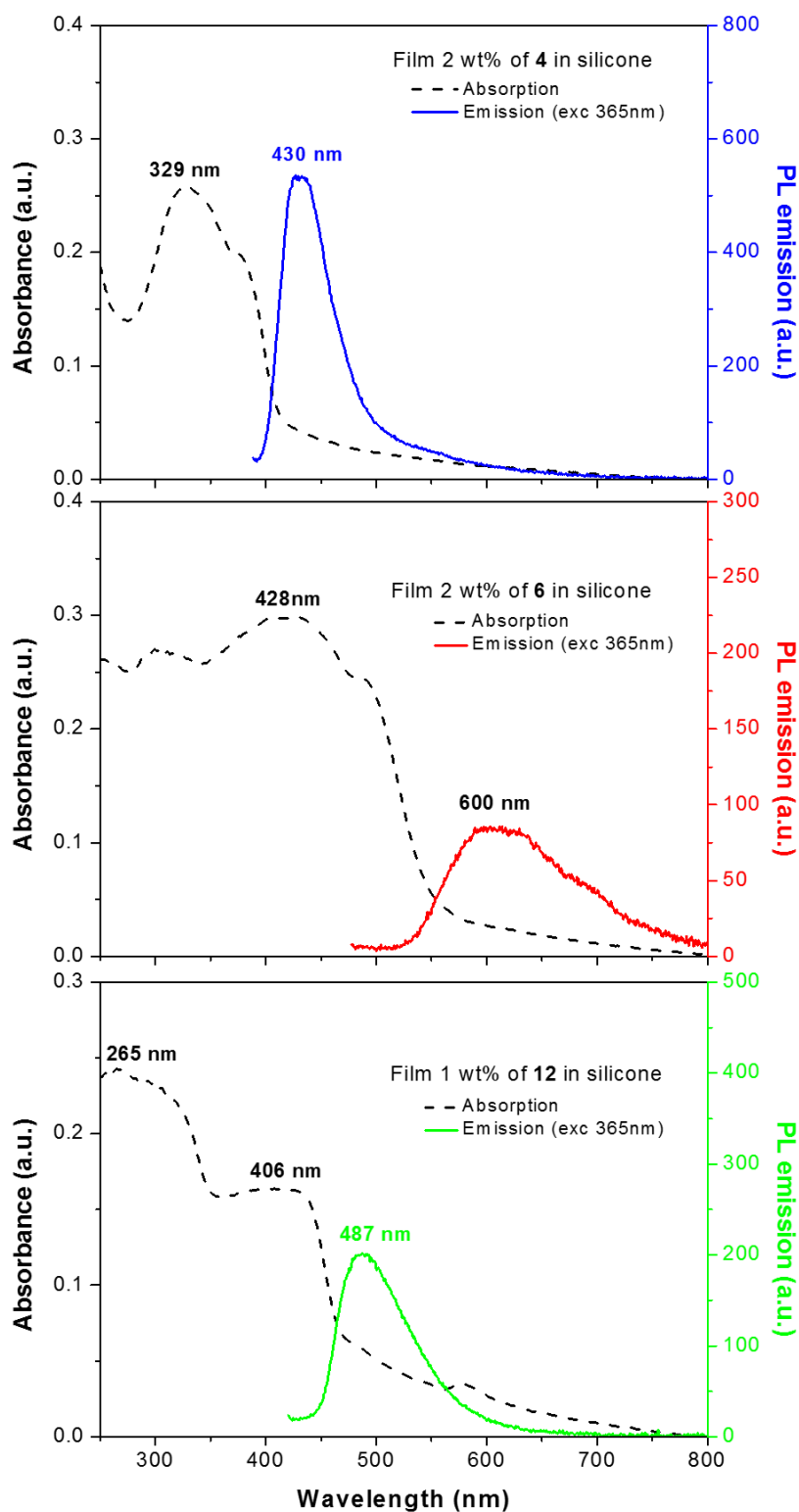


Figure 63 Absorption and PL emission spectra of selected organic phosphors (consisting of compound 4, 6 and 12) composite films

## **B. Color simulation for mixture of selected organic compounds**

The study of colorimetric simulation was investigated in collaboration with CEA-LETI in order to create the formulation of mixed organic phosphors to generate white light from a 365 nm UV-LED and meet the requirements of indoor lighting (CRI > 80, color temperature between 3000-4000 K). The simulation results were obtained with the assistance of Marianne Consonni from Laboratoire des Composants pour l'Eclairage (LCE), Grenoble.

The conditions of colorimetric simulation were determined as followed:

- The final spectrum from mixed organic phosphors should be the sum of emission spectra emitted by each organic phosphor.
- The organic phosphors could completely convert absorbed light energy emitted from a LED source.
- All phosphors were illuminated by the same incident power.
- There is no saturation of light emission.

Accordingly, the compound **4**, **6** and **12** in solid state were used for the colorimetric simulation as they were responsible for blue, red and green light emissions, respectively. The inorganic phosphor YAG: Ce<sup>3+</sup> were also used for another formulation. The theoretical results obtained by colorimetric simulation are presented in Table 22.

**Table 22 Results from colorimetric simulation upon excitation at 365 nm.**

	<b>Simulation results</b>	
	<i>Film A</i>	<i>Film B</i>
<b>TOTAL (weight)</b>	<b>100</b>	<b>100</b>
Compound <b>4</b> (hexylmine) (%wt.)	94.5	11.5
Compound <b>6</b> (phenyl) (%wt.)	2.9	30.3
Compound <b>12</b> (Al-MPBH) (%wt.)	-	59.2
Commercial YAG: Ce (%wt.)	2.6	-
Color temperature (K)	3037	3349
CRI	80	82
x	0.433	0.414
y	0.401	0.395

### C. Optical properties of mixed phosphors composite films

As shown in Table 22, the simulation results have been used as a guideline for preparing the mixed organic phosphors. However, the colorimetric simulation does not take into account the absorption factors of each organic phosphors. Therefore, the compositions of phosphors were developed and adjusted in order to achieve the nearest value of theoretical white color as  $(x,y) = (0.333, 0.333)$ . Consequently, we have developed one with only organic phosphors involving compound **4**, **6** and **12** (Film B) and another with two organic phosphors (compound **4** and **6**) and commercial YAG: Ce<sup>3+</sup> matrix (film A) for embedding into silicone resin. For the composite film B, the concentration of compound **4**, **6** and **12** were fixed at 14%, 0.72% and 0.38% by weight, respectively. The film A was prepared using compound **4** (14.88 wt. %), **6** (0.44 wt. %) and the commercial YAG: Ce (0.38 wt. %) in order to compare its optical properties with the film B. The composite phosphor films obtained after solvent evaporation showed a thickness between 130-170  $\mu\text{m}$ , and were remarkably flexible, robust, and free standing as well as high photoluminescence under 365 nm UV lamp (Figure 64). It should be noted that, however, the composite films are opaque but slightly translucent due to the thickness and the variation of compositions of phosphors within the films (15 wt. % of organic phosphors and 85 wt. % of silicone resin in composite films).

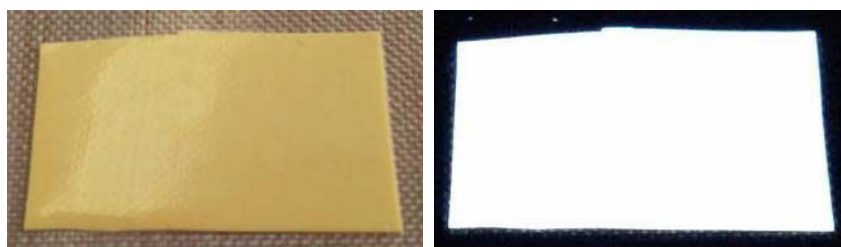


**Figure 64 Photographs of free-standing mixed organic phosphors-silicone composite film (Film B) (left) under normal light and (right) under a 365 nm UV-light illumination.**

In order to investigate the color of composite phosphor films, the films are deposited on the cup holder of UV-LEDs chip (365 nm excitation) as a remote phosphor configuration. The color point of composite phosphor films is defined according to the convention of the Commission Internationale de l’Eclairage (CIE) in a normalized two-dimensional color coordinate system. The CIE color coordinate and PL emission spectra of two luminescent composite films with 365 nm UV-LED in remote phosphor configuration are represented on the Figure 65a and b, respectively. The compositions of phosphors and their performance parameters of light (luminous efficacy, correlated color temperature, CIE coordinates and color rendering index) were summarized in Table 23.

**Table 23 Compositions and their lighting performance parameters of two composite films based on organic phosphors under 365 nm UV-light illumination.**

Film	Composition in silicone polymer film				Thickness (μm)	CIE (x, y)	PLQY <sub>abs</sub> (%)	IRC	CCT (K)
	Compound 4	Compound 6	Commercial YAG: Ce	Silicone resin					
A	Compound 4 14.18%	Compound 6 0.44%	Commercial YAG: Ce 0.38%	Silicone resin 85%	162 ± 12	(0.366, 0.362)	11.3	77.3	4315
B	Compound 4 14.00%	Compound 6 0.72%	Compound 12 0.38%	Silicone resin 85%	138 ± 10	(0.378, 0.398)	11.0	75.4	4214

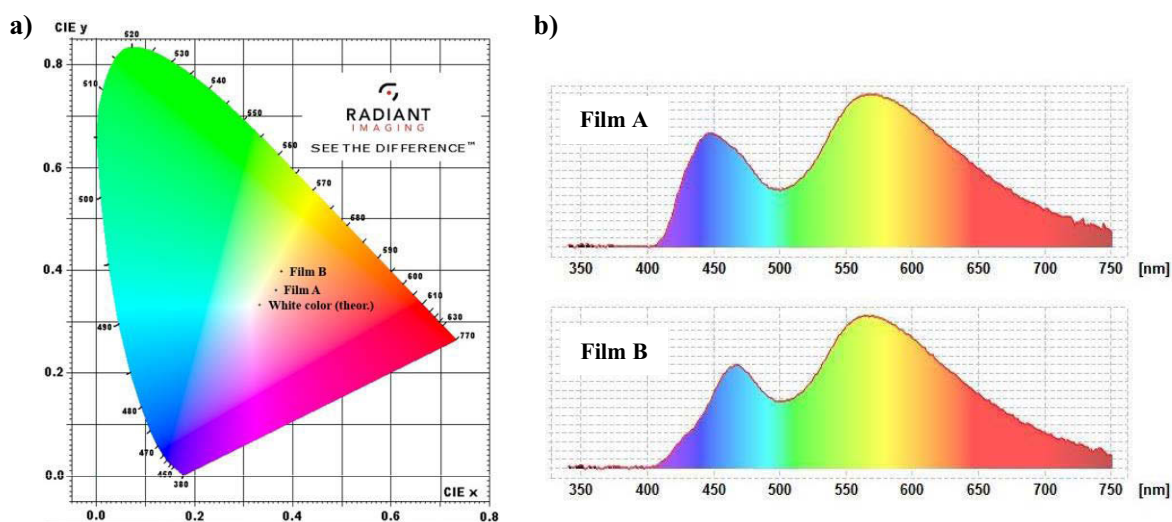


**Figure 65 (a) CIE color coordinates of white LEDs based on the mixed phosphor composite films excited by a 365 nm UV-LED. (b) The emission spectra of films-based white LEDs.**

The emission spectra of two composite films recorded after excitation with 365 nm UV-LEDs show a broad emission wavelength between 400 and 800 nm with two maxima around 460 and 570 nm. The absolute quantum efficiencies of both composite films are about 11% under 365-nm UV-light illumination. However, the two composite films are still requiring the improvement of the luminous efficiency due to the high values reported for a white LEDs using rare-earth activated nitride phosphors<sup>6</sup> and for a white LEDs using red quantum dots (CuInS<sub>2</sub>) and green phosphors<sup>208</sup>. Furthermore, the CRI values is lower than 90, which is the condition for the interior WLEDs lighting requirement<sup>209</sup>.

The color coordinates of film A and film B were recorded at (0.366, 0.362) and (0.378, 0.398), respectively, which were closed to the theoretical white color as (x, y) = (0.333, 0.333). Another parameter indicating the color quality is defined by the distance from the Planckian locus (see introduction) on the CIE color coordinates (Duv). It is known that sources at distances greater than 0.0054 ( $Duv = \sqrt{\Delta u^2 + \Delta v^2}$ ) from the Planckian locus are not true white light sources<sup>210</sup>. According to our composite films, the Duv value was found at about -0.003 (for film A) and +0.010 (for film B), indicating that white-light emission produced by our luminescent composite films based UV-LED were still necessary to improvement and needed more researches to overcome these challenges and further study for straightforward development of for better quality in photoluminescence performances for WLED and lighting applications.

### D. Study of photo-degradation of organic composite films

Photo-oxidation reaction is a chemical reaction with oxygen triggered by the absorption of photon energy resulting in the formation of molecules in excited states which presents different chemical and physical properties from the molecules at ground-state level. The photo-oxidation reaction is considerably spontaneous and can be carried out in several mediums (i.e. water, organic solvent, and thin-film polymer) at room temperature and atmospheric pressure.

It is well-known that various types of organic compounds are capable to react with oxygen molecules under irradiation because of functional groups in a molecule (sometimes are called chromophores) that are strongly active under UV-visible region<sup>211</sup>. The photo-oxidation reactions of organic compounds was generally investigated in various field of study such as organic synthesis<sup>212, 213</sup>, marine environment<sup>214</sup>, photodynamic therapy for cancer treatment<sup>215</sup>, and photocatalysis<sup>216-218</sup>. The photo-oxidation reaction of organic molecules is typically related to their singlet and triplet states as well as an active species of singlet oxygen ( $^1\text{O}_2$ ). The singlet oxygen can be generated by energy transfer from organic molecules or by chemical reaction. The organic molecules at excited state are more reactive than those at ground state which enhance the possibility to undergo several reactions. After irradiation, the organic molecules can react with another molecules to proceed the electron-transfer reaction or react with oxygen to produce the photo-oxidation products.

The photo-oxidation reactions are classified into two types: type I and type II reactions (Figure 66)<sup>219, 220</sup>. Considering type I reaction, the energy of photon absorbed by molecules can initialize photo-dissociation by dividing a bond via hemolytic cleavage and generating the radical species to react with oxygen. According to type II reaction, the photo-oxidation reaction is initiated by sensitizers which might be some pigments or aromatic hydrocarbons. The sensitizer molecules at the excited state ( $^1\text{A}$ ) can relax rapidly to the ground-state level or transition to the longer lifetime triplet state via intersystem crossing ( $\tau \approx 10^{-8}$  s for singlet state and  $\tau \approx 10^{-3}$  for triplet state)<sup>211</sup>. The ground state oxygen ( $^3\text{O}_2$ ) oxidizes the sensitizers at triplet state to form a highly reactive singlet of oxygen ( $^1\text{O}_2$ ) which reacts with organic molecules at excited state to produce the oxidation products.

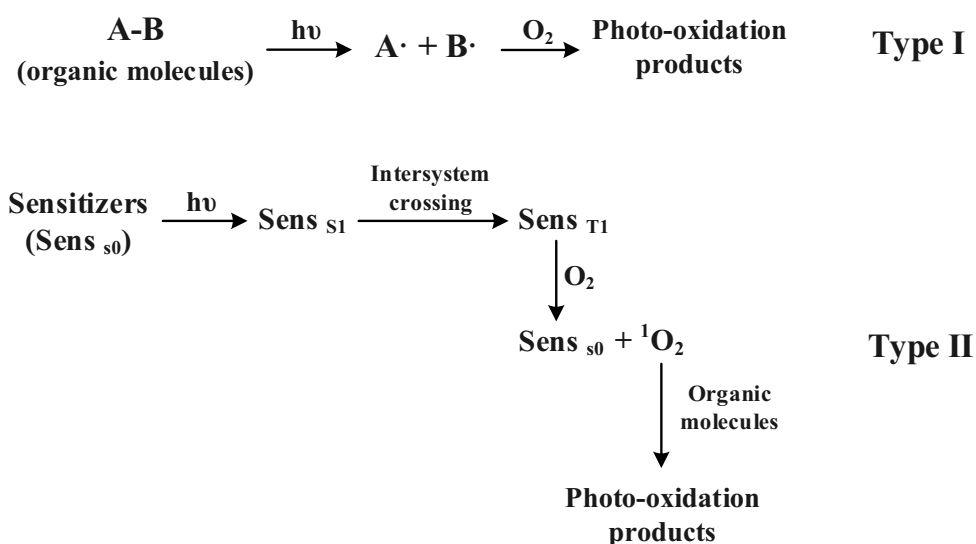
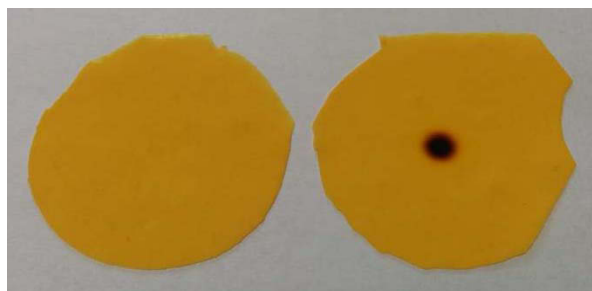


Figure 66 Typical photo-oxidation of organic molecules: type I and type II <sup>9</sup>.

Accordingly, the photo-oxidation reaction plays the important role in the photo-degradation process of organic compounds and becomes the critical barriers to improve many organic molecules for light-emitting applications. In order to prevent the organic molecules from photo-degradation, the encapsulation materials should be used such as polydimethylsiloxanes (PDMS), polyvinyl alcohol (PVA), poly(methyl methacrylate) (PMMA) and other polymer matrices in order to provide a barrier against water and oxygen of the environment and extend the lifetime of organic compounds in lighting devices. Therefore, the study in photo-oxidation of organic composite films under operation conditions of LEDs should be considered.

In our work, the preliminary investigation of photo-stability of mixed organic composite film (film B) was designed by placing the composite films at a distance of about 2 cm on the cup holder of 365 nm UV-LEDs chip as a remote phosphor configuration and then irradiating continuously under 365 nm UV illumination (at a power of 0.9W) for 2 hours. A dark spot was found at the center of the composite film, which were the same position as an UV-LED chip in the cup holder (Figure 67). This result shows that our mixed organic composite film is very sensitive and probably degraded under UV irradiation. Therefore, the photo-degradation of the organic composite films becomes a worthy topic to study in order to develop the organic composite films for further LED applications.





**Figure 67 Photographs of free-standing mixed organic phosphors-silicone composite films (left) before and (right) after UV illumination for 2 hours by UV-LED based remote phosphor configuration system.**

In this study, the individual organic composite films as well as the mixed organic composite film were exposed to 4 medium-pressure mercury arc lamps ( $\lambda > 300$  nm) in a SEPAP 12/24 unit under accelerated artificial conditions (air atmosphere, at 60°C). The experimental investigation of the stability of organic composite films under light and air exposure were analyzed through FTIR and UV-visible absorption spectroscopies. This work was performed in collaboration with the research group of Doctor Sandrine Therias (POPPI, Institut de Chimie de Clermont-Ferrand, France).

### **a. Photo-degradation of silicone**

In order to better understand the photo-degradation of composite films, the neat silicone film should be firstly investigated. Accordingly, a two-component silicone resin was selected because of highly optical transparency, possibility of adding fillers and low temperature of curing silicone. The film thickness was regulated by adjusting the distance between the doctor blade and the substrate (i.e. Teflon sheet) in order to avoid the IR saturation bands.

As indicated previously, the silicone resin typed polydimethylsiloxanes (PDMS) was synthesized by polyaddition reaction of silicon hydride and silicon vinyl group (see Figure 58). The formation of dimethylene group (Si-CH<sub>2</sub>CH<sub>2</sub>-Si) is **a point of interest for the study of degradation for photo-oxidation** in composite films because this group is unstable under UV irradiation<sup>221</sup>.

#### **UV irradiation > 300 nm**

The photo-oxidation of polydimethylsiloxanes at wavelengths higher than 300 nm has been studied by a group of J. Lemaire<sup>221</sup>. Figure 68 presents the photo-oxidation mechanism of polydimethylsiloxanes under UV irradiation ( $\lambda > 300$  nm). As with other polymers, the

degradation of silicone is generally derived from the reaction between polymer chains and oxygen in the presence of light such as UV or artificial light.

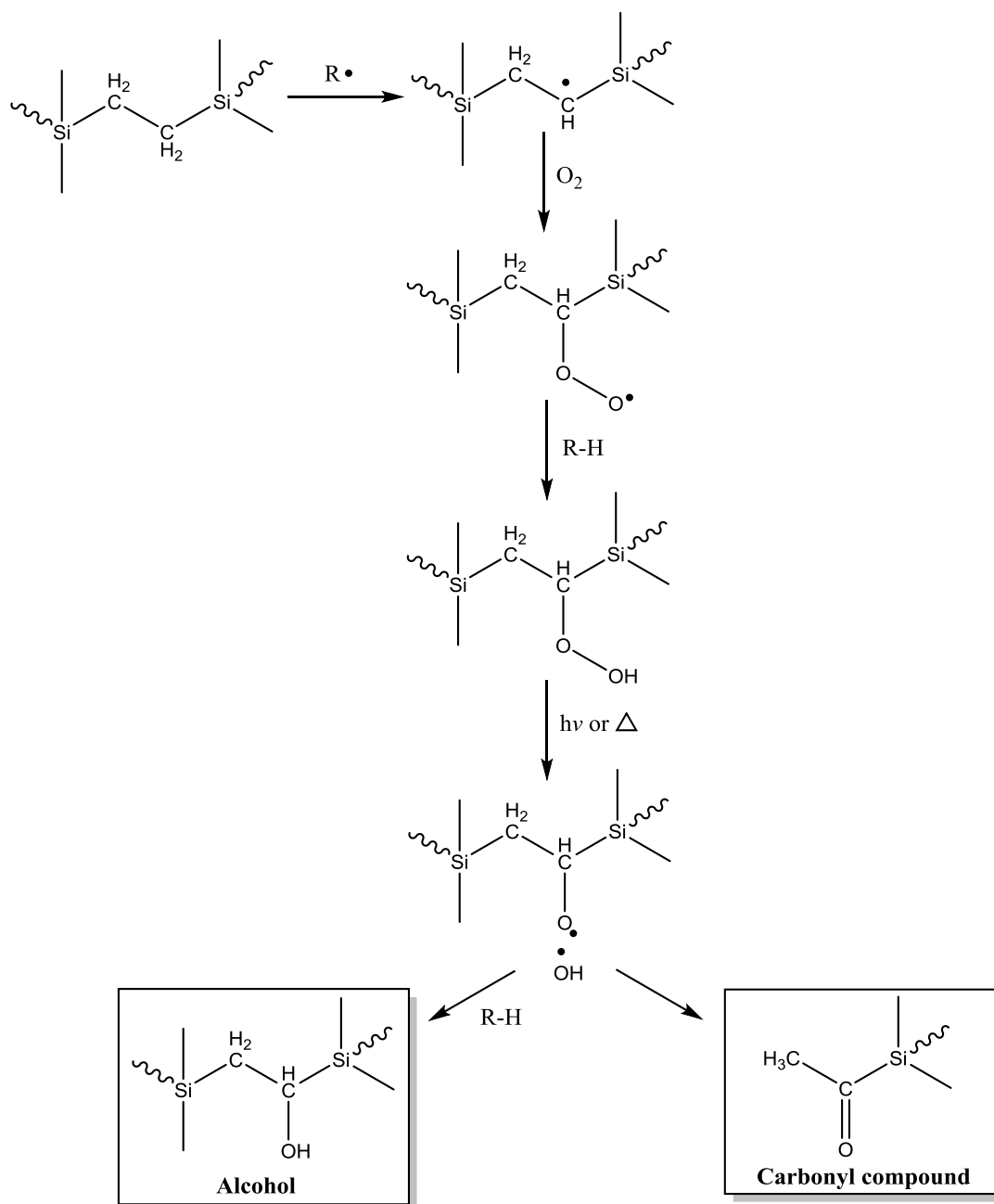
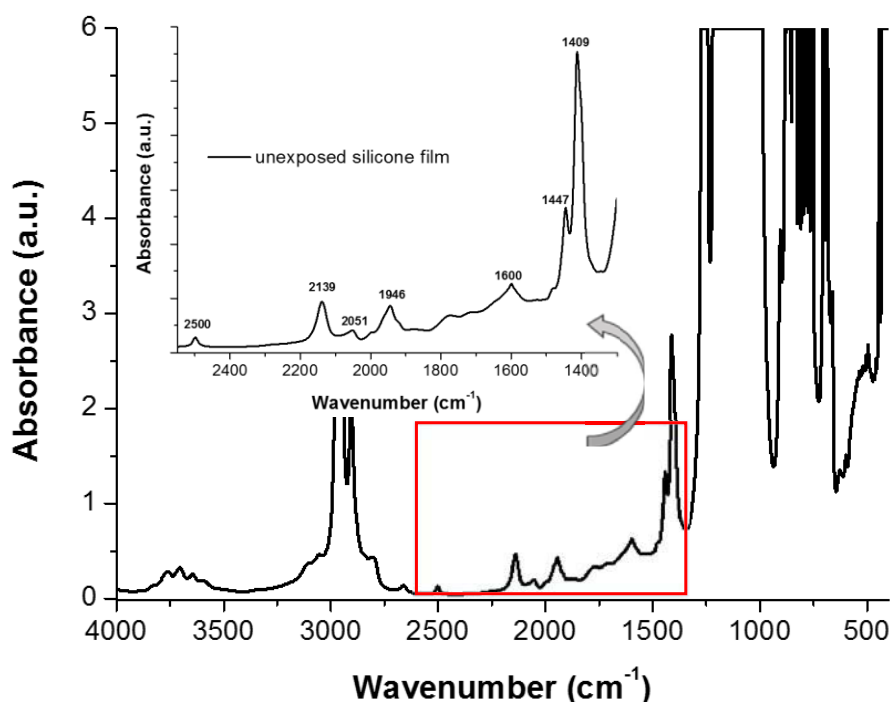


**Figure 68 Mechanism of photo-oxidation of polydimethylsiloxanes under UV irradiation ( $\lambda > 300$  nm).**

The photo-oxidation can be initiated by light absorption, intrinsic defects or impurities in polymers such as chromophores<sup>222, 223</sup>. At the first step, free radicals are formed with assistance of chromophores. The chromophores absorb the photon, raise to the higher energy level as free radicals form. At this state, the energy can transfer to another molecule or polymer chain by breaking molecular bonds and form macromolecular free radicals ( $R\cdot$ ). These activated free

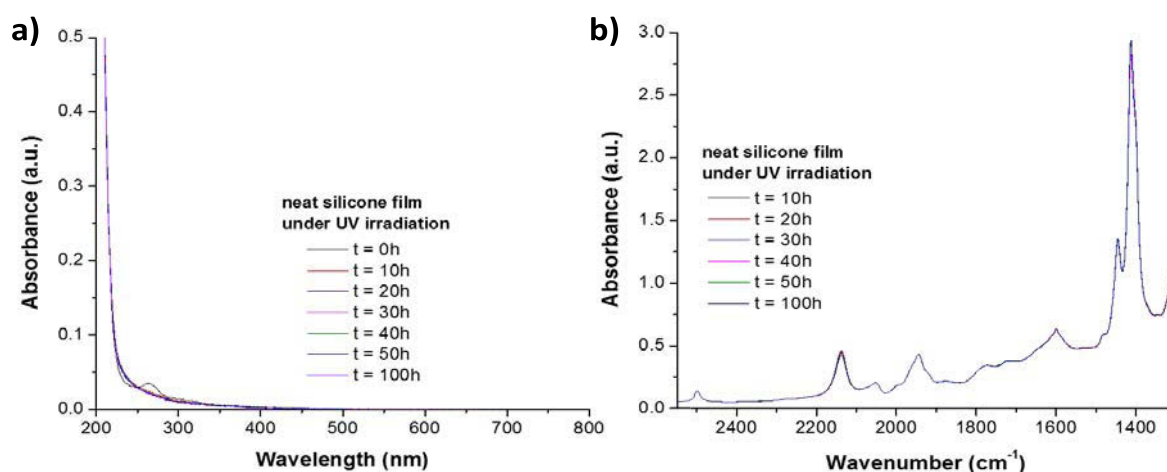
radicals are instable and can react with oxygen molecules to produce peroxy radicals ( $\text{RO}_2\bullet$ ). Next, these peroxy radicals react with a polymer molecule to generate polymer hydroperoxide ( $\text{ROOH}$ ) and a new polymer alkyl radical ( $\text{R}\bullet$ ). The polymer hydroperoxide is also instable and dissociated into polymeric oxy-radicals ( $\text{RO}\bullet$ ) and hydroxy radicals ( $\text{HO}\bullet$ ). As a result, the reactions generate many oxidation products such as hydroxyl compounds and carbonyl compounds which allow us to investigate the photo-oxidation in details by spectroscopic analysis.

Figure 69 presents the infrared spectrum of UV-unexposed neat silicone film in transmission mode. The infrared absorption data for some functional groups of silicone was listed in Table 20. It should be noted that most of IR absorption peaks are well-known and associated with stretching vibrations of silicone<sup>207,224</sup>. However, most of them are saturated and found as a sum of multiple absorption bands and then it is difficult to interpret the degradation behavior. In this case, we focused on the range of  $2800\text{-}1300\text{ cm}^{-1}$  and  $3800\text{-}3200\text{ cm}^{-1}$  in order to observe the formation of photo-oxidation products which must appear in these zones such as carbonyl compounds and hydroxyl compounds, respectively.



**Figure 69** Infrared spectrum of UV-unexposed silicone film. The inset graph presents the zoomed area from  $2550\text{-}1350\text{ cm}^{-1}$ .

The silicone film was then submitted to irradiation at  $\lambda > 300$  nm and heating at  $60^\circ\text{C}$ . The IR and UV-visible spectra showed that the spectra of silicone film are mostly identical for both before and after 100 h photo-ageing (Figure 70). This result indicates that no modification of UV visible and IR spectra of the UV-exposed silicone film and no photo-oxidation product was observed during the irradiation times up to 100 h. The small UV-visible absorption band at 265 nm might be due to the residual phenolic compounds in the silicone precursors, which disappeared after 10 h photo-ageing and might not affect the absorption bands of our samples. Thus, the silicone can be considered as a good candidate to study the photo-degradation of further silicone-based composite films due to its stability under UV-exposure time range from 1 to 100 h or more.



**Figure 70 (a) IR spectra and (b) UV-visible spectra of UV-exposed silicone film during photo-oxidation.**

### **b. Photo-degradation of organic-silicone composite films**

In order to investigate the photo-degradation of composite films, the optical properties and the photochemical behavior of organic compounds-silicone were characterized before and after ageing. Both infrared spectroscopy and UV-visible absorption spectroscopy have become an effective analytical tool to monitor the photo-degradation behavior. The three selected organic phosphors embedded in the silicone resin were investigated individually under irradiation at  $\lambda > 300$  nm and heating at  $60^\circ\text{C}$ , in the presence of oxygen and humidity. It should be noted that each organic composite films were selected for these studies prior to mixed organic composite film because the UV-visible and infrared spectra of latter were more sophisticated patterns to identify and analyze the evolution of spectra during photo-oxidation reaction. Contrary to the inorganic phosphors, the organic molecules have high molar absorption coefficients in the UV and visible regions. Therefore, the concentration of solid powders in silicone resin should be

adjusted to achieve readings in the instrument range. In the case, the concentration of organic phosphors in silicone resin were 1-2 wt. %. We particularly focused on the range 2250-1450  $\text{cm}^{-1}$  in which the evolution of photo-oxidation reaction can be clearly observed for organic phosphor-silicone composite films (Figure 71-73).

### Infrared spectra

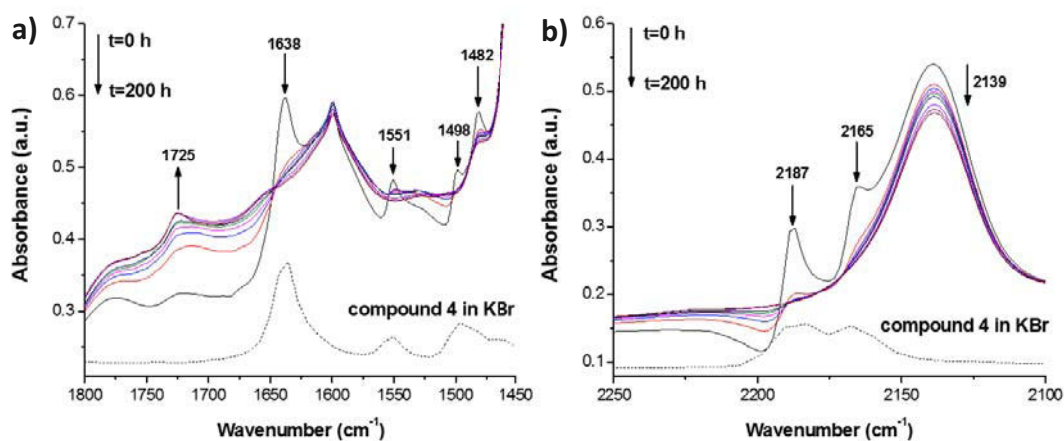


Figure 71 Evolution of infrared spectra of compound 4-silicone composite film during photo-oxidation for 200 h in the absorption range: (a) zone 2250-2100  $\text{cm}^{-1}$ , and (b) zone 1800-1450  $\text{cm}^{-1}$ .

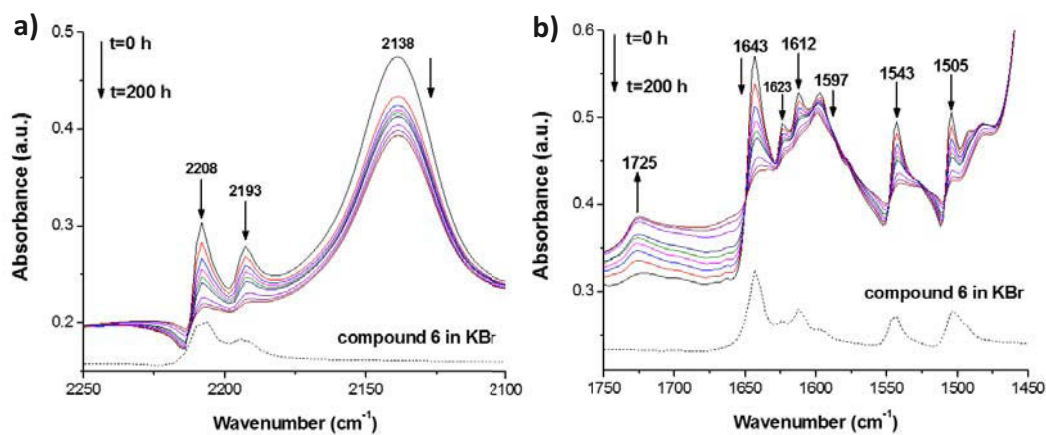
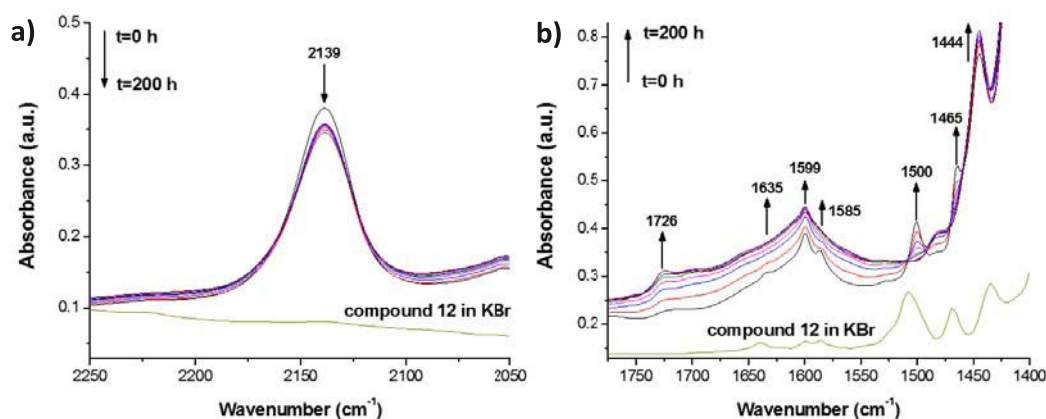


Figure 72 Evolution of infrared spectra of compound 6-silicone composite film during photo-oxidation for 200 h in the absorption range: (a) zone 2250-2100  $\text{cm}^{-1}$  and (b) zone 1750-1450  $\text{cm}^{-1}$ .



**Figure 73** Evolution of infrared spectra of compound 12-silicone composite film during photo-oxidation for 200 h in the absorption range: (a) zone 2250-2050  $\text{cm}^{-1}$ , and (b) zone 1775-1400  $\text{cm}^{-1}$ .

As with the previous studies, the compound **4** and **6** were derived from dicyanomethylene-4H-pyran derivatives, showing the characteristic vibration bands of the  $\text{C}\equiv\text{N}$  bonds (2210-2160  $\text{cm}^{-1}$ ) and the  $\text{C}=\text{C}$  conjugated bonds (1643-1638  $\text{cm}^{-1}$ ) as shown in Figure 71-73. The characteristic vibrations bands in the range of 1630-1400  $\text{cm}^{-1}$  were different in compound **4** and **6**, which were attributed to the characteristic vibration of each compound. The IR spectra of both compounds show the significant decrease in absorbance when the composite films were irradiated from 0 to 200 h. The increase in absorbance at around 1725  $\text{cm}^{-1}$  was obviously observed at the same time, which correspond to the functional group of carbonyl compounds. We suppose that the structure of carbonyl compounds is formed during the photo-degradation process of organic compounds by oxygen addition to the double bonds in conjugated system.

Similar organic molecules of dicyanomethylene-4H-pyran derivatives had been investigated for the photo-oxidation reactions. The degradation products could consist of carbonyl units which was resulted from oxidation of unsaturated bonds ( $\text{C}=\text{C}$ ). Akasaka and collaborators studied the molecule of 4-[2-(N,N-Dimethylhydrazono)ethylidene]-2,6-diphenyl-4H-pyran-3,4-dihydro-2H-pyran and found that it was capable of inhibiting oxidation of  $^1\text{O}_2$ <sup>225</sup>. That means this organic compound were sensitive and unstable to oxidation. The published work of R.S. Atkinson studied the photo-oxidation of aryl-dihydropyrans and suggested that the photo-oxidation of these dicyanomethylene-4H-pyran derivatives could be possibly derived from the formation of carbonium ions at  $\text{C}=\text{C}$  bond which gave the carbonyl fragments<sup>226</sup>. The similar results were also reported by Cao and collaborators which studied 3,4-dihydro-2H-pyran prepared in various oxygen-saturated solutions under UV irradiation (> 300 nm) and concluded

that the molecule could generate the carbonyl products resulting from the C=C oxidation by singlet oxygen<sup>227</sup>.

In the case of Al-MPBH complex (compound **12**), there is no study of this complex to photo-degradation in the literature. However, similar Al complex has been reported by Flávia P. Rosselli and collaborators for their study of thin-film tris-(8-hydroxy-quinolate) aluminum (Alq<sub>3</sub>) under UV photo degradation<sup>228</sup>. The photo-degradation of Alq<sub>3</sub> under UV irradiation was suggested by breaking the phenoxide ring and keeping the Al-O bond, which were thermodynamically favorable and presented a good agreement with their experimental results<sup>228</sup>. In our case, the evidence of characteristic vibrations of Al-MPBH complex as mentioned before (Table 15) were unfortunately sophisticated to investigate because the corresponding bands were overlapped with the large characteristic vibration bands of silicone resin. Thus, we observed the small bands in the range of 1600-1400 cm<sup>-1</sup> corresponding to the characteristic of C–C stretching in the aromatic ring<sup>229 †††</sup>. As shown in Figure 73, the characteristic vibration bands at 1500 and 1465 cm<sup>-1</sup> show the decrease in absorbance when the compound **12**-silicone composite film was irradiated from 0 to 200 h. The increase in absorbance around 1726 cm<sup>-1</sup> was also observed and allowed to the attribution of the carbonyl group. It should be noted that the compound **12** contains the electron-rich groups both on the phenyl ring and on the pyrazine ring. These groups might increase the possibility of 1,2-cycloaddition of oxygen molecule at the electron-rich double bonds, which can convert to C=O groups and further oxidative products easily<sup>230, 231</sup>.

### UV-visible absorption spectra

Figure 74 presents the UV-visible absorption spectra of organic composite films during photo-oxidation process under accelerated artificial conditions. After continuous irradiation of about 200 h, the absorption bands of organic compounds embedded in silicone resin were disappeared and the final composite films were colorless. Since there was no additional absorption peaks occurred in the UV-visible absorption spectra, the degradation and the colorless of organic phosphors composite films should be due to the destruction of  $\pi$ -conjugated structure of organic molecules by photo-bleaching process. The UV irradiation could provide the enough energy which allow the oxidation reaction by oxygen molecules to break up the  $\pi$ -conjugated systems into UV inactive bonds (i.e. C-C single bonds). As a consequence, the decrease in

---

††† See also: <http://orgchem.colorado.edu/Spectroscopy/irtutor/aromaticsir.html>

absorption bands can be detected across the entire UV-visible spectra because the organic phosphors composite films are no longer to absorb the light energy in such region, corresponding to the decrease in some characteristic vibration bands of  $\pi$ -conjugated systems or organic phosphors as mentioned previously.

**Table 24 Absolute quantum yield of each organic phosphors composite films before and after UV irradiation for 0 and 100 h under accelerated artificial conditions.**

Composite films	Before UV irradiation		After 200h UV irradiation	
	PLQY at 365 nm (%)	PLQY at 450 nm (%)	PLQY at 365 nm (%)	PLQY at 450 nm (%)
2wt.% compound 4 in silicone	18	-	1	-
2wt.% compound 6 in silicone	9	8	1	2
1wt.% compound 12 in silicone	9	6	0.4	0.3

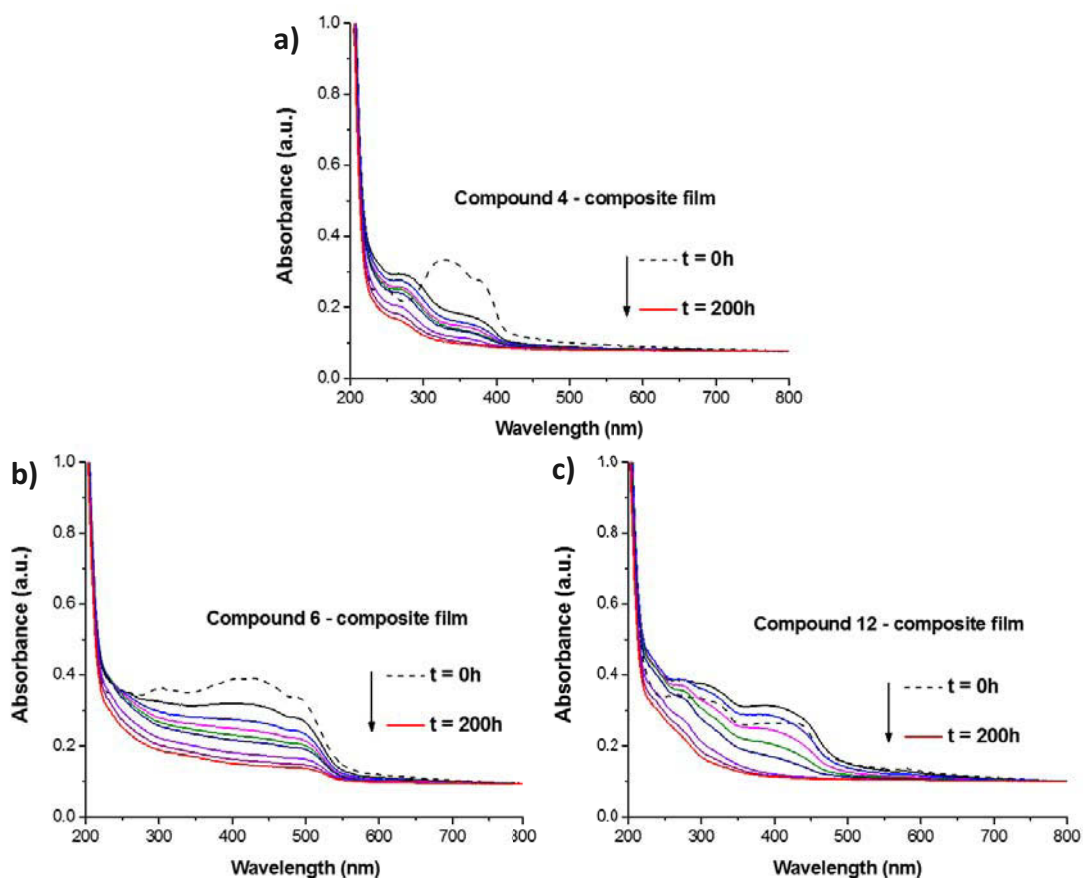


**Figure 74 Evolution of UV-visible absorption spectra of organic phosphors composite films during photo-oxidation for 200 h under accelerated artificial conditions.**



As the photo-degradation process can influence to the absorption spectra of organic composite films, the photoluminescence emission spectra after UV irradiation should be also investigated. The evolution of PL emission spectra of each organic composite films before and after 200 h UV irradiation was depicted in Figure 75. The photoluminescence quantum yield of these organic composite films were summarized in Table 24. The organic composite films were found to significantly lose their photoluminescence properties after continuous UV irradiation, presented by a large decrease in emission intensity and photoluminescence quantum yield after 200 h UV irradiation. Indeed, the work of Papadimitrakopoulos and collaborators have shown that the formation of carbonyl group by the photo-oxidation reaction can reduce photoluminescence properties of OLED materials<sup>231, 232</sup>. Accordingly, since the photo-bleaching process of organic composite films can be related to the photo-degradation of organic molecules by singlet oxygen, the studies of photo-degradation of organic molecules under vacuum have to be also investigated in comparison with the studies in atmospheric conditions.

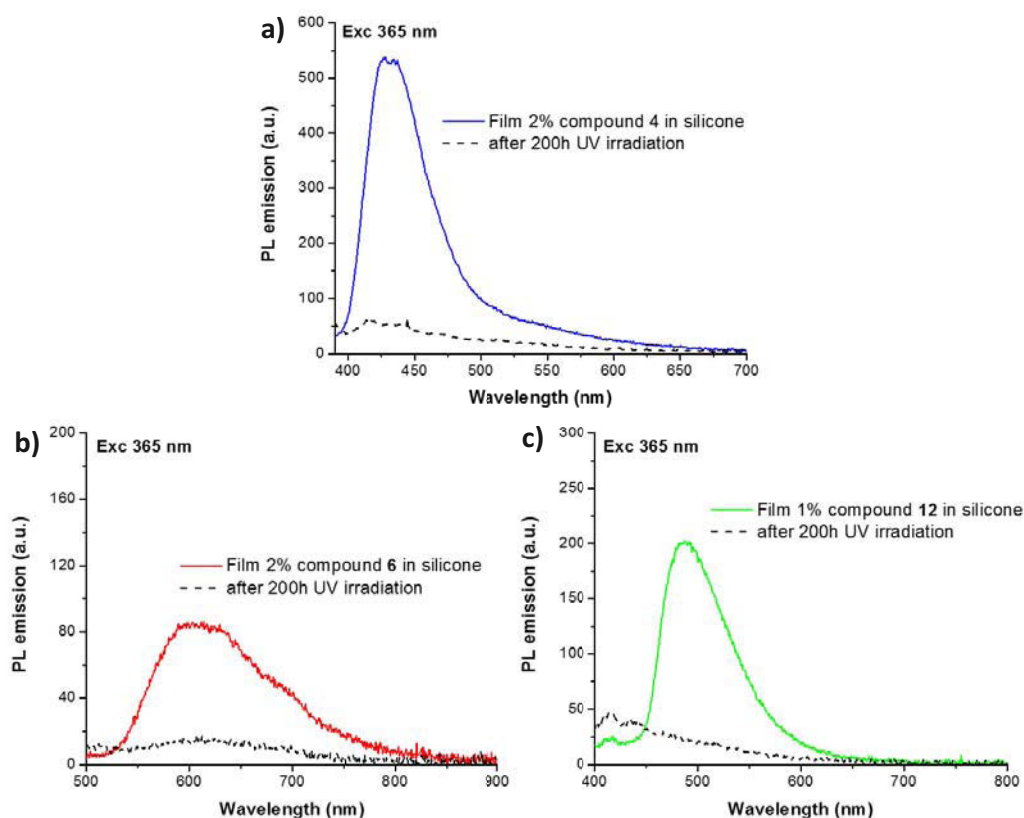


**Figure 75 Evolution of emission spectra of organic phosphors composite films before and after UV irradiation for 0 and 200 h under accelerated artificial conditions.**

In order to ensure that oxygen molecules can play an important role to the photo-bleaching of organic composite films, the composite films were prepared in the vacuum glass tube and then operate under the same conditions in air. The composite films were deposited into an open glass tube and sealed at room temperature under vacuum (pressure  $< 10^{-5}$  torr) in order to remove air from the tubes by use of a vacuum pump (Figure 76). The samples were investigated under irradiation at  $\lambda > 300$  nm and  $60^{\circ}\text{C}$ .



**Figure 76 Photographs of organic composite films in vacuum-sealed glass tubes.**

As shown in Figure 77-79, the IR spectra of composite films obtained in vacuum study presented very small different absorbance in comparison with the IR spectra of the same organic phosphors composite films recorded in air, especially in the range of  $2210\text{-}2160\text{ cm}^{-1}$  (for  $\text{C}\equiv\text{N}$  bonds) and  $1643\text{-}1638\text{ cm}^{-1}$  (for conjugated  $\text{C}=\text{C}$  bonds) for compound **4** and **6**. UV-visible absorption spectra of compound **4** and **6** exhibited the similar absorption profiles with slightly increase in absorbance after 200 h UV irradiation (Figure 80, a and b). These results should be a good evidence that oxygen can play an important role of photo-degradation of these dicyanomethylene-4H-pyran derivatives. However, the small modifications of both UV-visible absorption and IR spectra for compound **12**-silicone composite film were still presented after 100 h UV irradiation under vacuum (Figure 79 and Figure 80c). We suggest that the photo-oxidation of compound **12** seems to have occurred not only the presence of oxygen molecules.

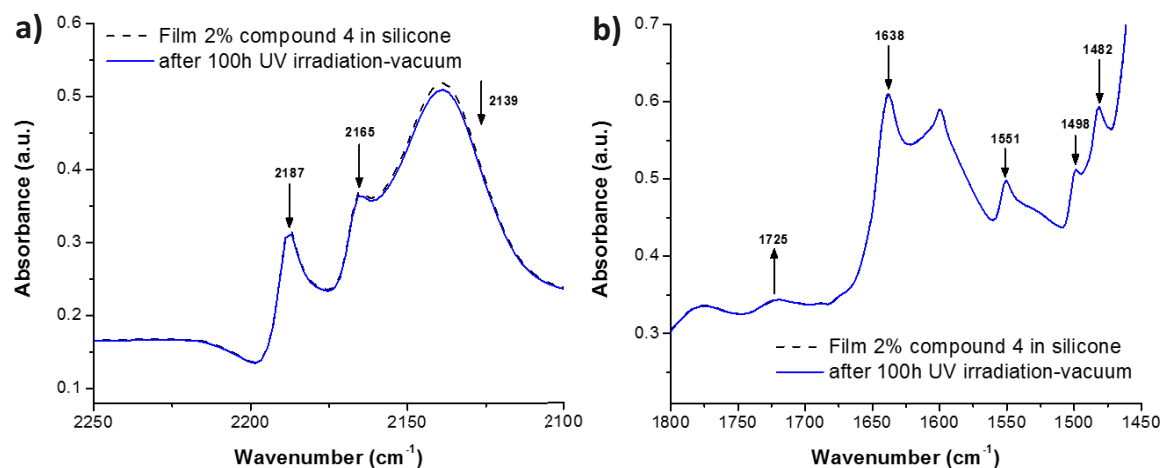


**Figure 77** Evolution of infrared spectra of compound 4-silicone composite film before and after UV irradiation for 0 and 100 h under vacuum and accelerated artificial conditions. The absorption range: (a) zone 2250-2100  $\text{cm}^{-1}$ , and (b) zone 1750-1450  $\text{cm}^{-1}$ .

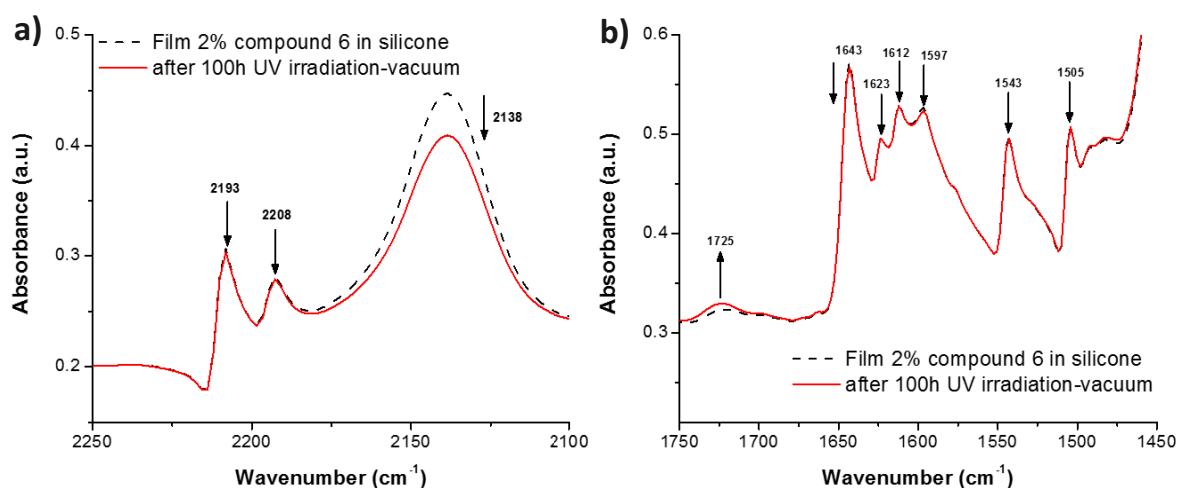


**Figure 78** Evolution of infrared spectra of compound 6-silicone composite film before and after UV irradiation for 0 and 100 h under vacuum and accelerated artificial conditions. The absorption range: (a) zone 2250-2100  $\text{cm}^{-1}$ , and (b) zone 1750-1450  $\text{cm}^{-1}$ .

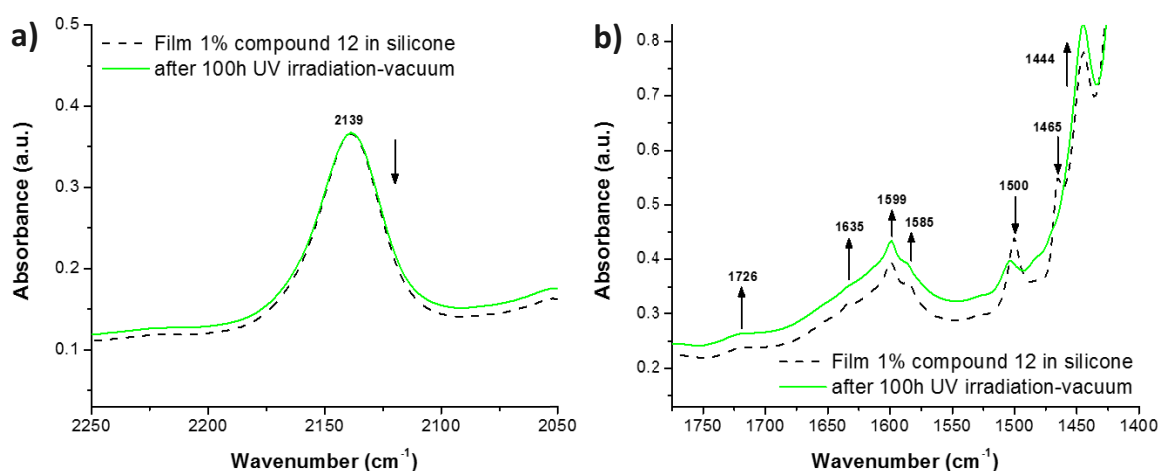


**Figure 79** Evolution of infrared spectra of compound 12-silicone composite film before and after UV irradiation for 0 and 100 h under vacuum and accelerated artificial conditions. The absorption range: (a) zone 2250-2050  $\text{cm}^{-1}$ , and (b) zone 1800-1400  $\text{cm}^{-1}$ .

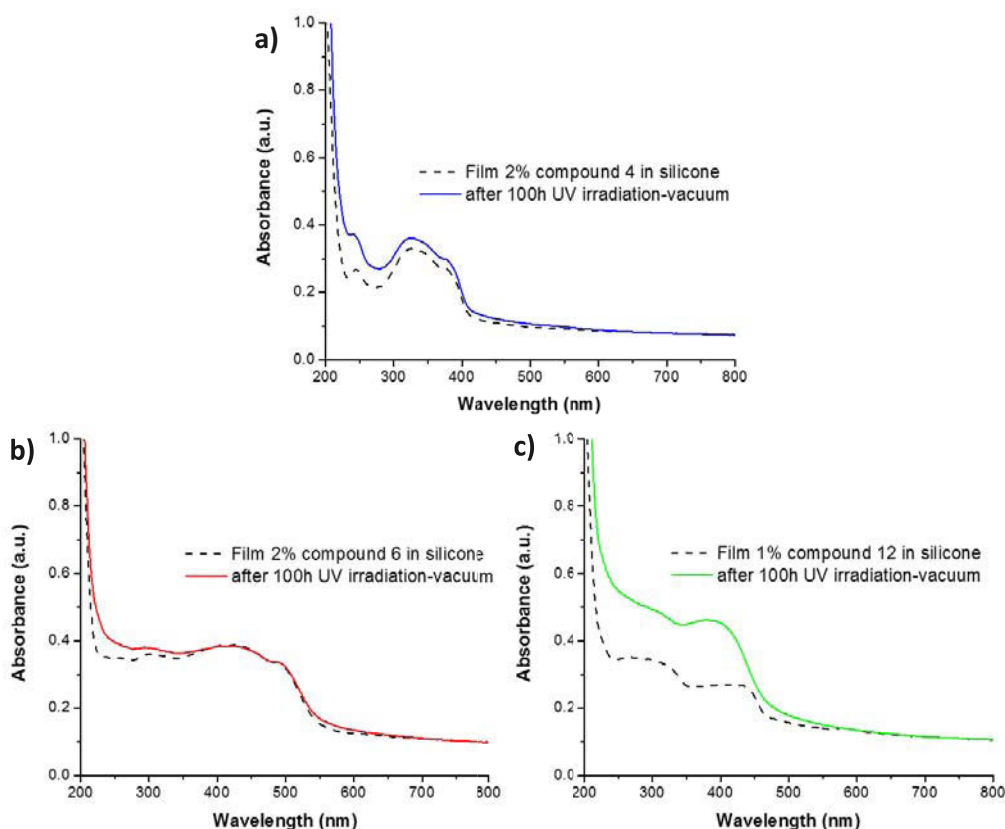


**Figure 80 Evolution of UV-visible absorption spectra of organic phosphors composite films before and after UV irradiation for 0 and 100 h under vacuum and accelerated artificial conditions.**

Figure 81 presents the photoluminescence emission spectra of organic composite films before and after 100h UV irradiation under vacuum. The PL emission spectra of organic composite films were observed with reduced intensity compared with the composite films before ageing. Interestingly, the composite films of compound **4** and **6** show a significant decrease in emission intensity after 100 h UV irradiation although the UV-visible and IR modifications were not observed. The absolute quantum yields of organic composite films were also lower than the values before UV irradiation (see Table 25), which was in agreement with their PL emission. However, we should point out that the absence of oxygen in the system can slow down the photo-degradation process of organic composite films.

**Table 25 Absolute quantum yield of each organic phosphors composite films before and after UV irradiation for 0 and 100 h under vacuum and accelerated artificial conditions.**

Composite films	Before UV irradiation		After 100h UV irradiation - vacuum	
	PLQY at 365 nm (%)	PLQY at 450 nm (%)	PLQY at 365 nm (%)	PLQY at 450 nm (%)
2wt.% compound <b>4</b> in silicone	18	-	7	-
2wt.% compound <b>6</b> in silicone	9	8	6	6
1wt.% compound <b>12</b> in silicone	9	6	4	1

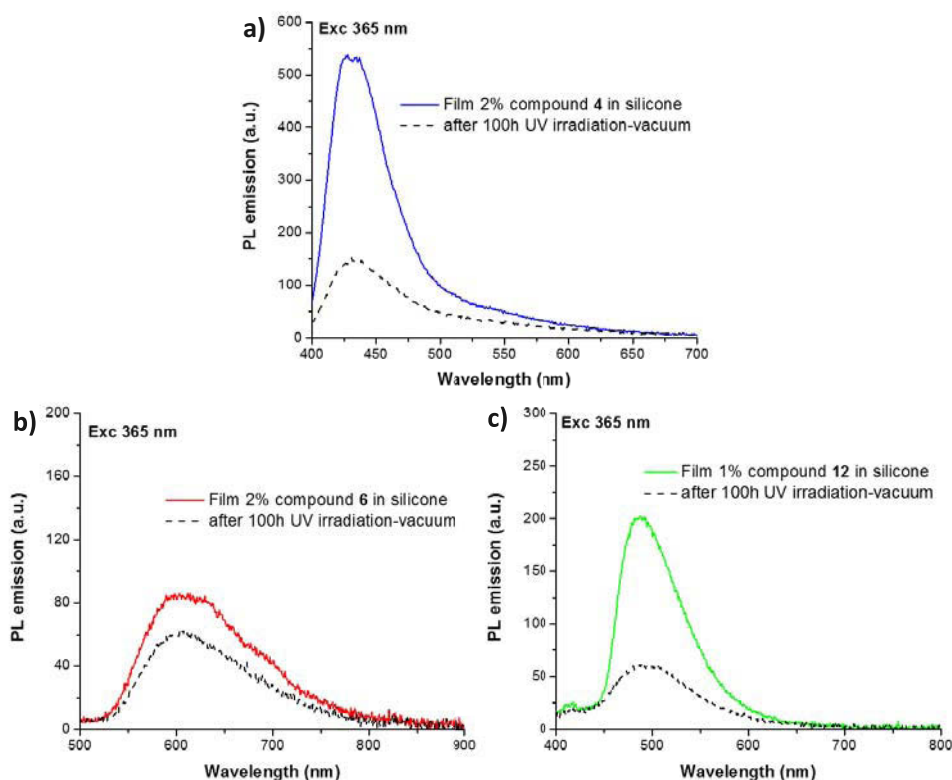


**Figure 81 Evolution of emission spectra of organic phosphors composite films before and after UV irradiation for 0 and 100 h under vacuum and accelerated artificial conditions.**

Although the presence of photo-oxidation products related to the photo-degradation of organic phosphors composite films are very small when the experiments are operated under vacuum, the photo-degradation is still observed. We suggest that either small amount of photo-oxidation products can affect the decrease in optical performances or these products are not solely responsible for decreasing the optical performance of organic phosphors composite films. Accordingly, the studies of photo-degradation of organic composite films are a valuable topic

of study, not only to fulfill our curiosity, but also to serve as a guideline in order to improve and develop the physical and optical properties of organic composite films for resisting the photo-oxidation for further use in LED devices and relevant photoluminescence applications.

### Summary

The rare-earth-free organic phosphors showing the aggregation-induced emission properties have become a promising candidate for lighting applications due to their good photoluminescence properties in solid state. The organic phosphors exhibit a broad absorption in UV to visible region and a strong emission, which can guarantee to be associated with UV/blue commercial LEDs to generate white light. Three different organic phosphors with three primary colors (RGB) having the best value in absolute quantum yield were selected to prepare the mixed phosphors composite films for building organic phosphors-based white light-emitting diodes using 365 nm UV-light excitation. The mixed phosphors composite film lead to a white emission with a CRI > 75 and a color temperature close to 4000 K when excited by a UV-LED. However, these organic phosphors composite films were confronted with their photo-stability during the operating conditions of LEDs. The main factor leading to the immense barrier to use organic phosphors for lighting applications was the photo-degradation of organic molecules under ageing condition and in the presence of oxygen. Further work should be dedicated to determining the novel method to protect these organic phosphors and also enhance the photoluminescence properties during the operating conditions.



---

**CHAPTER III**

**Encapsulation of organic  
phosphors for light-emitting  
applications**

---





### I. General introduction

Regarding the previous chapter, the organic phosphors exhibited high photoluminescence in solid state by their aggregation-induced emission (AIE) behavior. On the other hand, several organic molecules present the opposite behavior, which means that their photoluminescence becomes weaker or quenched in concentrated solutions as well as in the solid state. This photophysical behavior is commonly known as “concentration quenching” or “aggregated-caused quenching, (ACQ)” emission<sup>101, 102</sup>. It can be a major problem for development of white lighting-emitting diodes (WLEDs) by using these types of organic compounds. In order to maintain their photoluminescence in solid state, the organic molecules should be de-aggregated as in a dilute solution. Therefore, it is necessary to develop the encapsulation method of organic molecules in a solid matrix as playing the role of solvent in order to retain its characteristic luminescent properties. This chapter will be devoted to two encapsulation methods for entrapping organic phosphors into organosilane and inorganic-layered double hydroxide (LDH) structures as well as their physical and optical properties after encapsulation.

The organic phosphors are defined as a group of organic compounds that can emit light under light excitation. The main applications of organic phosphors are in the field of biochemistry and medical treatments as fluorescent biosensors and labels to biological targets because of their molecular size, biocompatibility, selectivity, sensitivity and high quantum yield<sup>233, 234</sup>. Regarding the lighting applications based on LEDs, the organic phosphors are becoming alternative luminescent materials over rare-earth based phosphors due to their high luminous efficiency, low-cost precursors, and large compatibility of organic phosphors with commercial LEDs to produce white light-emitting diodes (WLEDs). Furthermore, these organic phosphors are superior to inorganic phosphors towards the intensity of light absorption that is much higher and a numerous number of products available in the market. As a result, the development of organic phosphors represents an important challenge for the expansion of the WLEDs market. Table 26 demonstrates the examples of commercial organic phosphors with maximum excitation and emission wavelengths.

Regardless their excellent photoluminescence properties, many organic phosphors confront the immense drawback called concentration quenching or aggregated-caused quenching (ACQ), which decrease and/or quench their photoluminescence properties in concentrated solutions and in solid-state compounds by reasons of strong  $\pi$ - $\pi$  stacking interactions and high probability of non-radiative energy transfer from excited states<sup>235-237</sup>. Moreover, the limitations

of organic phosphors to use at the operating temperature of LEDs should be also considered due to their low thermal stability and their behavior of temperature-dependent emission<sup>33, 38</sup>. As we have mentioned before, the operating temperature of LEDs can reach the values of 120°C (in the remote phosphor configuration). In order to resolve these problems, several studies have been conducted by encapsulating the organic molecules into the inorganic matrices such as zeolites<sup>238</sup> or molecular sieves<sup>239</sup>, glass (sol-gel matrice)<sup>240, 241</sup>, or Ca-aluminosilicate structure<sup>242</sup>. The inorganic structures have been implicated in prevention to their aggregations and interactions with environment by hampering the aggregated-caused quenching, (ACQ) behavior and reducing the possibility of non-radiative energy transfer. In the next section, we will represent the encapsulation of organic phosphors in organosilane and inorganic-layered double hydroxide (LDH).

**Table 26 Examples of commercial organic phosphors<sup>\*\*\*</sup>**

Dye name	Max. Excitation (nm)	Max. Emission (nm)	Emission color
Alexa 350	346	442	<b>Blue</b>
Aminocoumarin	350	445	
Pacific Blue	416	451	
Marina Blue	362	459	<b>Blue-green</b>
Acridine	362	462	
Coumarin	432	472	<b>Green</b>
BODIPY 493/503	493	503	
Cy2	489	506	
Fluorescein	494	517	<b>Yellow-Green</b>
FITC	490	518	
Alexa 488	495	519	
Oregon Green 488	498	526	
Acridine orange	502	526	
NBD-X	466	535	
Alexa 430	434	541	
Eosin	525	545	<b>Yellow</b>
BODIPY R6G-X	529	547	
Yakima Yellow	531	549	
Alexa 532	532	554	
R6G	524	557	
Alexa 555	555	565	<b>Yellow-Orange</b>
BODIPY 564/570	563	569	
Cy3	550	570	
Alexa 546	556	573	
Rhodamine Red-X	560	580	
DiA	456	590	
Redmond Red	579	595	
ROX	575	602	
Alexa 568	578	603	<b>Orange</b>
Texas Red	596	615	
BODIPY TR-X	588	616	<b>Orange-Red</b>
Alexa 594	590	617	
Rhodamine B	540	625	<b>Red</b>
BODIPY 630/650-X	626	640	
LC Red 640	625	640	
Alexa 647	650	665	
Cy5	649	670	

<sup>\*\*\*</sup> Available online: <https://www.thermofisher.com/fr/fr/home/references/molecular-probes-the-handbook/tables/spectral-characteristics-and-recommended-bandpass-filter-sets-for-molecular-probes-dyes.html>

## **II. Silica encapsulated organic phosphors**

### **A. Introduction**

The chemistry behind the silica encapsulated organic phosphors is a sol-gel reaction. Briefly, the reaction undergoes by the formation of colloidal suspensions of soft particles or clusters in a liquid phase (sol) and subsequently to formation of three-dimensional oxide network filled with a solvent (gel)<sup>243</sup>. The principle of sol-gel reaction is based on two chemical reactions: hydrolysis and condensation (or polymerization) in the presence of acid or base catalysts in order to form glassy or ceramic materials in various forms such as nanoparticle powders, fibers, coating, thin films, monoliths, and porous membranes<sup>244</sup>. The advantages and disadvantages of sol-gel technology are represented as followed<sup>245, 246</sup>:

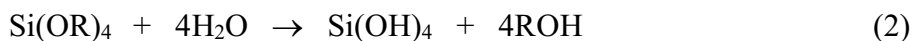
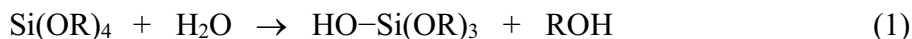
#### **Advantages**

- High purity of products
- Good homogeneity in compositions
- Low-temperature process
- Controllable shapes and designs

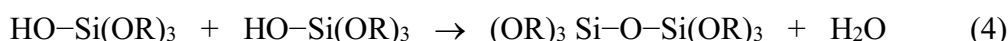
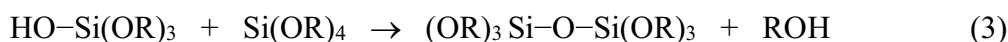
#### **Disadvantages**

- High cost of starting materials
- Easily cracking during drying
- Large volume shrinkage
- Long processing time

The sol-gel reaction is typically starting from liquid metal alkoxides  $M(OR)_4$  as common precursors where M can possibly be Si, Sn, Ti, Zr, Al, etc and R represents as a proton or alkoxide ligand<sup>247</sup>. The reactivity of metal alkoxides strongly depend on the electronegativity of metal center, which can affect the reaction rates of hydrolysis and condensation as well. For silicon alkoxides ( $Si(OR)_4$ ), the hydrolysis reaction occurs by the nucleophilic attack of oxygen in water molecules to Si atoms in the presence of acid or base catalysts to form silanol bonds and give alcohols as by-products.



The alkoxide molecules can be partially (equation 1) or completely (equation 2) hydrolyzed depending on the amount of water and catalysts<sup>247</sup>. In this case, the reaction in equation 2 can occur at low pH and high water concentrations. The hydroxyl alkoxide precursors are the unstable species and can undergo the condensation reaction by combining two (or more) hydroxyl alkoxide precursors and eliminating small molecules such as water or alcohol to form Si–O–Si bonds (equation 3 and 4). The hydrolysis and condensation reaction do not undergo individually but they occur simultaneously during sol-gel reaction<sup>248, 249</sup>. The condensation reaction can also continue to establish larger three-dimensional network by the process of polymerization.



It should be noted that the sol-gel reaction depends on processing parameters such as nature of alkoxide precursors, H<sub>2</sub>O/alkoxide molar ratio, nature and concentration of catalysts, and temperature, which are possible to design the structures and properties of final products<sup>246, 250</sup>.

### a. Silica encapsulated fluorescein molecules

Silica encapsulated organic dyes as a core-shell structure have been studied for entrapping organic dyes due to several advantages. Firstly, the reaction is simple and does not require extreme conditions (i.e. high temperature and pressure, inert atmosphere). Secondly, the silica is a biocompatible and non-toxic substance<sup>251</sup>. Thirdly, the silica matrix as a protective encapsulation can improve the thermal stability and the photostability of chromophores<sup>252, 253</sup>. Two main methods based on sol-gel process for silica coated organic dyes have been reported in the literature by using tetraethoxysilane (TEOS) as silica precursor. The first method is called the Stöber method<sup>254</sup>. The organic dye acts as a seed in the medium containing ethanol, TEOS, and ammonia solution is used for the growth of silica beads. However, the particle size and the size distribution are not well controlled. The second method is a water-in-oil reverse microemulsion<sup>252, 255, 256</sup>. The water-soluble organic dye (like fluorescein or rhodamine) is dissolved in a nanoscale droplet of the aqueous phase from a nonpolar medium and both hydrolysis and condensation of TEOS occur inside the water droplet to form silica beads and

entrap the organic dyes. Importantly, the formation of a reverse micelle is the key to create the template for controlling the shape and size of particles<sup>257</sup>. Since the silica encapsulated organic dyes bring some advantages especially the improvement of thermal and photo-stability, thus it is of interest to achieve hybrid organic-inorganic particles for LEDs applications.

According to the nature of the interface and the interactions between organic compounds and inorganic matrices, the hybrid organic-inorganic materials obtained from sol-gel technologies can be classified in to two classes<sup>258, 259</sup>. Hybrid class I is related to the hybrid systems that involves only weak interactions between organic and inorganic units such as Van der Waals, hydrogen bonding or electrostatic forces. On the other hand, hybrid class II implies the strong chemical interactions (i.e. covalent or coordinative bonds) between two different components, resulting the low phase separation and high homogeneous final products. Considering the nature of organic phosphors, the hybrid class II materials require the organic molecules with suitable functional groups towards functionalization and chemical reaction for incorporation of an organic molecules into sol-gel structures. However, the availability of functionalized organic phosphors, the solubility of organic phosphors in aqueous solution, and the difficulty of proper organic synthesis are sometimes the limitations of the chosen organic phosphors for particular hybrid materials. Hence, the synthesis of hybrid class I materials becomes the point of interest since many choices of organic phosphors are commonly available in the market with high optical properties in the range from UV light to infrared regions. In this study, we started from the studies of a common organic molecule such as fluorescein in order to investigate its optical and photoluminescence properties after encapsulation into silica particles. This point is of interest for the LEDs-based lighting applications at which the organic phosphors can be associated with UV or blue LEDs to produce white light.

Fluorescein is one of the most common organic compounds for biochemical research and health care applications because of its biocompatibility, high molar absorptivity and excellent fluorescence quantum yield<sup>260-262</sup>. These last years, several research groups have demonstrated that the combination of a blue LED combined with fluorescein exhibited high conversion efficiency<sup>94, 95, 263</sup>. However, the fluorescein can be bleached by light exposure, radicals and peroxide species, which lead to chemical destruction and thus the loss of its fluorescent properties<sup>264, 265</sup>. Moreover, the fluorescein is similar to many chromophores in that it exhibits a high fluorescence intensity in solution but not in the solid state due to the aggregation-caused quenching. The theoretical study of dynamic behavior of fluorescein sodium salt in water confirm the good stability and the formation of molecular aggregation of fluorescein<sup>266</sup>.

Moreover, the formation of aggregated-dye molecules in solution was also an evidence in which it modified its absorption spectrum and its photo-physical properties<sup>267-269</sup>. In order to maintain the fluorescence properties in the solid state, the chromophores should be deaggregated as in a dilute state. Therefore, it is necessary to develop the encapsulation of fluorescein in a solid matrix playing the role of solvent in order to retain its characteristic luminescent properties.

In the first section, we will present the synthesis of fluorescein-silica nanoparticles with core-shell structure from a reverse microemulsion method. Their optical and morphological features have been investigated as well as their stabilities under operating conditions of LEDs. After that, the fluorescein-silica nanoparticles exhibiting the best optical performances have been dispersed in silicone resin and combined with a blue LED to perform trials in remote phosphor configuration for white light emission. The photometric parameters of the system such as color temperature and color-rendering index were also determined.



### B. Experimental

#### a. Synthesis of fluorescein doped silica nanoparticles (FC@SiO<sub>2</sub>)

The fluorescein sodium salt was dispersed in silica nanoparticles using water-in-oil microemulsion method using TEOS, Igepal CO-520 and ammonium solution as described in reference<sup>270</sup>. Briefly, 350  $\mu$ L of ammonium solution (19%wt in water) and 75  $\mu$ L of fluorescein solution (concentration between 1-100 mM) in water were added to a mixture of Igepal CO-520 (4.05 g) and cyclohexane (93.3 mL). After 45 minutes of stirring at 25°C, 2.3 mL of TEOS were added and then let under stirring for 24 hours. In order to obtain more spherical, pure and denser silica surface, 470  $\mu$ L of TEOS were added to the mixture and then let under stirring for 24 hours. Then a large excess of acetone was added to the solution in order to precipitate the suspension and then left without stirring for 24 hours. The FC@SiO<sub>2</sub> nanoparticles were centrifuged and subsequently washed with acetone (x3) and absolute ethanol (x1). The nanoparticles were dried at 60°C overnight.

#### b. Preparation of composite films

The mixture was prepared by dispersing FC@SiO<sub>2</sub> nanoparticles in silicone resin/curing agent (Silicone Bluesil RTV 141 A&B). The mixture was mixed using a mechanical mixer to achieve highly homogenous particles/silicone mixture. The FC@SiO<sub>2</sub>/silicone film was prepared by casting onto a Teflon surface using an Elcometer 4340 automatic film applicator. The blade knife height was fixed at 400  $\mu$ m and the casting speed was 20mm/s. Then, the composite film was dried in the oven at 60°C overnight. The film thickness at final was measured using an Elcometer 456 coating thickness gauge.

## C. Results and discussion

### a. Fluorescein sodium salt doped silica nanoparticles (FC@SiO<sub>2</sub>)

Fluorescein sodium salt is a disodium salt of fluorescein which can be noted as a pH sensitive compound (Figure 82)<sup>94,271</sup>. The dianion and monoanion forms are the main fluorescent forms whereas the neutral and cationic forms are non-fluorescent species<sup>269</sup>. Among the different forms of fluorescein in water, the bivalent anion forms (pK<sub>a</sub> ≈ 6.4 in aqueous buffer solution) can present the highest fluorescence intensity. In our work, we attempted to use the bivalent anion forms of fluorescein by maintaining the pH higher than 9.

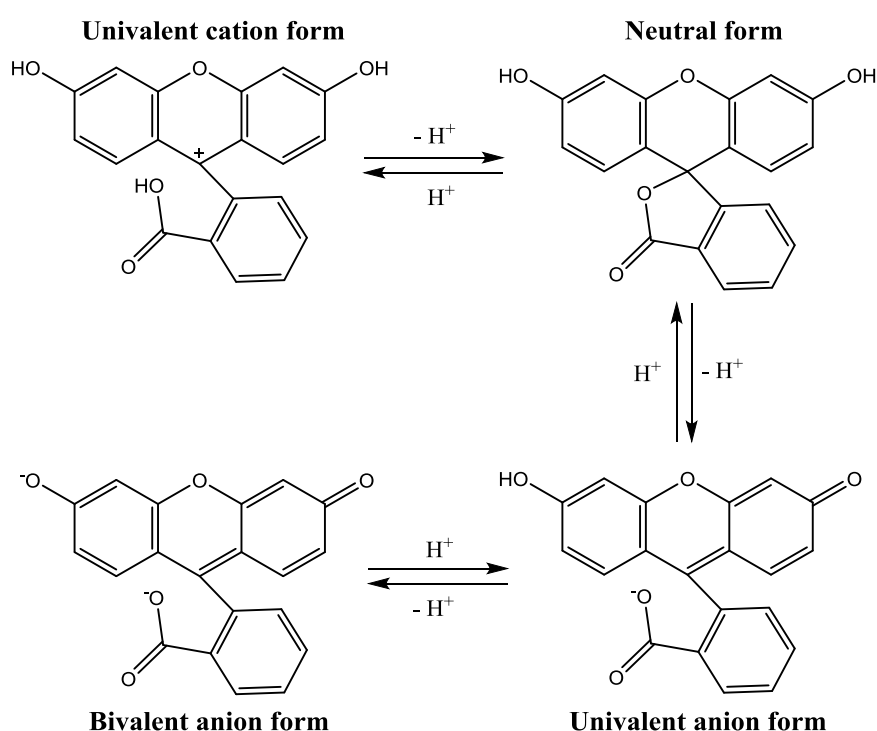


**Figure 82** Chemical structure of fluorescein molecule at various pH.

As described before, the core-shell fluorescein-silica nanoparticles (FC@SiO<sub>2</sub>) were prepared using water-in-oil (W/O) microemulsion method. The formation process of FC@SiO<sub>2</sub> nanoparticles via reverse microemulsion is shown in the schematic diagram (Figure 83).

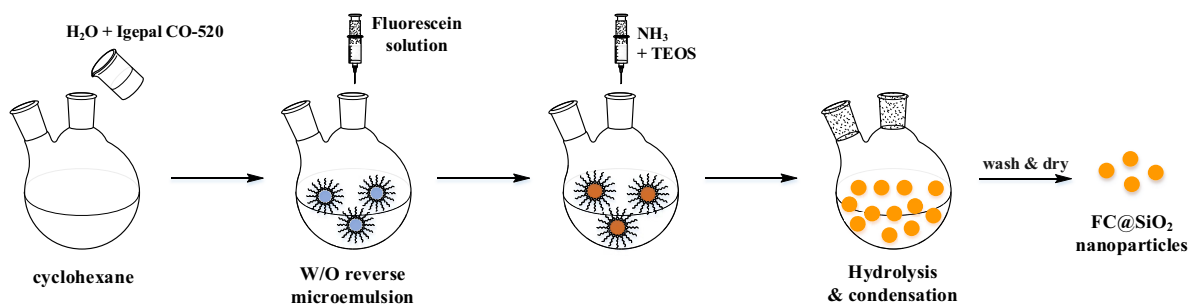


**Figure 83 Schematic diagram for the formation of FC@SiO<sub>2</sub> nanoparticles from a reverse microemulsion via hydrolysis and condensation.**

The FC@SiO<sub>2</sub> nanoparticles were prepared using Igepal CO-520 as a neutral surfactant in the reverse microemulsion system. The concentration of surfactant was maintained much greater than its critical micellar concentration (CMC  $\approx$ 25mM)<sup>272</sup> in order to ensure the formation of reverse micelle within the medium. The second step refers to the hydrolysis and the condensation of TEOS initiated by the presence of ammonium solution in the mixture. The TEOS in the third step was used for further capping of the produced spherical nanoparticles in order to obtain a denser silica surface and improve photostability of the organic dye molecules<sup>252, 273, 274</sup>. The drying process (60°C overnight) at the end was applied to densify the silica network. Several reports indicated that the tuning of optical characteristics of organic dyes can be performed by changing the concentration of organic dye<sup>275, 276</sup>. Thus, the optimal concentration of fluorescein for synthesizing the FC@SiO<sub>2</sub> nanoparticles should be determined. In our study, we have synthesized the nanoparticles based on silica embedded with different concentrations of fluorescein sodium salt (Table 27).

**Table 27 Optical characteristics of FC@SiO<sub>2</sub> nanoparticles.**

Sample	[fluorescein] added to W/O system (mM)	$\lambda_{\max}$ emission (nm)	PLQY <sub>abs</sub> (%)
A	1	528	14
B	4	534	22
C	10	537	29
D	22	536	20
E	53	537	14
F	100	536	3

The FT-IR spectra of FC@SiO<sub>2</sub> nanoparticles, SiO<sub>2</sub> nanoparticles, and fluorescein sodium salt powder are represented in the Figure 84. In the IR spectrum of SiO<sub>2</sub> nanoparticles, the absorption peaks at 3600-2500 and 1633 cm<sup>-1</sup> are attributed to the stretching vibration and the bending vibration of O-H silanol groups, respectively. The absorption peaks at 1082, 797, and 465 cm<sup>-1</sup> are ascribed to the bending vibration of Si-O-Si bonds. Similar characteristic vibration bands were observed for FC@SiO<sub>2</sub> nanoparticles. This result seems to be a good evidence that fluorescein molecules were embedded into SiO<sub>2</sub> matrix.

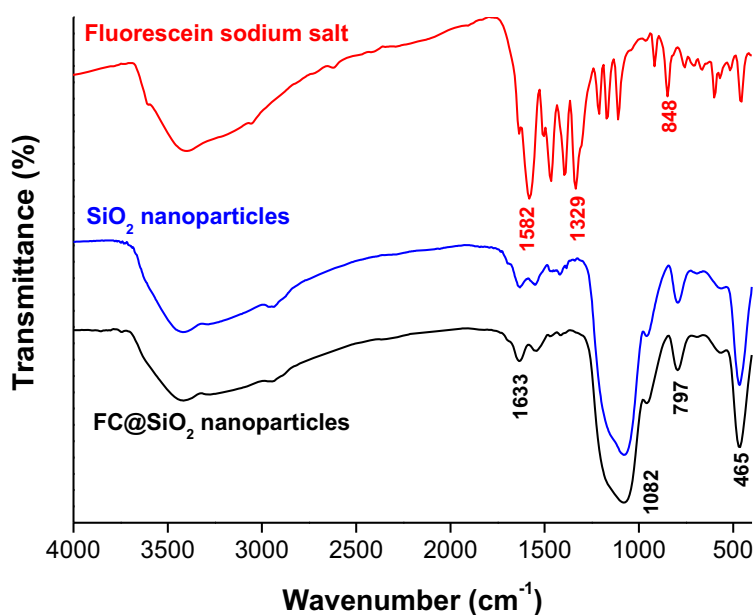


**Figure 84** FT-IR spectra of FC@SiO<sub>2</sub> nanoparticles and fluorescein sodium salt powder.

TEM microscopy was performed on selected FC@SiO<sub>2</sub> nanoparticles. The TEM images of FC@SiO<sub>2</sub> nanoparticles prepared at different concentrations of fluorescein are shown in Figure 85. From the TEM images, it should be noted that the FC@SiO<sub>2</sub> nanoparticles (with hydrophilic surface) tend to be aggregated by cause of the hydrophobic property of carbon grid. The morphologies of FC@SiO<sub>2</sub> nanoparticles showed that they are spherical in shape. It has been found that the concentration of fluorescein affects the size of the final nanoparticles. As shown in Figure 85, the size of the FC@SiO<sub>2</sub> nanoparticles increased with increasing the concentration of fluorescein. The particle size increased from 54.4 ± 2.1 nm for sample A to 68.9 ± 3.5 nm for sample F.

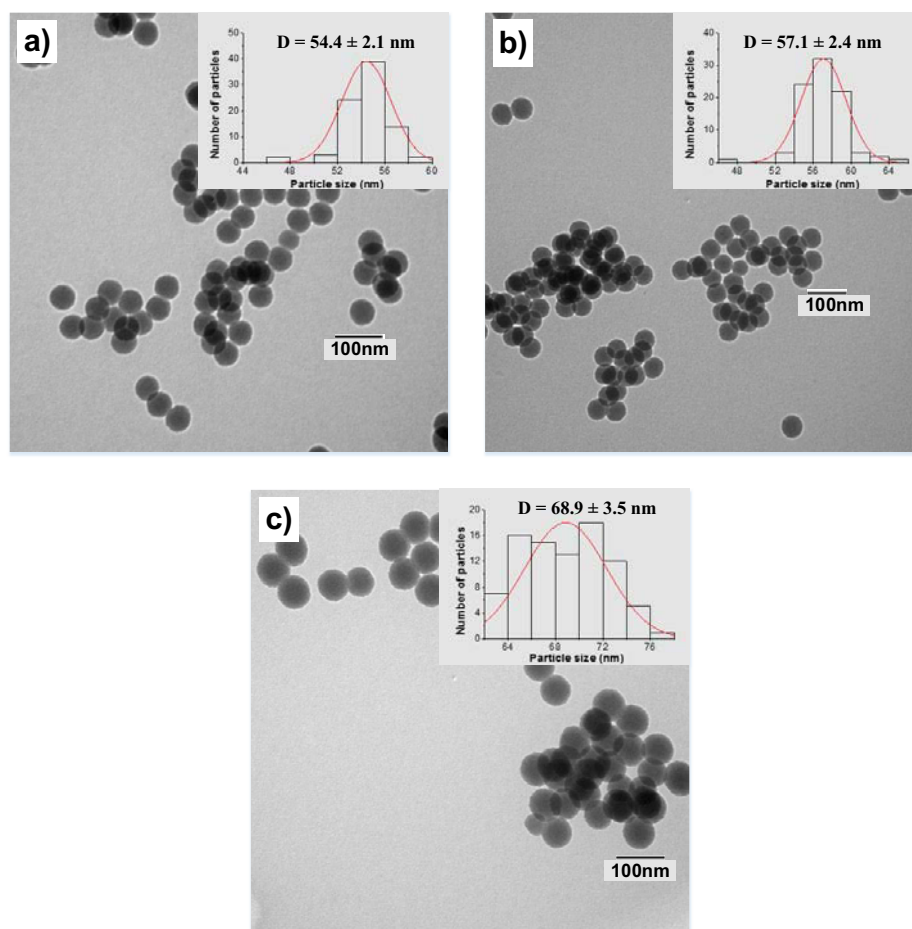


**Figure 85** TEM images and the corresponding particle size distribution of the FC@SiO<sub>2</sub> nanoparticles with the different concentrations of fluorescein in W/O system:  
a) sample A, b) sample C, and c) sample F.

The thermogravimetric analysis (TGA) and the differential thermogravimetric (DTG) curves of FC@SiO<sub>2</sub> nanoparticles were recorded in order to study their thermal stability (Figure 86). The TGA curve of FC@SiO<sub>2</sub> nanoparticles shows that the decomposition occurred in two steps and leaves the residue at 800°C with the weight loss of 3.6 wt. %. The small weight loss at the beginning to around 100°C was explained by desorption of absorbed water from the SiO<sub>2</sub> surface. The FC@SiO<sub>2</sub> nanoparticles were thermally stable up to 280°C. Then, the weight loss with respect to the increase in the temperature was observed in the range of 280-500°C, corresponding to 2 wt. % of weight loss. After that, the FC@SiO<sub>2</sub> nanoparticles were thermally stable up to 800°C. Similar result was observed for SiO<sub>2</sub> nanoparticles. Compared to FC@SiO<sub>2</sub> nanoparticles, the large weight loss phenomena of fluorescein powder were observed from 500°C, indicating fluorescein powder was thermally unstable at high temperature. Therefore, the fluorescein embedded into silica nanoparticles can enhance the thermal stability compared to fluorescein powder.

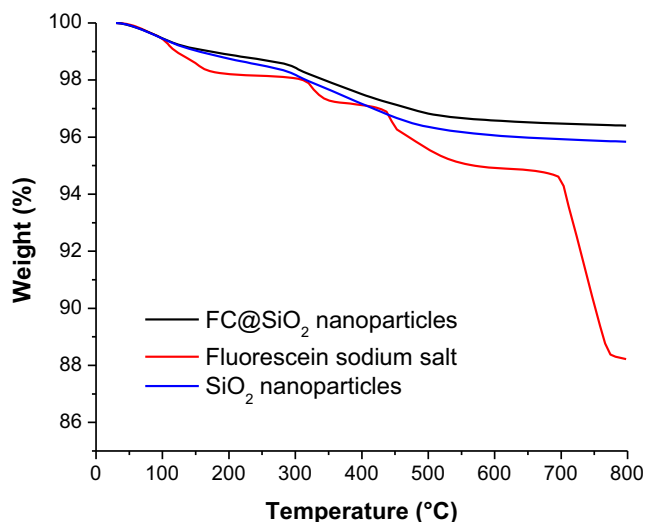


Figure 86 TGA plots of FC@SiO<sub>2</sub> nanoparticles, SiO<sub>2</sub> nanoparticles, and fluorescein sodium salt powder.

Figure 87 illustrates the absolute quantum yield and the fluorescence spectra of FC@SiO<sub>2</sub> nanoparticles with different concentration of fluorescein (sample A to F) upon continuous excitation at 450 nm. When the concentration are increased from 1 to 10 mM, the fluorescence intensity increases with a slightly red shift ( $\approx 8$  nm). After 10 mM, the fluorescence intensity decreased gradually with no any change in bathochromic shift. The maximum fluorescence intensity was observed for sample C and its absolute quantum yield efficiency reached the maximum value at about 29%.

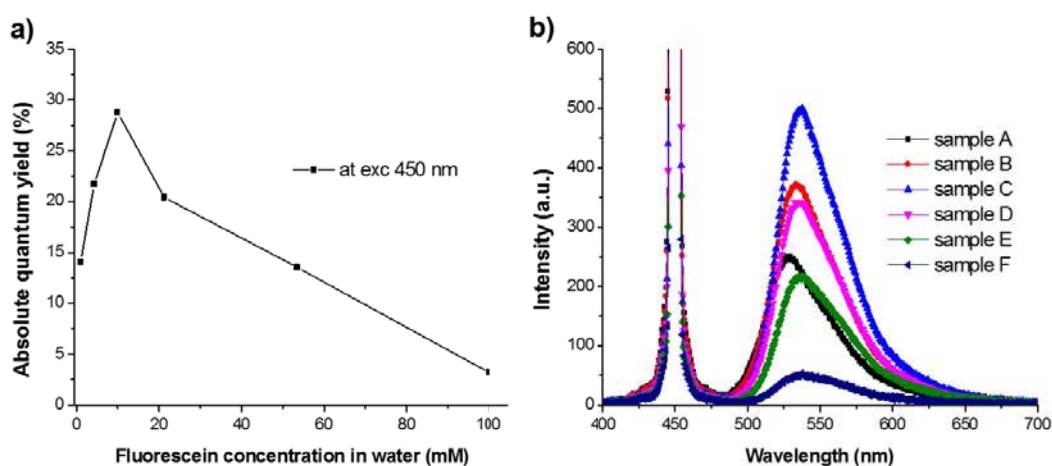
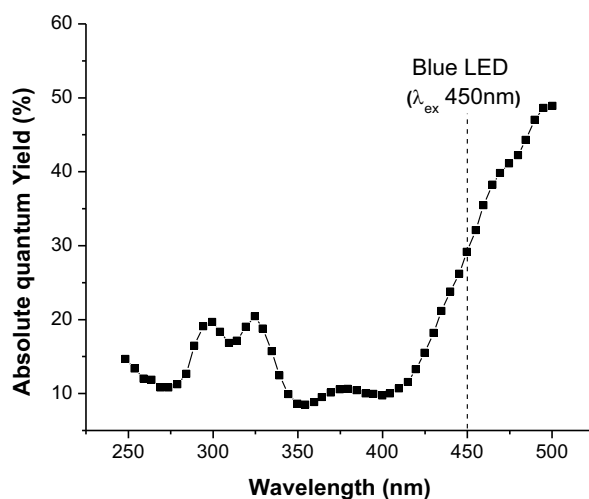


Figure 87 Concentration dependent of FC@SiO<sub>2</sub> nanoparticles of (a) absolute quantum yield and (b) PL emission spectra.

At low concentration of fluorescein, the increase in fluorescence intensity might be due to increasing the dianion forms in the mixture. The slight red-shifted fluorescence of FC@SiO<sub>2</sub> nanoparticles at low concentration are probably due to the formation of hydrogen bonds

between fluorescein molecules and their environments<sup>269, 277-279</sup>. However, the decrease in fluorescence intensity for high concentration of fluorescein arises from the self-quenching limit. This phenomenon of self-quenching could be due to an higher probability of energy transfer between neighbor fluorescein molecules<sup>280</sup>.

The absolute quantum yield efficiency of sample C was recorded by exciting the nanoparticle powders from 250 to 500 nm (Figure 88). The maximum intensity are observed above 450 nm. At the operated wavelength of 450 nm blue light LED, the absolute quantum yield was measured at about 29% (see Figure 87a). However, several reports indicate that the tuning of optical characteristics of organic dyes can be performed by changing the concentration of organic dye<sup>275, 276</sup>. Thus, the optimal concentration of fluorescein for synthesizing the FC@SiO<sub>2</sub> nanoparticles should be determined.



**Figure 88** The absolute quantum yield efficiency of FC@SiO<sub>2</sub> nanoparticles (prepared from 10mM fluorescein solution) presented between 250-500 nm light illuminations.

Figure 89a shows the temperature-dependent fluorescence intensity of FC@SiO<sub>2</sub> nanoparticles (sample C) and fluorescein sodium salt powder measured in 1 cycle upon continuous excitation at 450 nm. With alternating temperature from room temperature to 60°C and vice versa, the fluorescence intensity of both products becomes quite stable during the acquisition. Figure 89b presents the time-dependent fluorescence intensity of FC@SiO<sub>2</sub> nanoparticles (sample C) and fluorescein sodium salt powder upon continuous excitation at 450 nm and at temperature of 60°C. The fluorescence intensity of both products decreases slightly with increasing time from 0 to 4 hours. Our results confirm that FC@SiO<sub>2</sub> nanoparticles have a good stability at the operating temperature of remote-type phosphor around 60°C<sup>41, 204</sup>. Interestingly, the FC@SiO<sub>2</sub> nanoparticles exhibit a high green emission while the light emission observed from the

fluorescein powder is very weak. Thus, the role of silica shell can improve not only the thermal stability, but also the optical characteristics of fluorescein in solid-state.

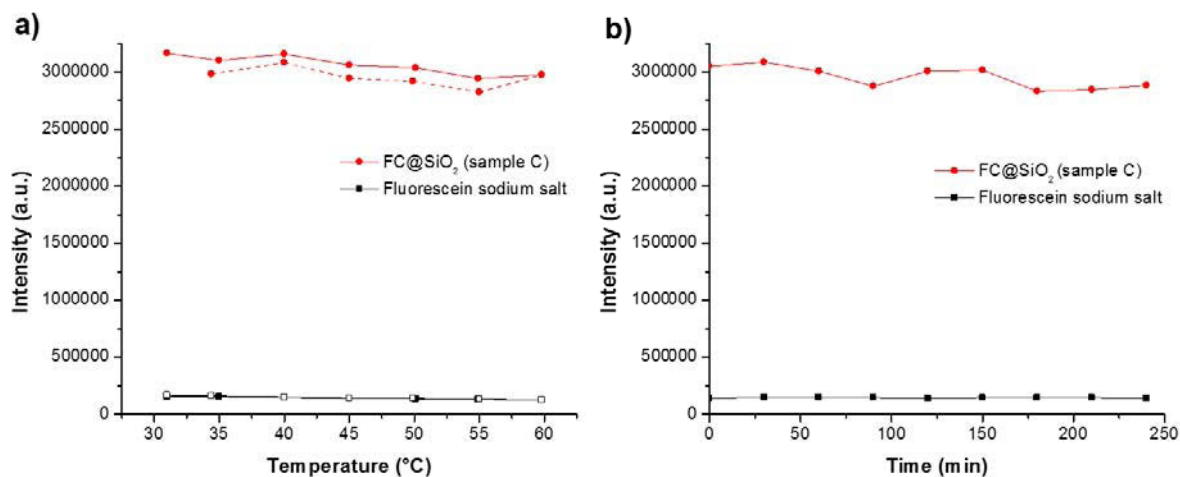


**Figure 89** a) Temperature-dependent measured in 1 cycle and b) time-dependent fluorescence intensity of FC@SiO<sub>2</sub> nanoparticles (sample C) and fluorescein sodium salt.

### b. Silica encapsulated other organic phosphors

In addition to fluorescein disodium salt, other commercial water-soluble organic phosphors were also studied for encapsulating into the silica matrices such as ATTO465, ATTO490LS or rhodamine 6g. These organic phosphors were selected due to their high emission and good quantum yield (QY) in dilute solution (Table 28). Table 29 represents silica nanoparticles of several water-soluble organic phosphors with their photoluminescence properties under 450 nm blue-light excitations.



**Table 28 Optical characteristics of commercial organic phosphors in dilute solution.**

Name	$\lambda_{\max}$ emission (nm)	PLQY <sub>abs</sub> (%)	Conditions for QY measurement	Remark
ATTO465	516	30	Aqueous solution, 1 mM, $\lambda_{\text{exc}} = 450$ nm	Commercial dye from ATTO-TEC GmbH, Germany
ATTO490LS	659	29	Aqueous solution, 3 mM, $\lambda_{\text{exc}} = 450$ nm	Commercial dye from ATTO-TEC GmbH, Germany
Rhodamine 6g	552	92	Aqueous solution, $\lambda_{\text{exc}} = 530$ nm	For more info: ref <sup>281</sup>

**Table 29 Optical characteristics of commercial organic phosphors encapsulated into silica nanoparticles.**

	Name	Concentration added to W/O system (mM)	$\lambda_{\max}$ emission (nm)	PLQY <sub>abs</sub> at 450 nm (%)
Np-I	ATTO465@SiO <sub>2</sub> nanoparticles	≈ 4	496	11.4
Np-II	ATTO490LS@SiO <sub>2</sub> nanoparticles	≈ 4	551	15.1
Np-III	Rhodamine 6g@SiO <sub>2</sub> nanoparticles	100	585	2.9

Likewise the synthesis of fluorescein encapsulated into silica nanoparticles, these organic phosphors-silica nanoparticles (Np-I for ATTO465, Np-II for ATTO490LS, and Np-III for rhodamine 6g) were also prepared by the same procedures. Figure 90 shows their PL emission spectra under excitation at 450 nm. The silica nanoparticles of both ATTO465 and ATTO490LS exhibited a good emission intensity with the maximum emission located at 496 and 551 nm, respectively. However, the silica nanoparticles of Rhodamine 6g gave very weak photoluminescence properties under 450 nm excitation. Accordingly, the silica encapsulated other organic phosphors present the possibility for the creation of silica nanoparticles by using a numerous number of commercial organic products. However, the synthetic conditions (i.e. concentration of organic phosphors and pH) must be optimized in order to reach the maximum values in photoluminescence properties compared with the FC@SiO<sub>2</sub> nanoparticles.

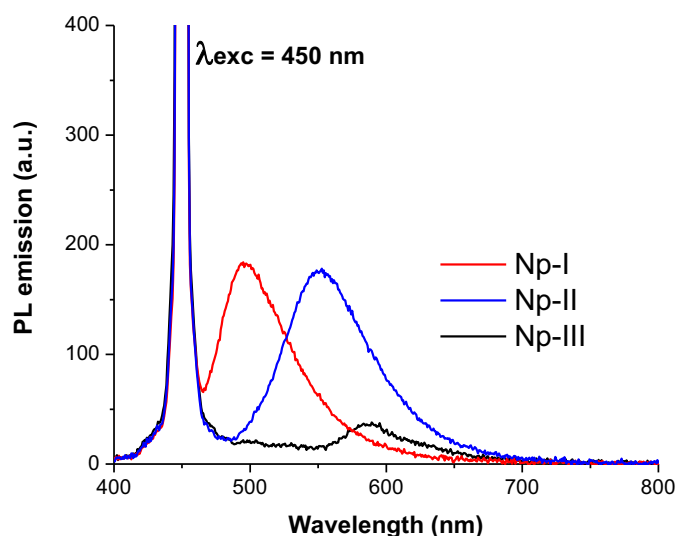


**Figure 90** PL emission spectra of commercial organic phosphors encapsulated into silica nanoparticles upon 450 nm blue-light illumination.

### c. FC@SiO<sub>2</sub> composite film

The FC@SiO<sub>2</sub> nanoparticles (sample C) having the highest absolute quantum yield were dispersed in a silicone resin in order to prepare the composite films. The composite films obtained have a thickness between 50-150 μm, depending on the percentage of FC@SiO<sub>2</sub> nanoparticles dispersed in the silicone.

At low percentage of FC@SiO<sub>2</sub> nanoparticles (5 wt. %), the emission light recorded was almost blue due to weak concentration of fluorescein to convert the photons coming out from the blue LED. On the other hand, if the percentage of FC@SiO<sub>2</sub> nanoparticles was too high (>15 wt. %), the composite films could not be hardened after solvent evaporation due to excessive quantities of nanoparticles compared to the silicone resin. Thus, the percentages of FC@SiO<sub>2</sub> nanoparticles dispersed in the silicone resin was fixed at 15 wt. % for further studies of composite films. Figure 91 shows the UV-visible absorption and the Fourier transform infrared (FTIR) spectra of FC@SiO<sub>2</sub> composite film and pure silicone film. The absorption bands of FC@SiO<sub>2</sub> embedded in the film were observed in the range of 200-300 nm and around 500 nm. The first absorption peak at 210 nm was attributed to the characteristic absorption band of Si-O-Si bond in silica nanoparticles as also reported in the literature<sup>282</sup>. The absorption peaks at 230 and 286 nm corresponds to the absorption values of fluorescein in aqueous solution<sup>283, 284</sup>. As with the previous mention in Chapter 2, the small absorption peak observed at about 263 nm in neat silicone film was probably the absorption of residual stabilizer (i.e. antioxidant or

UV absorber) in silicone resin film. The FTIR spectra of both samples exhibit the same vibrational characteristics as silicone, which is the major component in the composite film.

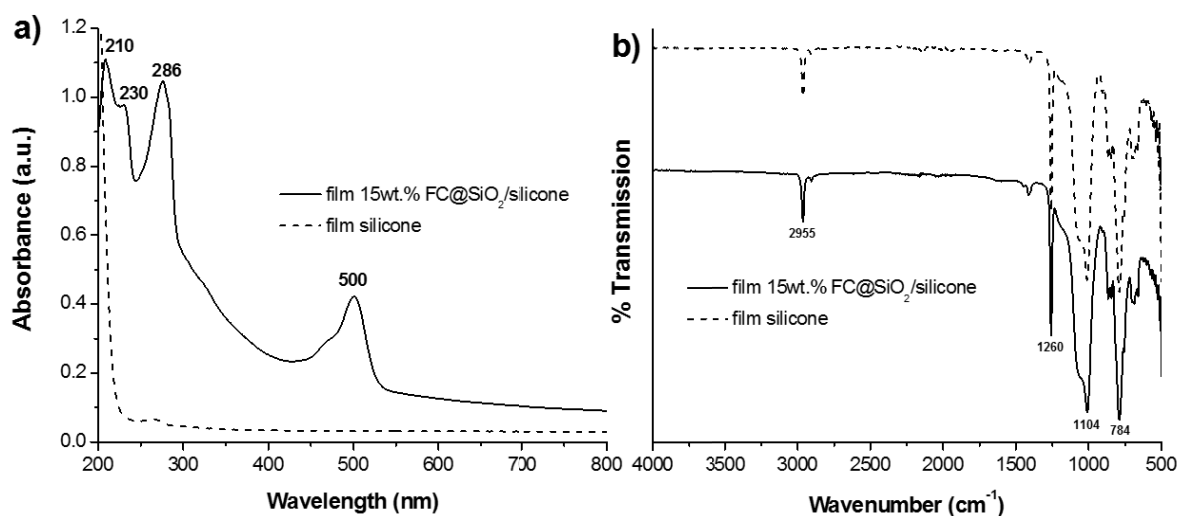


**Figure 91 a) UV-visible and b) FTIR spectra of both FC@SiO<sub>2</sub>-silicone composite film and pure silicone film.**

Figure 92 shows the cross-section of FC@SiO<sub>2</sub> composite films with different FC@SiO<sub>2</sub> nanoparticles contents. At 10 wt. % of nanoparticles, SEM images present a smooth surface of composite film with good dispersion of nanoparticles in the composite film. However, when nanoparticles loading reaches 15 wt. %, the modification of surface morphology can be observed with increasing the surface roughness of composite film. The absolute quantum yield of FC@SiO<sub>2</sub> nanoparticles in composite films were observed at about 19% and 26% for 10 wt. % and 15 wt. % of FC@SiO<sub>2</sub> nanoparticle powder in composite films, respectively. This absolute quantum yield was slightly less than the value of FC@SiO<sub>2</sub> nanoparticles recorded previously (about 29%).

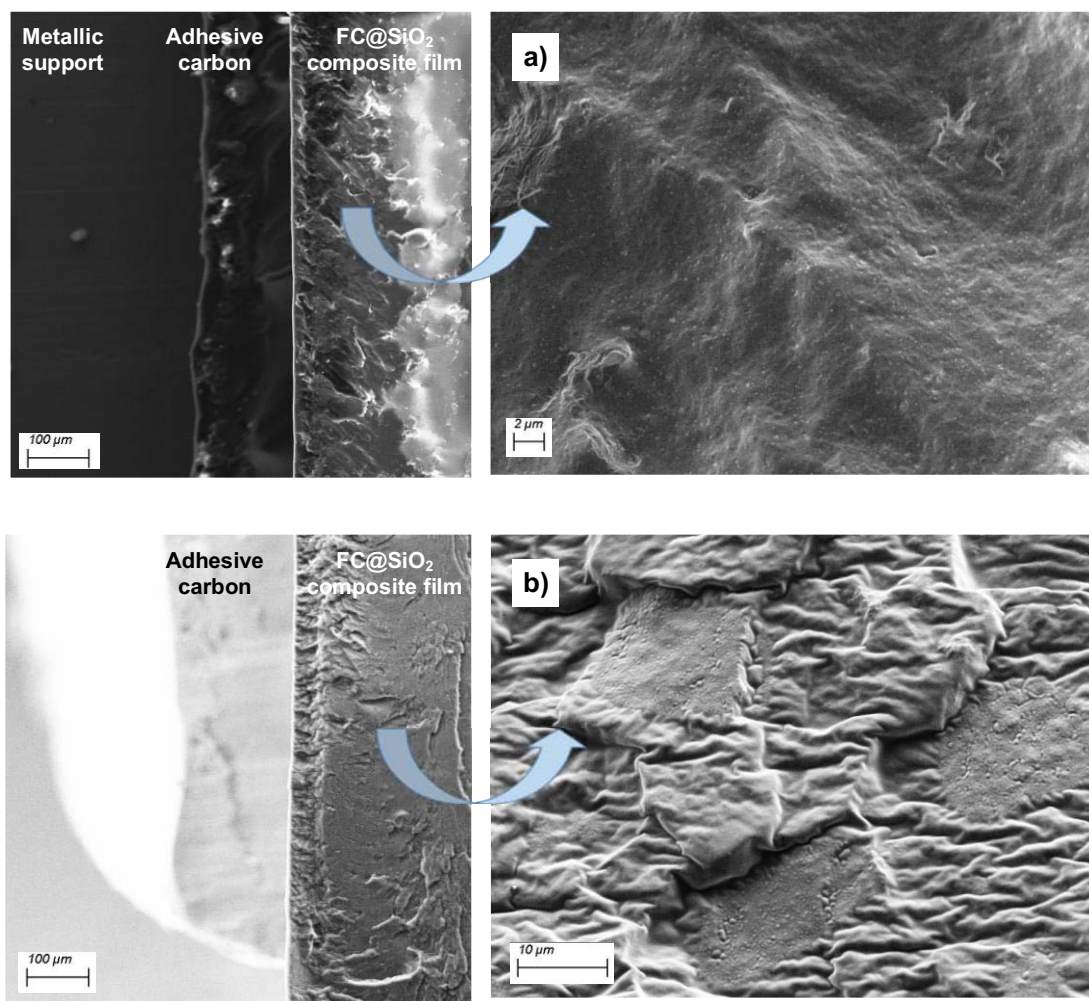


**Figure 92** SEM images of cross-section of a) 10 wt. % FC@SiO<sub>2</sub> and b) 15% FC@SiO<sub>2</sub>-silicone composite films.

A simple demonstration of FC@SiO<sub>2</sub> (15 wt. %-V)-silicone combined with LEDs was fabricated as a remote phosphor configuration, using the selected FC@SiO<sub>2</sub> nanoparticles dispersed in silicone and a 450 nm commercial blue LED. The color point of composite films is defined according to the convention of the Commission Internationale de l'Eclairage (CIE) in a normalized two-dimensional color coordinate system. Figure 93 shows the emission spectra and CIE chromaticity diagram for the FC@SiO<sub>2</sub>-silicone (15 wt. %-V)/LED system. The different thicknesses of composite films were integrated with the 450 nm blue LED at 3.2V and 500 mA (Table 30). The results showed the CIE color coordinates of (0.236, 0.288), CCT of 17539 K and CRI of 59, which are still too far away from the values of commercial YAG: Ce<sup>3+</sup> converted white LEDs<sup>285</sup>. With increasing film thickness, less blue light from LED was detected (a peak at about 450 nm) with slightly change in emission intensity at about 530 nm. The luminous efficacy was increased from 11.4 to 18.7 lm/W, when the thickness of composite film was increased. On the other hand, the color temperature and the color rendering index

were decreased as the thickness increased (CCT from 17539K to 6570K, CRI from 59 to 43.3, respectively) as described in Table 30.

**Table 30 The CIE color coordinates (x,y), color temperature (CCT), color rendering index (IRC), luminous flux (Y2), and luminous efficacy of an FC@SiO<sub>2</sub>-silicone hybrid LED under 450 nm blue light illumination.**

	Thickness	CIE1931 result					LED power		Luminous Efficacy (lm/W)
		x	y	Y2 (lumen)	CCT (K)	CRI (0-100)	Current (A)	Voltage (V)	
15% wt. FC@SiO <sub>2</sub> + 85 wt.% silicone + 450 nm LED	<i>IV</i> (67 μm)	0.2359	0.2875	18.24	17539	59.0	0.5	3.2	11.4
	<i>V</i> (135 μm)	0.2963	0.4322	29.98	6570	43.3	0.5	3.2	18.7

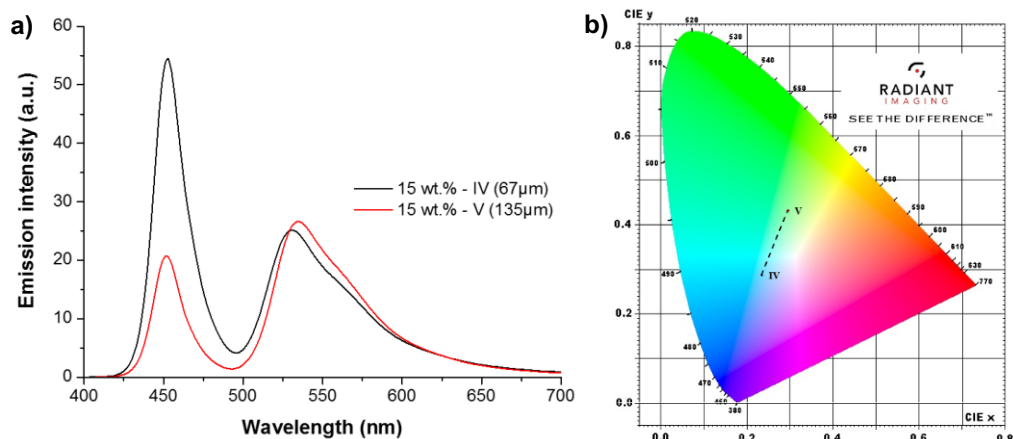


**Figure 93 a) Emission spectra and b) CIE chromaticity diagram measured for FC@SiO<sub>2</sub>-silicone/LED system, prepared using a blue LED (450nm) and 15 wt. % of FC@SiO<sub>2</sub> nanoparticles embedded in silicone.**

The color parameters can be also tuned by adjusting the forward current between 100 to 600 mA. Figure 94 shows the emission spectra of FC@SiO<sub>2</sub>-silicone/LED system (for 15 wt. %-V) at various forward currents from 100 to 600 mA.

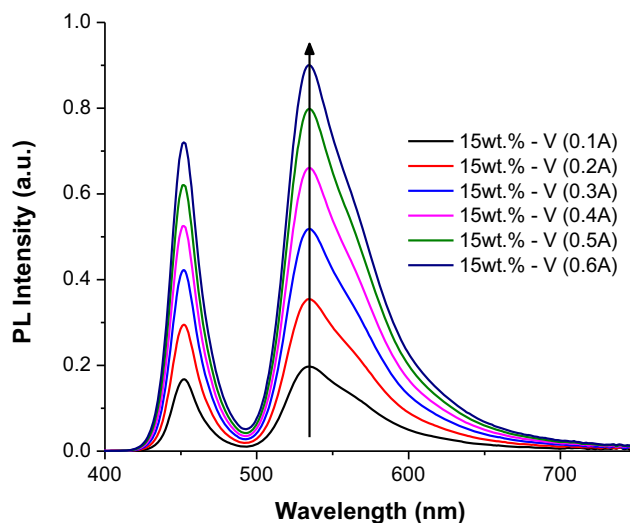


**Figure 94 Emission spectra of FC@SiO<sub>2</sub>-silicone hybrid LED (for 15 wt. %-V) at various forward currents from 100-500 mA.**

As shown in Figure 94, the emission intensity raised when the forward current was increased from 100 to 600 mA, indicating that the composite films present no saturation. However, the CIE color coordinates and color rendering index (CRI) value present a slightly change with increasing forward current (Figure 95). The correlated color temperatures (CCT) were found between 6570-6650 K related to the change in CIE color coordinates of  $x = 0.2946-0.2963$  and  $y = 0.4278-0.4322$ . The CRI values fluctuated in the range of 43.3-44.0 when the forward current increased from 100 to 600 mA, corresponding to a variation of 2%, as shown in Figure 95. However, the luminous efficacy dropped significantly from 26.6 lm/W to 17.7 lm/W when the forward current was increased. The distances from the Planckian locus on the CIE color coordinates ( $D_{uv}$ ) for the FC@SiO<sub>2</sub>-silicone (15 wt. %-V)/LED system were found from +0.0533 to +0.0542, which were higher than the accepted value of 0.0054 from the Planckian locus indicating that white-light emission produced by FC@SiO<sub>2</sub>-silicone composite films based LED was still far from a true white light system<sup>210</sup>. These results evidence that the FC@SiO<sub>2</sub>-silicone/LED system still lack the good stability against the increase in forward current, which need more researches to fulfil and overcome these problems for better performances for lighting applications.

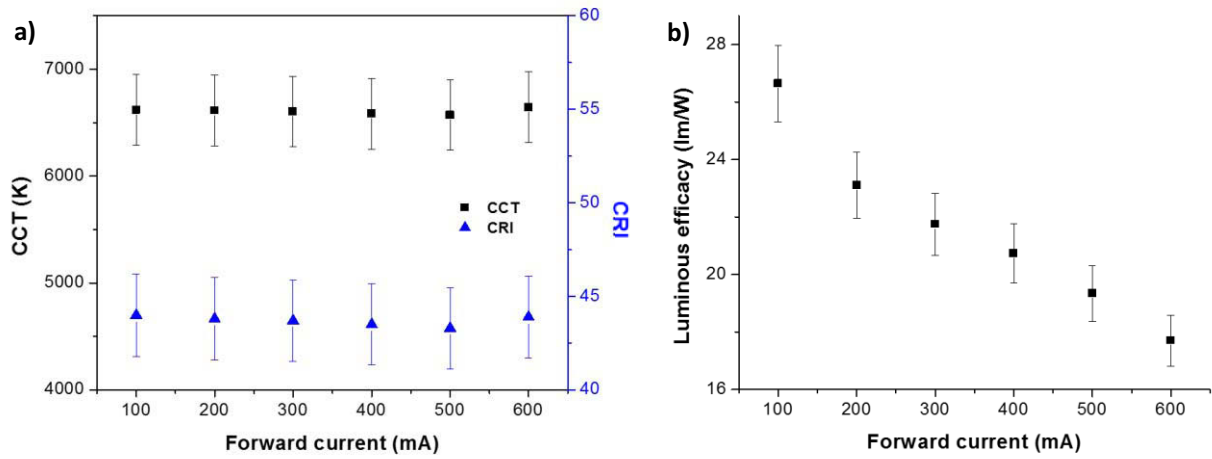


Figure 95 Evolution of (a) CCT and CRI and (b) luminous efficacy of FC@SiO<sub>2</sub>-silicone composite film base (for 15 wt. %-V) at various forward currents from 100-600 mA.

### III. Organic-inorganic hybrid-layered double hydroxides

#### A. Introduction

Layered double hydroxides (LDH) are known as lamellar materials or anion clay minerals with general formula of  $[M_x^{II}M_{1-x}^{III}(\text{OH})_2]^{x+} [A_{x/m}^{m-}]^{x-}, n\text{H}_2\text{O}$ , where  $M^{II}$  is divalent metals ( $\text{Mg}^{2+}$ ,  $\text{Ca}^{2+}$ ,  $\text{Zn}^{2+}$ ,  $\text{Co}^{2+}$ ,  $\text{Cu}^{2+}$ , etc),  $M^{III}$  is trivalent metals ( $\text{Al}^{3+}$ ,  $\text{Cr}^{3+}$ ,  $\text{Co}^{3+}$ ,  $\text{Fe}^{3+}$ ,  $\text{Mn}^{3+}$ , etc) and A is an counter anion ( $\text{SO}_4^{2-}$ ,  $\text{CO}_3^{2-}$ ,  $\text{Cl}^-$ ,  $\text{NO}_3^-$ ,  $\text{PO}_4^{3-}$ , etc) located at the interlayer space<sup>286</sup>. The LDH structures are also known as brucite-like layers built from edge-sharing  $\text{M}(\text{OH})_6$  octahedra<sup>287</sup>. The intra-layer part presents a net uniformly positive charge at an entire layer due to partial substitution of divalent metals ( $M^{II}$ ) by trivalent metals ( $M^{III}$ )<sup>287</sup>. The presence of positive charge on intra-layer part will balance out its charge by the anions in the interlayer space along with water molecules<sup>287</sup>. The schematic of LDH structure is given in Figure 96<sup>288</sup>.

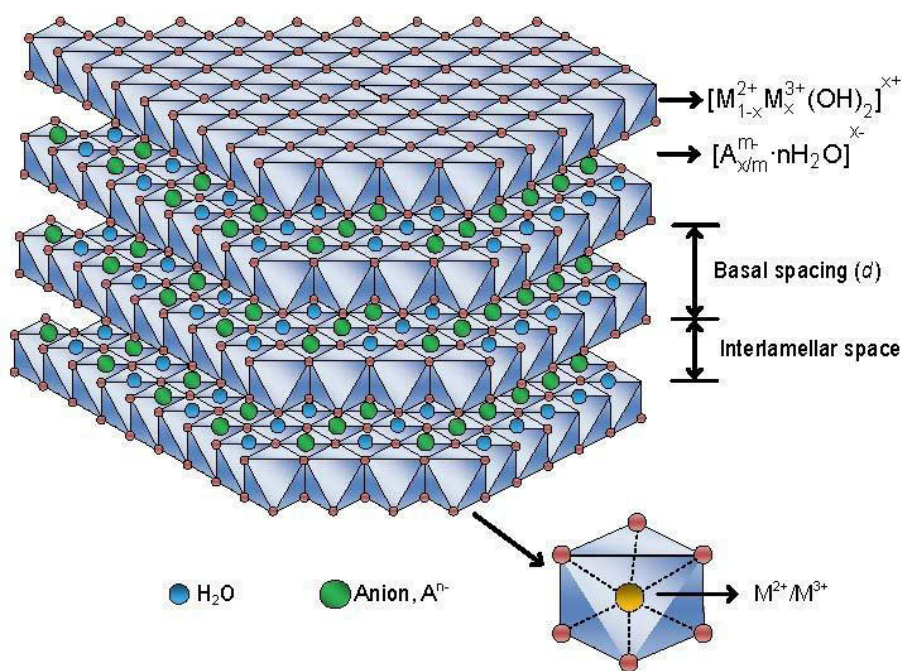


Figure 96 Schematic of LDH structure<sup>288</sup>.

The LDH structures are of interest in many field of applications such as catalysts<sup>289, 290</sup>, anionic pollutant trapping<sup>291, 292</sup>, drug delivery system for pharmaceuticals<sup>293, 294</sup>, fire retardant<sup>295</sup>, and filler in polymer composites<sup>287</sup> by reasons of their great advantages as tunable chemical compositions of LDHs, high purity inorganic compounds, and non-toxicity materials. Moreover, the LDHs represent the possibility to use tons of organic anionic species due to their



high reactivity of ion exchange towards various organic anions (about 80-100%), resulting the adjustment of interlayer distance (Basal spacing) in the LDH matrix<sup>296</sup>.

As the organic-inorganic LDH materials are generated from organic molecules and inorganic LDH matrix, they can also combine the physical and chemical properties of each component to the new materials as well. Organic molecules are responsible for the high absorption coefficient in the range of UV-visible light region and sometimes high optical properties under light excitations whereas inorganic LDH matrix takes a responsible for enhancement of thermal stability and hindrance of organic phosphors aggregation. For organic phosphors with ACQ effect, the dispersion of organic molecules in the LDH matrix by intercalation can de-aggregated the molecules as in a dilute solution, which could maintain their good photoluminescence properties in solid state. Furthermore, the presence of organic molecules intercalated into LDH structure can reduce the permeability of oxygen, which is the main factor influencing the photo-degradation<sup>211</sup>.

The use of LDHs with organic molecules have been published by many research groups. The organic molecules as azo dyes<sup>297</sup>, xanthene dyes<sup>298</sup>, perylene<sup>299</sup> and pyrene<sup>300</sup> derivatives, and functionalized polyaromatic compounds<sup>301, 302</sup> were such the examples of organic phosphors that can be intercalated into LDH structures. The organic molecules are immobilized in their LDH structure by weak interactions such as electrostatic, Van der Waals or hydrogen bonding. However, it should be noted that the choice of organic molecules is very important in order to ensure compatibility with the LDH matrix. The criteria of organic molecules for intercalation into LDH matrix should be considered:

- Presenting the net negative charges in order to have molecular interactions with positively charged LDH structure,
- Being soluble in the reaction medium (usually water or ethanol),
- Being stable at high pH (pH  $\approx$  8-10) at which the formation of LDH matrix is favored.

As with the published study of organic molecules intercalated into LDHs, the organic phosphors have been also reported to intercalate in the LDH structures. Fernando Júnior Quites and collaborators presented the successfully materials made of pyrene derivative dyes intercalation into zinc hydroxide-layered showing the improvement of photoluminescence quantum yield (13%) compared with pure dye solid (1%)<sup>303</sup>. The research group of Chanchal Chakraborty reported the intercalation of perylenediimide dye into LDH matrices that the new

materials can enhance both thermal stability and photostability of perylenediimide molecules<sup>304</sup>. However, there are few publications that developed luminescent organic-inorganic LDH materials for LED white light. Recently, Hong Chen and collaborators have published the organic-inorganic materials based on red, blue and green-emitting metal complexes into Mg<sub>2</sub>Al-LDH matrix which presented a good compromise closer to pure white light emission at (0.346, 0.339) under 370 nm excitation<sup>305</sup>. However, there was no evidence about its photoluminescence properties (i.e. emission intensity, color rendering index or photoluminescence quantum yield) to evaluate the light performance under operating conditions of LEDs.

In this section, a commercial organic phosphor fluorescein disodium salt was incorporated into Mg-Al-LDH matrix as hybrid materials for lighting applications based on LEDs. This work was performed in collaboration with the research group of Doctor Fabrice Leroux (LDH group, Institut de Chimie de Clermont-Ferrand, France). Magnesium-aluminium based LDH (Mg-Al-LDH) represents a hydrotalcite-like layered structure consisting of positively charged on intra-layer part with water and charge-compensating anions in the interlayer part as already mentioned in the section. The magnesium-aluminium based LDH (Mg-Al-LDH) matrix has been chosen for intercalation of organic phosphors (fluorescein) because of its typical metal hydroxide-like layered chemistry and conventional clay-like layered crystalline structure. Moreover, Mg-Al-LDH structure presents an interesting behavior called “memory effect” which can spontaneously regenerate its lamellar structure by intercalation of anions when the Mg-Al-LDH system is in aqueous solution with counter anions<sup>306, 307</sup>. This effect is a great advantage for the incorporation of different anions in the LDH structure. The morphological and optical properties of organic-inorganic LDHs will be discussed in this section. However, it should be noted that this work was similar to the published study by Umberto Costantino and his collaborators<sup>298</sup> in term of intercalation of fluorescein into LDH matrix.

### B. Experimental

There are several methods to synthesize LDH matrix. In this work, we selected a classical method called co-precipitation<sup>308</sup>, which is a common chemical reaction for synthesis of LDH matrix involving co-precipitation of metal ions in aqueous solution with a dilute solution of NaOH or NaHCO<sub>3</sub> or Na<sub>2</sub>CO<sub>3</sub> or NH<sub>4</sub>OH. The pH of the reaction medium is adjusted and maintained between 8 and 10, depending on the nature of the metal ions. The advantage of co-precipitation method is that the chemical composition (M<sup>II</sup>/M<sup>III</sup>) of hydroxide layers will be carefully controlled, resulting the well-controlled morphologies<sup>309</sup>.

#### a. Synthesis of fluorescein intercalated Mg-Al-LDH

Briefly, the fluorescein intercalated Mg-Al-LDH materials (Mg-Al-Fluo) were prepared by co-precipitation method. A mixture of Mg(NO<sub>3</sub>)<sub>2</sub> · 6H<sub>2</sub>O (0.1M), Al(NO<sub>3</sub>)<sub>3</sub> · 9H<sub>2</sub>O (0.1M), and fluorescein disodium salt as powder (36mM) were added into decarbonized water and then the mixture was stirred vigorously for 24 hours at room temperature under inert atmosphere with a constant flux of N<sub>2</sub> gas in order to avoid the formation of CO<sub>3</sub><sup>2-</sup> ions in the reaction mixture. The pH of the mixture was kept at around 9.5 by using 0.2M NaOH solution. The atomic ratio of Mg<sup>2+</sup>/Al<sup>3+</sup> metal components was fixed at 2. After that, the precipitate was collected by centrifugation and then washed with decarbonized water until the supernatant was clear. The final precipitate was dried overnight at 40°C before further characterizations. The theoretical formula of the final product should be:



where C<sub>20</sub>H<sub>10</sub>O<sub>5</sub> is a fluorescein ion.

### C. Results and discussion

Before starting the characterizations, it should be noted that the study of fluorescein intercalated Mg-Al-LDH structures are under preliminary studies in order to ensure the enhancement of photoluminescence properties of organic phosphors in solid state by de-aggregating the organic molecules as in solution state. As with the previous study of FC@SiO<sub>2</sub>, the fluorescein can be presented as bivalent anion forms due to basic (pH 9.5) condition of the reaction mixture. The X-ray powder diffraction patterns (XRPD) of Mg<sub>2</sub>Al(OH)<sub>6</sub>(C<sub>20</sub>H<sub>10</sub>O<sub>5</sub>)<sub>0.5</sub>·2H<sub>2</sub>O (Mg-Al-Fluo) and the originate nitrate and carbonate forms (shown as references) are presented in Figure 97. The positions (2θ) of reflections can be assigned as (hkl) series according to the published study of Mg-Al-LDH structures<sup>310, 311</sup>. It should be noted that the typical XRPD patterns of many LDH structures represent the sharp and intense peak corresponding to reflections from crystalline structures on the basis of hexagonal unit cell in the space group R $\bar{3}m$ . A peak at lowest 2θ angle is typically related to (003) reflection which corresponds to the interlayer distance d<sub>003</sub> (the distance between two intra-layer of brucite-like layers)<sup>312</sup>. This interlayer distance depends on the nature and size of intercalated anions<sup>313</sup> and can be calculated by using Bragg's Law:

$$d_{hkl} = \lambda / (2 \cdot \sin \theta) \quad (\text{Equation 2})$$

where λ is the wavelength of X-ray (1.5418 Å), d<sub>hkl</sub> is the reciprocal of the interplanar spacing and θ is the angle of reflection of a X-ray beam. The peaks at about 60°

The XRPD patterns of Mg-Al-Fluo structures show low crystallinity and disappearance in intercalated peak of fluorescein in the LDH structures. We suggested that the LDH structures could consisted of low stacked sheets and have random and directionless orientation of LDH sheets with absorbed fluorescein molecules at the surface. In order to obtain well-crystalline structure, the Mg-Al-fluo powders were subjected to hydrothermal treatment at 120°C in water for a long period of time (more than 24 hours). The XRDP patterns of Mg-Al-fluo structures after treatment present better crystallinity of the Mg-Al-fluo structure and also the presence of a peak indexed of d<sub>003</sub> reflection at 5.48 Å (\*), corresponding to the intercalation of fluorescein<sup>298</sup>, that shifted to lower 2θ angle from nitrate (NO<sub>3</sub>-LDH) and carbonate (CO<sub>3</sub>-LDH) phases.

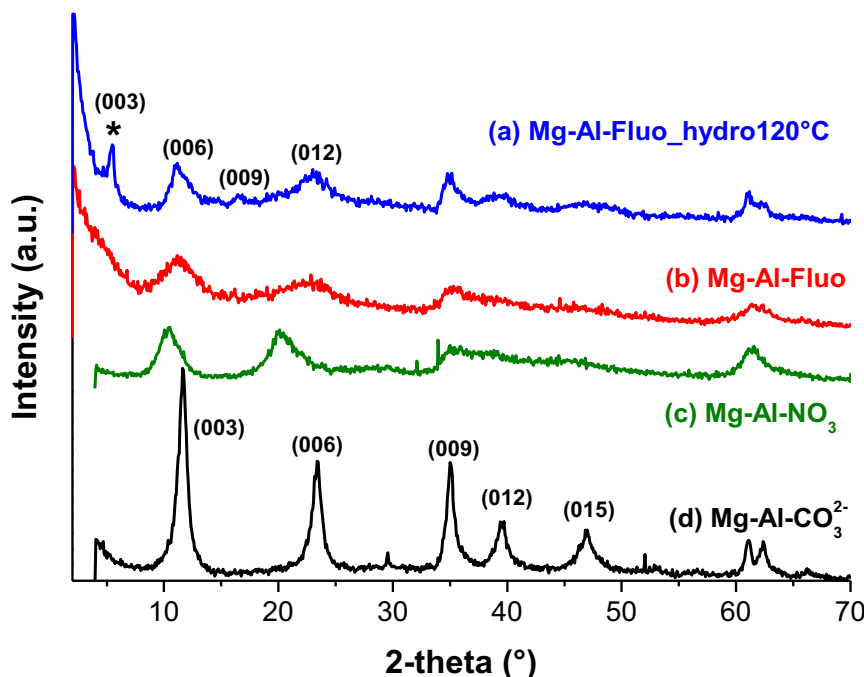


Figure 97 X-ray powder diffraction patterns of Mg-Al-Fluo (b) before and (a) after thermal treatment. (c) and (d) represent the originate forms of Mg-Al-LDH with intercalation of nitrate and carbonate ions.

Accordingly, the interlayer distance of Mg-Al-Fluo were calculated from the (003) reflection series and obtained at about 16.1 Å, which was close to the interlayer distance of the Mg-Al-Fluo powders reported in the literature (16.5 Å)<sup>298</sup> and expanded from the calculated values of NO<sub>3</sub>-LDH phase (8.8 Å) and CO<sub>3</sub>-LDH phase (7.6 Å). The width of reflection peaks can be related to the size of sub-micrometer particle or crystalline powder by Scherrer equation<sup>314</sup>:

$$L = K\lambda / \beta \cos \theta \quad (\text{Equation 3})$$

where L is the mean size of the coherent domains, K is a dimensionless shape factor (value close to unity),  $\lambda$  is the wavelength of X-ray,  $\beta$  is the width of a peak in diffraction pattern (or FWHM), and  $\theta$  is the angle of reflection of a X-ray beam.

Accordingly, the thickness of coherent domains along the (001) reflections represents the average number of stacked intra-layer sheets in the domains, which is given by:

$$N = L / d_{hkl} \quad (\text{Equation 4})$$

where N is a number of layered stacked along the (hkl) reflections. Using the Scherrer equation, the mean size of the coherent domains ( $L_{001}$ ) calculated was about 202 Å with 12.6 layers. The structure information of Mg-Al-fluo was investigated by comparison of IR spectra between

Mg-Al-fluo structure and fluorescein disodium salt powder as shown in Figure 98. The FTIR spectra of Mg-Al-fluo structures show the similar characteristic vibration bands as the fluorescein powder, which can ensure that the intercalated fluorescein in Mg-Al-LDH structures were presented in bivalent anion form. The appearance of the broad absorption band at around  $3400\text{ cm}^{-1}$  was due to O–H stretching of hydroxyl groups of LDHs and water molecules in the interlayer space. The absorption bands between  $1600$  and  $1450\text{ cm}^{-1}$  were attributed to the characteristic vibration bands of benzene rings and the conjugated system of fluorescein.

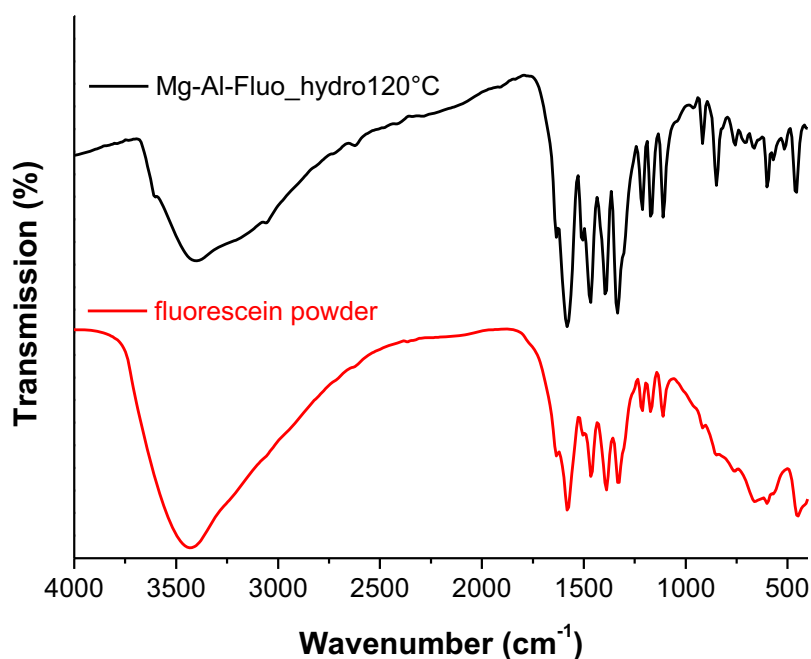


**Figure 98 FTIR spectra of Mg-Al-Fluo powders after thermal treatment and fluorescein disodium salt powders.**

The morphological structures of Mg-Al-Fluo powders was investigated with scanning electron microscopy (SEM). Typically, Mg-Al-LDH powders present plate-like morphology with the size distribution of particles varied from several nanometers to micrometer in the direction of intra-layer plane, which depending on the synthesis conditions and crystallinity of LDHs. Figure 99 shows the SEM images of  $\text{Mg}_2\text{Al}(\text{OH})_6(\text{C}_{20}\text{H}_{10}\text{O}_5)_{0.5} \cdot 2\text{H}_2\text{O}$  as a crystalline powder obtained before and after thermal treatment at  $120^\circ\text{C}$ . The Mg-Al-Fluo structures present very small plate-like particles, with a rough surface composed of randomly oriented LDH particles, with the size distribution in the range of 200 nm. As with the previous results of XRPD patterns, the SEM images can also confirm the enhancement of crystallinity of Mg-Al-Fluo structures as well as the increase in particle size after thermal treatment at  $120^\circ\text{C}$ .

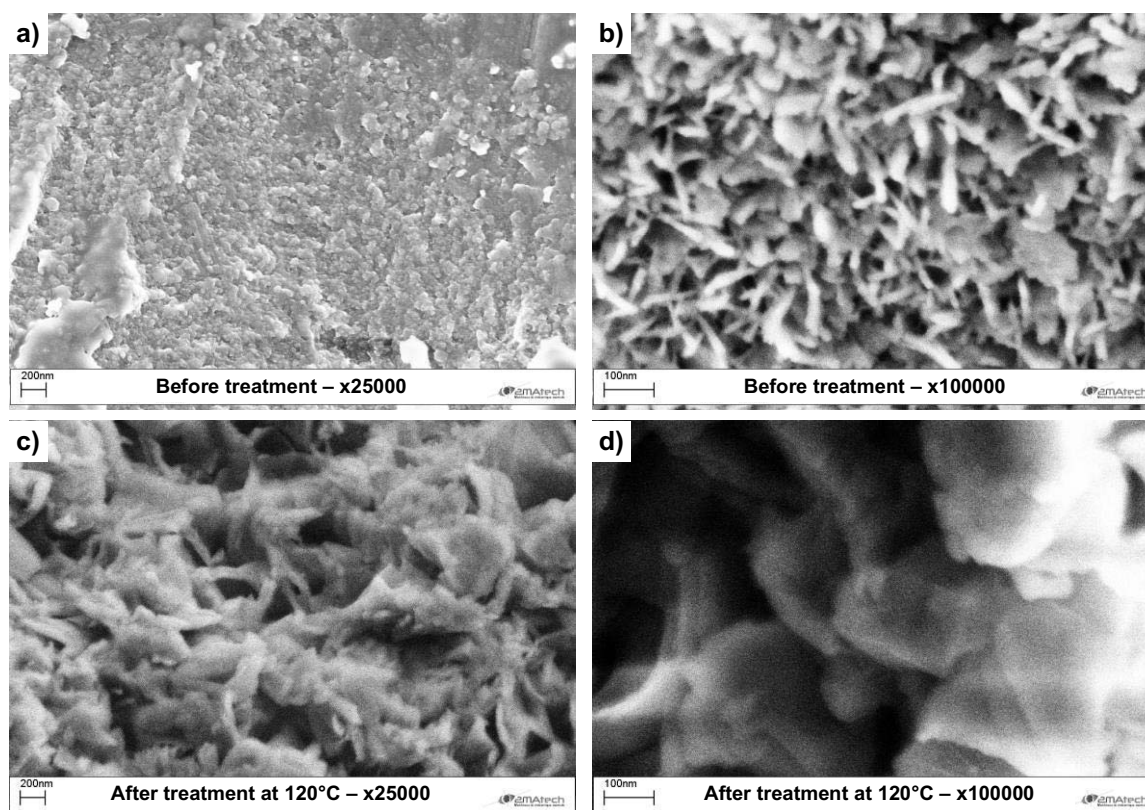


**Figure 99 SEM micrographs of Mg-Al-Fluo powders: (a) and (b) represent the structures before thermal treatment, (c) and (d) after thermal treatment at 120°C.**

As we highlighted previously, the photoluminescence properties of Mg-Al-Fluo materials is the main point of interest for further lighting applications with LEDs. Therefore, Mg-Al-Fluo powders were subjected to PLQY measurement system at room temperature. Figure 100 recorded the PL emission spectra of Mg-Al-Fluo powders under excitation at 365 nm UV-light and 450 nm blue-light illumination. The result shows that there is no PL emission observed for Mg-Al-Fluo powders after excitation at both wavelengths. We suggested that the emission loss of this materials might be due to the concentration-quenching of fluorescein in solid state.

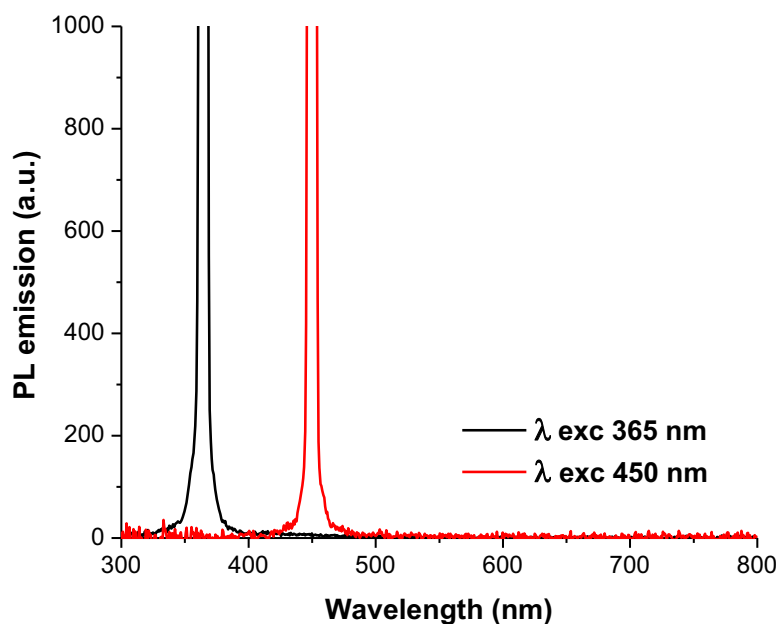
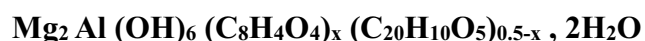


Figure 100 PL emission spectra of Mg-Al-Fluo powders after thermal treatment upon light excitation at 365 nm and 450 nm.

To minimize the concentration of fluorescein in Mg-Al-LDH system, another organic compound as terephthalate anions were introduced into the reaction mixture in proportion to fluorescein anions. Additionally, the presence of terephthalate can also improve the crystallinity of LDHs. The use of terephthalate for intercalation into LDHs have been studied by the research group of Fathi Kooli<sup>315</sup> and Sharon Mitchell<sup>316</sup>, which presented the highly crystalline phase of Mg-Al-LDHs with corresponding interlamellar spacing about 14 Å by the vertical orientation of terephthalate anion between layers. In this work, the amount of terephthalic anions (C<sub>8</sub>H<sub>4</sub>O<sub>4</sub>) as a form of terephthalic acid and the amount of fluorescein were added in the reaction mixture with different proportions by keeping the total amount of anion concentration in Mg-Al-LDH system as constant. The theoretical formula of the final product should be:



where  $x = 0.4, 0.475$  and  $0.495$  so that the amount of fluorescein in LDHs could be 20 wt. %, 5 wt. % and 1 wt. % with respect to 80 wt. %, 95 wt. % and 99 wt. % of terephthalate, respectively.

The X-ray powder diffraction patterns (XRPD) of Mg<sub>2</sub>Al(OH)<sub>6</sub>(C<sub>8</sub>H<sub>4</sub>O<sub>4</sub>)<sub>x</sub>(C<sub>20</sub>H<sub>10</sub>O<sub>5</sub>)<sub>0.5-x</sub>, 2H<sub>2</sub>O (Mg-Al-TP-Fluo) with different compositions of fluorescein and terephthalate were shown in Figure 101. The XRPD patterns of Mg-Al-TP-Fluo powders at peak of (003)



reflection was increased due to high crystallinity of products obtained after the addition of terephthalate. The presence of a peak indexed at about 6 Å (\* in Figure 101) corresponding to the intercalation of fluorescein<sup>298</sup> was clearly observed with respect to the amount of terephthalate in the Mg-Al-TP-Fluo structures. The supplementary data of chemical composition, interlayer distance, size of the coherent domains and number of stacking layers are summarized in Table 31.

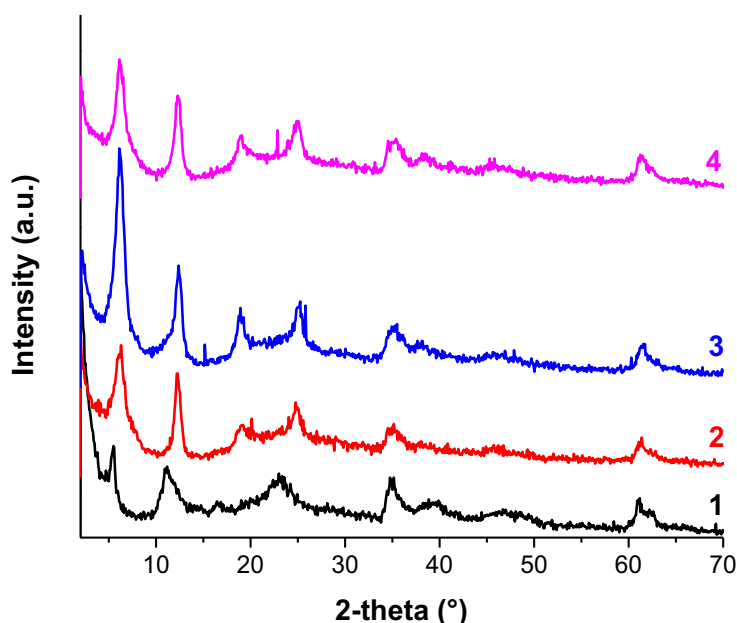


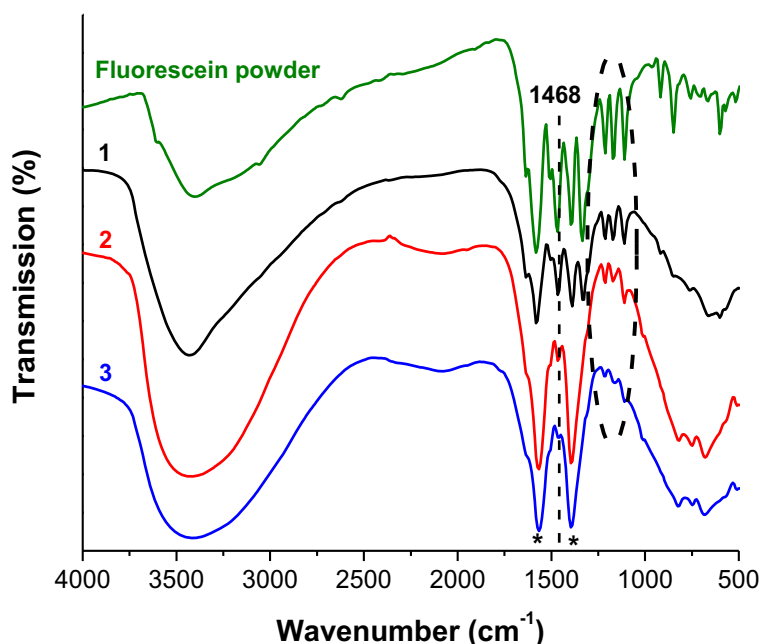
**Figure 101 X-ray powder diffraction patterns of Mg-Al-TP-Fluo with different compositions of fluorescein (Fluo) and terephthalate (TP): 1 = 100 wt. % Fluo, 2 = 20 wt. % Fluo + 80 wt. % TP, 3 = 5 wt. % Fluo + 95 wt. % TP and 4 = 1 wt. % Fluo + 99 wt. % TP.**

As reported above, the XRPD patterns show the Mg-Al-TP-Fluo structures with an interlayer spacing of 14.2 Å, which corresponds to the values in the literature<sup>315,316</sup> and smaller than that of Mg-Al-Fluo as reported previously (16.1 Å). The mean size of the coherent domains ( $L_{001}$ ), which is related to the thickness of ensemble stacked layers, decreased from 202 to 83 according to the solid composition. Moreover, the value of  $L_{001}$  and number of layers stacked along the (001) reflections ( $N_{001}$ ) increased with increasing the concentration of terephthalate in Mg-Al-TP-Fluo materials, resulting the expansion in its size distribution. The number of stacking layers was reduced twice by adding terephthalate into the Mg-Al-TP-Fluo structures. The results indicate that the formation of intercalated terephthalate can reduce the aggregation of stacking layers, which lower the possibility of fluorescein aggregates in the domains.

**Table 31 Solid composition of fluorescein intercalated Mg-Al-LDH with calculated parameters of intercalated layers.**

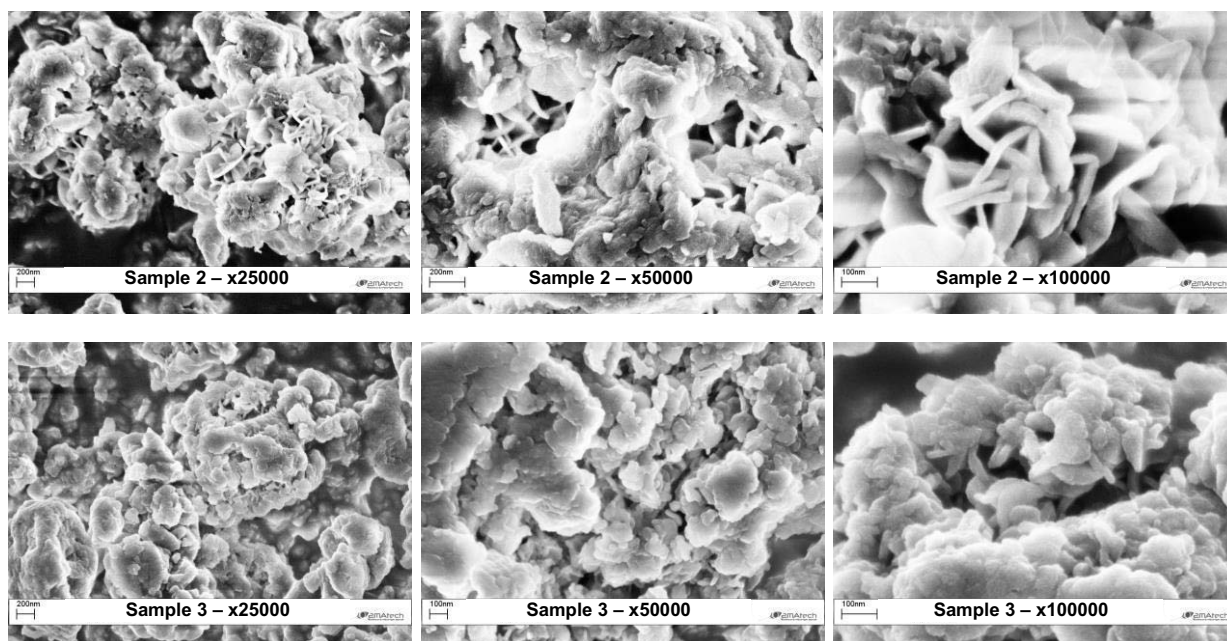
Sample	Solid compositions	Interlayer distance, $d_{hkl}$ (Å)	Size of the coherent domains, $L_{001}$ (Å)	Number of Layers s, N
1	$Mg_2Al(OH)_6(C_8H_4O_4)_0(C_{20}H_{10}O_5)_{0.5}, 2H_2O$	16.1	202	12.6
2	$Mg_2Al(OH)_6(C_8H_4O_4)_{0.4}(C_{20}H_{10}O_5)_{0.1}, 2H_2O$	14.2	83	5.8
3	$Mg_2Al(OH)_6(C_8H_4O_4)_{0.475}(C_{20}H_{10}O_5)_{0.025}, 2H_2O$	14.2	88	6.2
4	$Mg_2Al(OH)_6(C_8H_4O_4)_{0.495}(C_{20}H_{10}O_5)_{0.005}, 2H_2O$	14.2	93	6.5

The FTIR spectra of Mg-Al-TP-Fluo powders recorded for different amounts of fluorescein and terephthalate have been shown in Figure 102. The broad absorption band at around  $3400\text{ cm}^{-1}$  was attributed to O–H stretching of hydroxyl groups of LDHs and water molecules in the interlayer space. The strong absorption bands located at  $1568$  and  $1403\text{ cm}^{-1}$  (\* in Figure 102) were attributed to the characteristic vibration bands of terephthalate<sup>315</sup>. Furthermore, the evolution of the absorption band at  $1468\text{ cm}^{-1}$  as well as three small absorption bands from  $1260$  to  $1060\text{ cm}^{-1}$  were an evidence of diminution of fluorescein molecules in Mg-Al-TP-Fluo structures as we desired.



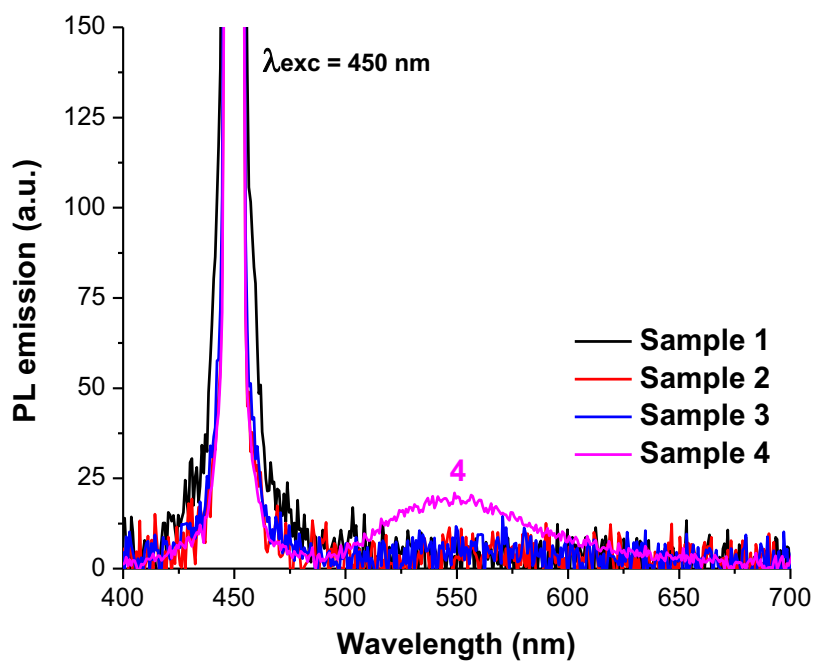
**Figure 102 FTIR spectra of Mg-Al-TP-Fluo with different compositions of fluorescein (Fluo) and terephthalate (TP): 1 = 100 wt. % Fluo, 2 = 20 wt. % Fluo + 80 wt. % TP and 3 = 5 wt. % Fluo + 95 wt. % TP.**

Figure 103 presents the morphological structures of Mg-Al-TP-Fluo powders for  $\text{Mg}_2\text{Al}(\text{OH})_6(\text{C}_8\text{H}_4\text{O}_4)_{0.4}(\text{C}_{20}\text{H}_{10}\text{O}_5)_{0.1}, 2\text{H}_2\text{O}$  (sample 2) and  $\text{Mg}_2\text{Al}(\text{OH})_6(\text{C}_8\text{H}_4\text{O}_4)_{0.475}(\text{C}_{20}\text{H}_{10}\text{O}_5)_{0.025}, 2\text{H}_2\text{O}$  (sample 3). The SEM images show plate-like particles with the thickness between 21 to 30 nm. The Mg-Al-TP-Fluo structure afforded the randomly oriented LDH particles. As with the previous results, both samples present in both crystallite size and crystallinity different from Mg-Al-Fluo powders, indicating that terephthalate has a strong influence on morphology of LDHs.



**Figure 103 SEM micrographs of of Mg-Al-TP-Fluo with different compositions of fluorescein (Fluo) and terephthalate (TP): sample 2 = 20 wt. % Fluo + 80 wt.% TP, sample 3 = 5 wt. % Fluo + 95 wt. % TP.**

Figure 104 recorded the PL emission spectra of Mg-Al-TP-Fluo powders with different compositions of fluorescein and terephthalate at room temperature under 450 nm excitation using PL-QY measurement system. The results show that only Mg-Al-TP-Fluo powders with 1 wt. Fluo and 99 wt. % TP (sample 4) can produce the weak light emission with the maximum emission wavelength located at 550 nm upon excitation at 450 nm. The absolute quantum yield of sample 4 was recorded about 1.6% under 450 nm excitation whereas other samples was found the values close to zero.



**Figure 104** PL emission spectra of of Mg-Al-TP-Fluo with different compositions of fluorescein (Fluo) and terephthalate (TP): 1 = 100 wt. % Fluo, 2 = 20 wt. % Fluo + 80 wt. % TP, 3 = 5 wt. % Fluo + 95 wt. % TP and 4 = 1 wt. % Fluo + 99 wt.% TP.

### Summary

This chapter reported the study of organic phosphors encapsulated in the inorganic matrix such as silica nanoparticles ( $\text{SiO}_2$ ) and layered double hydroxide (LDH) structures. In the first section, we have successfully synthesized fluorescein-silica nanoparticles from reverse microemulsion method which exhibit high optical properties and good thermal stability under 450 nm LED irradiation. The association of  $\text{FC@SiO}_2$  nanoparticles (15 wt. %) embedded in silicone with a blue LED chip can lead to a near-white emission with cool color temperature ( $> 6000$  K) and reach the maximum luminous efficacy of 26 lm/W under forward current of 100 mA. Although some parameters of light performance are still far away from the indoor-lighting conditions, the white-light LEDs based on  $\text{FC@SiO}_2$  nanoparticles can be able to undergo the improvement and development in order to increase photoluminescence properties. For example, the addition of  $\text{ATTO490LS@SiO}_2$  nanoparticles as red components in the proportion to  $\text{FC@SiO}_2$  nanoparticles could reduce the color temperature of system and also increase the red contribution of global emission spectrum. These interesting purpose of fluorescein-silica nanoparticles will be integrated not only in the field of lighting applications but also for visualization and biomedical applications.

In the second section, we have synthesized organic-inorganic hybrid-LDHs materials based on fluorescein and Mg-Al-LDH matrix. The LDH structures have been used to intercalate fluorescein molecules in order to de-aggregate the molecules as in a dilute solution. The result presented the good evidence of intercalated fluorescein into the LDH structure. However, the best result showed that the photoluminescence properties of Mg-Al-TP-Fluo were still low for lighting applications and much lower than the values of  $\text{FC@SiO}_2$  nanoparticles as reported in the first section. This kind of materials need more researches in order to enhance the photoluminescence properties and overcome the problems that cause the quenching effect the light emission.





---

# **CHAPTER IV**

# **Quantum dots-based white light-emitting diodes**

---





## I. Introduction

According to the bibliographic research in chapter 1, the use of quantum dots in lighting applications has become relevant choice instead of long-established technologies such as energy-inefficient incandescent lamps and mercury-containing fluorescent lamps. In addition, the quantum dots are an alternative energy materials without rare-earth metals that could help to reduce rare-earth element demand and production. By substituting the inorganic yellow phosphor (YAG: Ce) with quantum dots, several research studies of quantum dots-based white LEDs have been published with high luminous efficacy, good CRI value, and desired color temperature for domestic indoor lighting<sup>112, 317-319</sup>. This chapter will present three types of core-shell quantum dots and the hybrid white LEDs using mixed quantum dots. The morphological and optical characteristics of quantum dots as well as their composite films with silicone resin were studied. The colorimetric simulation of quantum dots can confirm the possibility to produce white light combined with a commercial UV/blue LED chip. The performance parameters of hybrid white LEDs (electroluminescent spectrum, luminous efficacy, correlated color temperature, CIE color coordinates and color rendering index) were also investigated. Finally, the photo-aging stability of quantum dots composite films were studied at wavelengths above 300 nm in order to confirm their optical stabilities under conditions close to operating conditions in LED devices.

## II. Experimental

### A. Synthesis of the blue/green-emitting CdSe/ZnS QDs, and the red-emitting CuInS<sub>2</sub> QDs.

The blue/green-emitting CdSe/ZnS QDs, and red-emitting CuInS<sub>2</sub>/ZnS QDs were received as a solid form sealed in plastic containers from the research group of Raphaël Schneider (Laboratoire Réactions et Génie des Procédés, University of Lorraine, Nancy, France) and dried out in a vacuum desiccator at room temperature for 2-3 hours before use. All quantum dots were synthesized according to published procedures, with slight modifications in the starting materials in order to tune-up the emission wavelength of QDs<sup>320-325</sup>.

### B. Preparation of QDs – silicone films for white light-emitting diodes

The free-standing quantum dots-silicone composite films were obtained as follows. Firstly, the mixture was prepared by dispersing the quantum dots in a small quantity of toluene before adding the silicone resin/curing agent (Silicone Bluesil RTV 141 A&B). For the mixed quantum dots, the ratios of each quantum dots were calculated using each emission spectra via LED color calculator (see in this chapter).<sup>§§§</sup> Secondly, the mixture was stirred at room temperature in order to partially evaporate the solvent and then the mixture was mixed using a mechanical mixer to achieve highly homogenous particles/silicone mixture. Next, the quantum dots – silicone films were prepared by casting onto a Teflon surface using an Elcometer 4340 automatic film applicator. The blade knife height was fixed at 400 μm and the casting speed was 20mm/s. The composite films were allowed to dry in the oven at 60°C overnight. The thickness of composite films were measured at final step using an Elcometer 456 coating thickness gauge.

---

<sup>§§§</sup> The software is also available at <http://www.sylvania.com/en-us/tools-and-resources/Pages/led-color-calculator.aspx>

### III. Results and discussion

Before realizing further characterizations, the quantum dots were firstly diluted in toluene (concentration  $\approx 1.15$  mg/mL) and their UV-visible absorption and PL emission spectra were recorded. Figure 105 shows the absorption and PL emission spectra of these three quantum dots prepared in toluene at concentration of 1.15 mg/mL under 365 nm excitation. The blue-emitting CdSe/ZnS QDs exhibited a cyan/blue emission involving a broadband peak centered at 493 nm with a full width at half maximum (FWHM) of 33 nm. The measurement of absolute quantum yield in toluene was about 44% under 365 nm excitation. The green-emitting CdSe/ZnS QDs presented a broad band in green range with a maximum emission peaking at 515 nm, with a full width at half maximum (FWHM) of 34 nm, under 365 nm excitation. The absolute quantum yield of green QDs was recorded at about 60% upon 365 nm excitation. The received CuInS<sub>2</sub>/ZnS QDs showed a large PL emission spectrum with a maximum situated at 620 nm (FWHM = 107 nm) and an absolute quantum yield of 42% upon 365 nm excitation. According to previous information, these three quantum dots have a large absorption spectrum ranging from UV to visible region (Figure 105-left).

Considering their wavelengths of absorption, it seems to be suited to combine these quantum dots with commercial 365 nm UV-light or 450 nm blue light LEDs in order to produce white light. In the next section, the morphological and optical characterizations of these three QDs were investigated.

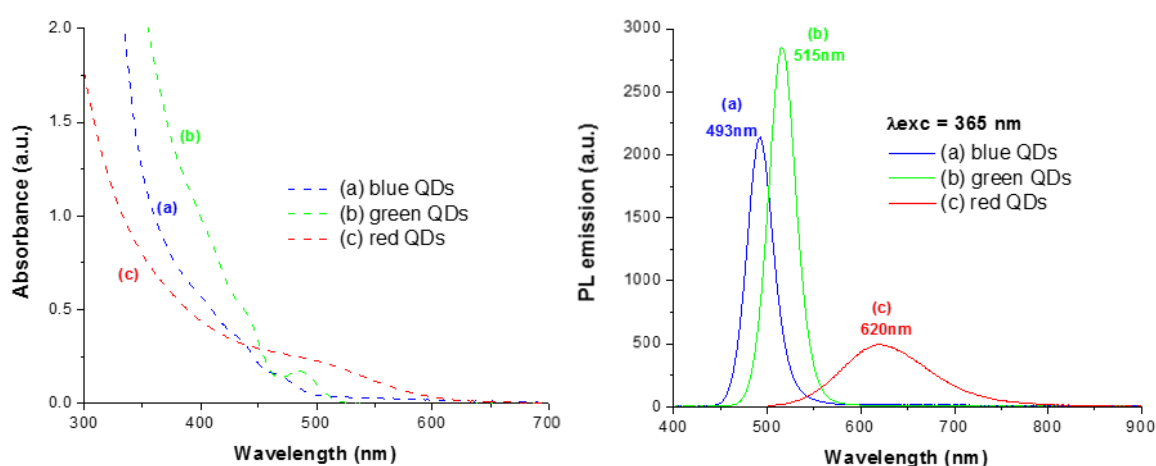


**Figure 105 (left) UV-visible absorption and (right) PL emission spectra of a) blue-emitting CdSe/ZnS QDs (b) green-emitting CdSe/ZnS QDs and (c) red-emitting CuInS<sub>2</sub>/ZnS QDs.**

### **A. Blue-emitting CdSe/ZnS quantum dots**

The semiconductor CdSe/ZnS QDs were selected for development of light-emitting diodes by reasons of their high photostability, their narrow emission bands, and their size-dependent color variation in visible range<sup>326</sup>. Actually, the CdSe/ZnS QDs have been presented as a highly efficient green-emitting components for QD-based light-emitting diodes (QLEDs) owing to its high brightness and high luminous efficiency<sup>327, 328</sup>. The blue-emitting light can also be obtained from CdSe/ZnS QDs with sophisticated method due to the synthetic route by modulating the composition ratio of Cd/Zn/Se/S<sup>5</sup>. Several approaches have been proposed to the synthesis of blue-emitting CdSe/ZnS QDs in order to improve the synthetic process<sup>329, 330</sup>.

In this work, the blue-emitting CdSe/ZnS QDs were synthesized by simultaneous injection of both selenium and sulfur into the reactor at the same time, followed by developing the ZnS shell over them as a passivation layer. The 1-dodecanethiol can serve as a strong binding ligand to the QD surfaces instead of surfactants with carboxylic or amine groups, which can more easily disconnect from the QD surfaces after purification step<sup>320</sup>. In the paper of B. El-Kareh, the defects on the surface such as a dangling bond are caused by the departure of ligands from the surface of semiconductor<sup>331</sup>, which can act as non-emission center resulting the drop of the photoluminescence quantum yield efficiency and chemical stability of quantum dots. The presence of 1-dodecanethiol (developed for the synthesis of QDs by the group of R. Schneider) can improve the photoluminescence properties of quantum dots<sup>332</sup> and also increase the solubility in various organic solvents.

#### **a. Morphological studies of blue-emitting CdSe/ZnS QDs**

The blue-emitting CdSe/ZnS QDs received as a solid form were firstly dispersed in an organic solvent. Figure 106 presents the transmission electron microscopy (TEM) image of blue QDs dispersed in toluene (1.14 mg/mL). The overview of TEM image exhibits a good size distribution with nearly spherical shape. The average size of blue QDs measured from image analysis of the TEM image was  $7.45 \pm 0.96$  nm.

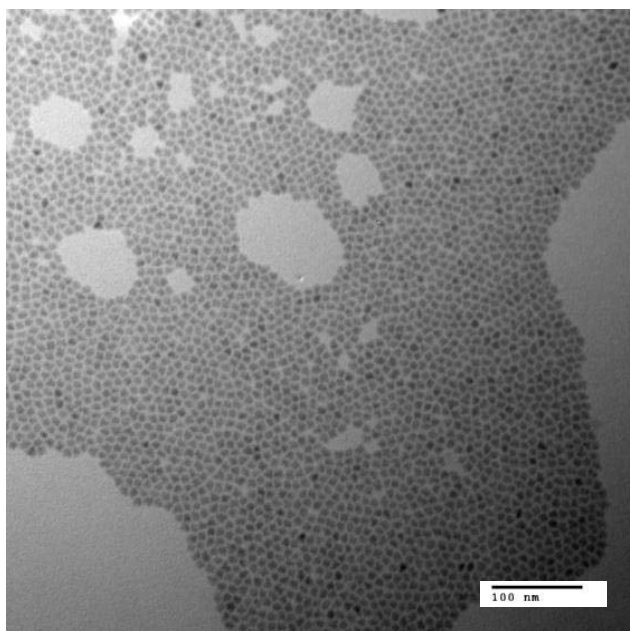


**Figure 106** TEM image of blue-emitting CdSe/ZnS core/shell QDs prepared by dispersing QDs in toluene.

### b. Optical studies of blue-emitting CdSe/ZnS QDs

In contrast to the organic molecules, the photoluminescence of CdSe core quantum dots is generated by the recombination between holes in the valence band and free electrons in the conduction band. Both bands represent the quantized energy levels which are known as the characteristic of each quantum dots and depend strongly on the quantum dots size. The inorganic shell ZnS serves as the passivation layer for CdSe cores in order to improve their stability of quantum yield efficiency<sup>324, 333</sup>.

**Table 32** Photoluminescence properties of blue-emitting CdSe/ZnS QDs.

	Nature of QDs	Exc $\lambda_{\max}$ (nm)	PL $\lambda_{\max}$ (nm)	FWHM of PL $\lambda_{\max}$ (nm) (at 365 nm)	PLQY <sub>abs</sub> at 365 nm (%)	PLQY <sub>abs</sub> at 450 nm (%)
CdSe/ZnS blue- emitting QDs	solid	318	504	39.78 ± 0.10	20.9	17.5
	1.14 mg/ml, toluene	337	493	32.92 ± 0.03	43.7	27.0
	0.114 mg/ml, toluene	315	486	34.87 ± 0.08	26.8	8.7
	1.16 mg/ml, chloroform	339	492	33.30 ± 0.04	43.7	26.6
	4.36 mg/ml, toluene	316	498	31.44 ± 0.09	44.5	36.5

According to Table 32, we have summarized the optical properties of blue-emitting CdSe/ZnS quantum dots measured on a solid-state QDs sample and on dilute solutions, involving their maximum excitation and emission wavelengths, their FWHM of the emission spectrum and their absolute quantum yield. The blue QDs were studied comparatively in the solid state and the liquid states (Figure 107). It should be noted that the photoluminescence properties of quantum dots are strongly dependent on the excitation wavelength, which are in accordance with the studies published by the group of Stephen R. Leone<sup>334</sup>. In this work, the blue QDs were excited at 365 and 450 nm corresponding to the maximum emission wavelength of commercial LEDs (see Table 32). The photoluminescence properties of blue QDs from 365 nm UV-light excitation were higher than those from 450 nm blue-light excitation. Therefore, we will represent the following results of blue QDs upon 365 nm UV-light excitation.

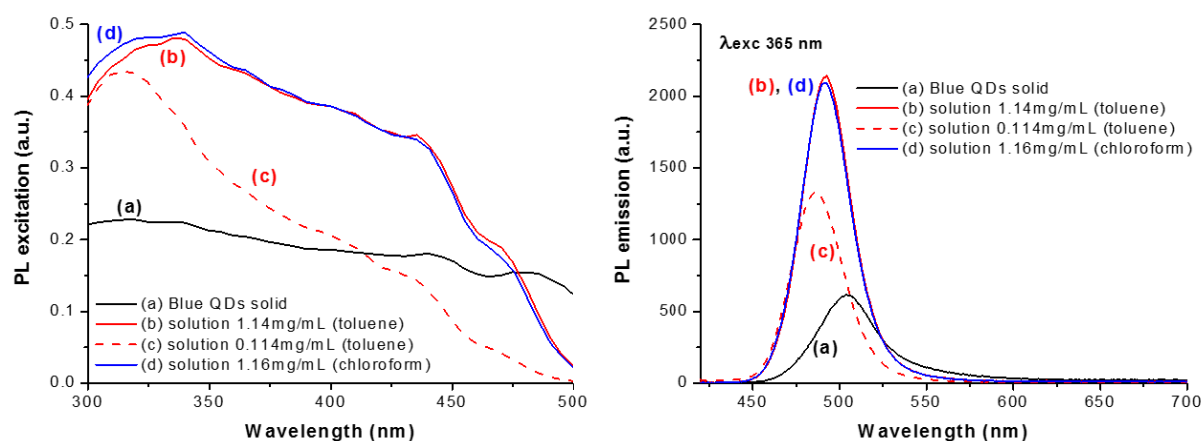


**Figure 107 (left) Excitation and (right) emission spectra of blue QDs of (a) solid form, (b) solution of 1.14 mg/mL in toluene, (c) solution of 0.114 mg/mL in toluene, and (d) solution of 1.16 mg/mL in chloroform.**

Generally, the quantum dots exhibited better photoluminescence properties when they are dispersed in the solution environment compared with those in solid-state. According to Figure 107, both excitation and emission spectra of their solid-state form result in lower intensity than their solution states. The absolute quantum yield measured for solid state was lower than that for solution states. Furthermore, the PL emission spectra have shifted to the red of spectra when the concentration of blue QDs increases (from dilute solution to solid state).

Considering the solid-state QDs, the distance between quantum dots is very small and the energy transfer of excitation energy from one fluorescence center to another is dominant due to long-range dipole interaction increase. The long-range dipole interaction of quantum dots have been explained by C.R. Kagan et al<sup>335</sup>. This interaction is a non-radiative process arising from coupling between transition dipole moments of one molecule or atom (called a donor)

and another molecule or atom (called an acceptor). The electronic energy is transferred from an excited state of a donor to the ground state of an acceptor. As a result, the donor returns to its ground state while the receptor promotes to its higher excited states, leading to a decrease in emission intensity and photoluminescence quantum yield. In addition, the reduction of absolute quantum yield probably comes from charge separation and energy transfer between dots which reduce the electron-hole recombination probability in the same molecule or atom<sup>335</sup>.

Regarding the solution states, the solvent molecules keep the quantum dots far away from each other to avoid both fluorescence quenching and the re-absorption effect. Furthermore, the solution state decreases the probability that QDs get closer together and prevent the nanoparticle aggregation, leading to a reduction of long-range dipole interaction. As the concentration of blue QDs is increased, more QDs can be excited by incident light and, as a consequence QDs can emit more fluorescence. Moreover, the emission spectra is shifted to a low energy (or a long wavelength) when the concentration of QDs is increased. A redshift was observed at about 7 nm in the emission spectra of both solution states. The results were consistent with published study that presented the relation of fluorescence intensity of blue QDs as a function of the concentration<sup>336</sup>.

**Table 33 Dipole, dielectric constant and polarity of chloroform and toluene<sup>337, 338</sup>.**

Solvent	Empirical formula	Dipole (D)	Dielectric constant (20°C)	Polarity (water = 100)
Chloroform	CHCl <sub>3</sub>	1.1	4.8	25.9
Toluene	C <sub>7</sub> H <sub>8</sub>	0.4	2.38	9.9

The solvent effect to photoluminescence properties of blue QDs were also investigated. The blue QDs showed a good dispersibility in several organic solvents (hexane, chloroform and toluene) due to the presence of 1-dodecanthiol as organic ligands on the QD surfaces. To investigate the photoluminescence of quantum dots in different solutions, toluene and chloroform were selected because of their different polarity and dielectric constant (Table 33) In this study, blue QDs were dispersed in chloroform and toluene at nearly the same concentration and then illuminated under 365 nm UV-light excitation (see Figure 107). As with the previous studies, the PL excitation spectra, the emission spectra, and the absolute quantum



yield of each blue QDs present no significant change in different solvents with the same concentration. Therefore, the optical properties of blue QDs exhibit no solvent effect.

## **B. Green-emitting CdSe/ZnS quantum dots**

Referring to our previous studies of blue-emitting CdSe/ZnS QDs, the CdSe/ZnS QDs can serve as a high color-saturated green light-emitting components for QD-based light-emitting diodes (QLEDs) owing to its high brightness and high luminous efficiency<sup>327, 328</sup>. The green-emitting CdSe/ZnS QDs were prepared according to published procedures by using the same chemical-composition ratio (Cd/Zn/Se/S) as QD 510 in order to produce the green-light emission<sup>5</sup>. The 1-dodecanethiol was used as a strong binding ligand in order to improve the photoluminescence properties and the dispersibility of quantum dots in organic solvents<sup>332</sup>.

### **a. Morphological studies of green-emitting CdSe/ZnS QDs**

The green-emitting CdSe/ZnS QDs received as solid products were dispersed in an organic solvent. Figure 108 shows the transmission electron microscopy (TEM) study of green-emitting QDs dispersed in toluene (1.15 mg/mL). The average size of green QDs was  $9.44 \pm 1.28$  nm having uniform nearly spherical shape.

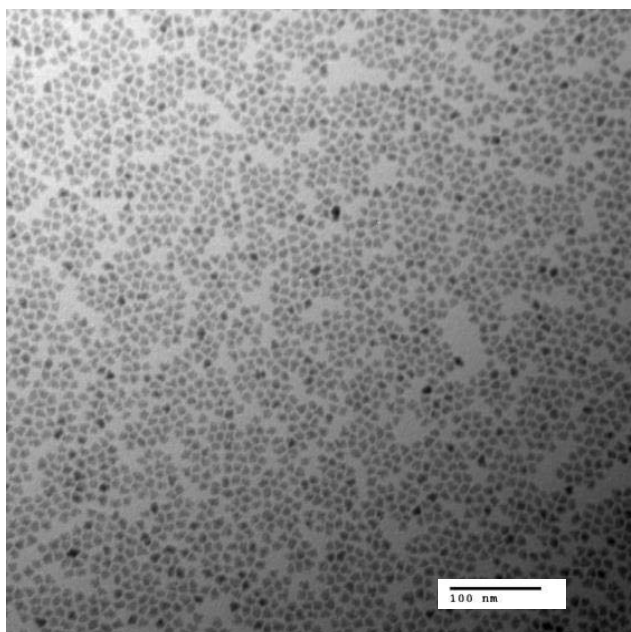


**Figure 108 TEM image of green-emitting CdSe/ZnS QDs prepared by dispersing QDs in toluene.**

### b. Optical studies of green-emitting CdSe/ZnS QDs

Figure 109 shows the excitation and emission spectra of green QDs in the solid state and the liquid states. The summary of their maximum excitation and emission wavelength, the FWHM of the emission spectrum, as well as the absolute quantum yield can be found in Table 34. As with the previous blue QDs, the emission intensity and the absolute quantum yield of the green QDs excited by 365 nm UV-light excitation were higher than those excited by 450 nm blue-light excitation. Therefore, we will present the results of green QDs upon 365 nm UV-light excitation.

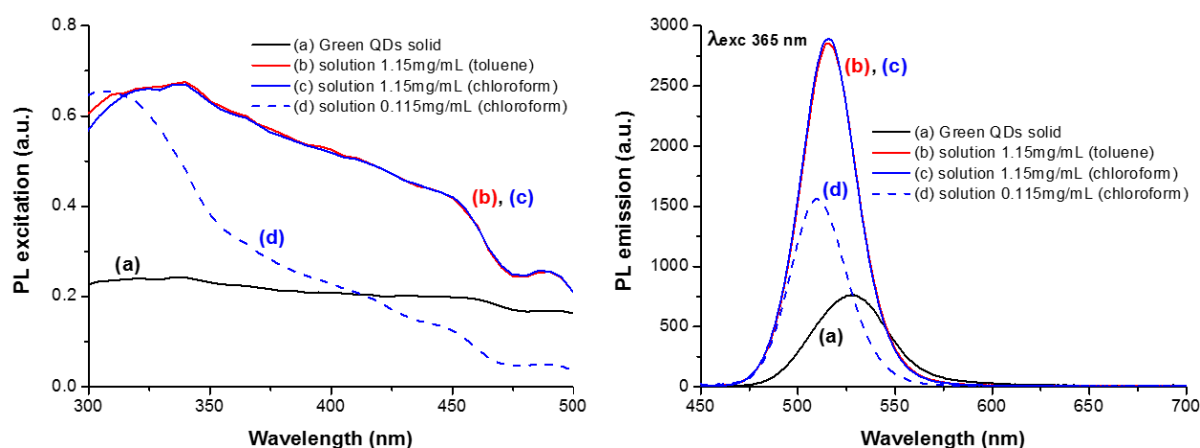


**Figure 109 (left) Excitation and (right) emission spectra of green QDs of (a) solid form, (b) solution of 1.15 mg/mL in toluene, (c) solution of 1.15 mg/mL and (d) 0.115 mg/mL in chloroform.**

The results show the photoluminescence properties of green QDs recorded in the solid state and in the dilute solutions. The PL emission spectra were found to be shifted toward the red end of the spectrum when the concentration of green QDs increases from the dilute solution to the solid form. The PL emission spectra in the dilute solution (0.115 mg/mL and 1.15 mg/mL in toluene) show the broad band in green range with a maximum emissions at 510 and 515 nm, respectively whereas the PL emission spectrum in the solid state presents a red-shift with a maximum emission at 527 nm. In addition, the absolute quantum yield measured for solid-state green QDs was lower than that for solution states. The photoluminescence properties of green QDs have similar behavior to blue QDs as we have mentioned previously by long-range dipole phenomena and the fluorescence quenching by concentration.

Table 34 Photoluminescence properties of green-emitting CdSe/ZnS QDs.

	Nature of QDs	Exc $\lambda_{\max}$ (nm)	PL $\lambda_{\max}$ (nm)	FWHM of PL $\lambda_{\max}$ (nm) (at 365 nm)	PLQY <sub>abs</sub> at 365 nm (%)	PLQY <sub>abs</sub> at 450 nm (%)
<b>CdSe/ZnS green- emitting QDs</b>	solid	338	527	45.42 ± 0.15	22.7	20.2
	1.15 mg/ml, toluene	339	515	34.04 ± 0.02	60.1	41.6
	0.115 mg/ml, chloroform	307	510	34.07 ± 0.05	31.5	12.3
	1.15 mg/ml, chloroform	338	515	33.76 ± 0.02	60.4	42.0
	4.16 mg/ml, toluene	312	520	33.52 ± 0.03	60.6	52.8

Considering the effect of solvent, the green-emitting CdSe/ZnS QDs were dispersed in chloroform and toluene at the same concentration and then illuminated under 365 nm UV-light excitation. The PL excitation spectra, the emission spectra, and the absolute quantum yield of green QDs in different solvents present no significant difference. Therefore, the photoluminescence properties of green QDs exhibit no solvent effect.

### C. Red-emitting CuInS<sub>2</sub>/ZnS quantum dots

CuInS<sub>2</sub> quantum dots are the semiconductors of ternary chalcopyrites (ABC<sub>2</sub> when A = Li, Na, Cu, Ag; B = Al, Ga, In; C = S, Se, Te) with high molar absorptivity in the visible to near-infrared (NIR) region<sup>324, 339</sup>. CuInS<sub>2</sub>/ZnS quantum dots have been considerably investigated as an alternative quantum dot due to the cadmium-free starting materials used, its high absorption coefficient and its long photoluminescence lifetime<sup>324</sup>. CuInS<sub>2</sub> quantum dots are an interesting candidate for lighting applications due to their large Stokes shift that reduces the probability of self-reabsorption at high concentration. However, the CuInS<sub>2</sub> QDs themselves generally exhibited low quantum yield efficiency (about 12%)<sup>324</sup>. In order to improve the stability and optical properties of CuInS<sub>2</sub> QDs, the inorganic shell ZnS is coated over the CuInS<sub>2</sub> QDs. The ZnS is a useful inorganic material for protecting the inner CuInS<sub>2</sub> core because of the increase in quantum yield efficiency, the reduction in surface oxidation by environmental surrounding, and the decrease in toxicity of QD by limiting the release of core ions<sup>324, 333</sup>. Moreover, the ZnS shell is suitable and stable for CuInS<sub>2</sub> core quantum dots because of the analogous crystallographic structure and the weak lattice mismatch (ca. 2%) between CuInS<sub>2</sub> and ZnS<sup>340</sup>,

### a. Morphological studies of red-emitting CuInS<sub>2</sub>/ZnS QDs

Figure 110 shows the transmission electron microscopy (TEM) micrograph of the red QDs prepared from 1.16 mg/mL QDs dispersion in toluene. The nanoparticles are very small and homogeneously dispersed with an average diameter less than 4 nm.

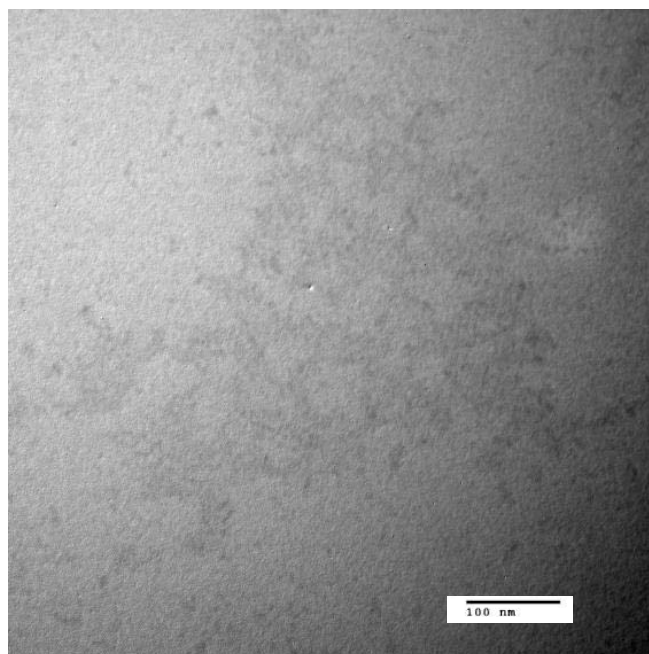


**Figure 110 TEM image of red-emitting CuInS<sub>2</sub>/ZnS QDs prepared by dispersing QDs in toluene.**

### b. Optical studies of red-emitting CuInS<sub>2</sub>/ZnS QDs

Figure 111 shows the excitation and emission spectra of red QDs along with different states (solid and diluted solutions). The maximum excitation and emission wavelength, the FWHM of the emission spectrum, and the absolute quantum yield of red QDs in various states can be found in Table 35. According to Figure 111, the red QDs exhibit the large Stokes shift and the broadband emission. The large Stokes shift from red QDs takes the advantage of photoluminescence in order to prevent the self-reabsorption process. Although, the group of Liang Li reported the concentration quenching of red QDs when the optical density was about 0.6 due to the small overlap of the absorption and the emission spectra<sup>342</sup>. The absorption and the emission spectra of red QDs is similar to the spectra published in the literature<sup>325, 343</sup>. The red QDs can be excited by photons of UV-visible light, in particularly at maximum wavelength of commercial LEDs. Table 35 shows that the emission intensity and the absolute quantum yield of red QDs excited by 365 nm UV-light excitation were greater than those excited by 450

nm blue-light excitation. Therefore, we will represent the results of red QDs alloyed QDs upon 365 nm UV-light excitation.

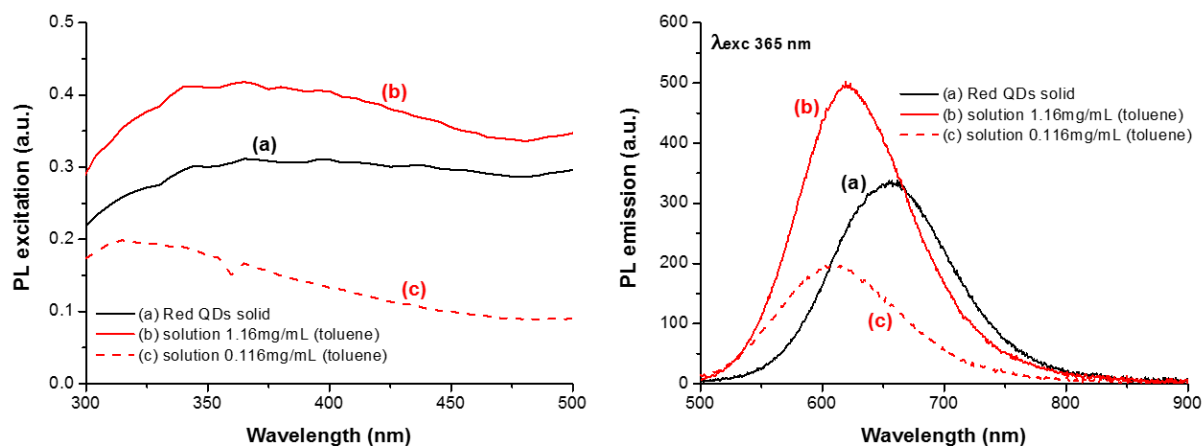


**Figure 111 (left) Excitation and (right) emission spectra of red QDs of (a) solid form, (b) solution of 1.16 mg/mL and (c) solution of 0.116 mg/mL in toluene.**

The red QDs solids emitted the red color with the maximum of the broad emission situated at 655 nm. The full-width at half maximum (FWHM) and the absolute quantum yield (PLQY<sub>abs</sub>) of red QDs solids were about 113 nm and 31% under excitation by light with a wavelength of 365 nm, respectively. Considering the solution states, the red QDs exhibit better photoluminescence properties when they are dispersed in the solution environment compared with those in solid-state. The red QDs show a good dispersibility in several organic solvents (hexane, chloroform and toluene) and reveal a deep-red color in dispersion as a result of high absorption coefficient in the visible region.

**Table 35 Photoluminescence properties of red-emitting CuInS<sub>2</sub>/ZnS QDs.**

	Nature of QDs	Exc $\lambda_{\max}$ (nm)	PL $\lambda_{\max}$ (nm)	FWHM of PL $\lambda_{\max}$ (nm) (at 365 nm)	PLQY <sub>abs</sub> at 365 nm (%)	PLQY <sub>abs</sub> at 450 nm (%)
<b>CuInS<sub>2</sub>/ZnS red-emitting QDs</b>	solid	367	655	113.34 ± 0.26	30.9	28.9
	1.16 mg/ml, toluene	364	620	107.17 ± 0.13	41.5	35.9
	0.116 mg/ml, toluene	315	609	117.37 ± 0.06	16.6	9.9
	4.42 mg/ml, toluene	415	650	105.60 ± 0.16	31.6	30.8

The emission spectrum of 1.16 mg/mL red QDs in solution shows a large single peak with a narrow bandwidth (FWHM  $\approx$  107 nm). The maximum emission wavelength is found at 620 nm. At lower concentration of red QDs in solution, the emission spectrum has a larger bandwidth (FWHM  $\approx$  117 nm) with the maximum wavelength at about 609 nm. The photoluminescence of red QDs in solution states shifted to blue, which is associated with a decrease in energy transfer in closely packed QDs<sup>335, 343</sup>.

### **D. Photoluminescence properties of QDs composite films**

As the advantages previously mentioned in remote-phosphor configuration (see introduction, Chapter 1), the composite films involving different quantum dots as a phosphor embedded in the silicone resin are of interest in solid state lighting technology as they combine the good points of quantum dots (i.e. tunable emission by controlling the nanocrystal size and composition, good brightness, high quantum yield, and thermal stability) together with the advantage of polymer matrices such as the mechanical flexibility, transparency and ease of use for fabrication of LED devices. In this part, we have prepared flexible QDs light-emitting thin films consisting of QDs and two-component silicone resin polymer. The dispersion of QDs in polymer matrices widens the optical performance of QDs in solutions, in particular to benefit as thin films QDs for light-emitting applications.

#### **a. Composite films: quantum dots/silicone film**

In this work, three types of QDs-silicone films were prepared by dispersing 1 wt. % of QDs solid in silicone resin. The concentration of QDs was optimized in order to avoid the reabsorption of emission of QDs. In addition, the organic residue from long-chain organic ligands and/or solvents should be eliminated because they can hamper the polymerization of two-component silicones by reacting against the platinum catalyst in the component B<sup>344</sup>. Figure 112 shows the absorption and emission spectra of each QDs dispersed in silicone resin.

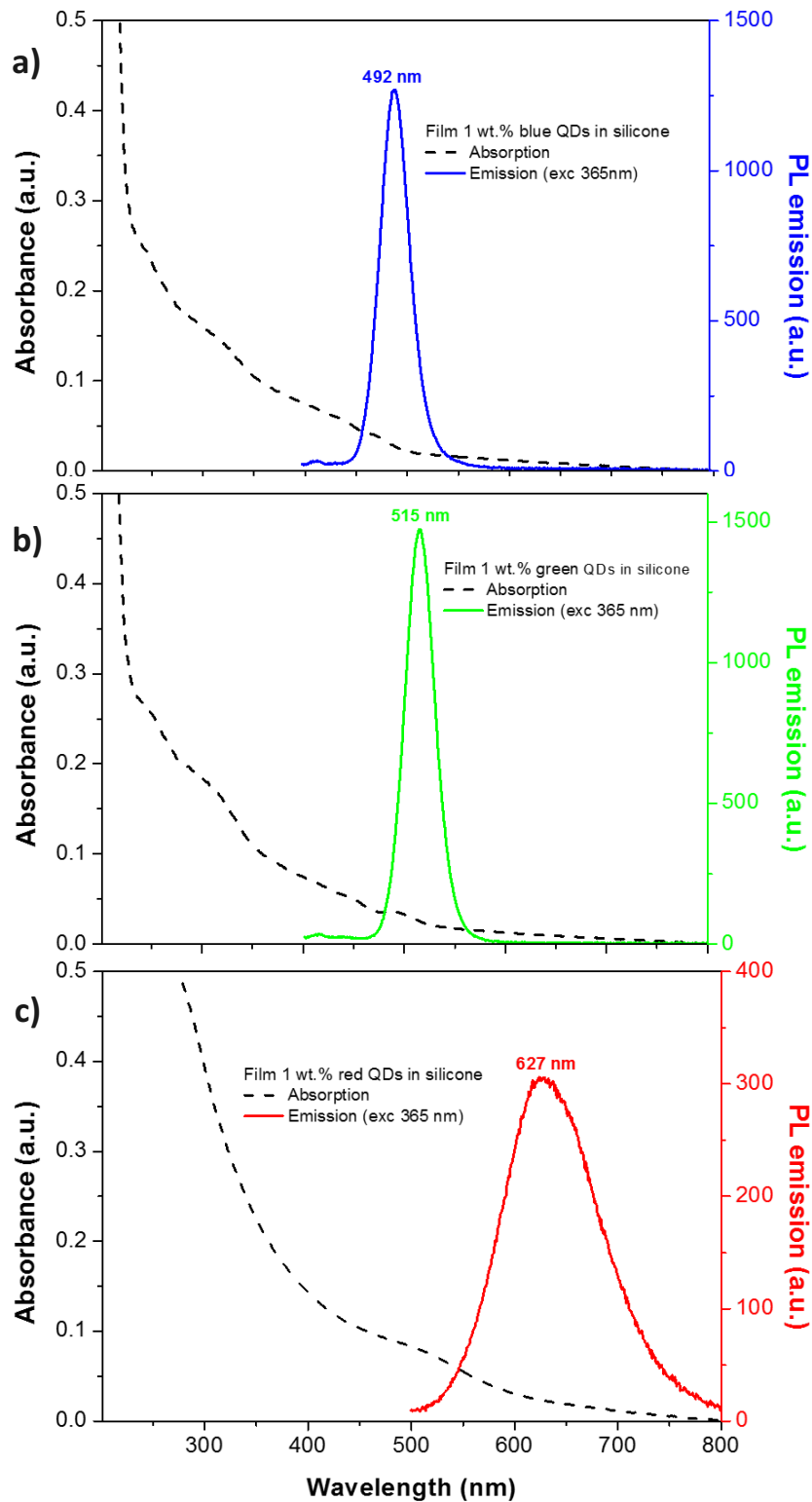


**Figure 112 Absorption and emission spectra of three types of QDs dispersed in silicone resin: (a) blue-emitting CdSe/ZnS-silicone film, (b) green-emitting CdSe/ZnS-silicone film, and (c) red-emitting CuInS<sub>2</sub>/ZnS-silicone film.**

The photoluminescence data of these QDs-silicone films were summarized in Table 36. As shown on Figure 112, we observe a large overlap between the absorption spectra of three kinds of QDs-silicone composite films. Thus, they could be excited at the same wavelength. This information provide the possibility of fabricating the QDs composite films offering a wide spectral range by mixing several types of QDs within the same polymer matrix.

**Table 36 Photoluminescence properties of QDs-silicone composite films. The photoluminescence properties of their QDs in solution are also presented in comparison.**

	Film thickness ( $\mu\text{m}$ )	PL $\lambda_{\text{max}}$ (nm)	FWHM of PL $\lambda_{\text{max}}$ (nm) (at 365 nm)	PLQY <sub>abs</sub> at 365 nm (%)	PLQY <sub>abs</sub> at 450 nm (%)
<b>1 wt. % blue QDs in QDs-silicone film</b>	245 ± 26	492	34.07 ± 0.02	26.5	15.1
1.14 mg/mL blue QDs in toluene	-	493	32.92 ± 0.03	43.7	27.0
<b>1 wt. % green QDs in QDs-silicone film</b>	212 ± 8	515	34.42 ± 0.04	30.7	18.7
1.15 mg/mL green QDs in toluene	-	515	34.04 ± 0.02	60.1	41.6
<b>1 wt. % red QDs in QDs-silicone film</b>	215 ± 14	627	110.36 ± 0.49	26.4	17.7
1.16 mg/mL red QDs in toluene	-	620	107.17 ± 0.13	41.5	35.9

Each QDs-silicone film exhibit a good transparency and a high photoluminescence under 365 nm UV-light excitation (Figure 113). These results of photographs might indicate that the QDs were homogeneously dispersed in the silicone resin with a very slightly agglomeration in the films. The emission spectra of both blue- and green-emitting CdSe/ZnS QDs-silicone films were nearly the same as their spectra in solution ( $\approx 1.15$  mg/mL). The emission spectrum of CuInS<sub>2</sub>/ZnS-silicone film was slightly shifted towards the red end (with a wavelength of maximum emission of 627 nm) compared to that of the QDs solution (1.16 mg/mL, with a wavelength of maximum emission of 620 nm). The absolute quantum yield (PLQY<sub>abs</sub>) of blue, green and red QDs-silicone film were about 26.5%, 30.7% and 26.4%, respectively. These absolute quantum yield of QDs-silicone films excited by 365 nm UV-light excitation were greater than those excited by 450 nm blue-light excitation (see Table 36), which were in



accordance with their related absorption spectra that indicated that the absorbance at 365 nm was much greater than of the same spectrum at 450 nm.

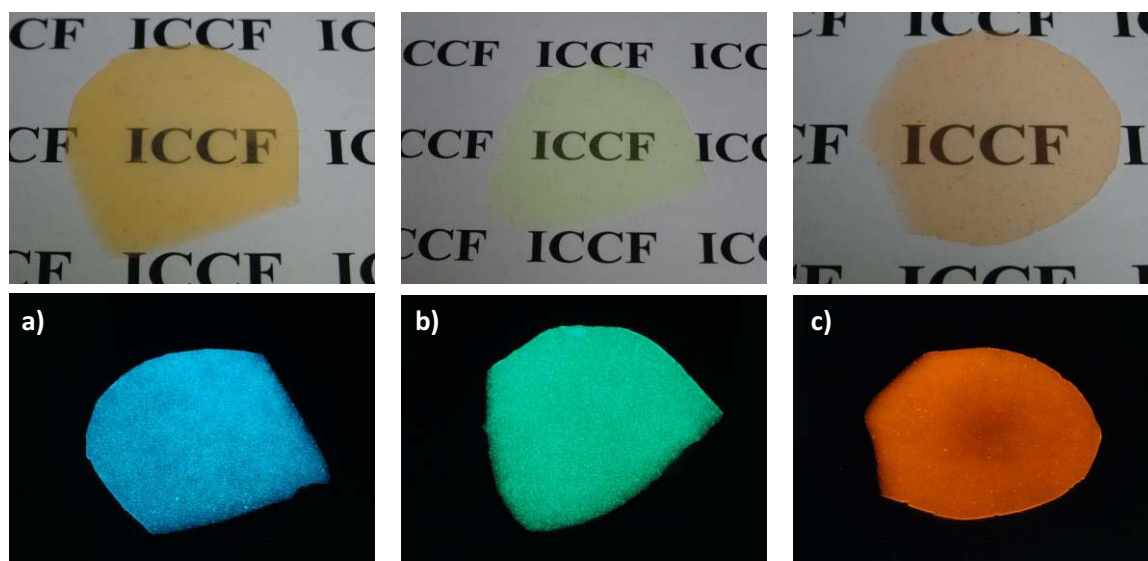


**Figure 113** Photographs of free-standing 1 wt. % QDs-silicone composite films (all above) under day light (all below) under a 365 nm UV illumination:  
(a) blue QDs, (b) green QDs, and (c) red QDs.

In order to investigate the performance parameters of light (electroluminescent spectrum, luminous efficacy, correlated color temperature, CIE color coordinates and color rendering index) emitted by QDs-silicone composite films, a piece of composite film with an appropriate size was placed remotely at a certain distance ( $\approx 2$  cm) above a LED chip and then tested in an integrating sphere under room temperature and applied voltage of 4 V. The composite films of blue-emitting CdSe/ZnS QDs (as noted by QD-I), green-emitting CdSe/ZnS QDs (as noted by QD-II), and red-emitting CuInS<sub>2</sub>/ZnS red-emitting QDs (as noted by QD-III) were selected for remote-phosphor system combined with 365 nm UV-LED irradiation. Figure 114 presents the photoluminescence (PL) spectra and the CIE coordinates of remote-phosphor configuration based on three QDs-silicone composite films excited by 365 nm UV-LED light. The PL emission peaks were found at 492, 515, and 627 nm, which were corresponding to the values recorded for PL emission of QDs-composite films.

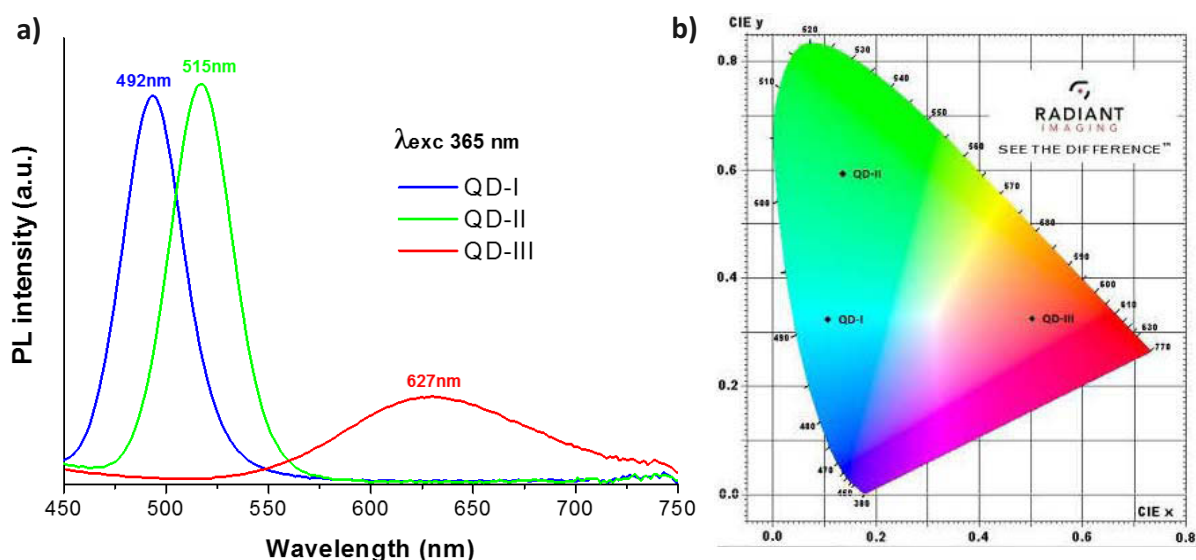


**Figure 114 (a) PL spectra and (b) CIE coordinates of blue-emitting CdSe/ZnS QDs (QD-I), green-emitting CdSe/ZnS QDs (QD-II) and red-emitting CuInS<sub>2</sub>/ZnS QDs (QD-III) composite films under 365 nm UV irradiation.**

Table 37 shows the performance parameters of light obtained from QDs-composite films in remote-phosphor configurations. This information can indicate the color point of different emitting lights in CIE color coordinate in which the possible combination of QDs emission can be optimized towards the white light point. Concerning all information previously, we could optimize the multicolored QDs system in order to produce white light.

**Table 37 Performance parameters of light obtained from remote-phosphor configurations consisting of 365 nm UV illumination and QDs-silicone composite films.**

Sample configuration	PL $\lambda_{max}$ (nm)	EL $\lambda_{max}$ (nm)	CIE (x,y)
365 nm UV-LED + 1%wt QD-I composite film	492	493	(0.108, 0.324)
365 nm UV-LED + 1%wt QD-II composite film	515	515	(0.136, 0.593)
365 nm UV-LED + 1%wt QD-III composite film	627	630	(0.503, 0.326)

**b. Color simulation for mixture of different QDs at 365 nm.**

In order to generate white light, a simulation of colorimetric properties (i.e. composition of QDs in composite films, chromaticity and color temperature) has been firstly studied. The simulation was performed by the color calculator software developed by OSRAM SYLVANIA.<sup>\*\*\*\*</sup> The simulation was used to determine the quantities of each QDs to be blended in order to get close to the ideal white light point with a CIE coordinate of (0.333, 0.333).

According to the different types of QDs as we had studied previously, the composite films of blue-emitting CdSe/ZnS QDs (as noted by QD-I) and red-emitting CuInS<sub>2</sub>/ZnS QDs (as noted by QD-III) were selected for operating the colorimetric simulation of white light emission combined with 365 nm UV-LED irradiation. The addition of green-emitting CdSe/ZnS QDs (as noted by QD-II) to the mixed QDs caused the shift in simulation spectrum away from the ideal white light point. It should be noted that the 365 nm UV-LED was used for colorimetric simulation because the photoluminescence properties of all quantum dots exhibited the better photoluminescence values with 365 nm UV-light excitation than those from 450 nm blue-light excitation.

The color calculator software calculated the luminous flux obtained from emission spectrum of selected QDs-silicone composite films combined with the luminous flux from 365 nm UV-LED chips. The final spectrum corresponded to the sum of each emission spectrum emitted by each selected QDs-silicone composite films and the emission spectrum from 365 nm UV-LED chips. However, the simulation results calculated by color calculator software did not perform the color rendering index (CRI) of each composition of mixed QDs. The results received by colorimetric simulation are presented in Table 38.

---

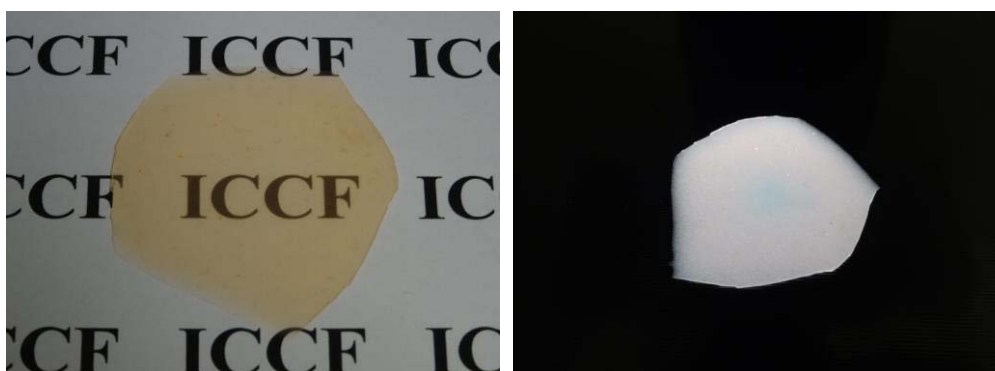
<sup>\*\*\*\*</sup> LED colorcalculator: available online at [www.sylvania.com/en-us/tools-and-resources/Pages/led-color-calculator.aspx](http://www.sylvania.com/en-us/tools-and-resources/Pages/led-color-calculator.aspx)

Table 38 Results obtained from colorimetric simulation with 365 nm LED chip for white light.

wt.% QD-I	wt.% QD-III	CIE x	CIE y	CCT (K)
27.3	72.7	0.4770	0.4137	2500
33.1	66.9	0.4369	0.4041	3000
37.2	62.8	0.4053	0.3907	3500
40.2	59.8	0.3804	0.3767	4000
42.4	57.6	0.3608	0.3635	4500
44.1	55.9	0.3451	0.3516	5000
44.4	55.6	0.3424	0.3494	5100
44.7	55.3	0.3397	0.3472	5200
45.0	55.0	0.3372	0.3451	5300
45.3	54.7	0.3348	0.3430	5400
45.5	54.5	0.3324	0.3410	5500
45.8	54.2	0.3302	0.3391	5600
46.0	54.0	0.3280	0.3372	5700
46.3	53.7	0.3260	0.3353	5800
46.5	53.5	0.3240	0.3335	5900
46.7	53.3	0.3221	0.3318	6000
46.9	53.1	0.3202	0.3300	6100
47.1	52.9	0.3185	0.3284	6200
47.3	52.7	0.3168	0.3267	6300
47.5	52.5	0.3151	0.3252	6400
47.6	52.4	0.3135	0.3236	6500

### c. Composite films: mixed quantum dots/silicone film

Considering the colorimetric simulation previously, we could prepare a mixture of quantum dots embedded in the silicone resin for white light-emitting system. The composite films of QDs mixture were provided by dispersing the mixture of 47 wt. % of blue-emitting CdSe/ZnS QDs and 53 wt. % of red-emitting CuInS<sub>2</sub>/ZnS QDs in a silicone resin. The volume ratio of QDs was selected in order to get close to the ideal white light point with a CIE coordinate of (0.333, 0.333). The concentration of mixed QDs in silicone resin were prepared at 1 wt. %. The composite films are a transparent with uniform thickness of  $278 \pm 13 \mu\text{m}$  as well as high photoluminescence under UV lamp (Figure 115). The absolute quantum yield of mixed QDs composite film was about 30% and 19% under 365 nm UV-light excitation and 450 nm blue-light excitation, respectively.



**Figure 115 Photographs of free-standing 1 wt. % mixed QDs-silicone composite film (left) under normal light and (right) under a 365 nm UV illumination.**

The PL spectra of white LEDs constructed by placing the composite film of mixed QDs at a distance of 2 cm over a LED chip was investigated as well as other the performance parameters of light (luminous efficacy, correlated color temperature, CIE color coordinates and color rendering index). It should be noted that, during the remote-phosphor test, the film thickness of composite films over a LED chip was an important parameter to be considered. Indeed, when the composite films was too thin, a high concentration of QDs should be required in order to extract the maximum light emitted from a LED chip. However, this effect would encounter with the QDs aggregation in the composite film, resulting fluorescence quenching. On the other hand, the much thick composite film could lead to weak transmittance.

Firstly, a monolayered 1 wt. % mixed QDs composite film based white LEDs was measured to testify the configuration. However, the UV light from the LED chip was not absorbed enough and led light pass through the composite film, resulting to the low UV to white light conversion.

Therefore, the multi-layered mixed QDs composite films were used at about 830  $\mu\text{m}$ , corresponding to three-stacked 1 wt. % mixed QDs monolayers, in order to minimize the light emission by LED chip. The PL spectra of multi-layered 1 wt. % mixed QDs composite films based white LED was studied under different forward currents ranging from 100 to 600 mA, as shown in Figure 116. The PL spectra show the increase in intensity without saturation effect when the forward current augments from 100 to 600 mA. The correlated color temperature (CCT) increased from 2988 K at 100 mA to 3449 K at 600 mA related to the change in CIE color coordinates of  $x = 0.4147$ - $0.3959$  and  $y = 0.3570$ - $0.3602$ . However, the color rendering index (CRI) was fallen off from 46 at 100 mA to 43 at 600 mA, corresponding to a drop of CRI about 6.7%, as shown in Figure 117a. Another parameter which can indicate the color quality is defined by the distance from the Planckian locus (see introduction) on the CIE color coordinates (Duv). It is well known that sources at distances greater than 0.0054 ( $Duv = \sqrt{\Delta u^2 + \Delta v^2}$ ) from the Planckian locus are not true white light sources.<sup>210</sup> In our study, the Duv values were found from  $-0.0119$  to  $-0.0170$ , indicating that white-light emission produced by our mixed QDs composite films based LED was still far from a true white light system. Accordingly, the evolution of the colorimetric parameters with increasing forward currents showed that the stability of our QDs based systems has become an important consideration to improve and develop in order to ensure the performances of white LED devices.

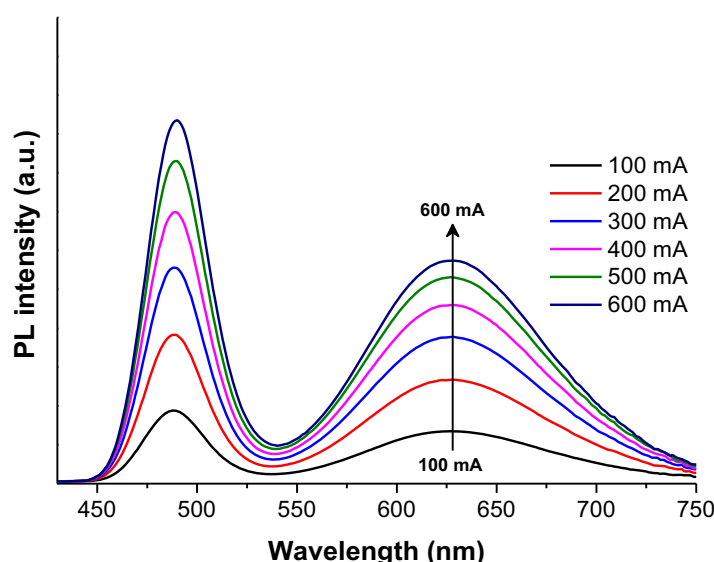
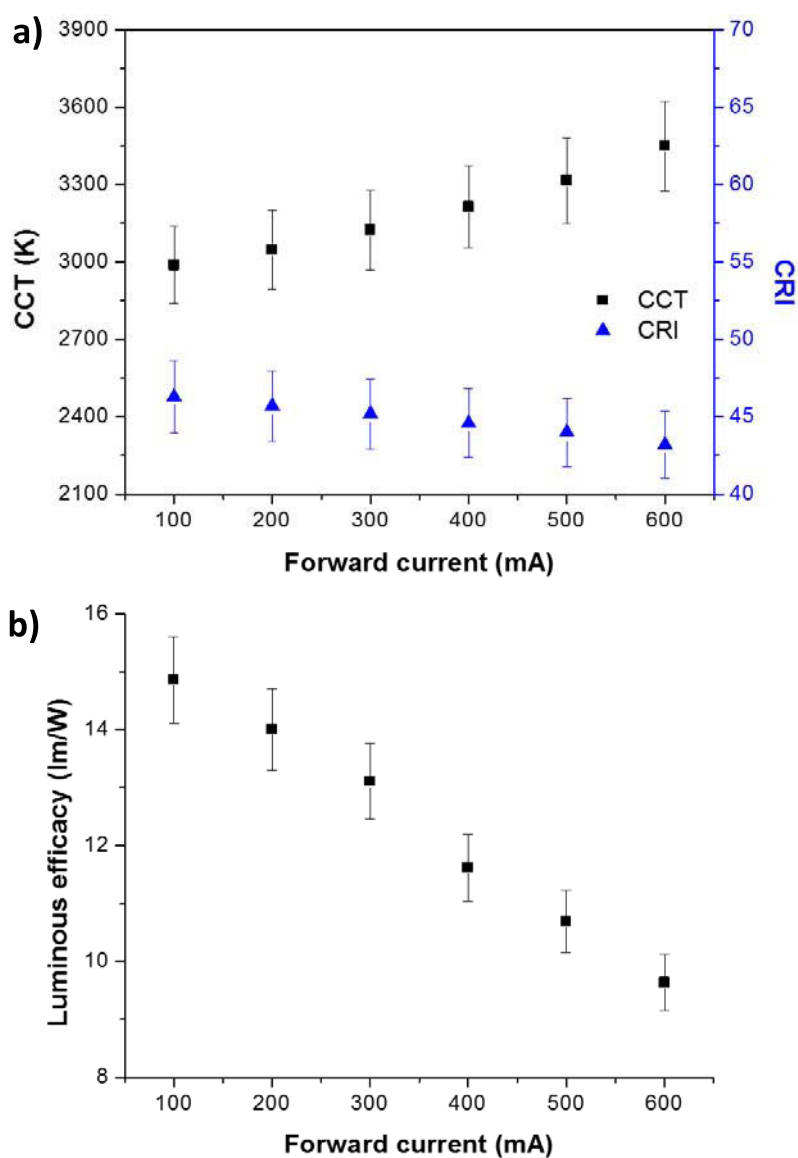


Figure 116 PL spectra of multi-layered 1 wt. % mixed QDs-silicone composite films based white LED with increasing forward currents.



**Figure 117 (a) Evolution of (a) CCT and CRI and (b) luminous efficacy of multi-layered mixed QDs-silicone composite films based white LED under different forward currents from 100 to 600 mA.**

Furthermore, the luminous efficacy of the white LED system decreased from 14.8 to 9.6 lm/W in the 100-600 mA range, corresponding to a drop of about 35% (Figure 117b). In order to ensure that the 365 nm UV-LED chip does not have any intrinsic influence on the drop in luminous efficacy of multi-layered mixed QDs composite films based white LED, the bare UV-LED chip was also measured under different forward currents from 100-600 mA. The result showed a small reduction of luminous efficacy from 0.86 lm/W at 100 mA to 0.81 lm/W at 600 mA, corresponding to a drop at about 6%. The result led to conclude that the 365 nm UV-LED chip has a small impact on the luminous efficacy of multi-layered mixed QDs composite films based white LED.

In comparison to 1 wt. % mixed QDs-silicone composite film, a concentration of mixed QDs in silicone resin were also prepared at 2 wt. %. A monolayered 2 wt. % mixed QDs composite film has a uniform thickness of  $177 \pm 15 \mu\text{m}$  presenting a good transparency in the visible light as well as high photoluminescence under UV lamp (Figure 118). The absolute quantum yield of mixed QDs composite film was about 34% and 23% under 365 nm UV-light excitation and 450 nm blue-light excitation, respectively.



**Figure 118 Photographs of free-standing 2 wt. % mixed QDs-silicone composite films (left) under normal light and (right) under a 365 nm UV illumination.**

As with the 1 wt. % mixed QDs-silicone composite film, the multi-layered mixed QDs composite films were also fabricated with the thickness of about  $531 \mu\text{m}$ , corresponding to three-stacked 2 wt. % mixed QDs monolayers. Figure 119 presents the PL spectra of multi-layered 2 wt. % mixed QDs-silicone composite films based white LED with various forward currents from 100 to 600 mA. The PL intensity of  $\text{CuInS}_2/\text{ZnS}$  QDs emission was starting to reach a saturation point with increasing forward bias from 500 mA. The saturation of  $\text{CuInS}_2/\text{ZnS}$  QDs emission was also reported as well as blue-sided shift of the CIE color coordinates without any further explanations in details<sup>345,346</sup>. In our study, the correlated color temperature (CCT) increased from 2712 K at 100 mA to 3594 K at 600 mA and were consistent with the blue-sided shift in CIE color coordinates of  $x = 0.4377\text{-}0.4001$  and  $y = 0.3722\text{-}0.3878$ . The shift from Planckian locus on the CIE color coordinates of this remote-phosphor system were obtained from  $-0.0001$  to  $-0.0131$ , which was quite moderate for white light source. The luminous efficacy also tends to drop from 14.3 lm/W at 100 mA to 7.8 lm/W at 600 mA, corresponding to a drop at about 45%.



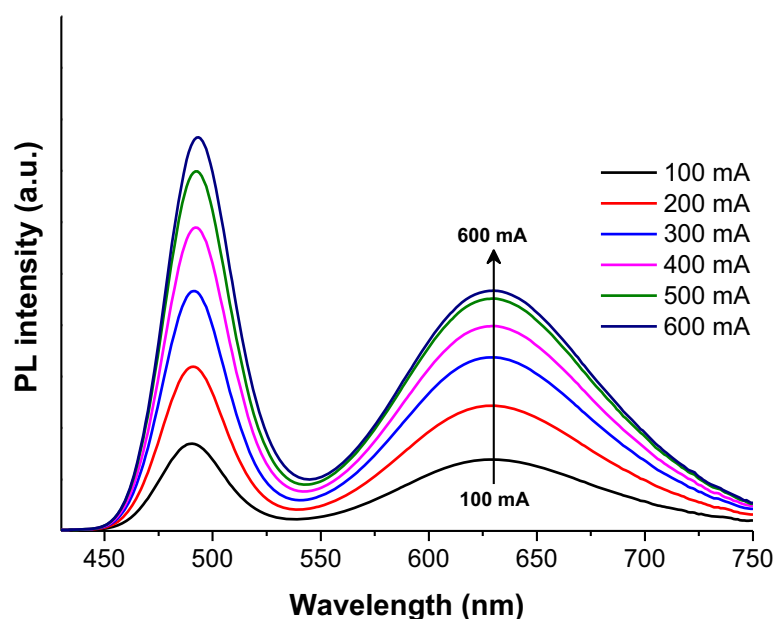


Figure 119 PL spectra of multi-layered 2 wt. % mixed QDs composite films based white LED with increasing forward currents.

### E. Study of photo-degradation of QDs composite films

It is well-known that polymers are sensitive to physical parameters such as temperature, light and also relative humidity. The degradation of polymers by these factors could decrease the lifetime of WLEDs. When a UV-LED chip was applied to the quantum dots-based WLEDs, the fundamental study on the mechanism of degradation and the properties of polymers at the operating conditions for WLED system is becoming an important point to take forward in order to further improve and guarantee the performance of quantum dots-based white LEDs. In this study, the individual and mixed quantum dots obtained as composite films were irradiated in a SEPAP 12/24 unit at wavelength longer than 300 nm ( $\lambda > 300$  nm), under control temperature at 60°C and rotation at a constant speed and distance from the source.

#### a. Photo-degradation of QDs composite films

Infrared spectroscopy and UV-visible absorption spectroscopy have become a useful analytical tool to follow the photo-oxidation process of composite films. In this case, each QDs composite films were investigated under irradiation at  $\lambda > 300$  nm and heating at 60°C as well as the QDs mixed composite film. Figure 120 gathers the infrared spectra of QDs-silicone composite film during photo-oxidation, in particularly the range of 4000-3200  $\text{cm}^{-1}$  and 1800-1650  $\text{cm}^{-1}$  in

which the photo-oxidation behaviors can obviously observed. The IR spectra show a slight increase in absorbance in both domains, which correspond to the hydroxyl and carbonyl regions. It should be noted that the IR absorption at  $3450\text{ cm}^{-1}$  was related to the harmonic vibration at  $1725\text{ cm}^{-1}$ , corresponding to the functional group of carbonyl compounds. The similar modifications of IR spectra of green QDs-silicone composite film were also observed under the same irradiation in the presence of oxygen (Figure 121). In the case of red QDs-silicone composite film, the modifications of IR spectra were more visible. The large increase in the absorbance was recorded in the domains of hydroxyl, carbonyl regions and also some adjacent areas (Figure 122).

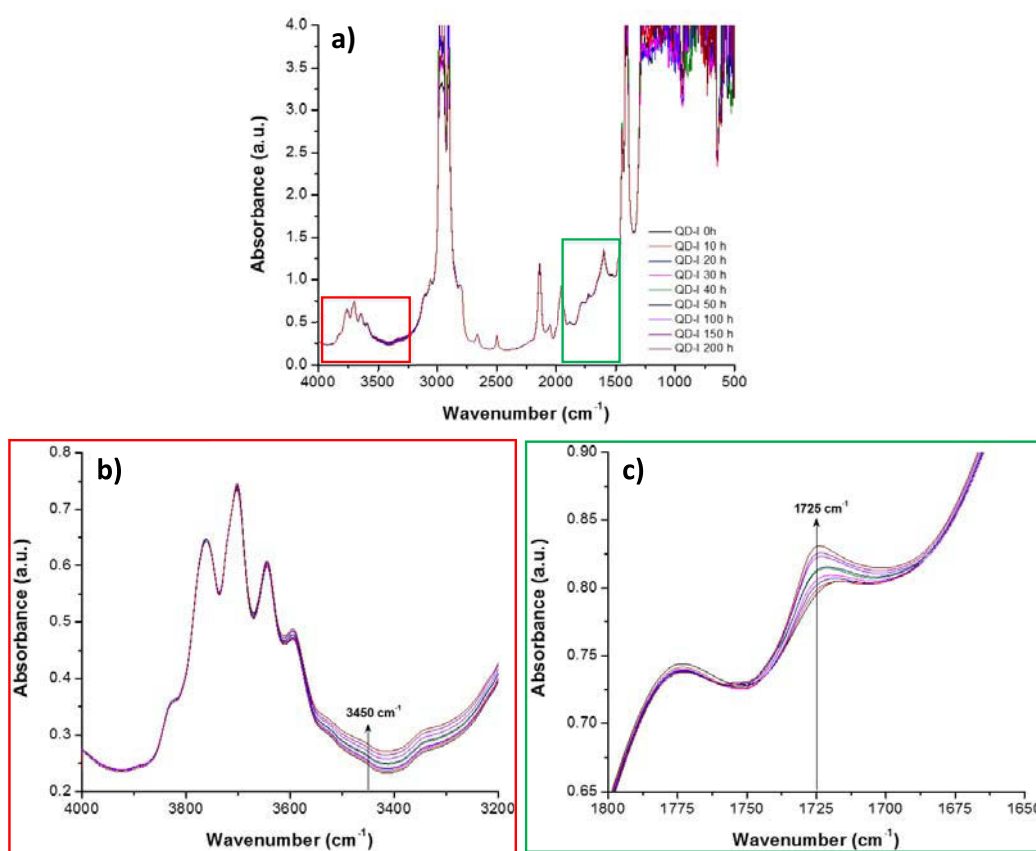


Figure 120 (a) Evolution of infrared spectra of 1 wt. % blue-emitting CdSe/ZnS QDs-silicone composite film during photo-oxidation in the absorption range, (b) zone  $4000\text{-}3200\text{ cm}^{-1}$  and (c) zone  $1800\text{-}1650\text{ cm}^{-1}$ .

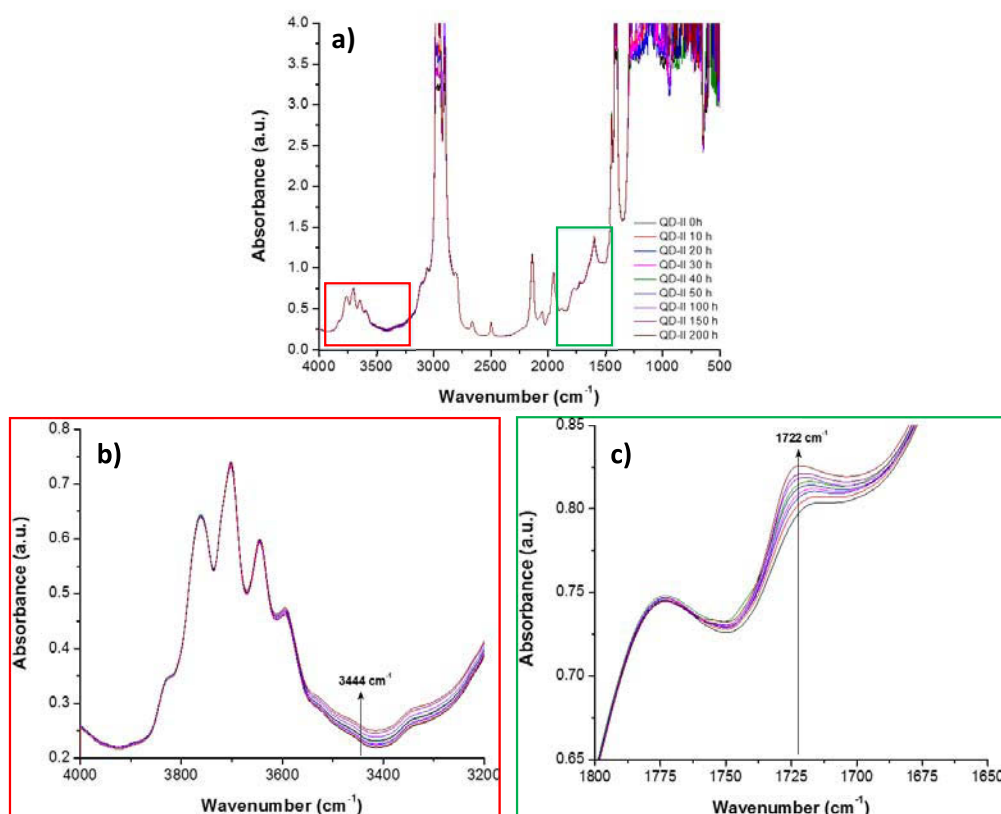


Figure 121 (a) Evolution of infrared spectra of 1 wt. % green-emitting CdSe/ZnS QDs-silicone composite film during photo-oxidation in the absorption range, (b) zone 4000-3200  $\text{cm}^{-1}$  and (c) zone 1800-1650  $\text{cm}^{-1}$ .

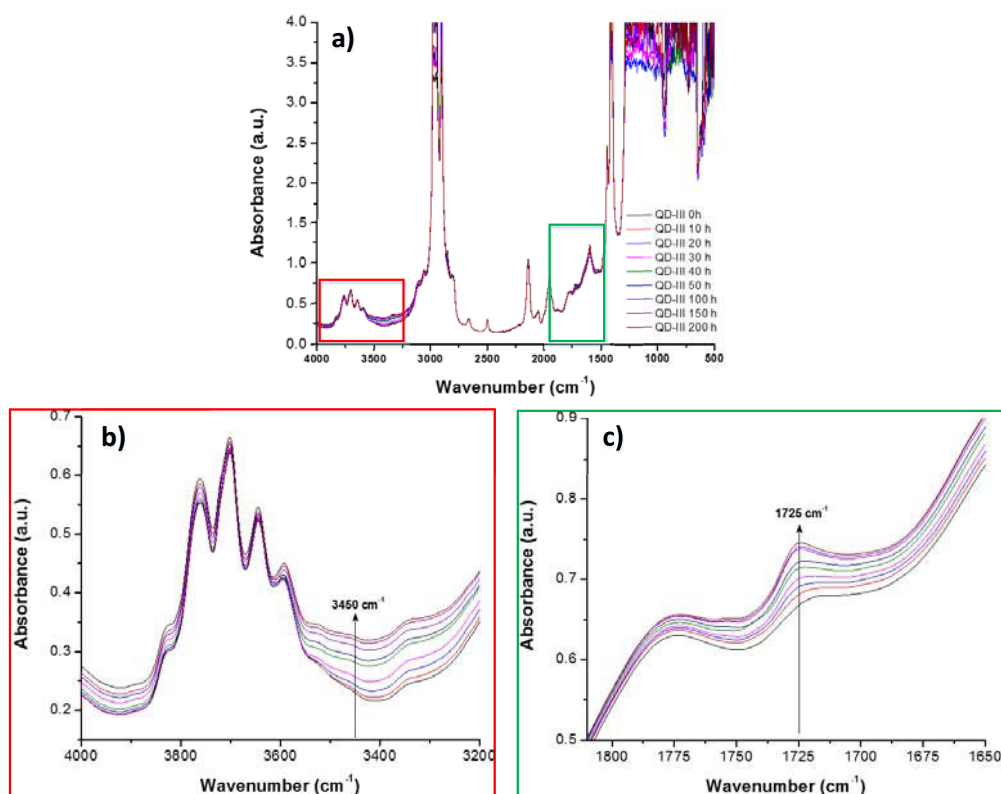
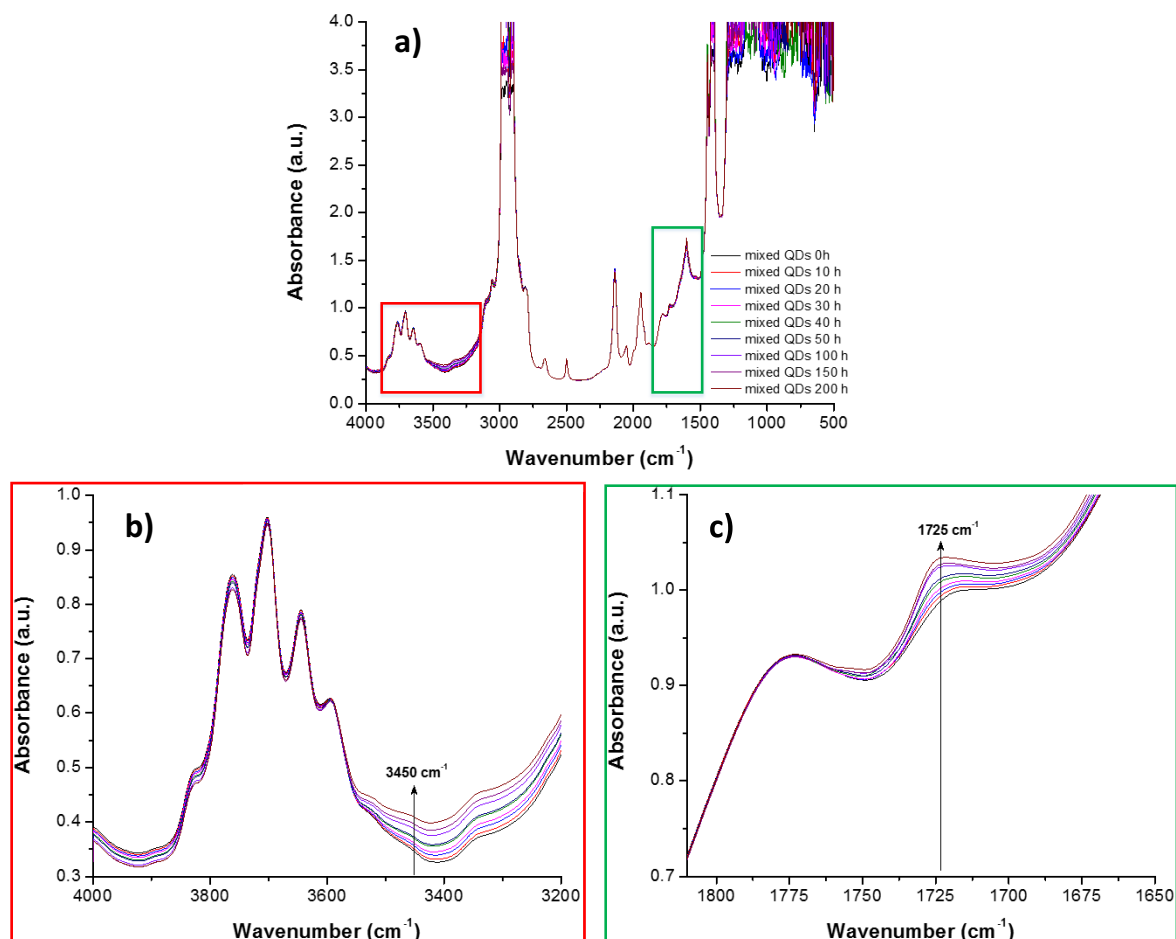


Figure 122 (a) Evolution of infrared spectra of 1 wt. % red-emitting  $\text{CuInS}_2/\text{ZnS}$  QDs-silicone composite film during photo-oxidation in the absorption range, (b) zone 4000-3200  $\text{cm}^{-1}$  and (c) zone 1800-1650  $\text{cm}^{-1}$ .

In the case of 1 wt.% mixed QDs-silicone composite films (Figure 123), the increase in both hydroxyl and carbonyl regions was caused by the combination degradation of blue-emitting CdSe/ZnS and red-emitting CuInS<sub>2</sub>/ZnS QD-silicone composite films under UV irradiation at wavelength longer than 300 nm.



**Figure 123 a) Evolution of infrared spectra of 1 wt. % mixed QDs-silicone composite films during photo-oxidation in the absorption range, (b) zone 4000-3200 cm<sup>-1</sup> and (c) zone 1800-1650 cm<sup>-1</sup>.**

Concerning the previous results, the detection of hydroxyl and carbonyl compounds by IR spectroscopy should be a good evidence for the presence of chromophores in our QDs composite films. According to the synthesis of QDs, the chromophores could be derived from the precursor used in the synthesis of QDs as well as the by-products. The blue- and green-emitting CdSe/ZnS QDs were synthesized by using 1-dodecanethiol as a binding ligand to the core/shell QD surfaces in order to improve the photoluminescence properties of quantum dots and also increase the solubility in various organic solvents. Regarding the synthesis of red-emitting CuInS<sub>2</sub>/ZnS QDs, 1-dodecanethiol was used as sulfur sources for the formation of

CuInS<sub>2</sub> nanocrystals as shown in Figure 124<sup>9</sup>. In addition, the residual by-products of QDs synthesis such as hydrocarbon compounds could remain in the QD nanocrystals as impurities.

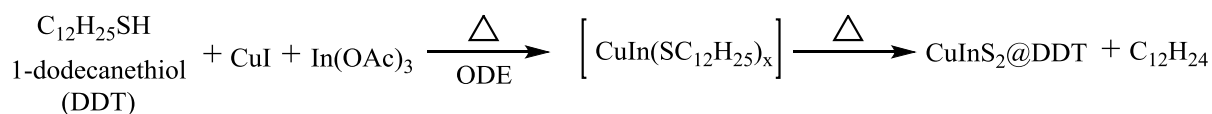


**Figure 124 Synthesis route of CuInS<sub>2</sub> QDs<sup>9</sup>.**

Referring to the previous point, the presence of chromophores as binding ligands and/or organic residues could activate the photo-oxidation of QDs composite films. However, this factor should hardly influence the optical properties of QDs composite films because the quantum dot cores were shielded by ZnS passivation layer with the purpose of protecting from the photo-oxidation in the presence of oxygen<sup>125</sup>. In addition, the ZnS shell can also enhance the quantum yield of QDs<sup>137, 140</sup>. In order to ensure the optical properties of QDs composite films after UV irradiation, the optical properties were performed at room temperature using an integrating sphere and a spectrophotometer.

### **UV-visible and photoluminescence properties of QDs composite films**

The UV-visible absorption spectra of QDs composite films were recorded before and after UV exposure for 200 h under accelerated artificial conditions (Figure 125). The inset in each UV-visible absorption spectrum showed the evolution of absorbance as a function of irradiation time at 237 nm. The absorbance reached the maximum values at the first 50 h UV irradiation and then simultaneously fallen back down. This absorption might be due to the presence of chromophores and/or oxidation products from QDs-silicone composite film. In the case of blue- and green-emitting CdSe/ZnS QDs composite film, the modification of absorbance were observed at the wavelengths < 400 nm. On the other hand, the red-emitting CuInS<sub>2</sub>/ZnS QDs composite films presented the increase in absorbance in the large range from UV to visible regions, resulting in the color change of film. The mixed QDs composite film was the combination of the absorption spectra of blue and red QDs.

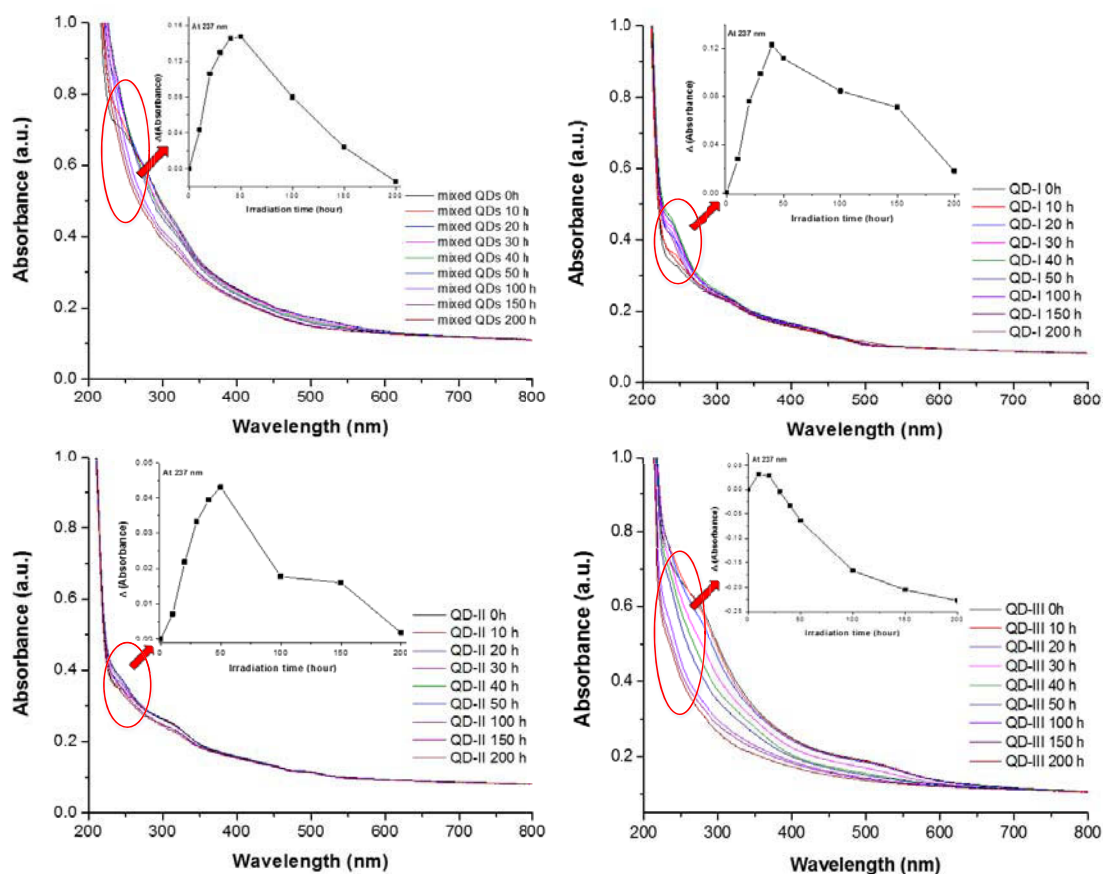


**Figure 125 Evolution of UV-visible absorption spectra of QDs composite films before and after UV irradiation for 0 and 200 h under accelerated artificial conditions. The inset in each graph illustrate the difference of absorbance at 237 nm as a function of irradiation time.**

Figure 126 illustrates the modification of PL emission spectra of each QDs composite film and mixed QDs composite film before and after 200 h UV irradiation under accelerated artificial conditions. The emission spectra of blue- and green-emitting CdSe/ZnS QDs-silicone composite films was approximately 10 nm of red-shifted with the decrease in emission intensity after 200 h UV irradiation (Figure 126, b and c). Furthermore, the emission spectra of red-emitting CuInS<sub>2</sub>/ZnS QDs-silicone composite film and the 1 wt. % mixed QDs-silicone composite film were disappeared after 200 h UV irradiation (Figure 126, a and d) relating to the decrease in absorbance recorded previously.

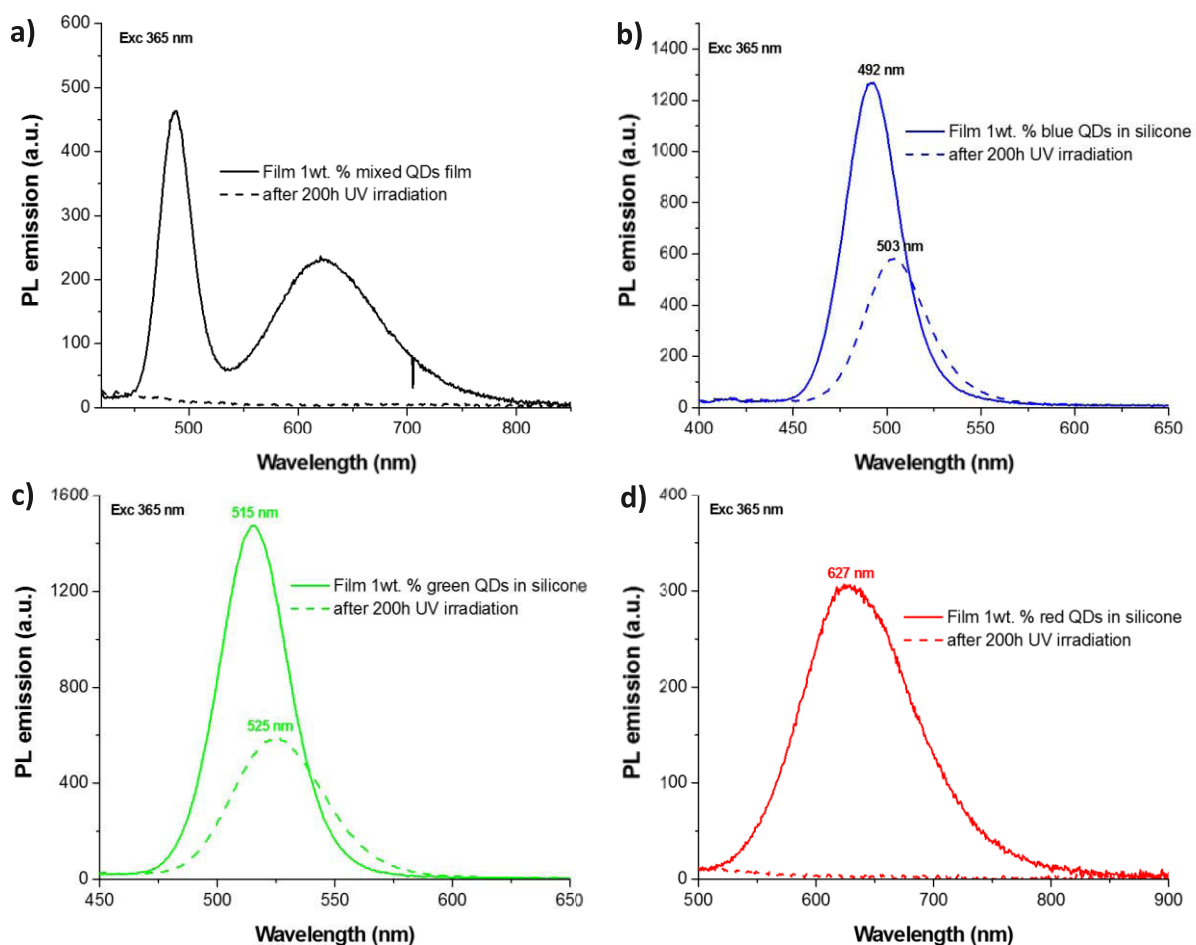


**Figure 126 Evolution of emission spectra of QDs composite films before and after UV irradiation for 0 and 200 h under accelerated artificial conditions.**

The photoluminescence quantum yield of QDs composite films under UV irradiation were also investigated. Table 39 presents the absolute quantum yields of QDs composite films before and after UV irradiation for 0 and 200 h under accelerated artificial conditions. The significant reduction of quantum yield were recorded for all QDs composite films after 200 h UV exposure under accelerated artificial conditions. Interestingly, the red QDs-based composite films showed a very weak quantum yield close to zero, corresponding to their weak emission spectra recorded previously.

**Table 39 Absolute quantum yields of QDs composite films before and after UV irradiation for 0 and 200 h under accelerated artificial conditions.**

Composite films	Before UV irradiation		After 200h UV irradiation	
	PLQY <sub>abs</sub> at 365 nm (%)	PLQY <sub>abs</sub> at 450 nm (%)	PLQY <sub>abs</sub> at 365 nm (%)	PLQY <sub>abs</sub> at 450 nm (%)
1wt.% blue QDs in silicone	26.5	15.1	14.6	8.1
1wt.% green QDs in silicone	30.7	18.7	16.3	10.3
1wt.% red QDs in silicone	26.4	17.7	0.1	0.1
1wt.% mixed QDs in silicone	30.0	18.7	0.9	0.5

Accordingly, it should be noted that the red-shifted phenomena and the decrease in emission intensity of blue and green QDs-silicone composite films appeared to contradict some studies carried out for CdSe/ZnS QDs. A blue-shifted emission of CdSe/ZnS QDs should be observed during illumination<sup>347, 348</sup>. The research group of Carrillo-Carrion explained the increase of optical properties of CdSe/ZnS QDs after exposure to UV light by further cross-linking and polymerization of polymer passivation layers which can strengthen the surface passivation of QDs<sup>348</sup>. Another explanation for the increase in optical properties of QDs was also proposed by the group of Andries Meijerink in that the UV curing and the photochemical reaction at the surface of the QDs enhanced their photoluminescence quantum yield<sup>349</sup>. In presence of oxygen, ZnS molecules can be photo-oxidized to oxidation products (such as ZnSO<sub>4</sub>) which served as a good passivation layer as well as ZnS layer in order to reduce nonradiative process of QDs<sup>349</sup>. However, this phenomenon was realized for a short moment. The same author assumed that the continuous UV irradiation for longer times in the presence of oxygen and humidity can lead to the coloration and the decrease in optical properties of ZnS-based QDs by darkening of ZnS itself<sup>349-351</sup>. In addition, the photo-oxidation of QD core can lead to the reduction of optical properties of CdSe/ZnS QDs by diffusion of oxygen through the imperfect passivation layer. The published studies of Van Sark et al, have described the formation of surface quenching states CdSe/CdSeO<sub>x</sub> that causes a decrease of the number of photons emitted, resulting to the reduction of photoluminescence quantum yield<sup>347</sup>.



In the case of red-emitting CuInS<sub>2</sub>/ZnS QDs and mixed QDs-composite films, the dramatic reduction in emission intensity and photoluminescence quantum yield could lead to the assumption that it should have another mechanism to explain the photo-degradation of QDs composite films, particularly with QDs nanocrystals. The group of Eun-Pyo Jang also reported the significant decrease of emission spectra for a prolonged duration up to 20 h when the QD plates were remotely placed on a blue LED chip. According to our results, the photo-degradation of red-emitting CuInS<sub>2</sub>/ZnS QDs was considerably more rapid than CdSe/ZnS QDs. The phenomenon of degradation of CuInS<sub>2</sub>/ZnS QDs could be explained by QD core photo-oxidation. When the ZnS shell was coated incompletely on the QD core, the passivation layer would not be fully functional to protect the QD core. Then oxygen could diffuse to the QD core and oxidize CuInS<sub>2</sub> to form CuInS<sub>2</sub>O<sub>x</sub>, resulting in decrease of emission intensity of QDs<sup>117, 352</sup>.

### Summary

The quantum dots-typed core/shell CdSe/ZnS and CuInS<sub>2</sub>/ZnS exhibit high photoluminescence properties with the absolute quantum yield up to 30% under UV-LED excitation to be proposed as good candidates for generating white light-emitting LEDs by combining three-colored QDs and UV-LEDs. However, the stability of CuInS<sub>2</sub>/ZnS QDs-silicone composite films has become a big remark due to the strong reduction of photoluminescence properties after photo-degradation under accelerated artificial conditions close to operating conditions of LEDs. Although the degradation of CdSe/ZnS QDs-silicone composite films represented with slower rate compared with CuInS<sub>2</sub>/ZnS system, this degradation of red QDs can also influence on the mixed QDs-composite films in term of both emission intensity and photoluminescence quantum yield. Therefore, the photo-degradation of QDs are the big issues that must be realized and resolved. The possibilities to improve the optical stabilities of QDs might be the use of other polymer matrices offering higher passivation barrier to oxygen and water than silicone resin (e.g. poly (ethylene terephthalate) or epoxy resin) and/or inorganic barrier layer (e.g. silica by sol-gel method).





---

**General conclusion  
and  
Perspectives**

---



### General conclusion and perspectives

The main objective of this thesis work was to develop the rare-earth-free luminescent materials which are compatible with commercial UV and/or blue light LEDs to generate white light for domestic indoor lighting (with the requirements of CRI > 80 and color temperature between 3000-4000K). These kinds of lighting devices based on LEDs are proposed to take over from energy-consuming lighting technologies due to their energy saving, environmental friendly and very long lifetimes with high luminous efficiency. As mentioned in the first chapter, we present the evolution of lighting technologies and arrival of LED-based lighting devices to the lighting markets. We have described deeply the LED technologies in term of the combination of commercial LEDs associated with luminescent materials, especially the rare-earth-free luminescent compounds to generate white light.

According to our results, the research studies have been conducted on organic phosphors and core-shell quantum dots. As with the reasons of low cost of production and the abundant of choices, these rare-earth-free luminescent materials can serve as promising materials for replacing current rare-earth luminescent compounds.

The remote phosphor configuration system is a remarkable technology for white light LEDs because of the phosphors (as thin composite films) can be located far away from the LED chips, leading to the reduction of operating temperature of device and providing many choices of phosphors to work with the system at lower operating temperatures.

The organic phosphors can be categorized into 2 groups corresponding to their emission behavior. The aggregated-induced emission (AIE) organic phosphors can produce the light emission in solid state, which serve as excellent alternative choices for solid-state lighting applications. On the other hand, many organic phosphors exhibit the contrary behavior as aggregated-caused quenching (ACQ) emission. This class of organic phosphors present no emission in solid state but highly photoluminescence in dilute solution. In order to maintain their photoluminescence as in dilute solution, y were embedded in inorganic matrices such as SiO<sub>2</sub> and LDH structures, producing the dilute state in solid state and reducing the possibility of molecular aggregation.

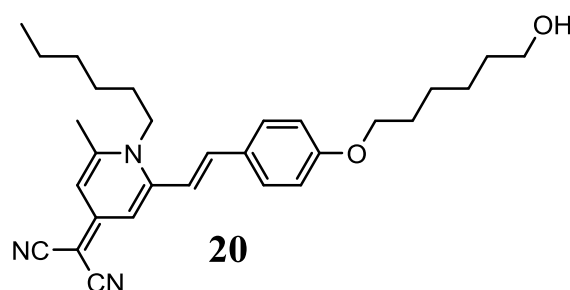
In the second chapter of our thesis, the organic phosphors presenting the AIE behavior were investigated and the organic molecules in each group having the best value in absolute quantum yield were chosen to prepare the mixed phosphors composite films for achieving organic phosphors-based white light-emitting diodes using 365 nm UV-light excitation. The blue-

## General Conclusion and perspectives

---

emitting organic phosphor with hexylamino group (compound 4 from DMPP derivatives) and the red-emitting one with phenyl part (compound 6 from DCMSP derivatives) have the highest emission intensity and the highest absolute quantum yield under 365 nm UV-light excitation (30% and 10%, respectively). The Al-MPBH (compound 12), which presented highly green emission in solid state with absolute quantum yield of 28% (under 365 nm UV-light excitation), was selected as green organic phosphor. We showed that the combination of mixed organic phosphors-silicone composite films with a 365 nm UV-LED can produce a white emission with a CRI > 75 and a color temperature close to 4000 K. However, the thermal stability and the photo-degradation of organic phosphors are still the big issue to resolve and develop for further work with LEDs.

According to the studies of DMPP and DCMSP derivatives, the synthesis of new molecule using the structural ideas which exhibit the best performance in absolute quantum yields are now under investigations such as compound 20. This molecule represents a promising choice of AIE behavior for solid-state organic luminescent materials. Moreover, it can be incorporated in the inorganic matrix by encapsulation in silica nanoparticles or by intercalation into layered double hydroxides (LDH) structures via the weak interactions of hydroxyl groups on **20** with inorganic structures as well.



Besides, the development of Al-complex series will be another goal in order to enhance their photoluminescence properties. The points of interest includes the nature of Al precursors as well as the synthesis methods (by tuning the synthetic conditions such as the composition between Al and ligands, reaction medium, temperature, etc.). Moreover, the study of crystal structure should be determined to understand the physical properties and also predict the optical properties of Al-complexes.

The study of encapsulation of organic phosphors in the inorganic matrix were proposed for the organic phosphors with ACQ effect in order to keep their excellent photoluminescence properties as in dilute state for solid-state lighting applications. The use of fluorescein was a

## General Conclusion and perspectives

---

great example of ACQ molecules for our investigations. The fluorescein encapsulated silica nanoparticles exhibited high photoluminescence properties in solid state and can be elaborated as luminescent composite films for lighting applications. The optical stability of the system was confirmed under 450 nm blue light excitation for several hours. The association of FC@SiO<sub>2</sub> nanoparticles (15 wt. %) embedded in silicone with a blue LED chip can lead to a near-white emission with cool color temperature (> 6000 K) and reach the maximum luminous efficacy of 26 lm/W under forward current of 100 mA. Moreover, the system of FC@SiO<sub>2</sub> nanoparticles can be able to undergo the improvement and development in order to increase photoluminescence properties and light performance by using red compounds such as ATTO490LS@SiO<sub>2</sub> nanoparticles in the suitable ratio to FC@SiO<sub>2</sub> nanoparticles. In contrast to FC@SiO<sub>2</sub> nanoparticles, the fluorescein intercalated Mg-Al-LDH matrix with the best result showed low photoluminescence properties, and still need further improvement for lighting applications.

The quantum dots-typed core/shell CdSe/ZnS and CuInS<sub>2</sub>/ZnS were investigated for their photoluminescence properties and the possibility to be associated with commercial LEDs. The QDs contained films presented high photoluminescence properties with absolute quantum yields up to 30% under UV-LED excitation. Thus, they can be considered as candidates for achieving white light-emitting LEDs by combining three-colored QDs. However, the drop of photoluminescence properties of red QDs hampers the stability of both sole QDs and mixed QDs for lighting applications based on LEDs.

The prospective study of core-shell semiconductor nanocrystal for lighting applications is another point of concern by using cadmium-free starting materials like CuInS<sub>2</sub> QDs in our report. The cadmium is known as a toxic element and can be harmful to human even at low levels. Although, the synthesis of core-shell QDs have been proposed in order to prevent the leakage of toxic elements from QD core structure, the role of this protective layer are needed some further investigations to ensure their properties of protection.

Accordingly, our studies of organic phosphors and also CuInS<sub>2</sub>/ZnS QDs were confronted with the stability under operating conditions of LEDs, resulting to the reduction of their photoluminescence properties. Since our studies pointed out the weakness in term of stability, there is still a lot of work to be done. The possibilities to increase the optical stabilities might be the use of other polymer matrices offering higher passivation barrier to oxygen and water than silicone resin (e.g. poly (ethylene terephthalate) or epoxy resin) and/or inorganic barrier



## **General Conclusion and perspectives**

---

layer (e.g. silica by sol-gel method). Moreover, the development of encapsulation methods for organic phosphors by changing the nature of inorganic matrix should be an endeavor to enhance their thermal stability and improve their photoluminescence properties. Furthermore, the profound investigation in photo-degradation of organic phosphors and/or core-shell quantum dots-silicone composite films is a point of interest in order to understand the mechanisms behind the reactions and also serve as a guideline to reduce or prevent the photo-degradation of composite films during operating conditions of WLEDs.

All our thesis work on rare-earth-free luminescent materials have opened to another kinds of luminescent components outside the world of inorganic luminescent materials that have been intensively studied by our group of Materials for Optics (MO). Although these rare-earth-free luminescent materials have presented lower photoluminescence properties compared with commercial rare-earth based inorganic phosphors, we have been encouraged to widen their interesting photoluminescence properties for several application field of luminescent materials such as luminescent probes, fluorescent indicators, luminescent signages, and also luminescent decorations. As reported in our studies, this dissertation work is still incomplete and we have identified some detailed aspects that merit further consideration. The study and development of organic phosphors and some core-shell quantum dots for light-emitting applications will never be discarded but the results have inspired us to push ourselves and conducted us to work harder on this field in order to understand the hidden part below the tip of the iceberg that reduced their photoluminescence properties and decreased the thermal and optical stability under operating conditions of LEDs.





---

# **Experimental section**

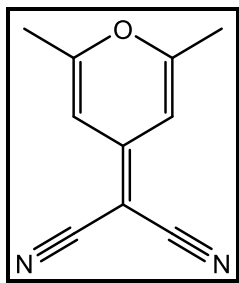
# **Organic phosphors**

---



## Experimental section: organic phosphors

### A. (2,6-dimethyl-4H-pyran-4-ylidene)propanedinitrile



1

The mixture of malononitrile (1 eq; 0.06 mol; 3.55 mL), 2,6-dimethyl-4-pyrone (1 eq; 0.06 mol; 7.06 g) and acetic anhydride (5.32 eq; 0.3 mol; 28.2 mL) were heated under reflux for 45 minutes. The unreacted acetic acid was aspirated off and the residue was washed with 50 mL of boiling water and collected to give a soft brown solid. Recrystallization from boiling ethanol produced 1 as a brown crystal (6.08 g; yield: 62.6%).

m.p.: 194.5 – 194.9°C.

IR: 2207 (C≡N); 1663 (C=C); 1578; 1505; 1430; 1379 (CH<sub>3</sub> bending); 1172; 923; 836 (C=C-H bending)

<sup>1</sup>H NMR (400 MHz, CDCl<sub>3</sub>, δ)

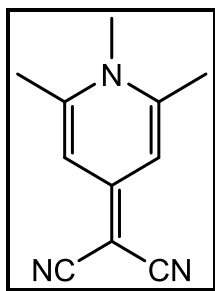
δ (ppm): 6.543 (s, 2H, C=C-H); 2.318 (s, 6H, CH<sub>3</sub>)

<sup>13</sup>C NMR (400 MHz, CDCl<sub>3</sub>, δ)

δ (ppm): 163.1; 156.8; 114.8; 106.46; 57.8; 19.7

GC-MS: - found: 172

**B. 2-(1,2,6-trimethylpyridin-4H-ylidene)malonitrile**



2

A solution of (2,6-dimethyl-4H-pyran-4-ylidene)propanedinitrile (1 eq; 1.2 mmol; 0.2 g) in methylamine (188 eq; 0.22 mol; 9 mL) was refluxed for 2 hrs. The precipitate was filtered then the excess of methylamine was removed at low pressure. The solid was recrystallized from acetonitrile resulting 2 as a white solid (0.14 g; yield: 63.5%).

m.p.: > 300°C.

IR: 2186(C≡N); 2157; 1633 (C=C); 1558; 1496; 1430; 1359; 1201; 1068; 847; 536

<sup>1</sup>H NMR (400 MHz, DMSO-d<sub>6</sub>, δ)

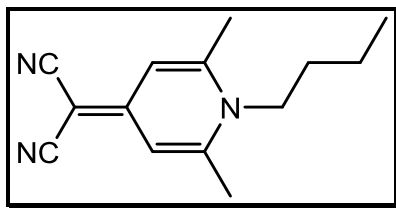
δ (ppm): 6.64 (s, 2H); 3.58 (s, 3H, CH<sub>3</sub>); 2.43 (s, 6H, CH<sub>3</sub>)

<sup>13</sup>C NMR (400 MHz, DMSO-d<sub>6</sub>, δ)

δ (ppm): 160.4; 150.3; 119.1; 112.1; 77.71; 36.5; 20.5

MS (ESI) m/z: [M+H]<sup>+</sup> calcd for C<sub>11</sub>H<sub>12</sub>N<sub>3</sub> 186.1031, found 186.1025

C. 2-(1-butyl-2,6-dimethylpyridin-4H-ylidene)malonitrile



3

A solution of (2,6-dimethyl-4H-pyran-4-ylidene)propanedinitrile (1 eq; 1.2 mmol; 0.2 g) in butylamine (87 eq; 0.1 mol; 10 mL) was refluxed for 2 hrs. The precipitate was filtered then the excess of butylamine was removed at low pressure. The solid was recrystallized from acetonitrile resulting 3 as a pale-yellow solid (0.22 g; yield: 82.7%).

m.p.: 208.6 - 209.5°C.

IR: 2956; 2868 (CH<sub>2</sub>, CH<sub>3</sub>); 2190 (C≡N); 2165; 1633 (C=C); 1554; 1504; 1480; 1363; 1342; 1226; 1184; 1068; 844

<sup>1</sup>H NMR (400 MHz, CDCl<sub>3</sub>, δ)

δ (ppm): 6.61 (s, 2H); 3.92 (t, J = 8.4 Hz, 2H, CH<sub>2</sub>); 2.47 (s, 6H, CH<sub>3</sub>); 1.76-1.62 (m, 2H, CH<sub>2</sub>); 1.64-1.38 (m, 2H, CH<sub>2</sub>); 1.01 (t, J = 7.4 Hz, 3H, CH<sub>3</sub>)

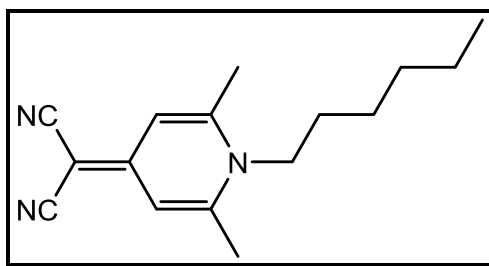
<sup>13</sup>C NMR (400 MHz, CDCl<sub>3</sub>, δ)

δ (ppm): 155.5; 147.7; 118.8; 113.6; 48.8; 44.0; 31.4; 20.4; 19.8; 13.4

MS (ESI) m/z: [M+H]<sup>+</sup> calcd for C<sub>14</sub>H<sub>18</sub>N<sub>3</sub> 228.1501, found 228.1499



**D. 2-(1-hexyl-2,6-dimethylpyridin-4(1H)-ylidene)malononitrile**



4

A solution of (2,6-dimethyl-4H-pyran-4-ylidene)propanedinitrile (1 eq; 1.2 mmol; 0.2 g) in hexylamine (65 eq; 75.7 mmol; 10 mL) was refluxed for 1-2 hrs. Removal of the excess of hexylamine at low pressure left a solid which was recrystallized from acetonitrile resulting 4 as a white crystal (0.2389 g; yield: 80.3%).

m.p.: 170.2 – 171.1°C.

IR: 2951, 2926 (CH<sub>2</sub>, CH<sub>3</sub>), 2186 (C≡N), 2165, 1633 (C=C), 1550, 1496, 1363, 1184, 1064, 839, 540

<sup>1</sup>H NMR (400 MHz, CDCl<sub>3</sub>, δ)

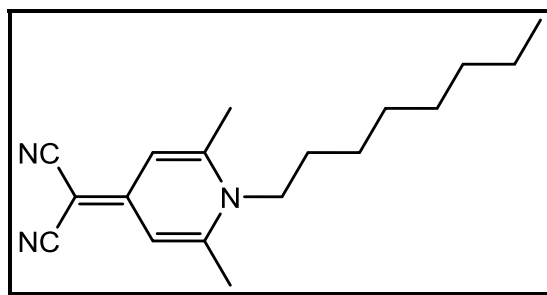
δ (ppm): 6.63 (s, 2H); 3.91 (t, J = 8.4 Hz, 2H, CH<sub>2</sub>); 2.47 (s, 6H, CH<sub>3</sub>); 1.75-1.64 (m, 2H, CH<sub>2</sub>); 1.47-1.29 (m, 6H, CH<sub>2</sub> chain); 0.92 (t, J = 7.2 Hz, 3H, CH<sub>3</sub>)

<sup>13</sup>C NMR (400 MHz, CDCl<sub>3</sub>, δ)

δ (ppm): 155.6; 147.6; 118.8; 113.7; 49.1; 31.0; 29.4; 26.2; 22.3; 20.5; 13.7

MS (ESI) m/z: [M+H]<sup>+</sup> calcd for C<sub>16</sub>H<sub>22</sub>N<sub>3</sub> 256.1814, found 256.1802

**E. 2-(1-octyl-2,6-dimethylpyridin-4H-ylidene)malonitrile**



5

A solution of (2,6-dimethyl-4H-pyran-4-ylidene)propanedinitrile (1 eq; 1.2 mmol; 0.2 g) in octylamine (65 eq; 75.4 mmol; 13 mL) was refluxed for 2 hrs. The precipitate was filtered then the excess of octylamine was removed at low pressure. The solid was recrystallized from acetonitrile resulting 5 as a white solid (0.28 g; yield: 84.5%).

m.p.: 155.8-157.1°C.

IR: 2918; 2856 (CH<sub>2</sub>, CH<sub>3</sub>); 2190 (C≡N); 2170; 1625 (C=C); 1546; 1508; 1484; 1380; 1351; 1313; 1184; 1068; 873; 536

<sup>1</sup>H NMR (400 MHz, CDCl<sub>3</sub>, δ)

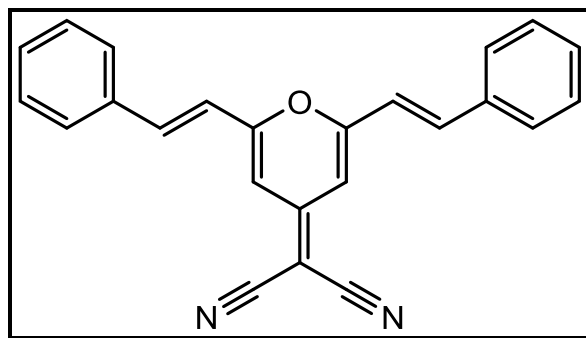
δ (ppm): 6.63 (s, 2H); 3.91 (t, J = 8.3 Hz, 2H, CH<sub>2</sub>); 2.47 (s, 6H, CH<sub>3</sub>); 1.74-1.64 (br, 2H, CH<sub>2</sub>); 1.44-1.17 (br, 10H, CH<sub>2</sub> chain); 0.89 (t, J = 7.0 Hz, 3H, CH<sub>3</sub>)

<sup>13</sup>C NMR (400 MHz, CDCl<sub>3</sub>, δ)

δ (ppm): 155.6; 147.6; 118.8; 113.7; 49.1; 44.2; 31.5; 29.5; 28.8; 26.5; 22.4; 20.5; 13.9

MS (ESI) m/z: [M+H]<sup>+</sup> calcd for C<sub>18</sub>H<sub>26</sub>N<sub>3</sub> 284.2127, found 284.2127

**F. 2-(2,6-distyryl-4H-pyran-4'-ylidene)malononitrile**



6

A mixture of (2,6-dimethyl-4H-pyran-4-ylidene)propanedinitrile (1 eq; 2.3 mmol; 0.4 g), benzaldehyde (2 eq; 4.7 mmol; 0.47 g), and piperidine (2 eq; 4.7 mmol; 0.460 mL) in 12 mL acetonitrile was heated under reflux until completion (TLC monitoring). After cooling down to room temperature, the precipitate solids was filtered and washed several times with cold methanol. The crude solids were purified by crystallization to give a product 6 as a red solid (0.81 g; yield: 43.6%).

m.p.: 252.9 - 253.4°C.

IR: 2207 (C≡N); 1642 (C=C); 1608; 1541; 1500; 1417; 1330; 1304; 1197; 1180; 972; 943; 831; 756; 697; 481

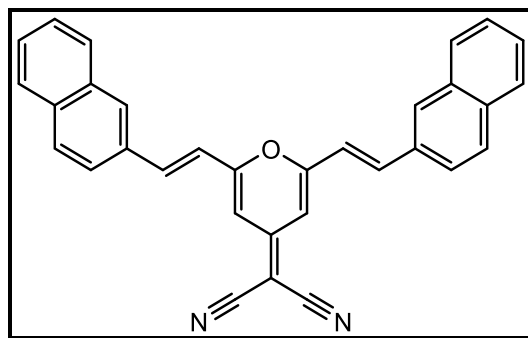
<sup>1</sup>H NMR (400 MHz, CDCl<sub>3</sub>, δ, the signal of TFA was not included)

δ (ppm): 7.63-7.58 (dd, 3H, Ar, J = 7.5, 1.65 Hz); 7.56 (d, J = 16.1 Hz, 2H, trans C=C); 7.50-7.43 (m, 6H, Ar); 6.79 (d, J = 16.1 Hz, 2H, trans C=C); 6.72 (s, 2H)

<sup>13</sup>C NMR (400 MHz, CDCl<sub>3</sub>, δ, the signal of TFA was not included)

δ (ppm): 158.4; 156.1; 138.4; 134.8; 130.8; 129.5; 128.1; 118.8; 115.4; 107.6

**G. 2-(2,6-bis(2-naphthalen-2-yl)vinyl)-4H-pyran-4'-ylidene)malononitrile**



7

A mixture of (2,6-dimethyl-4H-pyran-4-ylidene)propanedinitrile (1 eq; 2.4 mmol; 0.41 g), 2-naphthaldehyde (2 eq; 4.7 mmol; 0.73 g), and piperidine (2 eq; 8.8 mmol; 0.46 mL) in 12 mL acetonitrile was heated under reflux until completion (TLC monitoring). After cooling down to room temperature, the precipitate solids was filtered and washed several times with cold methanol. The crude solids were purified by crystallization to give a product 7 as a yellow solid (0.92 g; yield: 85.9%).

m.p.: 267.8 - 268.6°C

IR: 2207 (C≡N); 1643 (C=C); 1542; 1498; 1418; 1172; 955; 854; 810; 741; 472

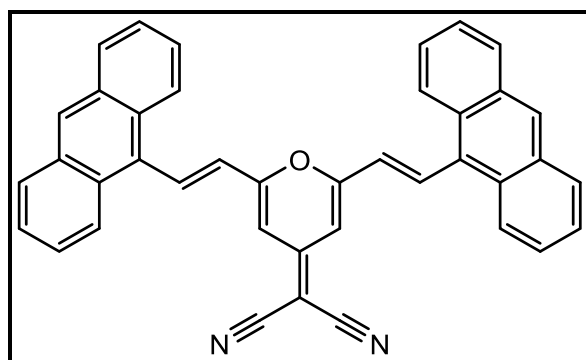
<sup>1</sup>H NMR (400 MHz, CDCl<sub>3</sub>, δ, the signal of TFA was not included)

δ (ppm): 8.06 (s, 2H, Ar); 7.96-7.86 (m, 6H, Ar); 7.78 (d, J = 16 Hz, 2H, trans C=C); 7.78 (d, J = 1.6 Hz, 2H, Ar); 7.61-7.55 (m, 4H, Ar); 6.94 (d, J = 16.1 Hz, 2H, trans C=C); 6.81 (s, 2H)

<sup>13</sup>C NMR (400 MHz, CDCl<sub>3</sub>, δ, the signal of TFA was not included)

δ (ppm): 190.9; 159.2; 138.9; 134.4; 133.4; 131.9; 130.1; 129.1; 128.6; 128.2; 127.9; 127.7; 127.1; 123.1; 118.4; 107.3; 57.4

**H. 2-(2,6-bis(2-(anthracen-9-yl)vinyl)-4H-pyran-4'-ylidene)malononitrile**



8

A mixture of (2,6-dimethyl-4H-pyran-4-ylidene)propanedinitrile (1 eq; 2.3 mmol; 0.4 g), 9-anthracenecarboxaldehyde (2 eq; 4.7 mmol; 0.96 g), and piperidine (2 eq; 4.7 mmol; 0.46 mL) in 30 mL acetonitrile was heated under reflux until completion (TLC monitoring). After cooling down to room temperature, the precipitate solids was filtered and washed several times with cold methanol. The crude solids were purified by crystallization to give a product 8 as a red solid (1.1 g; yield: 86.9%).

m.p.: >300°C

IR: 2207 (C≡N); 1643 (C=C); 1542; 1498; 1418; 1172; 955; 854; 810; 741; 472

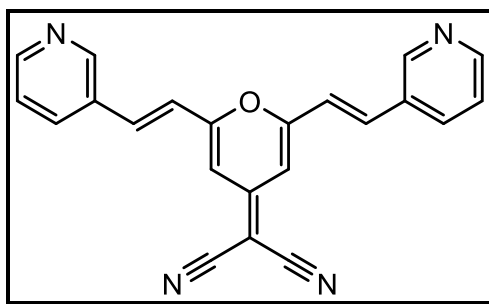
<sup>1</sup>H NMR (400 MHz, CDCl<sub>3</sub>, δ, the signal of TFA was not included)

δ (ppm): 8.79 (d, J = 16.3 Hz, 2H, trans C=C); 8.54 (s, 2H, Ar); 8.36 (d, J = 8.6 Hz, 4H, Ar); 8.08 (d, J = 8.3 Hz, 4H, Ar); 7.63-7.51 (m, J = 6.9 Hz, 8H, Ar); 7.00 (d, J = 16 Hz, 2H, trans C=C); 6.98 (s, 2H)

<sup>13</sup>C NMR (400 MHz, CDCl<sub>3</sub>, δ, the signal of TFA was not included)

δ (ppm): 197.3; 161.96; 131.4; 129.3; 127.1; 125.6; 124.7; 118.4; 115.6; 112.8; 109.9; 108.0; 59.5

I. 2-(2,6-bis(2-(pyridin-3-yl)vinyl)-4H-pyran-4'-ylidene)malononitrile



9

A mixture of (2,6-dimethyl-4H-pyran-4-ylidene)propanedinitrile (1 eq; 1.2 mmol; 0.2 g), 3-pyridinecarboxyaldehyde (2 eq; 2.3 mmol; 0.285 mL), and piperidine (2.6 eq; 3.0 mmol; 0.230 mL) in 15 mL acetonitrile was heated under reflux until completion (TLC monitoring). After cooling down to room temperature, the precipitate solids was filtered and washed several times with cold methanol. The crude solids were purified by crystallization to give a product 9 as a yellow solid (0.31 g; yield: 77.5%).

m.p.: >300°C

IR: 2207 (C≡N); 1646 (C=C); 1542; 1498; 1415; 1302; 1206; 1023; 972; 946; 833; 795; 700

<sup>1</sup>H NMR (400 MHz, CDCl<sub>3</sub>, δ, the signal of TFA was not included)

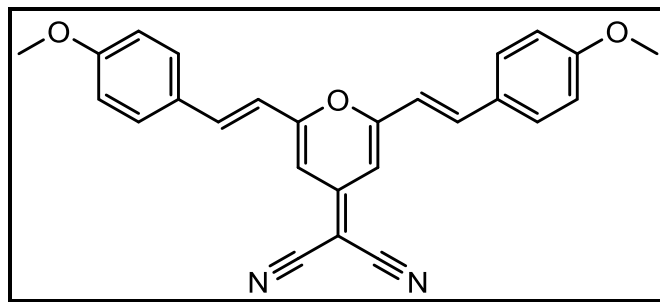
δ (ppm): 9.13 (s, 2H, Ar); 8.82 (d, J = 5.7 Hz, 2H, Ar); 8.21-8.10 (br, 2H, Ar); 7.78 (d, J = 16.1 Hz, 2H, trans C=C); 7.30 (d, J = 16.3 Hz, 2H, trans C=C); 7.15 (s, 2H)

<sup>13</sup>C NMR (400 MHz, CDCl<sub>3</sub>, δ, the signal of TFA was not included)

δ (ppm): 179.6; 157.7; 144.3; 141.3; 140.9; 136.0; 130.0; 128.2; 126.2; 113.0; 110.7; 61.2

MS (ESI) m/z: [M + H]<sup>+</sup> found for C<sub>22</sub>H<sub>14</sub>N<sub>4</sub>O 351.1246, found 351.1274

**J. 2-(2,6-bis(4-(methoxystyryl)-4H-pyran-4'-ylidene)malononitrile**



10

A mixture of (2,6-dimethyl-4H-pyran-4-ylidene)propanedinitrile (1 eq; 1.2 mmol; 0.2 g), 3-pyridinecarboxyaldehyde (2 eq; 2.3 mmol; 0.285 mL), and piperidine (2 eq; 2.4 mmol; 0.24 mL) in 15 mL acetonitrile was heated under reflux until completion (TLC monitoring). After cooling down to room temperature, the precipitate solids was filtered and washed several times with cold methanol. The crude solids were purified by crystallization to give a product 10 as a yellow solid (0.20 g; yield: 42.6%).

m.p.: 236.0 - 238.2°C

IR: 2207 (C≡N); 1640 (C=C); 1605; 1536; 1492; 1418; 1302; 1261; 1172; 1029; 964; 827; 507

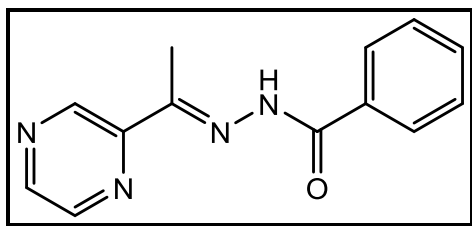
<sup>1</sup>H NMR (400 MHz, CDCl<sub>3</sub>, δ, the signal of TFA was not included)

δ (ppm): 7.56 (d, J = 8.4 Hz, 2H, Ar); 7.53 (d, J = 15.2 Hz, 2H, trans C=C); 6.98 (d, J = 8.8 Hz, 2H, Ar); 6.71 (s, 2H); 6.67 (d, J = 16.1 Hz, 2H, trans C=C)

<sup>13</sup>C NMR (400 MHz, CDCl<sub>3</sub>, δ, the signal of TFA was not included)

δ (ppm): 161.6; 159.5; 157.4; 138.4; 129.7; 127.3; 115.9; 114.7; 113.0; 106.5; 56.2; 55.5

### K. Methyl pyrazinylketone benzoyl hydrazine (MPBH) ligand



11

Benzhydrazide (1 eq; 1 mmol; 0.4 g) and 2-acetylpyrazine (1 eq; 1 mmol; 0.36 g) are added in 30 mL ethanol. The reaction mixture is refluxed overnight. The reaction mixture is cooled down to room temperature and the solvent is evaporated. The crude solid is recrystallized in ethanol and the final product 11 afford as a white crystal (0.32 g; yield: 45.1 %).

m.p.: 175.8 - 177.1°C.

IR: 3380; 3054; 1688 (C=O); 1640 (C=N of Schiff base); 1599 (C=N of pyrazine); 1579; 1532; 1516; 1492; 1467; 1427; 1407; 1365; 1324; 1254; 1172; 1155; 1141; 1126; 1075; 1047; 1017; 905; 841; 801; 755; 713; 688; 658; 580; 504; 480; 453; 421

<sup>1</sup>H NMR (400 MHz, DMSO-d<sub>6</sub>, δ)

δ (ppm): 11.05 (s, 1H, NH); 9.25 (s, 1H); 8.69-8.60 (d, 2H); 7.88 (s, 2H); 7.64-7.49 (m, 3H); 2.45 (s, 3H, CH<sub>3</sub>)

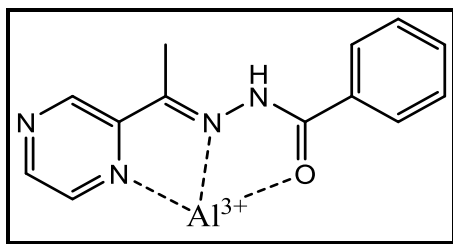
<sup>13</sup>C NMR (400 MHz, DMSO-d<sub>6</sub>, δ)

δ (ppm): 150.1; 144.2; 142.2; 141.1; 133.0; 131.5; 128.2; 127.8; 127.0; 126.7; 21.4

MS (ESI) m/z: [M + H]<sup>+</sup> found for C<sub>13</sub>H<sub>12</sub>N<sub>4</sub>O, 241.11.



### L. Al-MPBH complex



12

The product was then synthesized by addition of aluminium nitrate nonahydrate (1 eq; 0.64 mmol; 0.24 g) to a solution containing of MPBH (1 eq; 0.63 mmol; 0.15 g) in 30 mL ethanol. The reaction mixture is then refluxed for 2 hrs. The precipitate solid is filtered, washed with ethanol and dried at 50°C in vacuum. The final product 12 affords as a green powder (0.16 g; yield: 57.6 %).

m.p.: > 300°C.

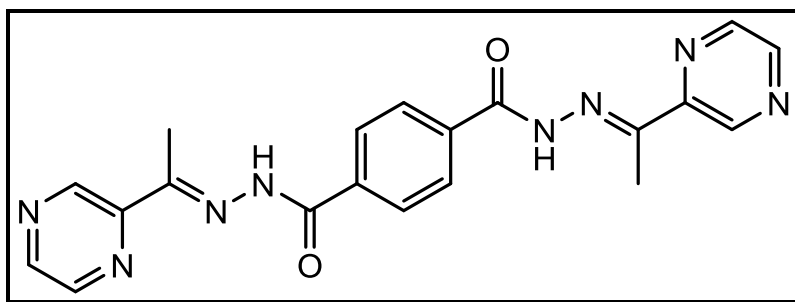
IR: 3600-2500 (broad); 1639; 1599; 1585; 1508; 1469; 1435; 1388; 1327; 1296; 1203; 1153; 1072; 1045; 725; 694; 660; 574

<sup>1</sup>H NMR (400 MHz, DMSO-d<sub>6</sub>, δ)

δ (ppm): 9.70 (s, 1H); 9.44 (s, 1H); 9.14 (s, 1H); 8.71-8.53 (m, 1H); 8.30-8.00 (m, 1H); 7.80-7.46 (m, 2H); 2.62 (s, 3H, CH<sub>3</sub>)

MS (ESI) m/z: [MPBH + Al + 3NO<sub>3</sub> + CH<sub>3</sub>OH + H<sub>2</sub>O]<sup>+</sup> found for Al-MPBH complex, 503.1963.

**M.N'1,N'4-bis((E)-1-(pyrazin-2-yl)ethylidene)terephthalohydrazide  
(MPTH)**



13

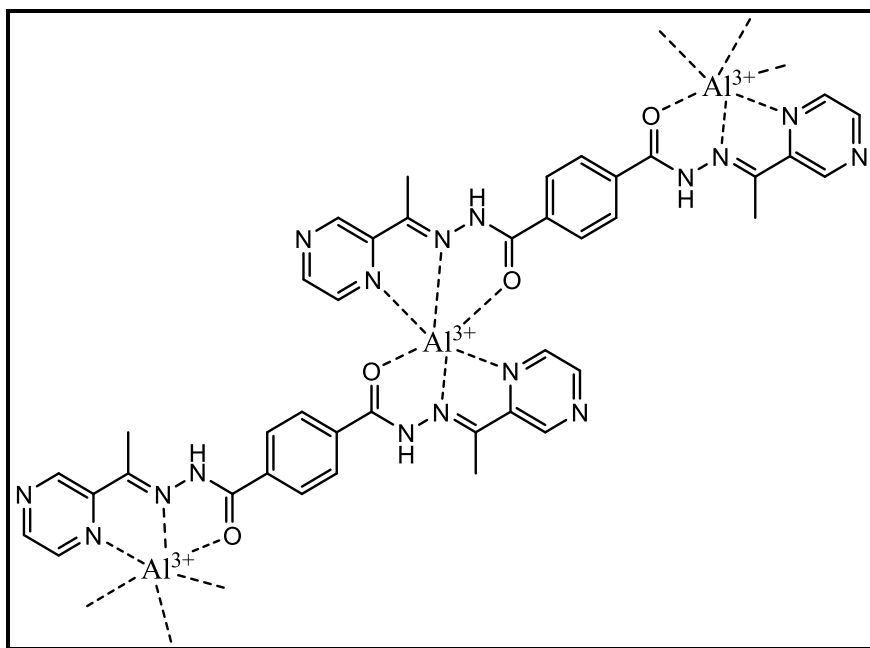
Terephthalohydrazide (1 eq; 1.5 mmol; 0.29 g) and 2-acetylpyrazine (2.1 eq; 3.1 mmol; 0.38 g) are added in 30 mL ethanol. The reaction mixture is refluxed overnight. The reaction mixture is cooled down to room temperature and the solvent is evaporated. The crude solid is recrystallized in ethanol and the final product 13 is afforded as a white crystal (0.51 g; yield: 82%).

IR: 3449 (broad); 3218; 3045; 1660; 1610; 1543; 1473; 1433; 1282; 1157; 1014; 900; 859; 676

<sup>1</sup>H NMR (400 MHz, 600 μL CDCl<sub>3</sub> + 100 μL TFA, δ, the signal of TFA was not included)

δ (ppm): 12.53 (small, br); 9.70 (s, 1H); 9.40 (d, 2H); 9.09 (s, 1H); 8.87 (d, 2H); 8.10 (s, 4H); 2.65 (s, 6H)

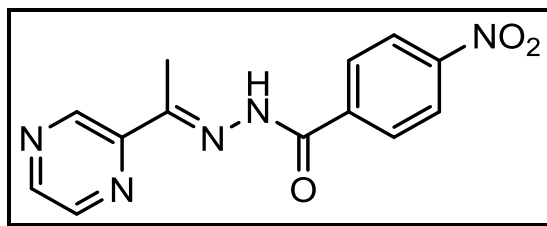
N. Al-MPTH complex



14

The synthesis method of complex was modified from the reference.<sup>353</sup> To a suspension of ligand 13 (1 eq; 0.48 mmol; 0.19 g) in 20 mL three neck round-bottom flask containing of ethanol was added  $\text{Al}(\text{NO}_3)_3 \cdot 9\text{H}_2\text{O}$  (1.26 eq; 0.61 mmol; 0.23 g). The mixture was refluxed for 1h and then allowed to cool to room temperature. The product precipitate was filtered off and washed with ethanol to yield a final product 14 as a yellow powder.

**O. (E)-4-nitro-N'-(1-(pyrazin-2-yl)ethylidene)benzohydrazide (MPNBH)**



15

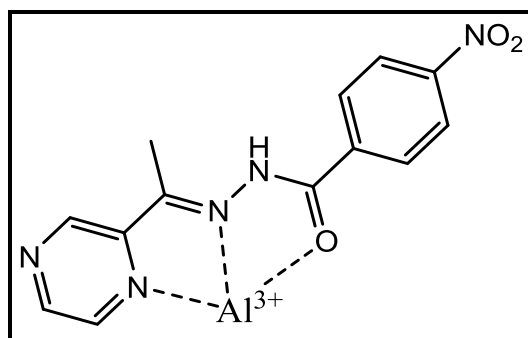
A solution of 2-acetylpyrazine (1 eq; 4.7 mmol; 0.70 g) in ethanol was added to a solution containing 4-nitrobenzohydrazide (1.2 eq; 5.7 mmol; 0.85 g) in ethanol. The mixture was refluxed for 24 h. The solution was then cooled to room temperature, and the solvent was evaporated. The final product 15 was recrystallized in ethanol and found as a white crystal (0.57 g; yield: 42%).

<sup>1</sup>H NMR (400 MHz, DMSO-d<sub>6</sub>, δ) – mixture with 4-nitrobenzohydrazide

δ (ppm): 11.34 (s, 1H); 9.27 (s, 1H); 8.75 – 8.58 (m, 2H); 8.37 – 8.35 (d, 2H); 8.15 – 8.14 (d, 1H); 7.98 (d, 1H)

GC-MS: - found: 285

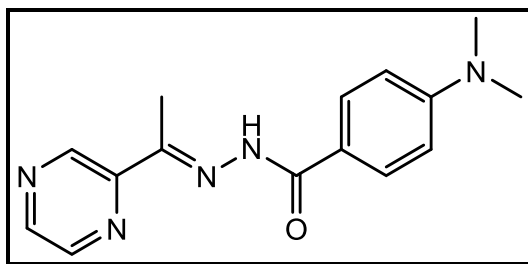
**P. Al-MPNBH complex**



16

The product was then synthesized by addition of aluminium nitrate nonahydrate (1 eq; 0.52 mmol; 0.20 g) to a solution containing of product 15 (2 eq; 1.0 mmol; 0.30 g) in 50 mL ethanol. The reaction mixture is then refluxed for 2 hrs. The precipitate solid is filtered, washed with ethanol and dried at 50°C in vacuum. The final product 16 affords as a yellow powder (0.17 g; yield: 67.5%).

**Q. (E)-4-(dimethylamino)-N'-(1-(pyrazin-2-yl)ethylidene)benzohydrazide (MPMABH)**



17

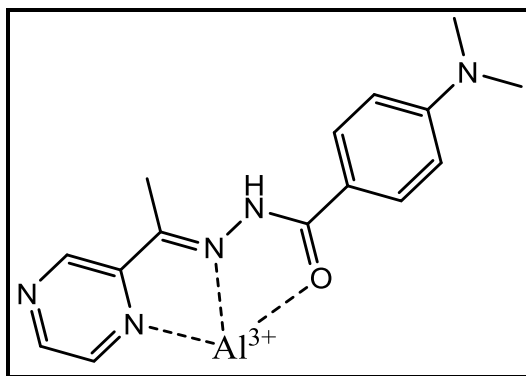
A solution of 2-acetylpyrazine (1 eq; 3.5 mmol; 0.43 g) in ethanol was added to a solution containing 4-(dimethylamino)benzohydrazide (1.2 eq; 4.2 mmol; 0.76 g) in ethanol. The mixture was refluxed for 24h. The solution was then cooled to room temperature, and the solvent was evaporated. The final product 17 was recrystallized in ethanol and found as a white crystal (0.56 g; yield: 56%).

<sup>1</sup>H NMR (400 MHz, DMSO-d<sub>6</sub>, δ) – mixture with 4-nitrobenzohydrazide

δ (ppm): 10.66 (s, 1H); 9.20 (s, 1H); 8.65 – 8.62 (d, 2H); 7.83 – 7.81 (d, 2H); 6.77 – 6.75 (d, 2H); 3.01 (s, 6H, CH<sub>3</sub>); 2.44 (s, 3H, CH<sub>3</sub>)

GC-MS: - found: 283

**R. Al-MPMABH complex**



18

The product was then synthesized by addition of aluminium nitrate nonahydrate (1 eq; 0.53 mmol; 0.2 g) to a solution containing of product 17 (2 eq; 1.0 mmol; 0.3 g) in 50 mL ethanol. The reaction mixture is then refluxed for 2 hrs. The precipitate solid is filtered, washed with ethanol and dried at 50°C in vacuum. The final product 18 affords as a red powder (0.20 g; yield: 76.7%).







---

**Annex**

---



## Annex

### I. Annex A: Characterization techniques

According to our works, the characterization techniques were applied to collect information about chemical, physical, morphological, and optical properties of organic compounds and quantum dots. All characterization techniques are presented in this section.

#### A. NMR spectroscopy

The nuclear magnetic resonance (NMR) spectroscopy is a powerful technique of analysis for many organic molecules in order to identify their entire structure. The principle of NMR is based on the nuclear spin and the splitting of energy levels of molecules in a magnetic field. Therefore, the molecules involving nuclei with nuclear spins can be affected by this technique such as  $^1\text{H}$ ,  $^{13}\text{C}$ ,  $^{15}\text{N}$ ,  $^{19}\text{F}$ ,  $^{31}\text{P}$ .

For example (see Figure S1), when a nucleus with spin =  $1/2$  is placed in an external magnetic field, it can either align itself with the field (lower energy) or against it (higher energy). The energy splitting between the lower and higher energy corresponds to radio frequencies. If radio waves are applied, the nuclei in the lower energy state can absorb this energy and transition to the higher energy state. We can observe either the energy absorption, or the release of energy as the nucleus "relaxes" back to the lower energy state.

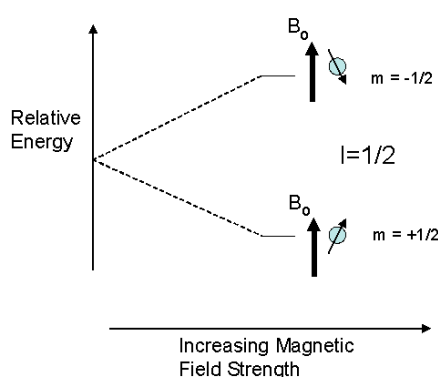


**Figure S1 Schematic of arrangements for a nucleus with nuclear spin =  $1/2$  under an external magnetic field<sup>††††</sup>**

<sup>††††</sup> <http://www.process-nmr.com/nmr1.htm>

In this work,  $^1\text{H}$  and  $^{13}\text{C}$  NMR spectra were performed with a Bruker AVANCE spectrometer at 400.13 and 100.61 MHz respectively, at 298 K. The chemical shifts ( $\delta$ ) are reported in ppm relative to solvent residual signal. The coupling constants ( $J$ ) are reported in Hertz (Hz). The samples were prepared by dissolving in deuterated organic solvent (i.e.  $\text{CDCl}_3$ ,  $\text{D}_2\text{O}$ ,  $\text{DMSO-d}_6$ ) and then transferring to a thin-walled glass tube. All NMR spectra are calibrated using solvent residual proton peak in deuterated solvent.

### **B. UV-visible spectroscopy**

The UV-visible spectroscopy is one of the most common technique used in several areas of chemistry. This technique is related to the probability of electronic transitions from the ground states to the excited states of molecules after absorbing the energy in the form of ultraviolet or visible light. When the molecules are exposed to light having an energy that matches their electronic transitions, the light energy will be absorbed and the electrons are promoted to a higher energy. The wavelengths at which the absorption occurred can be presented by a graph of absorbance versus wavelength. According to Beer-Lambert law, the absorbance of matter is proportional to the number of absorbing species (or concentration), the path length through the matter, and the molar absorptivity.

#### **a. For powder samples**

The UV-visible spectra of solutions were recorded on Nicolet Evolution 500 UV-visible spectrophotometer between 200-800 nm. The prepared solutions were placed in a quartz cuvette (path-length = 1 cm) and the baseline correction was done by subtracting the absorbance of pure solvent used.

#### **b. For composite films**

The UV-visible spectra of composite films were recorded on Shimadzu 2101 UV spectrometer PC with an integrating sphere between 200-800 nm. The composite films were fixed in the sample holder and placed at the beam port with the front surface toward the integrating sphere (Figure S2). Typically, the particles embedded in the film can scatter or diffuse the incident light. Then the integrating sphere was applied in order to collect all of the transmitted light, not only the linearly transmitted light, but the diffused transmitted light as well.

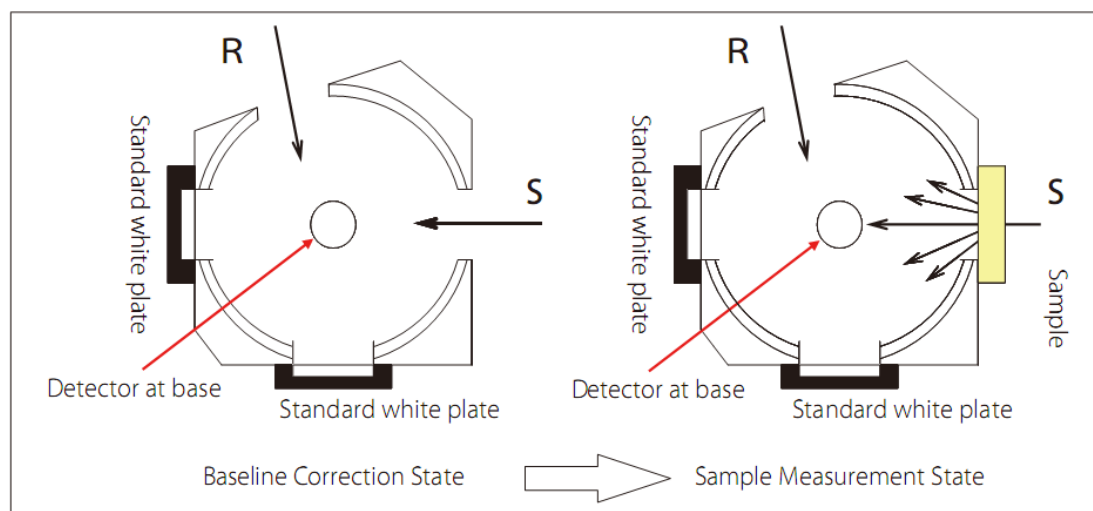


**Figure S2 Total light transmittance measurement.**

### **C. Fourier transform infrared (FTIR) spectroscopy**

FTIR spectroscopy is a useful analytical technique to identify the functional groups and the structures of organic and inorganic materials by measuring the absorption of infrared radiation versus wavelength. Typically, the materials absorb the specific frequencies that are related to the transition energy of the bonds or groups that vibrates. Then the particular frequencies that are absorbed by the materials are the vibrational characteristic of materials themselves. In common, the FTIR spectroscopy can provide several measurement methods according to the sample form.

#### **c. Alkali halide pressed method**

The infrared spectra were recorded on a Nicolet 5700 FTIR spectrometer using the KBr pellet technique in the  $4000\text{--}400\text{ cm}^{-1}$  region. This is a simple method that is suitable for many organic samples with non-hygroscopic property or water-containing. The sample is prepared by mixing the sample powder (0.1-1 wt. %) into 200-250 mg of fine alkali halide (potassium bromide, KBr, in common) and then pressing in an evacuated die to form a pellet. The alkali halides is practically used for a pellet method because it becomes transparent in the infrared region.

### **e. Attenuated total reflection (ATR) method**

In addition to alkali halide pellet method, the infrared spectra can be measured on a Nicolet 5700 FTIR spectrometer using the ATR mode in the 4000–400  $\text{cm}^{-1}$  region. This method is able to measure powder samples directly (without sample preparation) by pressing the sample with a high-refractive-index prism and measuring the infrared spectrum using the infrared light that is totally internally reflected in the prism. This method is very useful for inorganic or other high-refractive-index samples.

### **f. Film method**

The infrared spectra in transmission mode were carried out using a Nicolet 760 Magna-IR infrared spectrometer with the purge of dry air inside the sample chamber. The composite films were obtained by preparing the powder samples embedded homogeneously in polymer matrices. This method is very attractive for the analysis of aging of composite films in order to monitor the variation of functional groups as a function of aging time.

## **D. Melting point**

The melting points were measured by B-540 melting point analyzer.

## **E. Thin layer chromatography (TLC)**

Thin layer chromatography is a chromatographic technique used to separate the components in the mixture using a thin-coated stationary phase and a mobile phase (a solvent or a mixing solvent). In this work, the TLC were used to monitor the progress of a reaction, to identify compounds presented in a reaction mixture, and also to evaluate the purity of products obtained. The TLC analysis was performed on pre-coated aluminium backed silica plates 60 with fluorescent indicator UV254.

## F. Scanning electron microscopy (SEM)

Scanning electron microscopy is a non-destructive technique that provides surface morphology and topology of materials. This technique uses a high-energy electron beam to bombard the sample surface in order to generate a variety of signals such as secondary electrons (SE2), back-scattered electrons (BSE) and X-rays (Figure S3). The signals generated from the interactions between the electron beam and the atoms of materials at the surface provide high resolution images better than an optical microscope. The most common detector for all SEMs is secondary electron detectors, which records the secondary electrons emitted by atoms excited by the electron beam. The micrographs of SE2 provide high-resolution images of sample surfaces down to the nanoscales. The back-scattered electrons are produced from the samples by elastic scattering, which contribute information about the distribution of different elements (with different atomic numbers) in sample surfaces. The X-rays can also emitted from the samples when the electron beam have enough energy to remove an inner-shell electron. This X-rays are used to analyze the composition and the abundance of elements in the sample.

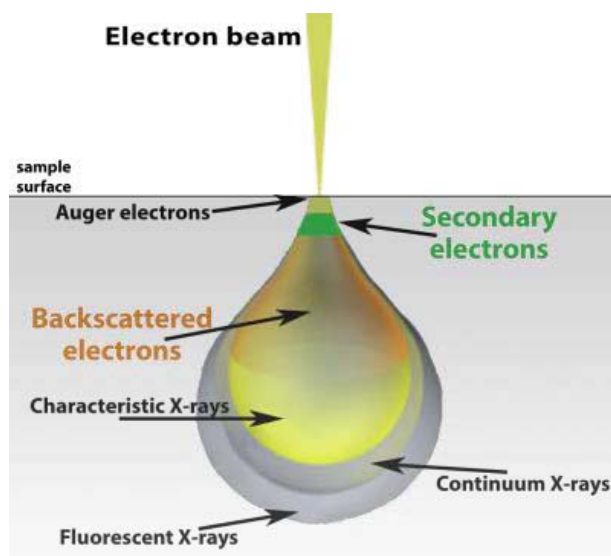


**Figure S3 Signals generated from the interaction between an electron beam and a sample surface. \*\*\*\***

Micrographs were taken at 2MATech technology center and recorded using a microscope ZEISS SUPRA 55VP with a field emission electron gun (FEG)) and the secondary electron detector (SE2). All dried samples were prepared on a surface of an adhesive carbon film before metalizing using a carbon/gold coating.

---

\*\*\*\* <http://www.nanoscience.com/products/sem/technology-overview/sample-electron-interaction/>



### **G. Transmission electron microscopy (TEM)**

Transmission electron microscopy is a non-destructive method that provides information about the microstructures in more detailed and higher resolution than other microscopic techniques. The TEM is particularly used for determination of morphology and particle sizes under microscopic levels. A high-energy electron beam is focused and transmitted through a thinned sample. The images are produced from the interaction of the electrons with samples. In this work, the TEM images were carried out by Centre d'Imagerie Cellulaire Santé (CICS). Transmission Electron Microscopy (TEM) images were taken by placing a drop of the particle suspension onto a carbon film-supported copper grid and then recorded using a Hitachi H7650 120 kV microscope operating at 80 kV and combined with a Hamamatsu AMT HR 1Kx1K CCD camera placed in a side position. The particle suspension was prepared by dispersing the particles in appropriate solution (water, ethanol, or toluene) followed by sonication in an ultrasonic bath for 10 minutes. The TEM images are generated from the interaction of the transmitted electron through the sample. The image is magnified and focused on a fluorescent screen, on a layer of photographic film, or to be detected by a CCD camera.

### **H. Luminescence spectroscopy**

The photoluminescence spectra were recorded with a Jobin-Yvon set-up consisting of a xenon lamp operating at 400 W and two monochromators (Triax 550 and Triax 180) combined with a cryogenically cold charge coupled device (CCD) camera (Jobin-Yvon Symphony LN2 series) for emission spectra and with a Hamamatsu 980 photomultiplier for excitation ones. One photon excited (OPE) luminescence intensity dependence and decays were obtained by pulsed excitation using a Jobin-Yvon LA-04 Nitrogen Laser (337.1 nm, 5 ns pulse, 25 Hz) and analyzed through a Jobin-Yvon HR 1000 monochromator, the detector was a R1104 Hamamatsu photomultiplier tube.

## I. Photoluminescence quantum yield

Photoluminescence quantum yields were measured using C9920-02G PL-QY measurement system from Hamamatsu. The set-up consisting of a 150W monochromatized Xe lamp, an integrating sphere (Spectralon coating, f = 3.3 in.) and a high sensibility CCD camera (Figure S4). This system can be used to analyze many sample forms (powders, films and solutions) with minimal sample preparation. Several optical properties are recorded as followed:

- ✓ PL excitation and PL emission spectra
- ✓ Quantum yield
- ✓ CIE chromaticity coordinates

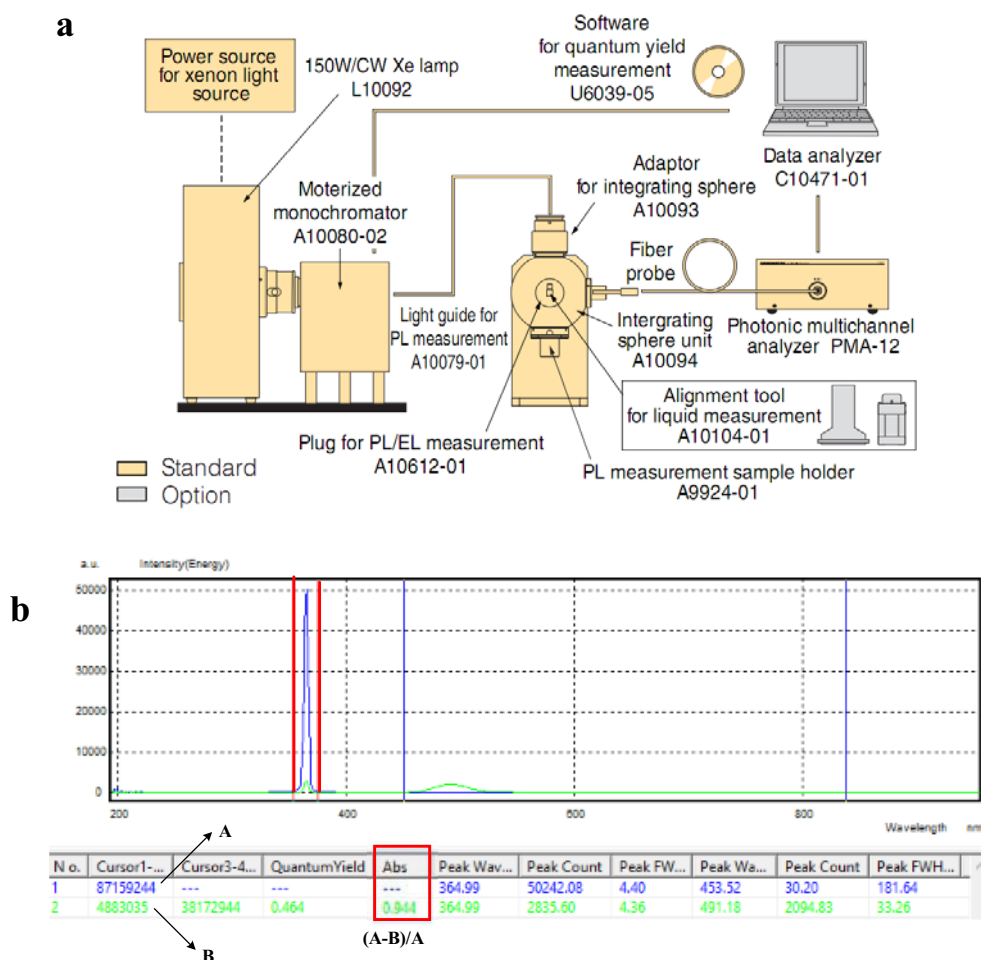


Figure S4 a) Schematic drawing for PL quantum yield measurements using the C9920-02G model (Hamamatsu) and b) definition of absorption ratio for calculating the absolute quantum yield.

Figure S4-b demonstrates the software screen for photoluminescence quantum yield measurements. The absolute quantum yield can be determined by the product of internal quantum efficiency (PLQY<sub>int</sub>) and its relative absorption. The relative absorption is defined as an equation below:

$$\text{Relative absorption} = (A - B)/A$$

where, A represents the area under emission spectrum obtained from the excitation source (blue peak between two red lines) corresponding to the number of photons emitted by source; B represents the area under emission spectrum recorded from the remained excitation source after absorbed by phosphors (see **Error! Reference source not found.b**). Therefore, the value of A-B is related to the number of photons that are absorbed by phosphors.

### **J. Photoluminescence decays**

The photoluminescence lifetimes of phosphors were investigated by plotting the variation of fluorescence intensity as a function of time. Fluorescence decays were recorded at room temperature by using a Jobin-Yvon LA-04 pulsed nitrogen laser ( $\lambda_{\text{exc}} = 337.1 \text{ nm}$ ) as excitation source and a Lecroy 9310A-400 MHz digital oscilloscope.

### **K. Photoluminescence by integration sphere**

The Electroluminescent (EL) spectrum, luminous efficacy, correlated color temperature (CCT), Commission Internationale de l'Eclairage (CIE) chromaticity coordinates and color rendering index (CRI) of composite films associated with LEDs were measured at room temperature using an integrating sphere with a diode array rapid analyzer system (GL Optic integrating sphere GLS 500). The measurement was collected inside the integration sphere (Figure S5) by GL spectrometer (GL spectis 1.0). The inner walls of the sphere are coated with high reflective inorganic material such as barium sulfate (BaSO<sub>4</sub>).



Figure S5 Sphere integration GL OPTI SPHERE 500. §§§§

### L. X-rays diffraction (XRD)

The powder XRD patterns of sample powders were recorded using a diffractometer X-Pert Pro from Philips scanning using Bragg-Brentano geometry (Figure S6). X-ray are produced by the Cu X-ray source ( $K\alpha$  radiation of copper located at  $1.5406 \text{ \AA}$ ). In this work, this technique is important to study the structure of inorganic layered double hydroxide.

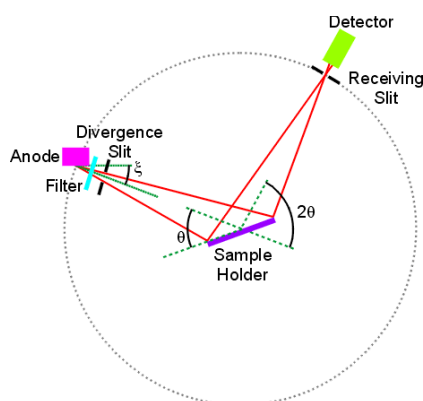


Figure S6 Schematic of Bragg-Brentano geometry. \*\*\*\*\*

---

§§§§ <http://gloptic.com/products/gl-opti-sphere-500/?lang=en>

\*\*\*\*\* <http://pd.chem.ucl.ac.uk/pdnn/inst1/optics1.htm>

## M. UV irradiation

The UV irradiation of composite films were carried out in a SEPAP 12/24 unit (**Error! Reference source not found.**)<sup>††††</sup> This system has been designed to achieve the accelerated artificial weathering conditions which are related to natural ageing. The composite films are placed on a rotating carousel positioned in the center and four polychromatic mercury lamps (400 W) with wavelengths higher than 300 nm (see Figure S7) are installed at the corners of a SEPAP 12/24 chamber. The temperature is regulated at 60 °C and controlled by a Pt thermocouple.

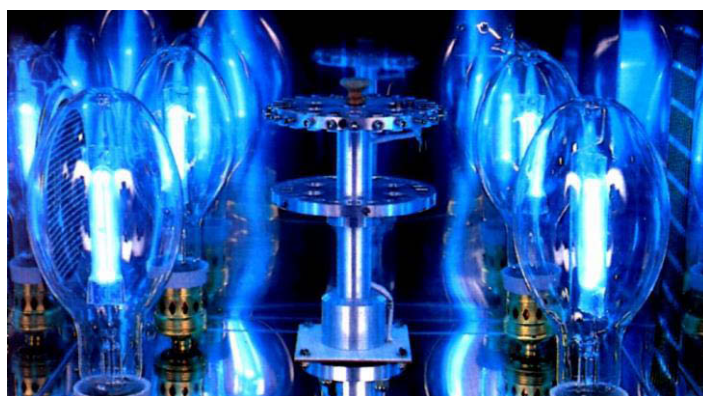
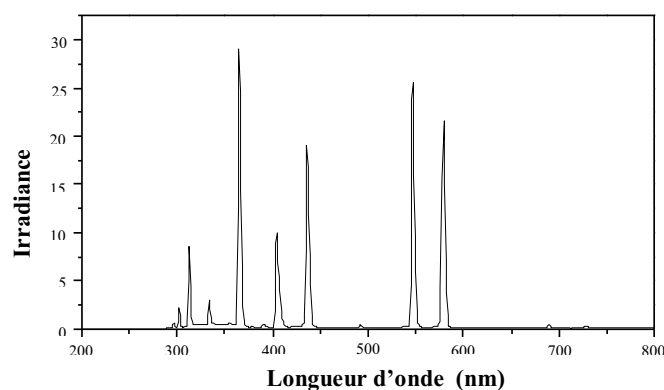


**Figure S7 (above) PL emission spectra of polychromatic mercury lamp in SEPAP 12/24 unit.  
(below) view inside a SEPAP 12/24 chamber.**

---

<sup>††††</sup> J.-L. Philippart, C. Sinturel, R. Arnaud and J.-L. Gardette, *Polymer Degradation and Stability*, 1999, 64, 213-225

## II. Annex B: Glossary terms and definitions

**Black body curve** (or Planckian curve) is the path of black body irradiation when the temperature increases. The black body irradiation is drawn up to the CIE 1931 chromaticity coordinate diagram (as shown in Figure 7, page 14). As the black body is heated, it glows red, then yellow, white and blue because the wavelength related to the black body irradiation becomes shorter with increased temperature.

**Distance to the Plankian Locus (Duv)** is the color parameter that indicates the deviation of the color coordinate of light source from the blackbody source (Plankian locus) from to the Plankian locus. Duv can be calculated by using this equation ( $Duv = \sqrt{\Delta u^2 + \Delta v^2}$ ). Generally, the Duv value should be in the range of  $\pm 0.0054$  to be accepted as a true white light.

**External quantum efficiency (EQE)** is determined by how efficiency the device can convert the electron injected. The EQE can be defined by the ratio of the number of photons emitted from the LED packages to the number of electrons passing through the device.

**Fluorescence lifetime** is an average time which an excited phosphor remains at the excited state before returns to the ground state. The lifetime is measured in the time or the frequency domain.

**Illuminance of the light** is the luminous flux incident per unit area. The illuminance is an SI unit of lux or  $\text{lm}/\text{m}^2$ .

**Luminous efficiency of irradiation** is a parameter describing the brightness of radiation detected by the average human eye. The luminous efficiency is the conversion efficiency from optical unit power to luminous flux as defined in the formula below<sup>13</sup> :

$$\text{Luminous efficiency} = \frac{\Phi_{lum}}{\text{optical power}} = \left[ 683 \times \frac{\text{lm}}{\text{W}} \int_{\lambda} V(\lambda)P(\lambda)d\lambda \right] / \left[ \int_{\lambda} P(\lambda)d\lambda \right]$$

, where  $P(\lambda)$  is the power spectral density and  $V(\lambda)$  is the eye sensitivity function.

For multicolor and white light sources, the luminous efficiency can be calculated by integration of all wavelength. In SI unit, its scale has units of lumens per watt ( $\text{lm}/\text{W}$ ) and the maximum value of  $683 \text{ lm}/\text{W}$  (obtained from monochromatic light at 555 nm).

**Luminous intensity** indicates the light intensity given by a source as perceived by the human sensitivity. The luminous intensity is recorded in SI units of candela (cd). The luminous intensity can be calculated by the luminous flux emitted in a transmitted direction per solid angle.

**Luminous flux** is the light power of a source as perceived by the human eyes. The luminous flux is measured in units of lumens (lm). It is defined that 683 lumens equals to 1 watt of power which is carried by light with the wavelength of 555 nm. The wavelength of 555 nm corresponds to the brightness of monochromatic light where the eyes are most sensitive.

**Solid angle** is a two-dimensional angle with units of steradians. The solid angle can be imagined as measured from beginning at a point and encompassing an area with certain radius.







---

# References

---

## References

1. T. A. Edison, Google Patents, 1880.
2. EU, Energy and climate change – Elements of the final compromise *Council of the European Union note 17215/08* [online], 2008, 'Accessed' 28 November 2015.
3. COM, An energy policy for Europe: Communication from the commission to the European council and the European parliament, *Commission of the European communities, Brussels, 2007* [online], 2007, 'Accessed' 28 November 2015.
4. C. C. Lin and R.-S. Liu, *The Journal of Physical Chemistry Letters*, 2011, 2, 1268-1277.
5. R.-J. Xie and N. Hirosaki, *Science and Technology of Advanced Materials*, 2007, 8, 588-600.
6. R.-J. Xie, N. Hirosaki, Y. Li and T. Takeda, *Materials*, 2010, 3, 3777-3793.
7. Luís Dias Carlos and F. Palacio, *Thermometry at the Nanoscale : Techniques and Selected Applications*, 2015, 240-241.
8. G. Kickelbick, in *Hybrid Materials*, Wiley-VCH Verlag GmbH & Co. KGaA, 2007, DOI: 10.1002/9783527610495.ch1, pp. 1-48.
9. eia, International Energy Statistics, *U.S. Energy Information Administration* [online], 2015, 'Accessed' 27 November 2015.
10. EIA, Annual Energy Review 2006, *Energy Information Administration* [online], 2007, 'Accessed' 27 November 2015.
11. IEA, *Light's Labour's Lost*, IEA Publications, France, 2006.
12. IEA, CO2 emissions from fuel combustion: Highlights, *International Energy Agency* [online], 2015, 'Accessed' 28 November 2015.
13. E. F. Schubert, *Light-Emitting Diodes*, 2006.
14. L. Halonen, Energy efficient electric lighting for buildings, *IEA Technical Conference, Copenhagen* [online], 2010.
15. ENERGYSTAR, *Lighting Technologies: A Guide to Energy-efficiency Illumination*, online: [www.energystar.gov](http://www.energystar.gov), 2015.
16. M. Rea, M. Figueiro and J. Bullough, *Lighting Research and Technology*, 2002, 34, 177-187.
17. M. S. Rea, M. G. Figueiro, J. D. Bullough and A. Bierman, *Brain Research Reviews*, 2005, 50, 213-228.
18. G. C. Brainard, J. P. Hanifin, J. M. Greeson, B. Byrne, G. Glickman, E. Gerner and M. D. Rollag, *The Journal of Neuroscience*, 2001, 21, 6405-6412.
19. K. Thapan, J. Arendt and D. J. Skene, *The Journal of Physiology*, 2001, 535, 261-267.
20. J. S. Speck, Solid State Lighting, *CA: SSLEC - Solid State Lighting and Energy Center* [online], 2011.
21. P. Waide;, N. Surmeli;, A. Gardiner;, J. Tait;, P. Fonseca;, J. Fong;, N. Quaresma; and C. Evans, *Impacts of the EU's Ecodesign and Energy/Tyre Labelling Legislation on Third Jurisdictions*, European Commission, 2014.
22. M. Valentova, M. Quicheron and P. Bertoldi, *LED Projects and Economic Test Cases in Europe*, European Commission, 2012.
23. Anses, Effets sanitaires des systèmes d'éclairage utilisant des diodes électroluminescentes, <https://www.anses.fr/fr/content/led-diodes-%C3%A9lectroluminescentes>, Accessed 26 October, 2015.
24. Anses, *Effets sanitaires des systèmes d'éclairage utilisant des diodes électroluminescentes (LED)*, 2010.
25. DEA (Danish Energy Agency), European LED market evolution and policy impacts, *European Commission, No 244/2009* [online], 2015.
26. U.S. (Department of Energy), Life-cycle assessment of energy and environmental impacts of LED lighting products Part I, *Solid-State lighting program* [online], 2012, 'Accessed' 26 November 2015.
27. The 2014 Nobel Prize in Physics - Press Release, *Nobelprize.org*, Nobel Media A B 2014, Accessed 29 November 2015.
28. H. Bechtel, P. J. Schmidt, A. Tücks, M. Heidemann, D. Chamberlin, R. Müller-Mach, G. O. Müller and O. Shchekin, 2010.

## References

---

29. N. Narendran, N. Maliyagoda, L. Deng and R. M. Pysar, 2001.
30. M. H. Crawford, J.J. Wierrer, A.J. Fischer, G.T. Wang, D.D. Koleske, G.S. Subramania, M.E. Coltrin, J.Y. Tsao and R. F. Karlicek, *Photonics Technology and Instrumentation*, 2013, 3.
31. W. D. Collins, M. R. Krames, G. J. Verhoeckx and N. J. M. Van Leth, Google Patents, 2003.
32. Y. Shimizu, K. Sakano, Y. Noguchi and T. Moriguchi, Google Patents, 1999.
33. LED Color Mixing: Basics and Backgrounds 2010-2015 - Press Release, [www.cree.com/xlamp](http://www.cree.com/xlamp).
34. Cree, Cree First to Break 300 Lumens-Per-Watt Barrier, <http://www.cree.com/News-and-Events/Cree-News/Press-Releases/2014/March/300LPW-LED-barrier>, Accessed 26 October, 2015.
35. Nichia, Highest Efficacy 200lm/W LED. 3030 packages that achieve the highest luminous efficacy, [http://www.nichia.co.jp/en/about\\_nichia/index.html](http://www.nichia.co.jp/en/about_nichia/index.html), Accessed 26 October, 2015.
36. O. O. Semiconductors, Osram constructs the world's most efficient LED lamp, [http://www.osram.com/osram\\_com/press/press-releases/trade\\_press/2014/osram-constructs-the-worlds-most-efficient-led-lamp/index.jsp](http://www.osram.com/osram_com/press/press-releases/trade_press/2014/osram-constructs-the-worlds-most-efficient-led-lamp/index.jsp), Accessed 26 October, 2015.
37. Philips, Details of the 200lm/W TLED lighting technology breakthrough unraveled, <http://www.newscenter.philips.com/main/standard/news/articles/20130411-details-of-the-200lm-w-tled-lighting-technology-breakthrough-unraveled.wpd#.Vi0OW7cvfIU>, Accessed 26 October 2015.
38. Product family data sheet: Cree XLamp XR-C LEDs - Press Release, <http://www.cree.com/~media/Files/Cree/LED-Components-and-Modules/XLamp/Data-and-Binning/XLampXRC.pdf>.
39. ETAP, *Dossier LED: Lighting with a new light source*, online: <http://www.etaplighting.com/>, 2014.
40. T. Whitaker, in *ledsmagazine*, LEDs magazine, online: <http://www.ledsmagazine.com/articles/2005/05/fact-or-fiction-leds-don-t-produce-heat.html>, 2005.
41. M. Dal Lago, M. Meneghini, N. Trivellin, G. Mura, M. Vanzi, G. Meneghesso and E. Zanoni, *Microelectronics Reliability*, 2012, 52, 2164-2167.
42. H.-C. Kuo, C.-W. Hung, H.-C. Chen, K.-J. Chen, C.-H. Wang, C.-W. Sher, C.-C. Yeh, C.-C. Lin, C.-H. Chen and Y.-J. Cheng, *Opt. Express*, 2011, 19, A930-A936.
43. C. Sommer, P. Hartmann, P. Pachler, M. Schweighart, S. Tasch, G. Leising and F. P. Wenzl, *Optical Materials*, 2009, 31, 837-848.
44. Application note: Mixing chamber design considerations for ChromaLit remote phosphor light sources - Press Release, <http://www.cree.com/~media/Files/Cree/LED-Components-and-Modules/XLamp/Data-and-Binning/XLampXRC.pdf>.
45. C.-W. Sher, K.-J. Chen, C.-C. Lin, H.-V. Han, H.-Y. Lin, Z.-Y. Tu, H.-H. Tu, K. Honjo, H.-Y. Jiang, S.-L. Ou, R.-H. Horng, X. Li, C.-C. Fu and H.-C. Kuo, *Opt. Express*, 2015, 23, A1167-A1178.
46. China's LED Fab Industry Will Install More than 1,000 MOCVD Tools from 2014 to 2018 - Press Release, <http://www.semi.org/en/node/51891>.
47. Global LED lighting market to reach US \$25.7 billion in 2015 - Press Release, [http://www.ledinside.com/intelligence/2014/11/global\\_led\\_lighting\\_market\\_to\\_reach\\_us\\_25\\_7\\_billion\\_in\\_2015](http://www.ledinside.com/intelligence/2014/11/global_led_lighting_market_to_reach_us_25_7_billion_in_2015).
48. LEDinside Projects Commercial LED Lighting Sector to Reach US\$26.65 B by 2015 - Press Release, [http://www.ledinside.com/intelligence/2015/5/ledinside\\_projects\\_commercial\\_led\\_lighting\\_sector\\_to\\_reach\\_27b](http://www.ledinside.com/intelligence/2015/5/ledinside_projects_commercial_led_lighting_sector_to_reach_27b).
49. Enterprise LED 2012: Commercial and Industrial Market Trends, Opportunities & Leading Companies - Press Release, <https://www.greentechmedia.com/research/report/enterprise-led-2012>.
50. K. M. Goodenough, J. Schilling, E. Jonsson, P. Kalvig, N. Charles, J. Tuduri, E. A. Deady, M. Sadeghi, H. Schiellerup, A. Müller, G. Bertrand, N. Arvanitidis, D. G. Eliopoulos, R. A. Shaw, K. Thrane and N. Keulen, *Ore Geology Reviews*, 2016, 72, Part 1, 838-856.
51. N. A. Mancheri, *Resources Policy*, 2015, 46, Part 2, 262-271.

## References

---

52. J. Wübbeke, *Resources Policy*, 2013, 38, 384-394.
53. B. C. G. G. Blasse, *Luminescent Materials*, Berlin, 1994.
54. S. E. Braslavsky, *Pure and Applied Chemistry*, 2007, 79, 293-465.
55. S. Shionoya and W. M. Yen, *Phosphor Handbook*, FL, 1999.
56. M. Sauer, J. Hofkens and J. Enderlein, in *Handbook of Fluorescence Spectroscopy and Imaging*, Wiley-VCH Verlag GmbH & Co. KGaA, 2011, DOI: 10.1002/9783527633500.ch1, pp. 1-30.
57. W. Nau, *ChemPhysChem*, 2011, 12, 2496-2497.
58. N. J. Turro, J. C. Scaiano and V. Ramamurthy, *Modern molecular photochemistry of organic molecules.*, 2010.
59. S. Reineke and M. A. Baldo, *Scientific Reports*, 2014, 4, 3797.
60. Z.-C. Liao, Z.-Y. Yang, Y. Li, B.-D. Wang and Q.-X. Zhou, *Dyes and Pigments*, 2013, 97, 124-128.
61. S. Kim, J. Y. Noh, K. Y. Kim, J. H. Kim, H. K. Kang, S.-W. Nam, S. H. Kim, S. Park, C. Kim and J. Kim, *Inorganic Chemistry*, 2012, 51, 3597-3602.
62. M. Tian, X. Peng, J. Fan, J. Wang and S. Sun, *Dyes and Pigments*, 2012, 95, 112-115.
63. J. Y. Choi, D. Kim and J. Yoon, *Dyes and Pigments*, 2013, 96, 176-179.
64. A. Köhler, J. S. Wilson and R. H. Friend, *Advanced Materials*, 2002, 14, 701-707.
65. J. Yoshino, N. Kano and T. Kawashima, *Dalton Transactions*, 2013, 42, 15826-15834.
66. F. Shao, H. Yuan, L. Josephson, R. Weissleder and S. A. Hilderbrand, *Dyes and pigments : an international journal*, 2011, 90, 119-122.
67. M. A. Baldo, M. E. Thompson and S. R. Forrest, *Pure and Applied Chemistry* 1999, 71, 2095-2106.
68. D. R. Kearns and W. A. Case, *Journal of the American Chemical Society*, 1966, 88, 5087-5097.
69. T. Takemura and H. Baba, *Bulletin of the Chemical Society of Japan*, 1969, 42, 2756-2762.
70. T. Itoh, *Spectrochimica Acta Part A: Molecular and Biomolecular Spectroscopy*, 2003, 59, 61-68.
71. H. J. Pownall and J. R. Huber, *Journal of the American Chemical Society*, 1971, 93, 6429-6436.
72. T. Itoh, *The Journal of Chemical Physics*, 1988, 88, 7257-7257.
73. T. Itoh, *Chemical Reviews*, 1995, 95, 2351-2368.
74. T. Takemura, Y. Yamada and H. Baba, *Chemical Physics*, 1982, 68, 171-177.
75. T. Takemura, Y. Yamada, M. Sugawara and H. Baba, *The Journal of Physical Chemistry*, 1986, 90, 2324-2330.
76. T. Okutsu, T. Kageyama, N. Kounose, J. Tsuchiya and H. Hiratsuka, *Chemical Physics Letters*, 1999, 299, 597-602.
77. T. Okutsu, A. Ishihara, N. Kounose, H. H. T. Suzuki, T. Ichimura and H. Hiratsuka, *Journal of Photochemistry and Photobiology A: Chemistry*, 2007, 186, 229-233.
78. O. Bolton, K. Lee, H.-J. Kim, K. Y. Lin and J. Kim, *Nat Chem*, 2011, 3, 205-210.
79. W. Z. Yuan, X. Y. Shen, H. Zhao, J. W. Y. Lam, L. Tang, P. Lu, C. Wang, Y. Liu, Z. Wang, Q. Zheng, J. Z. Sun, Y. Ma and B. Z. Tang, *The Journal of Physical Chemistry C*, 2010, 114, 6090-6099.
80. S. Reineke, N. Seidler, S. R. Yost, F. Prins, W. A. Tisdale and M. A. Baldo, *Applied Physics Letters*, 2013, 103, 093302.
81. D. Levy and D. Avnir, *Journal of Photochemistry and Photobiology A: Chemistry*, 1991, 57, 41-63.
82. A. Penzkofer, A. Tyagi, E. Slyusareva and A. Sizykh, *Chemical Physics*, 2010, 378, 58-65.
83. G. Oster, N. Geacintov and A. Ullah Khan, *Nature*, 1962, 196, 1089-1090.
84. A. Lobnik and O. Wolfbeis, *Journal of Sol-Gel Science and Technology*, 2001, 20, 303-311.
85. R. Reisfeld, *Chemical Physics Letters*, 1983, 95, 95-96.
86. D. Avnir, V. R. Kaufman and R. Reisfeld, *Journal of Non-Crystalline Solids*, 1985, 74, 395-406.
87. G. Heliotis, E. Gu, C. Griffin, C. W. Jeon, P. N. Stavrinou, M. D. Dawson and D. D. C. Bradley, *Journal of Optics A: Pure and Applied Optics*, 2006, 8, S445.

## References

---

88. F. Hide, P. Kozodoy, S. P. DenBaars and A. J. Heeger, *Applied Physics Letters*, 1997, 70, 2664-2666.
89. B. Geffroy, P. le Roy and C. Prat, *Polymer International*, 2006, 55, 572-582.
90. D. Di Martino, L. Beverina, M. Sassi, S. Brovelli, R. Tubino and F. Meinardi, *Scientific Reports*, 2014, 4, 4400.
91. S.-Y. Kwak, S. Yang, N. R. Kim, J. H. Kim and B.-S. Bae, *Advanced Materials*, 2011, 23, 5767-5772.
92. P. Schlotter, R. Schmidt and J. Schneider, *Applied Physics A*, 1997, 64, 417-418.
93. J. Baur, P. Schlotter and J. Schneider, in *Advances in Solid State Physics 37*, ed. R. Helbig, Springer Berlin Heidelberg, Berlin, Heidelberg, 1998, DOI: 10.1007/BFb0108239, pp. 67-78.
94. J.-Y. Jin, H.-G. Kim, C.-H. Hong, E.-K. Suh and Y.-S. Lee, *Synthetic Metals*, 2007, 157, 138-141.
95. P. Uthirakumar, C.-H. Hong, E.-K. Suh and Y.-S. Lee, *Reactive and Functional Polymers*, 2007, 67, 341-347.
96. Y. Hong, J. W. Y. Lam and B. Z. Tang, *Chemical Communications*, 2009, DOI: 10.1039/B904665H, 4332-4353.
97. A. Singh, R. Singh, M. Shellaiah, E. C. Prakash, H.-C. Chang, P. Raghunath, M.-C. Lin and H.-C. Lin, *Sensors and Actuators B: Chemical*, 2015, 207, Part A, 338-345.
98. T. Zhang, H. Ma, Y. Niu, W. Li, D. Wang, Q. Peng, Z. Shuai and W. Liang, *The Journal of Physical Chemistry C*, 2015, 119, 5040-5047.
99. B.-K. An, S.-K. Kwon, S.-D. Jung and S. Y. Park, *Journal of the American Chemical Society*, 2002, 124, 14410-14415.
100. Y. Q. Dong, J. W. Y. Lam and B. Z. Tang, *The Journal of Physical Chemistry Letters*, 2015, 6, 3429-3436.
101. J. Malkin, *CRC, Boca Raton, FL*, 1992.
102. T. B. de Queiroz, M. B. S. Botelho, L. De Boni, H. Eckert and A. S. S. de Camargo, *Journal of Applied Physics*, 2013, 113, 113508.
103. K. E. Sapsford, L. Berti and I. L. Medintz, *Angewandte Chemie International Edition*, 2006, 45, 4562-4589.
104. W. Tan, K. Wang and T. J. Drake, *Current Opinion in Chemical Biology*, 2004, 8, 547-553.
105. R. Jakubiak, Z. Bao and L. Rothberg, *Synthetic Metals*, 2000, 114, 61-64.
106. B. S. Gaylord, S. Wang, A. J. Heeger and G. C. Bazan, *Journal of the American Chemical Society*, 2001, 123, 6417-6418.
107. J. Chen, C. C. W. Law, J. W. Y. Lam, Y. Dong, S. M. F. Lo, I. D. Williams, D. Zhu and B. Z. Tang, *Chemistry of Materials*, 2003, 15, 1535-1546.
108. C. S. McCamy, *Color Research & Application*, 1992, 17, 142-144.
109. Z. Yue, Y. F. Cheung, H. W. Choi, Z. Zhao, B. Z. Tang and K. S. Wong, *Opt. Mater. Express*, 2013, 3, 1906-1911.
110. S. L. Sonawane and S. K. Asha, *The Journal of Physical Chemistry B*, 2014, 118, 9467-9475.
111. E. Jang, S. Jun, H. Jang, J. Lim, B. Kim and Y. Kim, *Advanced Materials*, 2010, 22, 3076-3080.
112. X. Yuan, R. Ma, W. Zhang, J. Hua, X. Meng, X. Zhong, J. Zhang, J. Zhao and H. Li, *ACS Applied Materials & Interfaces*, 2015, 7, 8659-8666.
113. I. S. Sohn, S. Unithrattil and W. B. Im, *ACS Applied Materials & Interfaces*, 2014, 6, 5744-5748.
114. S. Jun, J. Lee and E. Jang, *ACS Nano*, 2013, 7, 1472-1477.
115. H. Li, Z. Xu, B. Bao, N. Sun and Y. Song, *Journal of Materials Chemistry C*, 2016, 4, 39-44.
116. D. Hongyan, J. Yang, Z. Yugang, S. Dapeng, L. Chao, H. Jian, L. Xinzheng, Z. Hongyang, C. Lei and Z. Honghai, *Nanotechnology*, 2013, 24, 285201.
117. J. Eun-Pyo, S. Woo-Seuk, L. Ki-Heon and Y. Heesun, *Nanotechnology*, 2013, 24, 045607.
118. A. I. Ekimov, A. L. Efros and A. A. Onushchenko, *Solid State Communications*, 1985, 56, 921-924.
119. W. C. W. Chan and S. Nie, *Science*, 1998, 281, 2016-2018.
120. Y. Huang and S.-T. Ho, *Opt. Express*, 2006, 14, 3569-3587.
121. K. Chou and A. Dennis, *Sensors*, 2015, 15, 13288.

## References

---

122. F. Knittel, E. Gravel, E. Cassette, T. Pons, F. Pillon, B. Dubertret and E. Doris, *Nano Letters*, 2013, 13, 5075-5078.
123. X. Michalet, F. F. Pinaud, L. A. Bentolila, J. M. Tsay, S. Doose, J. J. Li, G. Sundaresan, A. M. Wu, S. S. Gambhir and S. Weiss, *Science*, 2005, 307, 538-544.
124. L.-M. Lacroix, F. Delpech, C. Nayral, S. Lachaize and B. Chaudret, *Interface Focus*, 2013, 3.
125. J. E. B. Katari, V. L. Colvin and A. P. Alivisatos, *The Journal of Physical Chemistry*, 1994, 98, 4109-4117.
126. L. Spanhel, M. Haase, H. Weller and A. Henglein, *Journal of the American Chemical Society*, 1987, 109, 5649-5655.
127. X. Peng, M. C. Schlamp, A. V. Kadavanich and A. P. Alivisatos, *Journal of the American Chemical Society*, 1997, 119, 7019-7029.
128. P. Reiss, M. Protière and L. Li, *Small*, 2009, 5, 154-168.
129. M. Cirillo, T. Aubert, R. Gomes, R. Van Deun, P. Emplit, A. Biermann, H. Lange, C. Thomsen, E. Brainis and Z. Hens, *Chemistry of Materials*, 2014, 26, 1154-1160.
130. J. Ziegler, A. Merkulov, M. Grabolle, U. Resch-Genger and T. Nann, *Langmuir*, 2007, 23, 7751-7759.
131. W. Zhang and X. Zhong, *Inorganic Chemistry*, 2011, 50, 4065-4072.
132. C. de Mello Donegá, *Physical Review B*, 2010, 81, 165303.
133. O. Schöps, N. Le Thomas, U. Woggon and M. V. Artemyev, *The Journal of Physical Chemistry B*, 2006, 110, 2074-2079.
134. E. Groeneveld, L. Witteman, M. Lefferts, X. Ke, S. Bals, G. Van Tendeloo and C. de Mello Donega, *ACS Nano*, 2013, 7, 7913-7930.
135. G. I. Maikov, R. Vaxenburg, A. Sashchiuk and E. Lifshitz, *ACS Nano*, 2010, 4, 6547-6556.
136. S. A. Ivanov, A. Piryatinski, J. Nanda, S. Tretiak, K. R. Zavadil, W. O. Wallace, D. Werder and V. I. Klimov, *Journal of the American Chemical Society*, 2007, 129, 11708-11719.
137. M. A. Hines and P. Guyot-Sionnest, *The Journal of Physical Chemistry*, 1996, 100, 468-471.
138. J. Donegan and Y. Rakovich, *Cadmium Telluride Quantum Dots: Advances and Applications*, 2013, 180.
139. L. Peng, M. He, B. Chen, Y. Qiao and B. Hu, *ACS Nano*, 2015, 9, 10324-10334.
140. B. O. Dabbousi, J. Rodriguez-Viejo, F. V. Mikulec, J. R. Heine, H. Mattoussi, R. Ober, K. F. Jensen and M. G. Bawendi, *The Journal of Physical Chemistry B*, 1997, 101, 9463-9475.
141. D. Bera, L. Qian, T.-K. Tseng and P. H. Holloway, *Materials*, 2010, 3, 2260.
142. J. Kwak, W. K. Bae, D. Lee, I. Park, J. Lim, M. Park, H. Cho, H. Woo, D. Y. Yoon, K. Char, S. Lee and C. Lee, *Nano Letters*, 2012, 12, 2362-2366.
143. P. O. Anikeeva, J. E. Halpert, M. G. Bawendi and V. Bulović, *Nano Letters*, 2009, 9, 2532-2536.
144. J. Lim, M. Park, W. K. Bae, D. Lee, S. Lee, C. Lee and K. Char, *ACS Nano*, 2013, 7, 9019-9026.
145. UV LED - Technology, Manufacturing and Application Trends - Press Release, Available at: [http://www.yole.fr/UVLED\\_2015.aspx#.VpwmcfnhDcc](http://www.yole.fr/UVLED_2015.aspx#.VpwmcfnhDcc).
146. H. Chen, H. Huang, X. Huang, J. N. Clifford, A. Forneli, E. Palomares, X. Zheng, L. Zheng, X. Wang, P. Shen, B. Zhao and S. Tan, *The Journal of Physical Chemistry C*, 2010, 114, 3280-3286.
147. M. C. Mota, P. Carvalho, J. Ramalho and E. Leite, *International Ophthalmology*, 15, 321-326.
148. X. Liu, J. M. Cole, P. G. Waddell, T.-C. Lin and S. McKechnie, *The Journal of Physical Chemistry C*, 2013, 117, 14130-14141.
149. K. Rurack and M. Spieles, *Analytical Chemistry*, 2011, 83, 1232-1242.
150. K. P. Wall, R. Dillon and M. K. Knowles, *Biochemistry and Molecular Biology Education*, 2015, 43, 52-59.
151. W. W. Yu, L. Qu, W. Guo and X. Peng, *Chem. Mater.*, 2003, 15, 2854-2860.
152. E. Kucur, F. M. Boldt, S. Cavaliere-Jaricot, J. Ziegler and T. Nann, *Anal. Chem.*, 2007, 79, 8987-8993.
153. P. G. Seybold, M. Gouterman and J. Callis, *Photochemistry and Photobiology*, 1969, 9, 229-242.

## References

---

154. H. J. Gruber, C. D. Hahn, G. Kada, C. K. Riener, G. S. Harms, W. Ahrer, T. G. Dax and H.-G. Knaus, *Bioconjugate Chemistry*, 2000, 11, 696-704.
155. S. A. Soper and Q. L. Mattingly, *Journal of the American Chemical Society*, 1994, 116, 3744-3752.
156. X. Wang, L. Qu, J. Zhang, X. Peng and M. Xiao, *Nano Letters*, 2003, 3, 1103-1106.
157. S. Hinds, S. Myrskog, L. Levina, G. Koleilat, J. Yang, S. O. Kelley and E. H. Sargent, *Journal of the American Chemical Society*, 2007, 129, 7218-7219.
158. C.-T. Chen, *Chemistry of Materials*, 2004, 16, 4389-4400.
159. B. Zhao, T. Zhang, B. Chu, W. Li, Z. Su, H. Wu, X. Yan, F. Jin, Y. Gao and C. Liu, *Scientific Reports*, 2015, 5, 10697.
160. D. Joly, L. Pellejà, S. Narbey, F. Oswald, J. Chiron, J. N. Clifford, E. Palomares and R. Demadrille, *Scientific Reports*, 2014, 4, 4033.
161. X. Wang, A. R. Morales, T. Urakami, L. Zhang, M. V. Bondar, M. Komatsu and K. D. Belfield, *Bioconjugate Chemistry*, 2011, 22, 1438-1450.
162. P. R. Hammond, *Optics Communications*, 1979, 29, 331-333.
163. C. W. Tang, S. A. VanSlyke and C. H. Chen, *Journal of Applied Physics*, 1989, 65, 3610-3616.
164. C.-B. Moon, W. Song, M. Meng, N. H. Kim, J.-A. Yoon, W. Y. Kim, R. Wood and P. Mascher, *Journal of Luminescence*, 2014, 146, 314-320.
165. Z. R. Li, *Organic Light-Emitting Materials and Devices, Second Edition*, 2015.
166. S. A. Jenekhe and J. A. Osaheni, *Science*, 1994, 265, 765-768.
167. Y.-H. Zhang, P.-Y. Gu, J.-B. Zhou, Y.-J. Xu, W. Liu, Q.-F. Gu, D.-Y. Chen, N.-J. Li, Q.-F. Xu and J.-M. Lu, *Journal of Materials Chemistry C*, 2014, 2, 2082-2088.
168. H. Li, Y. Guo, G. Li, H. Xiao, Y. Lei, X. Huang, J. Chen, H. Wu, J. Ding and Y. Cheng, *The Journal of Physical Chemistry C*, 2015, 119, 6737-6748.
169. R. Boonsin, G. Chadeyron, J.-P. Roblin, D. Boyer and R. Mahiou, *Journal of Materials Chemistry C*, 2015, 3, 9580-9587.
170. M. S. Shin, S. J. Lee, S. M. Chin, S. H. Lee, D. M. Pore, Y. Park, S.-G. Lee and K.-J. Hwang, *Bull. Korean Chem. Soc.*, 2011, 32, 3152-3154.
171. L. L. Woods, *Journal of the American Chemical Society*, 1958, 80, 1440-1442.
172. A. Eisfeld and J. S. Briggs, *Chemical Physics*, 2006, 324, 376-384.
173. Bruker, **SADABS, APEX2 and SAINT**, Bruker AXS Inc., Madison, Wisconsin, USA 2008.
174. G. Sheldrick, *Acta Crystallographica Section A*, 2008, 64, 112-122.
175. S. Chakraborty, P. Debnath, D. Dey, D. Bhattacharjee and S. A. Hussain, *Journal of Photochemistry and Photobiology A: Chemistry*, 2014, 293, 57-64.
176. E. G. McRae and M. Kasha, *The Journal of Chemical Physics*, 1958, 28, 721-722.
177. S. S. Park, Y. S. Won, W. Lee and J. H. Kim, *The Journal of Physical Chemistry A*, 2011, 115, 2830-2836.
178. Y. Lei, Y. Liu, Y. Guo, J. Chen, X. Huang, W. Gao, L. Qian, H. Wu, M. Liu and Y. Cheng, *The Journal of Physical Chemistry C*, 2015, 119, 23138-23148.
179. Y. Zhao, L. Xiao, F. Wu and X. Fang, *Optical Materials*, 2007, 29, 1206-1210.
180. H. Tong, Y. Dong, M. Häußler, Y. Hong, J. W. Y. Lam, H. H. Y. Sung, I. D. Williams, H. S. Kwok and B. Z. Tang, *Chemical Physics Letters*, 2006, 428, 326-330.
181. H. Tong, Y. Hong, Y. Dong, Y. Ren, M. Häußler, J. W. Y. Lam, K. S. Wong and B. Z. Tang, *The Journal of Physical Chemistry B*, 2007, 111, 2000-2007.
182. T. Itoh, *Chemical Reviews*, 2012, 112, 4541-4568.
183. D. M. Epstein, S. Choudhary, M. R. Churchill, K. M. Keil, A. V. Eliseev and J. R. Morrow, *Inorganic Chemistry*, 2001, 40, 1591-1596.
184. J. Liu, X. Meng, H. Duan, T. Xu, Z. Ding, Y. Liu and L. Lucia, *Sensors and Actuators B: Chemical*, 2016, 227, 296-303.
185. J. Cheng, K. Wei, X. Ma, X. Zhou and H. Xiang, *The Journal of Physical Chemistry C*, 2013, 117, 16552-16563.
186. C. Gou, S.-H. Qin, H.-Q. Wu, Y. Wang, J. Luo and X.-Y. Liu, *Inorganic Chemistry Communications*, 2011, 14, 1622-1625.



## References

---

187. N. Roy, A. Dutta, P. Mondal, P. C. Paul and T. Sanjoy Singh, *Journal of Luminescence*, 2015, 165, 167-173.
188. J. R. Lakowicz, in *Principles of Fluorescence Spectroscopy*, ed. J. R. Lakowicz, Springer US, Boston, MA, 2006, DOI: 10.1007/978-0-387-46312-4\_6, pp. 205-235.
189. T. S. Singh, P. C. Paul and H. A. R. Pramanik, *Spectrochimica Acta Part A: Molecular and Biomolecular Spectroscopy*, 2014, 121, 520-526.
190. P. Puri and T. P. S. University, *Multi Scale Modeling of Ignition and Combustion of Micro and Nano Aluminum Particles*, 2008.
191. R. E. Krebs, *The History and Use of Our Earth's Chemical Elements: A Reference Guide*, 2006.
192. V. A. Montes, R. Pohl, J. Shinar and P. Anzenbacher, *Chemistry – A European Journal*, 2006, 12, 4523-4535.
193. X. Ma, G. K. Lim, K. D. M. Harris, D. C. Apperley, P. N. Horton, M. B. Hursthouse and S. L. James, *Crystal Growth & Design*, 2012, 12, 5869-5872.
194. D. S. Kalinowski, P. C. Sharpe, P. V. Bernhardt and D. R. Richardson, *Journal of Medicinal Chemistry*, 2008, 51, 331-344.
195. J. R. Lakowicz, *Topics in Fluorescence Spectroscopy: Volume 4: Probe Design and Chemical Sensing*, 2006.
196. G.-q. Wang, J.-c. Qin, C.-R. Li and Z.-y. Yang, *Spectrochimica Acta Part A: Molecular and Biomolecular Spectroscopy*, 2015, 150, 21-25.
197. B. Mondal, M. G. B. Drew and T. Ghosh, *Inorganica Chimica Acta*, 2010, 363, 2296-2306.
198. H. Hosseini-Monfared, N. Asghari-Lalami, A. Pazio, K. Wozniak and C. Janiak, *Inorganica Chimica Acta*, 2013, 406, 241-250.
199. J. Yu, Y. Yin, W. Liu, W. Zhang, L. Zhang, W. Xie and H. Zhao, *Organic Electronics*, 2014, 15, 2817-2821.
200. R. Pązik, D. Hreniak, W. Stręk, A. Speghini and M. Bettinelli, *Optical Materials*, 2006, 28, 1284-1288.
201. S. Mukherjee and P. Thilagar, *Chemical Communications*, 2015, 51, 10988-11003.
202. M. Talhavini, W. Corradini and T. D. Z. Atvars, *Journal of Photochemistry and Photobiology A: Chemistry*, 2001, 139, 187-197.
203. W. J. Akers, M. Y. Berezin, H. Lee and S. Achilefu, *Journal of biomedical optics*, 2008, 13, 054042-054042.
204. M. Yazdan Mehr, W. D. van Driel and G. Q. Zhang, *Microelectronics Reliability*, 2014, 54, 1544-1548.
205. W. Falicoff, *Scaling Up: Kilolumen Solid-State Lighting Exceeding 100 LPW via Remote Phosphor*, 2008.
206. C. V. Horie, *Materials for Conservation: Organic Consolidants, Adhesives and Coatings*, 2013.
207. D. Cai, A. Neyer, R. Kuckuk and H. M. Heise, *Journal of Molecular Structure*, 2010, 976, 274-281.
208. B. Chen, Q. Zhou, J. Li, F. Zhang, R. Liu, H. Zhong and B. Zou, *Opt. Express*, 2013, 21, 10105-10110.
209. G. He, J. Xu and H. Yan, *AIP Advances*, 2011, 1.
210. R. Mirhosseini, M. F. Schubert, S. Chhajed, J. Cho, J. K. Kim and E. F. Schubert, *Opt. Express*, 2009, 17, 10806-10813.
211. M. C. DeRosa and R. J. Crutchley, *Coordination Chemistry Reviews*, 2002, 233-234, 351-371.
212. M. K. Boyd and G. M. Zopp, *Annual Reports Section "B" (Organic Chemistry)*, 2004, 100, 351-375.
213. D. C. Neckers, *Annual Reports Section "B" (Organic Chemistry)*, 2008, 104, 349-369.
214. J.-F. Rontani, in *Environmental Photochemistry*, ed. P. Boule, Springer Berlin Heidelberg, Berlin, Heidelberg, 1999, DOI: 10.1007/978-3-540-69044-3\_10, pp. 263-284.
215. T. J. Dougherty, *Photochemistry and Photobiology*, 1987, 45, 879-889.
216. C.-S. Lu, C.-C. Chen, F.-D. Mai and Y.-C. Wu, *Journal of Photochemistry and Photobiology A: Chemistry*, 2007, 187, 167-176.

## References

---

217. M. Elvington, J. Brown, S. M. Arachchige and K. J. Brewer, *Journal of the American Chemical Society*, 2007, 129, 10644-10645.
218. S. Jana, S. Praharaj, S. Panigrahi, S. Basu, S. Pande, C.-H. Chang and T. Pal, *Organic Letters*, 2007, 9, 2191-2193.
219. R. S. Davidson, *Pesticide Science*, 1979, 10, 158-170.
220. I. U. o. Pure and A. C. O. C. Division, *Organic Photochemistry--2: Plenary Lectures*, 1968.
221. Y. Israëli, J. Lacoste, J. Cavezzan and J. Lemaire, *Polymer Degradation and Stability*, 1993, 42, 267-279.
222. C. Maier and T. Calafut, *Polypropylene: The Definitive User's Guide and Databook*, 1998.
223. J. L. Bolland and G. Gee, *Transactions of the Faraday Society*, 1946, 42, 236-243.
224. B. Arkles, G. L. Larson and R. Anderson, *Silicone Compounds, Register and Review*, 1987.
225. T. Akasaka, M. Nakagawa and W. Ando, *The Journal of Organic Chemistry*, 1986, 51, 4477-4479.
226. R. S. Atkinson, *Journal of the Chemical Society C: Organic*, 1971, DOI: 10.1039/J39710000784, 784-788.
227. Y. Cao, B. W. Zhang, Y. F. Ming and J. X. Chen, *Journal of Photochemistry*, 1987, 38, 131-144.
228. F. P. Rosselli, W. G. Quirino, C. Legnani, V. L. Calil, K. C. Teixeira, A. A. Leitão, R. B. Capaz, M. Cremona and C. A. Achete, *Organic Electronics*, 2009, 10, 1417-1423.
229. P. Simova, *Atlas of Vibrational Spectra of Liquid Crystals*, 1988.
230. A. Bruylants, L. Ghosez and H. G. Viehe, *Organic Synthesis: First International Conference on Organic Synthesis*, 2013.
231. J. Shinar, *Organic Light-Emitting Devices: A Survey*, 2013.
232. F. Papadimitrakopoulos, K. Konstadinidis, T. M. Miller, R. Opila, E. A. Chandross and M. E. Galvin, *Chemistry of Materials*, 1994, 6, 1563-1568.
233. D. W. Domaille, E. L. Que and C. J. Chang, *Nat Chem Biol*, 2008, 4, 168-175.
234. S. M. Borisov and O. S. Wolfbeis, *Chemical Reviews*, 2008, 108, 423-461.
235. S. W. Thomas, G. D. Joly and T. M. Swager, *Chemical Reviews*, 2007, 107, 1339-1386.
236. Z. Zhu, J. Qian, X. Zhao, W. Qin, R. Hu, H. Zhang, D. Li, Z. Xu, B. Z. Tang and S. He, *ACS Nano*, 2016, 10, 588-597.
237. J. Weiss, *Nature*, 1943, 152, 176-178.
238. V. Ramamurthy, D. R. Sanderson and D. F. Eaton, *Journal of the American Chemical Society*, 1993, 115, 10438-10439.
239. D. Wöhrle and G. Schulz-ekloff, *Advanced Materials*, 1994, 6, 875-880.
240. F. del Monte and D. Levy, *Chemistry of Materials*, 1995, 7, 292-298.
241. W. Lian, S. A. Litherland, H. Badrane, W. Tan, D. Wu, H. V. Baker, P. A. Gulig, D. V. Lim and S. Jin, *Analytical Biochemistry*, 2004, 334, 135-144.
242. Z. Gabelica, S. Valange, M. Shibata, H. Hotta and T. Suzuki, *Microporous and Mesoporous Materials*, 2001, 44-45, 645-652.
243. L. L. Hench and J. K. West, *Chemical Reviews*, 1990, 90, 33-72.
244. M. A. Aegerter and M. Mennig, *Sol-Gel Technologies for Glass Producers and Users*, 2004.
245. J. D. Mackenzie, *Journal of Non-Crystalline Solids*, 1982, 48, 1-10.
246. in *Ceramic Materials: Science and Engineering*, Springer New York, New York, NY, 2007, DOI: 10.1007/978-0-387-46271-4\_22, pp. 400-411.
247. C. J. Brinker and G. W. Scherer, *Sol-Gel Science: The Physics and Chemistry of Sol-Gel Processing*, 2013.
248. J. Texter, *Reactions And Synthesis In Surfactant Systems*, 2001.
249. U. Schubert, in *The Sol-Gel Handbook*, Wiley-VCH Verlag GmbH & Co. KGaA, 2015, DOI: 10.1002/9783527670819.ch01, pp. 1-28.
250. C. J. Brinker, *Journal of Non-Crystalline Solids*, 1988, 100, 31-50.
251. S. Santra, H. Yang, D. Dutta, J. T. Stanley, P. H. Holloway, W. Tan, B. M. Moudgil and R. A. Mericle, *Chemical Communications*, 2004, DOI: 10.1039/B411916A, 2810-2811.
252. S. Santra, P. Zhang, K. Wang, R. Tapeç and W. Tan, *Analytical Chemistry*, 2001, 73, 4988-4993.
253. H. Wang, K. Schaefer, A. Pich and M. Moeller, *Chemistry of Materials*, 2011, 23, 4748-4755.

## References

---

254. W. Stöber, A. Fink and E. Bohn, *Journal of Colloid and Interface Science*, 1968, 26, 62-69.
255. P. Adumeau, C. Gaillard, D. Boyer, J.-L. Canet, A. Gautier and R. Mahiou, *European Journal of Inorganic Chemistry*, 2015, 2015, 1233-1242.
256. R. P. Bagwe, C. Yang, L. R. Hilliard and W. Tan, *Langmuir*, 2004, 20, 8336-8342.
257. N. M. Correa, J. J. Silber, R. E. Riter and N. E. Levinger, *Chemical Reviews*, 2012, 112, 4569-4602.
258. C. Sanchez, L. Rozes, F. Ribot, C. Laberty-Robert, D. Grosso, C. Sassoie, C. Boissiere and L. Nicole, *Comptes Rendus Chimie*, 2010, 13, 3-39.
259. C. Sanchez, F. Ribot, L. Rozes and B. Alonso, *Molecular Crystals and Liquid Crystals Science and Technology. Section A. Molecular Crystals and Liquid Crystals*, 2000, 354, 143-158.
260. B. M. Krasovitsky and B. M. Bolotin, *Wiley-VCH, Weinheim*, 1988.
261. S. A. Kim, K. G. Heinze and P. Schwille, *Nat Meth*, 2007, 4, 963-973.
262. H. Wallrabe and A. Periasamy, *Current Opinion in Biotechnology*, 2005, 16, 19-27.
263. J.-Y. Jin, H.-Y. Lee, S.-H. Lee, S.-B. Ko, K. Zong and Y.-S. Lee, *Journal of Luminescence*, 2007, 127, 665-670.
264. R. S. Davidson and J. E. Pratt, *Journal of Photochemistry and Photobiology B: Biology*, 1988, 1, 361-369.
265. L. Song, E. J. Hennink, I. T. Young and H. J. Tanke, *Biophysical Journal*, 1995, 68, 2588-2600.
266. T. Casalini, M. Salvalaglio, G. Perale, M. Masi and C. Cavallotti, *The Journal of Physical Chemistry B*, 2011, 115, 12896-12904.
267. I. López Arbeloa, *Dyes and Pigments*, 1983, 4, 213-220.
268. I. L. Arbeloa, *Journal of the Chemical Society, Faraday Transactions 2: Molecular and Chemical Physics*, 1981, 77, 1725-1733.
269. S. De and R. Kundu, *Journal of Photochemistry and Photobiology A: Chemistry*, 2011, 223, 71-81.
270. C. Gaillard, P. Adumeau, J.-L. Canet, A. Gautier, D. Boyer, C. Beaudoin, C. Hesling, L. Morel and R. Mahiou, *Journal of Materials Chemistry B*, 2013, 1, 4306-4312.
271. M. Ali, P. Dutta and S. Pandey, *The Journal of Physical Chemistry B*, 2010, 114, 15042-15051.
272. M. v. Zanten, Doctor of Philosophy in Chemical Engineering, University of California Santa Barbara, 2007.
273. S. Santra, K. Wang, R. Tapeç and W. Tan, *BIOMEDO*, 2001, 6, 160-166.
274. S. Santra, B. Liesenfeld, C. Bertolino, D. Dutta, Z. Cao, W. Tan, B. M. Moudgil and R. A. Mericle, *Journal of Luminescence*, 2006, 117, 75-82.
275. S. De, S. Das and A. Girigoswami, *Colloids and Surfaces B: Biointerfaces*, 2007, 54, 74-81.
276. S. Das, A. P. Chattopadhyay and S. De, *Journal of Photochemistry and Photobiology A: Chemistry*, 2008, 197, 402-414.
277. K. K. Rohatgi and A. K. Mukhopadhyay, *Journal of Indian Chemical Society*, 1972, 49, 1311.
278. K. L. Arvan and N. E. Zaitseva, *Optics and Spectroscopy*, 1961, 10, 137.
279. J. Paczkowski, J. J. M. Lamberts, B. Paczkowska and D. C. Neckers, *Journal of Free Radicals in Biology & Medicine*, 1985, 1, 341-351.
280. R. F. Chen and J. R. Knutson, *Analytical Biochemistry*, 1988, 172, 61-77.
281. A. M. Brouwer, *Pure and Applied Chemistry*, 2011, 83, 2213-2228.
282. T. Amirthalingam, J. Kalirajan and A. Chockalingam, *Journal of Nanomedicine & Nanotechnology*, 2011, 2, 1000119.
283. M. J. Doughty, *Ophthalmic and Physiological Optics*, 2010, 30, 167-174.
284. A. Earp, C. E. Hanson, P. J. Ralph, V. E. Brando, S. Allen, M. Baird, L. Clementson, P. Daniel, A. G. Dekker, P. R. C. S. Fearn, J. Parslow, P. G. Stratton, P. A. Thompson, M. Underwood, S. Weeks and M. A. Doblin, *Opt. Express*, 2011, 19, 26768-26782.
285. H. S. Jang, H. Yang, S. W. Kim, J. Y. Han, S.-G. Lee and D. Y. Jeon, *Advanced Materials*, 2008, 20, 2696-2702.

## References

---

286. C. Forano, U. Costantino, V. Prévot and C. Taviot-Gueho, in *Handbook of Clay Science*, ed. G. L. E. Faiza Bergaya, Elsevier Amsterdam, The Netherlands, 2013, pp. Volume 5 Techniques and Applications Chapter 14.11, 745-782.
287. A. Illaik, C. Vuillermoz, S. Commereuc, C. Taviot-Guého, V. Verney and F. Leroux, *Journal of Physics and Chemistry of Solids*, 2008, 69, 1362-1366.
288. J. Tronto, A. C. Bordonal, Z. Naal and J. B. Valim, *Conducting Polymers / Layered Double Hydroxides Intercalated Nanocomposites*, 2013, DOI: 42654.
289. A. Corma, V. Fornés, R. M. Martín-Aranda and F. Rey, *Journal of Catalysis*, 1992, 134, 58-65.
290. K. Takagi, T. Shichi, H. Usami and Y. Sawaki, *Journal of the American Chemical Society*, 1993, 115, 4339-4344.
291. S. Ma, Q. Chen, H. Li, P. Wang, S. M. Islam, Q. Gu, X. Yang and M. G. Kanatzidis, *Journal of Materials Chemistry A*, 2014, 2, 10280-10289.
292. J. Serrano, V. Bertin and S. Bulbulian, *Langmuir*, 2000, 16, 3355-3360.
293. G. Choi, O.-J. Kwon, Y. Oh, C.-O. Yun and J.-H. Choy, *Scientific Reports*, 2014, 4, 4430.
294. M. Z. bin Hussein, Z. Zainal, A. H. Yahaya and D. W. V. Foo, *Journal of Controlled Release*, 2002, 82, 417-427.
295. Z. Matusinovic and C. A. Wilkie, *Journal of Materials Chemistry*, 2012, 22, 18701-18704.
296. M. Meyn, K. Beneke and G. Lagaly, *Inorganic Chemistry*, 1990, 29, 5201-5207.
297. I. Y. Park, K. Kuroda and C. Kato, *Journal of the Chemical Society, Dalton Transactions*, 1990, DOI: 10.1039/DT9900003071, 3071-3074.
298. U. Costantino, N. Coletti, M. Nocchetti, G. G. Aloisi, F. Elisei and L. Latterini, *Langmuir*, 2000, 16, 10351-10358.
299. J. Bauer, P. Behrens, M. Speckbacher and H. Langhals, *Advanced Functional Materials*, 2003, 13, 241-248.
300. S. Gago, T. Costa, J. Seixas de Melo, I. S. Goncalves and M. Pillinger, *Journal of Materials Chemistry*, 2008, 18, 894-904.
301. L. Latterini, F. Elisei, G. G. Aloisi, U. Costantino and M. Nocchetti, *Physical Chemistry Chemical Physics*, 2002, 4, 2792-2798.
302. G. G. Aloisi, U. Costantino, F. Elisei, L. Latterini, C. Natali and M. Nocchetti, *Journal of Materials Chemistry*, 2002, 12, 3316-3323.
303. F. J. Quites, J. C. Germino and T. D. Z. Atvars, *Colloids and Surfaces A: Physicochemical and Engineering Aspects*, 2014, 459, 194-201.
304. C. Chakraborty, K. Dana and S. Malik, *The Journal of Physical Chemistry C*, 2011, 115, 1996-2004.
305. H. Chen, W. Zhang, Z. Lin and Q. Ling, *Opt. Mater. Express*, 2013, 3, 105-113.
306. E. Angelescu, O. D. Pavel, R. Bîrjega, M. Florea and R. Zăvoianu, *Applied Catalysis A: General*, 2008, 341, 50-57.
307. O. D. Pavel, R. Bîrjega, M. Che, G. Costentin, E. Angelescu and S. Şerban, *Catalysis Communications*, 2008, 9, 1974-1978.
308. S. Miyata, *Clays and Clay Minerals*, 1975, 23, 369-375.
309. W. Jones and C. N. R. Rao, *Supramolecular Organization and Materials Design*, 2008.
310. M. Ogawa and H. Kaiho, *Langmuir*, 2002, 18, 4240-4242.
311. U. Costantino, F. Marmottini, M. Nocchetti and R. Vivani, *European Journal of Inorganic Chemistry*, 1998, 10, 1439-1446.
312. T. S. Stanimirova, G. Kirov and E. Dinolova, *Journal of Materials Science Letters*, 20, 453-455.
313. A. d. Roy, C. Forano and J. P. Besse, in *Layered Double Hydroxides: Present and Future*, ed. V. Rives, Nova Science Publishers, 2006, ch. 1, pp. 1-39.
314. G. W. Brindley and G. Brown, *Crystal Structures of Clay Minerals and their X-Ray Identification*, 1982.
315. F. Kooli, I. C. Chisem, M. Vucelic and W. Jones, *Chemistry of Materials*, 1996, 8, 1969-1977.
316. S. Mitchell, C. Gardner and W. Jones, *Sociedad Española de Mineralogía*, 2008, 9, 161-162.

## References

---

317. S. Kim, T. Kim, M. Kang, S. K. Kwak, T. W. Yoo, L. S. Park, I. Yang, S. Hwang, J. E. Lee, S. K. Kim and S.-W. Kim, *Journal of the American Chemical Society*, 2012, 134, 3804-3809.
318. H. S. Choi, Y. Kim, J. C. Park, M. H. Oh, D. Y. Jeon and Y. S. Nam, *RSC Advances*, 2015, 5, 43449-43455.
319. K. Gugula, L. Stegemann, P. J. Cywinski, C. A. Strassert and M. Bredol, *RSC Advances*, 2016, 6, 10086-10093.
320. W. K. Bae, J. Kwak, J. W. Park, K. Char, C. Lee and S. Lee, *Advanced Materials*, 2009, 21, 1690-1694.
321. J. S. Steckel, P. Snee, S. Coe-Sullivan, J. P. Zimmer, J. E. Halpert, P. Anikeeva, L.-A. Kim, V. Bulovic and M. G. Bawendi, *Angewandte Chemie International Edition*, 2006, 45, 5796-5799.
322. F. Aldeek, C. Mustin, L. Balan, G. Medjahdi, T. Roques-Carmes, P. Arnoux and R. Schneider, *European Journal of Inorganic Chemistry*, 2011, 2011, 794-801.
323. F.-A. Kauffer, C. Merlin, L. Balan and R. Schneider, *Journal of Hazardous Materials*, 2014, 268, 246-255.
324. M. Michalska, A. Aboulaich, G. Medjahdi, R. Mahiou, S. Jurga and R. Schneider, *Journal of Alloys and Compounds*, 2015, 645, 184-192.
325. A. Aboulaich, M. Michalska, R. Schneider, A. Potdevin, J. Deschamps, R. Deloncle, G. Chadeyron and R. Mahiou, *ACS Applied Materials & Interfaces*, 2014, 6, 252-258.
326. A. P. Alivisatos, *The Journal of Physical Chemistry*, 1996, 100, 13226-13239.
327. W. K. Bae, K. Char, H. Hur and S. Lee, *Chemistry of Materials*, 2008, 20, 531-539.
328. Q. Sun, Y. A. Wang, L. S. Li, D. Wang, T. Zhu, J. Xu, C. Yang and Y. Li, *Nat Photon*, 2007, 1, 717-722.
329. A. Rizzo, Y. Li, S. Kudera, F. Della Sala, M. Zanella, W. J. Parak, R. Cingolani, L. Manna and G. Gigli, *Applied Physics Letters*, 2007, 90, 051106.
330. S.-W. Baek, J.-H. Shim, H.-M. Seung, G.-S. Lee, J.-P. Hong, K.-S. Lee and J.-G. Park, *Nanoscale*, 2014, 6, 12524-12531.
331. B. El-Kareh, *Fundamentals of Semiconductor Processing Technology*, 1995, 43-44.
332. Z. Wu, J. Liu, Y. Gao, H. Liu, T. Li, H. Zou, Z. Wang, K. Zhang, Y. Wang, H. Zhang and B. Yang, *Journal of the American Chemical Society*, 2015, 137, 12906-12913.
333. H. Sun, F. Zhang, H. Wei and B. Yang, *Journal of Materials Chemistry B*, 2013, 1, 6485-6494.
334. K. L. Knappenberger, D. B. Wong, W. Xu, A. M. Schwartzberg, A. Wolcott, J. Z. Zhang and S. R. Leone, *ACS Nano*, 2008, 2, 2143-2153.
335. C. R. Kagan, C. B. Murray and M. G. Bawendi, *Physical Review B*, 1996, 54, 8633-8643.
336. J. Laverdant, W. D. d. Marcillac, C. Barthou, V. D. Chinh, C. Schwob, L. Coolen, P. Benalloul, P. T. Nga and A. Maître, *Materials*, 2011, 4, 1182.
337. I. M. Smallwood, in *Handbook of Organic Solvent Properties*, Butterworth-Heinemann, Oxford, 1996, DOI: <http://dx.doi.org/10.1016/B978-0-08-052378-1.50014-1>, pp. 39-41.
338. I. M. Smallwood, in *Handbook of Organic Solvent Properties*, Butterworth-Heinemann, Oxford, 1996, DOI: <http://dx.doi.org/10.1016/B978-0-08-052378-1.50038-4>, pp. 141-143.
339. J. E. Jaffe and A. Zunger, *Physical Review B*, 1983, 28, 5822-5847.
340. D.-E. Nam, W.-S. Song and H. Yang, *Journal of Materials Chemistry*, 2011, 21, 18220-18226.
341. M. Fu, W. Luan, S.-T. Tu and L. Mleczko, *Journal of Nanomaterials*, 2015, 2015, 9.
342. M. Liu, W. Yao, C. Li, Z. Wu and L. Li, *RSC Advances*, 2015, 5, 628-634.
343. J. Hua, H. Cheng, X. Yuan, Y. Zhang, M. Liu, X. Meng, H. Li and J. Zhao, *RSC Advances*, 2015, 5, 30981-30988.
344. J. Ziegler, S. Xu, E. Kucur, F. Meister, M. Batentschuk, F. Gindele and T. Nann, *Advanced Materials*, 2008, 20, 4068-4073.
345. A. Aboulaich, D. Billaud, M. Abyan, L. Balan, J. J. Gaumet, G. Medjadhi, J. Ghanbaja and R. Schneider, *ACS Appl. Mater. Interfaces*, 2012, 4, 2561.
346. W.-S. Song and H. Yang, *Chemistry of Materials*, 2012, 24, 1961-1967.

## References

---

347. W. G. J. H. M. van Sark, P. L. T. M. Frederix, D. J. Van den Heuvel, H. C. Gerritsen, A. A. Bol, J. N. J. van Lingen, C. de Mello Donegá and A. Meijerink, *The Journal of Physical Chemistry B*, 2001, 105, 8281-8284.
348. C. Carrillo-Carrion, S. Cardenas, B. M. Simonet and M. Valcarcel, *Chemical Communications*, 2009, DOI: 10.1039/B904381K, 5214-5226.
349. A. A. Bol and A. Meijerink, *The Journal of Physical Chemistry B*, 2001, 105, 10203-10209.
350. P. E. Simmonds and L. Eaves, *Applied Physics Letters*, 1981, 39, 558-560.
351. H. Platz and P. W. Schenk, *Angewandte Chemie*, 1936, 49, 822-826.
352. H. Kim, B.-H. Kwon, M. Suh, D. S. Kang, Y. Kim and D. Y. Jeon, *Electrochemical and Solid-State Letters*, 2011, 14, K55-K57.
353. Z. He, C. He, Z.-M. Wang, E.-Q. Gao, Y. Liu and C.-H. Yan, *Dalton Transactions*, 2004, DOI: 10.1039/B315281B, 502-504.



# International and national conferences

## Oral communications

- 1. European Materials Research Society, 2-6 May 2016, Lille, France.**  
“Development of rare-earth-free luminescent composites for blue-LED based lighting devices”  
**Rachod Boonsin**, Pierre Vialat, Damien Boyer, Jean-Philippe Roblin, Geneviève Chadeyron, Rachid Mahiou.
- 2. Congrès National Optique Bretagne 2015, 6-9 July 2015, Rennes, France.**  
“Poudres et films composites luminescents sans terres rares pour des dispositifs d'éclairage à base de LEDs”  
**Rachod Boonsin**, Geneviève Chadeyron, Damien Boyer, Jean-Philippe Roblin, Rachid Mahiou.
- 3. XI Journée Sol-Gel et Chimie Liquide Rhône-Alpes-Auvergne, 26 March 2015, Saint-Etienne, France.**  
“Des luminophores organiques sans terres rares pour des LEDs blanches”  
**Rachod Boonsin**, Geneviève Chadeyron, Damien Boyer, Jean-Philippe Roblin, Rachid Mahiou.
- 4. 8<sup>th</sup> French - Spanish Meeting Solid State Chemistry and Physics, 2-4 April 2014, Auditorium of Vila - real, Castellón, Spain.**  
“Eco-friendly lighting system based on LEDs and organic phosphors”  
**Rachod Boonsin**, Geneviève Chadeyron, Damien Boyer, Jean-Philippe Roblin, Rachid Mahiou.
- 5. 4<sup>e</sup> Colloque Recherche de la Fédération Gay-Lussac, 4-6 December 2013, ESPCI ParisTech, Paris, France.**  
“Eco-friendly lighting system based on LEDs and organic phosphors”  
**Rachod Boonsin**, Geneviève Chadeyron, Damien Boyer, Jean-Philippe Roblin, Rachid Mahiou.



# Développement de luminophores organiques sans terres rares pour l'éclairage éco-énergétique à base de LED

Rachod Boonsin, Geneviève Chadeyron, Jean-Philippe Roblin, Damien Boyer et Rachid Mahiou

**Résumé** Cet article concerne la synthèse et l'étude optique de luminophores organiques sans terres rares pour la conception de dispositifs d'éclairage à base de diodes électroluminescentes (LED). Les synthèses des matériaux luminescents ainsi que leurs performances optiques sous excitation LED UV sont présentées et discutées.

**Mots-clés** Luminophores organiques, LED, éclairage.

**Abstract** Development of rare-earth free organic phosphors for eco-energy lighting based LEDs. This paper aims to present some rare-earth-free organic phosphors derived from pyran molecule and Schiff base ligand. Their spectroscopic and optical properties under ultraviolet and visible light excitation are characterized and discussed.

**Keywords** Organic phosphors, LEDs, lighting.

En France, l'éclairage consomme 49 TWh<sup>(1)</sup> annuellement, soit plus de 10 % de la consommation nationale totale d'électricité. Les luminaires à LED<sup>(2)</sup> représentent une alternative « verte » aux lampes fluorescentes en répondant notamment à des critères de préservation de l'environnement : réduction de la consommation d'énergie, technologies sans mercure ni plomb, recyclabilité à 98 %. Les prévisions à l'horizon 2020 laissent espérer pour les LED une efficacité lumineuse de 100 lm/W pour un coût divisé par quatre, ce qui les rend très prometteuses. Parallèlement, le marché de l'éclairage utilisant des sources de type LED pourrait croître d'un facteur 10 d'ici à 2020. Une demande très forte en luminophores, qui sont actuellement utilisés dans les luminaires à LED, va apparaître pour produire de la lumière blanche à partir de LED émettant dans le bleu ou l'ultraviolet.

Cependant, ces luminophores utilisent aujourd'hui des éléments de terres rares qui proviennent à 95 % de Chine, créant de fait une situation de quasi-monopole [1]. L'association d'une explosion de la demande et d'une source d'approvisionnement monopolistique représente un risque réel pour le déploiement de la technologie LED dans les années à venir en France et en Europe. Développer des luminophores sans terres rares dans les luminaires à LED représente donc un enjeu majeur.

Les travaux présentés dans cet article s'inscrivent dans ce contexte avec le développement de luminophores organiques sans terres rares qui, associés à une LED UV émettant à 365 nm, produisent de la lumière blanche. Pour cela, il convient de générer les trois couleurs primaires en même temps (bleu, rouge et vert), donc de synthétiser trois luminophores différents. Ces luminophores offrent une alternative

intéressante du fait de leur grande efficacité lumineuse, de leur faible coût, et également de la grande variété de couleurs qui peuvent être générées simplement en jouant sur les groupes fonctionnels.

## Résultats et discussion

Trois séries de luminophores organiques ont été étudiées (figure 1) ; deux d'entre elles sont dérivées du 2-(2,6-diméthyl-4H-pyran-4-ylidène)malononitrile [2-3] et la dernière repose sur un ligand de type base de Schiff [4]. Ces luminophores ont été choisis suite à une étude bibliographique qui a montré qu'ils génèrent les trois couleurs primaires après excitation dans le domaine de l'UV et que cette excitation est compatible avec des diodes UV commerciales. La synthèse de ces luminophores est aisée et les techniques classiques de caractérisation (RMN <sup>1</sup>H et <sup>13</sup>C, FTIR, GC-MS, etc.) ont été mises en œuvre pour identifier et confirmer leur structure.

Pour les luminophores de la série I, nous nous sommes intéressés à l'effet de la longueur des chaînes alkyles (n = 1, 4, 6, 8) sur les performances optiques (les études optiques de ces luminophores ont été réalisées à l'état solide). Les spectres d'émission enregistrés après excitation à la longueur d'onde appropriée (voir tableau) montrent une bande large comprise entre 400 et 600 nm avec une émission bleue majoritaire. Le luminophore ayant une chaîne constituée de six carbones présente la meilleure intensité d'émission et le rendement quantique absolu le plus élevé (33 %). Ce résultat pourrait être dû à un effet d'organisation particulier des chaînes aliphatiques à l'état solide qui éloignerait spatialement les noyaux de pyranyle malononitrile et aurait de ce



Cite this: *J. Mater. Chem. C*, 2015, **3**, 9580

Received 27th May 2015,  
Accepted 8th August 2015

DOI: 10.1039/c5tc01516b

www.rsc.org/MaterialsC

## Development of rare-earth-free phosphors for eco-energy lighting based LEDs†

Rachod Boonsin,<sup>a</sup> Geneviève Chadeyron,<sup>\*ab</sup> Jean-Philippe Roblin,<sup>ab</sup>  
Damien Boyer<sup>ab</sup> and Rachid Mahiou<sup>bc</sup>

Several phosphors without rare-earth elements were synthesized by a simple and practical method. Depending on their wavelength emitting range upon UV excitation, *i.e.* blue, green or red, they were classified in three groups. The phosphors exhibiting the best performances in optical properties were selected to be incorporated in free-standing silicon films and combined with a 365 nm LED. The thermal quenching of phosphors as well as the photometric parameters of the luminescent composite films were investigated. This white emission of the combination between the rare-earth-free phosphors based silicon film and LED shows a CRI >75 and CCT around 4000 K which can fulfil the requirements for indoor domestic lighting source.

### Introduction

White light emitting diodes (WLEDs) have reached efficiencies which should allow them to be candidates as light sources for future domestic indoor lighting.<sup>1</sup> The great interest in these WLEDs arises from their unique properties including low power consumption, environmental friendliness, small volume and long lifetime, making these devices very promising candidates to replace presently used incandescent and fluorescent lamps.<sup>2–5</sup> Current commercial WLEDs consist of a 460 nm InGaN blue LED chip combined with Ce-doped yttrium aluminum garnet (YAG:Ce) phosphor, which efficiently convert the blue light arising from the LED into a very broad yellow emission band, producing a white light.

However, this association suffers from some weaknesses such as poor color rendering index (CRI) and low stability of color temperature. Actually, in such a device, the deterioration of the chip or the YAG:Ce phosphor can result in significant color changes. Moreover, the color temperature of the combination is much too cold for indoor domestic lighting (>4500 K) due to a lack of red contribution. These drawbacks prevent this type of WLEDs from penetrating the general lighting market. In particular, the highly valued indoor domestic lighting requires a CRI better than 90, the color temperature comprises between

3000 and 4000 K with a luminous efficiency should be greater than or equal to 150 lumen per watts.<sup>6–8</sup> Combining deep-ultraviolet (DUV – 200 nm ≤ λ<sub>em</sub> ≤ 300 nm) or near-ultraviolet (UV – 300 nm ≤ λ<sub>em</sub> ≤ 400 nm) diode chips with a mixture of red, green and blue phosphors for producing white light appears as a promising alternative with several advantages for a better control of photometric parameters. One of the key points of this combination is an invisible emission of the LED chip contrary to blue chip.<sup>6</sup> This device can dominate a large panel of applications notably because they give access to the wide range of luminance and the tunable color rendering index (CRI) value. The versatility of the combination “UV LED/phosphors” is due to the possibility to play with the phosphors formulation, using the suitable phosphors with such an excitation, as well as the phosphors ratio. However, at this stage, according to the lighting market players, the aim of this combination in the lighting market should keep its focus on improving the UV LEDs technology, especially for DUV LEDs which still exhibit inadequate performances.<sup>9–12</sup> In recent years, the remote phosphors, which combine the UV/blue chip and phosphors in appreciable distance, have been investigated.<sup>13–15</sup> This kind of combination between LEDs and phosphors is of interest because these remote-type phosphor-LEDs overcome some technological limitations including thermal degradation of organic phosphors, light extraction efficiency and light distribution within remote-type designed packaging.

Today, according to the materials currently used, several problems have been identified. For example, the availability of rare earth materials is being affected by rising their prices and limiting the export products imposed by rare earth producing countries.<sup>16</sup> Thus, the development of alternative phosphors such as rare-earth-free phosphors<sup>17–20</sup> to preserve natural resources is highly important.

<sup>a</sup> Université Clermont Auvergne, ENSCCF, Institut de Chimie de Clermont-Ferrand, BP 10448, F-63000 Clermont-Ferrand, France.

E-mail: Geneviève.Chadeyron@univ-bpclermont.fr; Fax: +33 (0)4 73 40 71 08; Tel: +33 (0)4 73 40 71 09

<sup>b</sup> CNRS, UMR 6296, ICCF, F-63171 Aubière, France

<sup>c</sup> Université Clermont Auvergne, Université Blaise Pascal, Institut de Chimie de Clermont-Ferrand, BP 10448, F-63000 Clermont-Ferrand, France

† Electronic supplementary information (ESI) available: Experimental procedures and additional data of luminescent compounds. See DOI: 10.1039/c5tc01516b

Silica encapsulated fluorescein as a hybrid dye for  
blue-LED based lighting devices†

Cite this: DOI: 10.1039/c6tc01039c

R. Boonsin,<sup>ab</sup> G. Chadeyron,<sup>\*ab</sup> J.-P. Roblin,<sup>ab</sup> D. Boyer<sup>ab</sup> and R. Mahiou<sup>bc</sup>Received 10th March 2016,  
Accepted 7th June 2016

DOI: 10.1039/c6tc01039c

www.rsc.org/MaterialsC

Fluorescein–silica nanoparticles with a core–shell structure were prepared by a reverse microemulsion method. The nanoparticles exhibited suitable optical performances matching with a 450 nm LED for white-light emitting diodes. Their optical and thermal stability were investigated. Upon excitation at 450 nm the composite film comprised of fluorescein–silica nanoparticles and silicone led to white light with CCT around 6600 K and a maximum luminous efficacy of 26 lm W<sup>-1</sup>.

## Introduction

White light-emitting diode (WLED) based lighting devices have reached efficiencies which should allow them to be candidates as light sources for future domestic indoor lighting.<sup>1</sup> Among the different techniques for producing white light, the WLEDs are of great interest because of their properties including low power consumption, environmental friendliness, small volume and long lifetime, making these devices very promising candidates to replace the presently used incandescent and fluorescent lamps.<sup>2–5</sup> Generally, the commercial WLEDs consist of an InGaN blue-LED chip (with a monochromatic wavelength between 450 and 480 nm) combined with a Ce-doped yttrium aluminum garnet (YAG:Ce<sup>3+</sup>) phosphor as a luminescence converting material. The latter converts one part of the blue light arising from the LED into a very broad yellow emission band, producing a white light.

Although the WLED lighting devices offer many advantages over the conventional light sources, the average WLEDs remain more expensive than other lighting technologies. According to the report published by the U.S. Department of Energy (September 2013),<sup>6</sup> the phosphors represent 12% of the total manufacturing cost of WLEDs and the majority of the cost related to phosphors arises from the cost of rare earth materials. Then one possible way to cost reduction is to reduce the amount of phosphors in the packaged phosphor-converted LEDs (pc-LEDs) or replace these rare earth materials by low-cost rare earth-free luminescent compounds. As a result, the

development of phosphors without rare earth elements represents an important challenge for the expansion of the WLED market.

Fluorescein is one of the most common fluorophores employed for biochemical research and health care applications because of its biocompatibility, high molar absorptivity and excellent fluorescence quantum yield.<sup>7–9</sup> In the last few years, several research groups have demonstrated that the combination of a blue LED with fluorescein exhibited high conversion efficiency.<sup>10–12</sup> However, the fluorescein can be bleached by light exposure, radicals and peroxide species, which leads to chemical destruction and thus the loss of its fluorescence properties.<sup>13,14</sup> Moreover, the fluorescein is similar to many fluorophores in that it exhibits high fluorescence intensity in solution but not in the solid state due to the aggregation-induced quenching. In order to maintain the fluorescence properties in the solid state, the fluorophores should be de-aggregated as in a diluted state. Therefore, it is necessary to develop the encapsulation of fluorescein in a solid matrix playing the role of solvent in order to retain its characteristic luminescence properties.

Silica encapsulated organic dyes with a core–shell structure have been studied for entrapping organic dyes due to several advantages. Firstly, the reaction is simple and does not require extreme conditions (*i.e.* high temperature and pressure, inert atmosphere). Secondly, silica is a biocompatible and non-toxic substance.<sup>15</sup> Thirdly, the silica matrix as a protective encapsulator can improve the thermal stability and the photostability of fluorophores.<sup>16,17</sup> Two main methods based on the sol-gel process for silica coated organic dyes have been reported by using TEOS as a silica precursor. The first method is called the Stöber method.<sup>18</sup> The organic dye acts as a seed in the medium containing ethanol, TEOS, and ammonia for the growth of silica beads. However, the particle size and the size distribution are not well controlled. The second method is water-in-oil reverse microemulsion.<sup>16,19,20</sup> A water-soluble organic dye (like

<sup>a</sup> Université Clermont Auvergne, Sigma-Clermont, Institut de Chimie de Clermont-Ferrand, BP 10448, F-63000 Clermont-Ferrand, France.  
E-mail: Geneviève.Chadeyron@sigma-clermont.fr; Fax: +33 (0)4 73 40 71 08;  
Tel: +33 (0)4 73 40 71 09

<sup>b</sup> CNRS, UMR 6296, ICCF, F-63178 Aubière, France

<sup>c</sup> Université Clermont Auvergne, Université Blaise Pascal, Institut de Chimie de Clermont-Ferrand, BP 10448, F-63000 Clermont-Ferrand, France

† Electronic supplementary information (ESI) available. See DOI: 10.1039/c6tc01039c



# **Titre : Développement des luminophores sans terres rares pour l'éclairage éco-énergétique à base de diodes électroluminescentes**

## **Résumé**

Les luminaires à LEDs représentent une alternative "verte" aux lampes fluorescentes et aux lampes à incandescence en répondant notamment à des critères de préservation de l'environnement : réduction de la consommation d'énergie, technologies sans mercure ni plomb et recyclables à 98%. Cependant, ces luminophores, qui sont actuellement utilisés dans les luminaires à LEDs, contiennent aujourd'hui des éléments de terres rares qui sont issus à 95% de Chine, créant de ce fait une situation de quasi-monopole et un risque réel pour le déploiement de la technologie LED dans les années à venir. Dans le cadre de cette thèse, nous nous sommes intéressés au développement de luminophores sans terres rares pour produire de la lumière blanche dans les luminaires à LEDs. Au cours de ces travaux nous avons étudié trois types de luminophores sans terres rares: luminophores organiques, luminophores hybrides (organiques-inorganiques) et quantum dots (QDs) type cœur-coquille. Les études optiques réalisées sur ces luminophores sous excitation LEDs UV ou bleue nous ont permis de déterminer leurs caractéristiques colorimétriques (IRC, T(K), PLQY(%)) et de mettre en évidence l'évolution de leurs performances dans les conditions d'usage. Pour obtenir une lumière la plus proche du blanc idéal, les luminophores les plus performants ont été sélectionnés puis mélangés en proportion adéquate avec une matrice polymère de type silicone pour conduire à un film composite offrant une émission blanche de qualité sous excitation LEDs UV ou bleue. Un autre volet de ce travail a été dédié à l'étude de la stabilité de ces luminophores (films ou poudres) en fonction du temps et de la température. L'influence de ces paramètres sur les propriétés optiques a été déterminée. Des performances optiques de 30% ont été enregistrées avec des caractéristiques photométriques intéressantes. Aussi, l'ensemble des résultats obtenus montre l'intérêt de poursuivre ces études sur les luminophores sans terres rares qui offrent des propriétés optiques intéressantes. Même s'ils ne concurrencent pas encore les luminophores inorganiques pour l'application « éclairage grand public », les luminophores sans terres rares peuvent déjà se positionner sur d'autres secteurs d'activité comme par exemple : l'éclairage d'ambiance, la signalétique le marquage anti-contrefaçons.

**Mots-clés:** LEDs, luminophores sans terres rares, photoluminescence, photo-dégradation

## **Abstract**

Lighting technologies based on light-emitting diodes have become an alternative solution over the obsolete technologies (fluorescent lamps and incandescent lamps) due to their positive key criteria of environmental conservation: reduction of energy consumption and mercury/lead-free with 98% recycling technologies. However, the rare-earth elements, which are currently used in LED lightings, are produced by China at about 95%, thereby creating a monopoly situation on the rare-earth elements' market and also a risk to the deployment of LED technologies in coming years. In this work, we have been interested in the development of rare-earth-free luminescent materials for LED lighting applications in order to produce a white light emission. Three kinds of rare-earth-free luminescent materials have been investigated: organic phosphors, hybrid (organic-inorganic) phosphors and core-shell quantum dots (QDs). The optical studies of these phosphors recorded upon UV and/or blue excitations allow us to determine their colorimetric parameters (CRI, T(K), PLQY(%)) and to demonstrate their optical performances for use in lighting devices. In order to yield a color emission close to ideal white light, the best phosphors were selected and then introduced by mixing them in appropriate proportions into silicone polymers. Another part of this work was devoted to the studies of stability of phosphors (films or powders) under operating conditions of LEDs, moreover, variation of their optical properties as a function of time and temperature were also determined. The optical performances about 30% have been recorded with some interesting colorimetric parameters. Although these materials have presented lower photoluminescence properties compared with commercial rare-earth based inorganic phosphors for "public lighting" applications, they can already be positioned on other luminescent sectors such as indoor lighting, signage anti-counterfeit marking.

**Keywords:** LEDs, rare-earth-free phosphor, photoluminescence, photodegradation